University of Nevada, Reno

Mineralization and Timing of the Lover's Lane Breccia, Santa Rita Porphyry Cu-Mo Deposit, Grant County, New Mexico

A thesis submitted in partial fulfillment of the requirements for the degree of Master of Science in Geology

by

Randall L. Hannink

Dr. Tommy Thompson/Thesis Advisor

May, 2010

ProQuest LLC
789 East Eisenhower Parkway
P.O. Box 1346
Ann Arbor, MI 48106-1346

University of Nevada, Reno
Statewide • Worldwide

THE GRADUATE SCHOOL

We recommend that the thesis
prepared under our supervision by

RANDALL L. HANNINK

entitled

**Mineralization And Timing Of The Lover's Lane Breccia,
Santa Rita Porphyry Cu-Mo Deposit, Grant County, New Mexico**

be accepted in partial fulfillment of the
requirements for the degree of

MASTER OF SCIENCE

Tommy B. Thompson, Ph.D, Advisor

John Muntean, Ph.D, Committee Member

Victor Vasquez, Ph.D, Graduate School Representative

Marsha H. Read, Ph. D., Associate Dean, Graduate School

May, 2010

Abstract

The Lover's Lane breccia at Santa Rita is a magmatic-hydrothermal breccia with several distinct stages of mineral development. Mineralized clasts of stockwork and skarn ore are present and truncated by the matrix of the breccia. The matrix of the breccia hosts locally abundant molybdenite and chalcopyrite, associated with primary matrix-forming quartz, orthoclase, and biotite, and also with hydrothermal alteration of the matrix. Fluid inclusion and stable isotope analyses suggest meteoric water infiltrated the breccia shortly after the matrix had formed, and accompanied much of the chalcopyrite and pyrite. Molybdenite is intimately associated with the matrix-forming assemblage, as a late breccia feature which uses the matrix as a fluid pathway, with hydrous alteration of breccia in zones of Mg-rich skarn, and in post-breccia veinlets that cross-cut the matrix.

Documentation of cross cutting relationships during logging of drill core has led to the development of a model, in which the formation of the Lover's Lane breccia is a later phase of the 60 Ma Santa Rita system as a whole. Following intrusion of the Santa Rita stock and associated hypogene mineralization including the Cu- and Mo-mineralized Whim Hill breccia, a second stage of vapor bubble generation led to the brecciation in the Lover's Lane area. Magmatic fluid from this second event precipitated quartz, orthoclase, biotite, and sulfides, predominantly molybdenite, in the matrix. Meteoric influx into the breccia influenced various later alteration assemblages including chlorite-chalcopyrite and retrograde, hydrous alteration. Upon lithification of the breccia, a volumetrically minor breccia phase with an igneous matrix rebrecciated portions of the Lover's Lane breccia. Further magmatic crystallization produced fluids which entered the breccia, mixed with meteoric fluids present in the breccia, and precipitated

quartz±molybdenite±anhydrite±pyrite veinlets. The Hanover Hole diatreme breccia, a deep, post-mineral infill breccia, cross-cuts mineralization in the area, and is only intruded by an unaltered, barren rhyodacite dike.

Uranium/lead dating of zircons on selected intrusive phases that constrain the relative ages of the Lover's Lane breccia and Hanover Hole diatreme yielded ages which are several million years younger than previously determined Re-Os radiometric ages.

Acknowledgements

This project was made possible through funding by the Center for Research in Economic Geology at the University of Nevada, Reno. Phelps Dodge Exploration was the direct contributor to this project, and Ralph Stegen was responsible for the generous financial backing by Phelps Dodge. Many individuals have aided me greatly, including Mark Thoman, Victor Espinoza, Andy Lande, Bonnie Ertel, Dave Tulloch, and Robert Waidler, all Phelps Dodge mine staff and geologists with whom I interacted during my field work at Chino. My advisor Tommy Thompson has enlightened me on many aspects related to ore deposit geology and exploration. My classmates at UNR have also contributed insights, often in strong debates about the geology of ore deposits. Other people I would like to acknowledge are William Worthington, Holly Stein, Ray Donelick, and other unknown geologists whose data and core logging have added to the knowledge of the Lover's Lane breccia. My family and friends were also invaluable for their motivational support.

Table of Contents

List of Tables

Page

List of Figures

Page

List of Plates

Page

Introduction

The Santa Rita deposit in one of many large Laramide porphyry deposits in the southwest US across Arizona, New Mexico, and into Mexico. A location map is shown in Figure 1. Copper remains the bulk of the metal budget at Santa Rita, but molybdenite is also recovered. This study addresses the Lover's Lane breccia and associated molybdenite mineralization at Santa Rita. The Lover's Lane breccia was first recognized in the 1950's, when various workers mapped the outcrops of brecciated rock that straddle Lover's Lane in the Turnerville area northwest of the Chino pit at the Santa Rita deposit. Various drilling campaigns targeting the breccia body have been conducted over several decades, from the 1960's to the present. While elevated molybdenite values have been known since the early drilling, drilling in 2006 intersected a very high grade zone with a few hundred feet of >1% Mo in breccia. The unpredictable nature of this mineralized zone in the breccia, combined with variations in interpretation during core logging that spans decades and many workers, were important motivations to carry out this project.

Figure 1. Location map of Laramide porphyry copper deposits in the southwestern US, including Santa Rita. Modified from Titley (1982).

The anomalous nature of this breccia is two-fold. The timing of the breccia is clearly later than the main porphyry Cu mineralization at Santa Rita, based on clasts of mineralized porphyry and skarn ore in the breccia. There is another mineralized breccia pipe which is associated with the main hypogene mineralization at Santa Rita, the Whim Hill breccia, that is centered above the Santa Rita stock. The Lover's Lane breccia is not centered on the Santa Rita Stock (as typical in many porphyry-related breccias), but is located adjacent to the porphyry system and continues out into unmineralized rock. The

distal end of the Lover's Lane breccia is truncated by the Hanover Hole diatreme, a very weakly-mineralized phreatomagmatic breccia, based on the criteria listed in Sillitoe's (1985) classification scheme of breccias. The Lover's Lane breccia is a composite breccia body showing multiple phases of brecciation and mineralization, which complicates description as a single breccia.

This project was designed to combine detailed field study and laboratory work to describe the breccia and develop a better understanding of the processes that formed it and introduced the molybdenite. The field work included re-logging of drill core and some mapping of the surface exposures of breccia. The laboratory work included thin section petrography, fluid inclusion analyses, sulfur and oxygen isotope analyses, and U-Pb dating of certain intrusive phases. Combining the work done for this project and available data from previous studies has resulted in construction of cross sections through the breccia body which show lithology, mineralization type, breccia expression, and alteration. A model has also been developed for the formation and mineralization of the Lover's Lane breccia and Hanover Hole diatreme.

Mining History

Mining at Santa Rita has been documented to have occurred as early as 880 AD, evidenced by trace element studies that indicate Santa Rita to be the source of native copper artifacts found at an archeological site in Georgia. The Spanish presence in the area began at about 1598, but actual organized mining did not begin until 1801 (Thoman et al., 2006), when a period of mining by Spanish and Mexican merchants began, and

copper from Santa Rita was used for making coins in Chihuahua. Mining continued until 1837, when trouble with the Mimbres Apaches caused mining to cease until about 1850.

The Gadsden Purchase in 1854 made Santa Rita part of the United States, and mining was resumed in 1860, with only a brief hiatus due to control of New Mexico by the Confederacy in 1862. Introduction of dynamite in 1866 increased productivity, to about 300 tons of ore per day, with an estimated grade of 50% copper from native copper and chalcocite. Some of the high grade ore was direct-smelted in the vicinity of Santa Rita (Thoman et al., 2006).

During the period between 1874 and 1911 several enterprises operated the underground mines. The total copper production prior to the open pit mining is estimated at 40,000 tons (Rose and Baltosser, 1966). In 1911 large scale, open pit mining was initiated by the Chino Copper Company, using an estimate by J. Sully of General Electric of 9 million tons of ore at 2 to 3% Cu. This estimate was increased to 90 Mt at 1.8% Cu in 1912. The Chino Copper Company operated Santa Rita until it became part of the Chino Mines Division of Kennecott Copper Corp. in 1933. Kennecott owned and operated the mine until 1986, with production rates between 20,000 and 25,000 tons per day. Molybdenite recovery began in 1937, and heap leaching of lower grade copper ore was started in the early 1960's (Thoman et al., 2006).

Phelps Dodge purchased the mine in 1986, and implemented SX/EW in 1988. The mine has been in continuous operation except for a shutdown from 2002-2003. In 2007 Phelps Dodge was purchased by Freeport-McMoran.

District and Deposit Geology

The geologic understanding of the Santa Rita Quadrangle culminated in USGS Professional Paper 555, by William R. Jones, Robert M. Hernon, and Samuel L. Moore, published in 1967 (Jones et al., 1967). This excellent work remains the most comprehensive publication about the regional geology in the district. Subsequent publications and mine documents have added more detail and understanding of the geology and ore deposit genesis of the Santa Rita deposit. Figure 2 is the portion of the map published in Jones et al. (1967) that contains the Santa Rita deposit, area underlain by the Lover's Lane breccia, and outcrops of the Hanover Hole Diatreme breccia. Figure 3 is the outcrop map done by Kennecott geologists of the Lover's Lane and Turnerville area, which shows the outcrops of the Lover's Lane breccia (region of Fig. 3 is boxed in Fig. 2). The summary of the district and deposit geology presented here is from previously published works mentioned above, with additional information gained from the work done for this project.

The Santa Rita quadrangle is located near the transition between the Basin and Range Province of the Southwest and the Colorado Plateau. Relatively thin Paleozoic and Mesozoic sedimentary rocks overlie Precambrian basement, as this region was subject to subaereal exposure and uplift since deposition of the strata.

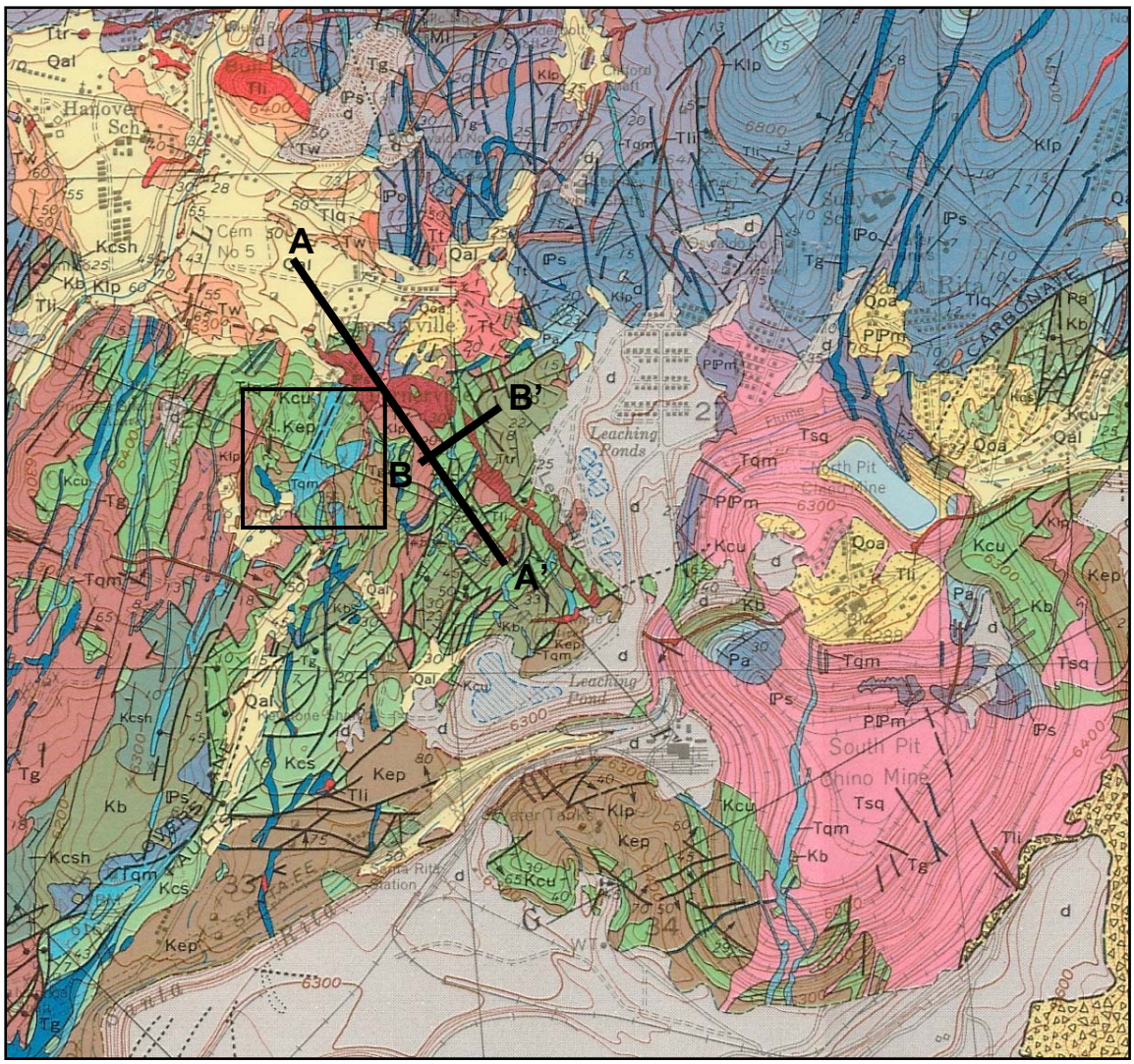

Figure 2. Geologic map of the Santa Rita deposit published by Jones et al. (1967). Tli = rhyodacite dikes; Tlq = quartz latite dikes and plugs; Tw = Tertiary Wimsattville Fm. (outcrops of Hanover Hole diatreme breccia); Ttr = Turnerville quartz latite dike; Tqm = quartz monzonite dikes; Tg = granodiorite porphyry dikes; Tsq = Santa Rita stock granodiorite; Klp = hornblende quartz diorite sills; Kep = quartz diorite porphyry sills; Kcu = Colorado Fm. of sandstone, shale, and limestone; Kb = Beartooth Fm. quartzite; Pa = Abo Fm. mudstone; lPs = Syrena Fm. limestone and shale. The locations of cross sections A-A' and B-B' completed for this study are shown, as is the location of Figure 3 (boxed area).

Figure 3. Outcrop map of the Lover's Lane breccia with the brecciated outcrops outlined with white dashed lines, located slightly northwest of the Chino pit, completed by Kennecott geologists in the 1950's. The road on the right side of the map is Lover's Lane, and Turnerville is the cluster of buildings in the upper right corner.

Stratigraphic Section

Figure 4 depicts the stratigraphy and generalized intrusive phases in the vicinity of the Santa Rita deposit. According to Jones et al. (1967), a small amount of Precambrian gneiss is exposed on the east flank of the Hanover-Fierro pluton, and was also intersected by drilling nearby. Deep drilling subsequent to that publication has identified Precambrian granite in place and as breccia clasts (Thoman et al, 2006). In the district, Precambrian rocks are described as granite, granite gneiss, and greenstone.

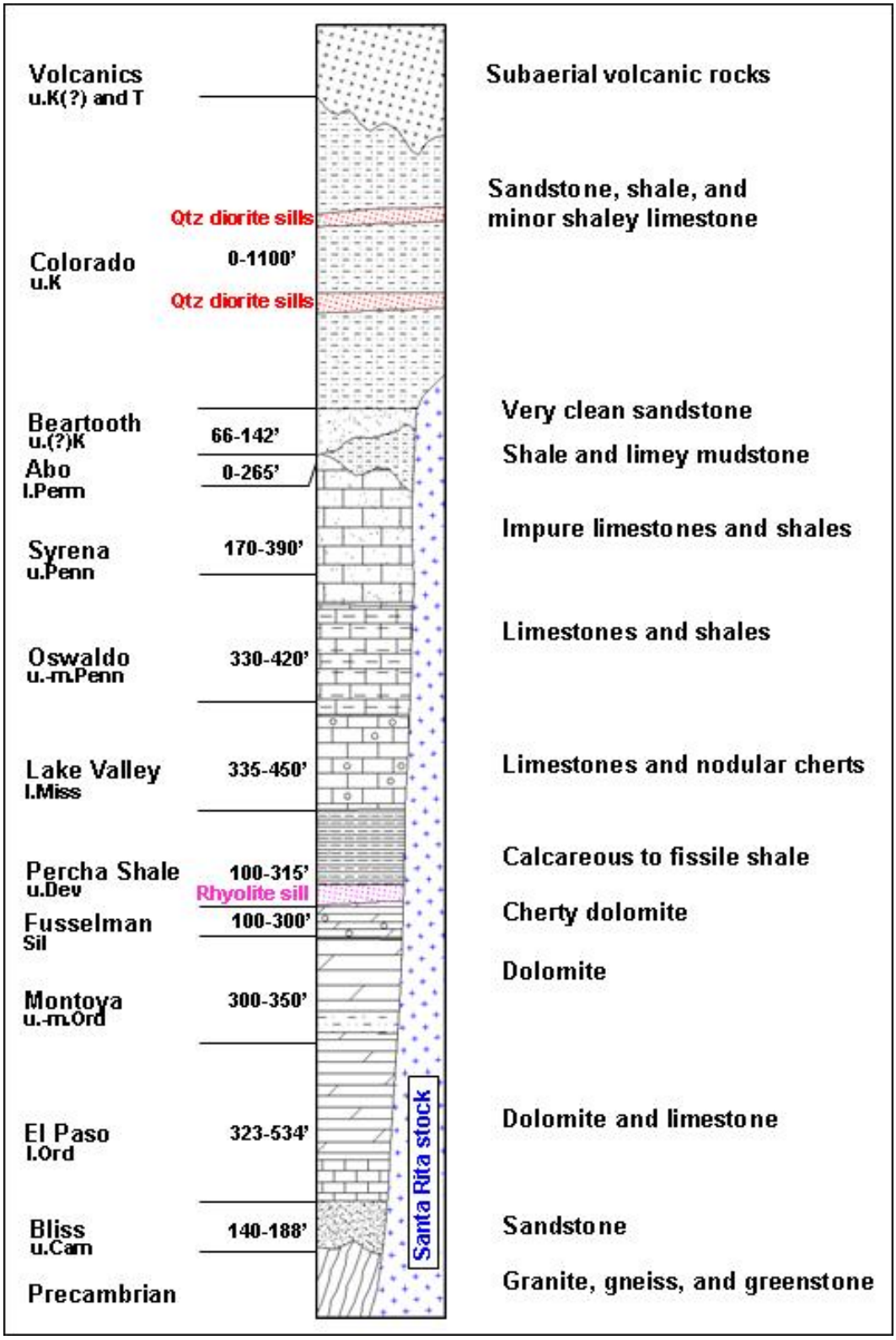

Figure 4. Stratigraphy and generalized intrusive phases in the vicinity of the Santa Rita deposit. Modified from Thoman et al (2006).

Paleozoic sedimentary rocks uncomformably overlie the Precambrian basement. The oldest Paleozoic rocks present are the sandstone, quartzite, and carbonate beds of the Bliss Formation, which is Upper Cambrian and Lower Ordovician (Jones et al., 1967). The total thickness of the Bliss Formation in measured sections in the Santa Rita area ranges from 146 ft. to 188 ft. (Jones et al., 1967).

The Lower Ordovician El Paso limestone apparently conformably overlies the Bliss Formation in the Santa Rita district. It is composed of 323 to 534 ft. of limestone, which varies from thinly bedded to massive, with local dolomitization especially near the ore deposits (Jones et al., 1967).

The Middle Ordovician, Late Ordovician, and Silurian are represented in the area near the Santa Rita deposit by the Montoya and Fusselman formations, which are dominantly dolomite with some sandstone. Metamorphic effects of intrusive rocks which masks primary features has led to the combination of these formations in the mine area. Total thickness of these formations is about 450 ft. These dolomite rocks commonly form massive magnesian silicate-rich, magnetite-rich skarns with local high grade copper mineralization.

The Late Devonian Percha Shale disconformably overlies the Fusselman-Montoya formations (Jones et al., 1967). The contact near the mine area hosts a rhyolite sill. Across the district the Percha Shale ranges in thickness from 100 to 315 ft. Near the mine, seen in core studied for this project, the Percha Shale has significant hornfels alteration, and is commonly mineralized with veins and local breccia, as seen in drill core for this study.

The Lake Valley Formation conformably overlies the Percha Shale. It consists of thin to thick bedded limestone with minor argillaceous beds and chert nodules. There is very little magnesium in the Lake Valley Formation. The upper 50 to 100 ft. of this formation is an important host for skarn mineralization in the district (Thoman et al, 2006). Total thickness ranges from 335 to 450 ft. Fossil evidence indicates that this formation is Early Mississippian (Jones et al., 1967).

An angular unconformity exists between the Mississippian and older rocks and the overlying Pennsylvanian strata. The Middle to Late Pennsylvanian Oswaldo Formation overlies the Lake Valley Formation, and consists of about 400 ft. of limestone with many thinly bedded shale units throughout and is an important host for skarn mineralization. Another host for copper skarn mineralization is the Late Pennsylvanian Syrena Formation consisting of argillaceous limestone, limy mudstone, silty limestone, with some cherty conglomerate horizons. Total thickness is about 350 ft.

The Permian Abo Formation conformably overlies the Syrena Formation, but is locally not present due to erosion. Maximum measured thickness is 265 ft. and consists of shale, limestone, limestone conglomerate, and mudstone. This is the uppermost Paleozoic unit, because of uplift and erosion from the Permian to the Middle Cretaceous.

The Cretaceous Beartooth Quartzite is present in outcrops surrounding the mine area. It has a maximum thickness of about 140 ft. and consists of silicified fine-grained sandstone with some shale interbeds. Remnant cross-bedding is also present. The Upper Cretaceous Colorado Formation apparently conformably overlies the Beartooth Quartzite. It consists of as much as 1100 ft. of thick sandstone, some sandy limestone, and sandy shale.

At Santa Rita Late Cretaceous and Early Tertiary(?) andesite breccia of both pyroclastic and epiclastic origin, rests on an erosional surface that cuts across the Colorado Formation (Jones et al., 1967). According to Jones et al. (1967), the minimum thickness of this andesite breccia is 1100 ft. These Late Cretaceous or Early Tertiary extrusive rocks are likely older than the Santa Rita stock and mineralization episodes (Jones et al., 1967), so they likely covered the area during mineralization.

The total thickness of rocks covering the deposit during mineralization would thus be the sum of the Paleozoic section above the intrusion (about 1,000 ft. of Colorado Shale), various sills intruded into the Paleozoic section (about 500 ft. of quartz diorite sills), and the volcanic rocks (minimum 1100 ft.). Jones et al. (1967) report that thicknesses of similar Late Cretaceous/Early Tertiary volcanics in other parts of New Mexico attain thicknesses of up to 3,000 ft. in the Caballo Mountains. Thus the maximum overburden during mineralization could have been about 4,500 ft. Neilson (1968) states that the Santa Rita stock is a very shallow intrusion (within 1500 ft. of the surface), but only the Paleozoic Colorado Shale and quartz diorite sills were included in the calculation.

Intrusive phases near Santa Rita

One of the main focii of Jones et al. (1967) was to classify the intrusive rocks in the district, and determine chronology of intrusion especially where they are related to mineralization. The following is a summary of their work and other observations pertaining to intrusive phases within and near the Santa Rita deposit. Specific phases that were intersected in core studied for this project are discussed in greater detail in a following section.

The sills of quartz diorite porphyry and rhyolite porphyry predate the intrusion of the Santa Rita stock and its apophyses. The relationship between the rhyolite and quartz diorite is unclear, as the rhyolite sill is intruded at the base of the Devonian Percha Shale and the quartz diorite sills intrude the Cretaceous Colorado Formation in the Santa Rita area. The quartz diorite sills have been divided into two separate phases based on texture, with an earlier, more porphyritic-appearing phase with phenocrysts of plagioclase, quartz, biotite, and hornblende in a fine grained groundmass (Rose and Baltosser, 1966). The later phase appears more equigranular, but thin section petrography has determined that it has phenocrysts of plagioclase and hornblende in a groundmass of mostly quartz and feldspar. Jones et al. (1967) indicate that the later quartz diorite (their "hornblende quartz diorite") is later than the rhyolite porphyry. The rhyolite sill has undergone alteration in the mine area and is described below in the lithology section.

The Santa Rita stock and Hanover-Fierro pluton to the north are compositionally and temporally similar. They both intrude through quartz diorite sills, and are cut by quartz monzonite dikes and post-ore dikes. Various authors have given different compositional names to the Santa Rita stock, from quartz monzonite to granodiorite, and variable (Jones et al., 1967; Rose and Baltosser, 1966; and Neilson, 1968). It is referred to in this paper as granodiorite, though the composition does range to quartz monzonite. The Santa Rita stock is intruded by texturally and compositionally slightly different dikes that also have been called granodiorite and quartz monzonite, adding to the confusion.

The granodiorite stocks and dikes and quartz monzonite dikes are cut by dikes of the quartz latite group. Included in this group is the Turnerville dike, which is called

quartz monzonite by Rose and Baltosser (1966), but is called quartz latite by Jones et al. (1967). In core studied for this project the dike has a different appearance than the quartz monzonite dikes. In either case, the Turnerville dike and other quartz latite dikes cut the mineralization and alteration in the majority of the Lover's Lane breccia, except for the late, high grade molybdenite (discussed below). The latest intrusion near the mine area is the rhyodacite dike, which is described below.

Structure

The Santa Rita quadrangle is dominated by both northeast and northwest-striking faults. The district is located in a large horst, bounded on the northwest and northeast by the Barringer and Mimbres faults, respectively (Jones et al., 1967). The southern extent of this somewhat triangular horst block is less defined, as there are several discontinuous faults that take up the movement. In the district and within the Santa Rita deposit, there is a very prominent northeast orientation to faulting, such as the Carbonate fault which drops the southern half of the Santa Rita deposit. A northwest orientation to faulting is present locally in to the Santa Rita deposit, and it is likely that the intrusion and ore deposit were facilitated by the intersections of these northwest and northeast-trending fault zones (Rose and Baltosser, 1966). The Lover's Lane breccia, the Hanover Hole diatreme, and the Santa Rita and Hanover-Fierro stocks all show northwest alignment.

Ore Deposit Geology at Santa Rita

The Santa Rita and Hanover-Fierro stocks are surrounded by zinc, lead, iron, and silver deposits, as well as copper skarns. The porphyry deposit at Santa Rita is by far the largest deposit in the district, and consists of supergene and hypogene porphyry-hosted ore, and skarn ore. Hypogene ore in the stock consists of veinlet-controlled chalcopyrite

and minor molybdenite in a zone surrounding a barren core of the stock, but surrounded by a very pyrite-rich zone that encompasses the margins of the stock (Neilson, 1968). The skarn ore at Santa Rita is located in the northern portions of the deposit, and consists of magnetite-rich and pyrite-rich calc-silicate and magnesium-silicate alteration of the limestone and dolomite wall rocks that contains local high grade chalcopyrite mineralization. Supergene enrichment of primary chalcopyrite ore composes most of the ore that has been mined at Santa Rita, in an irregular blanket that is very thin on the north side of the deposit (where the Paleozoic section is higher north of the Carbonate fault) and thicker to the south. Several episodes of enrichment are proposed to have occurred to generate the supergene grades at Santa Rita (Thoman et al., 2006). Locally, along faults, the supergene enrichment goes to substantial depth, and oxidation of these ores produced the very high grade veins that the early miners focused on. Santa Rita is well known for its native copper that occurs along these veins.

Hypogene breccia-hosted ore in the Lover's Lane breccia is the focus of this study. The southern extent of the Lover's Lane breccia is interpreted to be down-dropped to the south by the Carbonate Fault, and the footwall portion is known as the Estrella breccia (Thoman et al., 2006). The Estrella breccia is similar to the Lover's Lane breccia, but has been subjected to stronger oxidation and has much more hematite. The Estrella breccia was not studied for this project. Mineralization in the Lover's Lane breccia is discussed in detail in following sections.

Previous work and publications on the Santa Rita Deposit

The Santa Rita deposit has been the focus of many publications in the last 60 years. The three main publications on the Santa Rita deposit are Rose and Baltosser (1966), Jones et al. (1967), and Neilson (1968). Thoman et al. (2006) is the most recent summary the geology of the deposit and includes the most complete description of the Lover's Lane breccia in publication.

The geologic background of Rose and Baltosser (1966), Jones et al. (1967), and Neilson (1968) provided a basis for more detailed study of the Santa Rita deposit, which has led to the understanding of porphyry systems in general. The landmark fluid inclusion study of Reynolds and Beane (1985) was instrumental in furthering understanding of porphyry deposits in general.

Norton and Cathles (1973) proposed a model for the formation of magmatic-hydrothermal breccias in porphyry systems, to account for the void space that zbreccias fill. They use the Whim Hill breccia, the Lover's Lane breccia, and breccia pipes in Chile as type examples for their model. They calculate that the volume of water exsolving from a magma similar to the Santa Rita stock, if accumulated at the apex of the intrusion, would be sufficient to create a void large enough to account for the space necessary for the Whim Hill and Lover's Lane breccias. This fluid would concentrate beneath a chilled rind of the intrusion, forming the large void in the rock, and eventual piercement would lead to brecciation by block expulsion and stope caving, and the effects of alteration and mineralization seen in the breccias would follow. Aspects of this model concur with what is seen in core studied for this project, but it is not stated what was studied to develop their model.

Ahmad and Rose (1980) performed analyses on over 760 fluid inclusions in quartz and garnet from the Santa Rita deposit. Their data indicate that there were two distinct fluids present during the mineralization at Santa Rita. Intimately associated on a microscopic scale are low salinity (1 to 20% NaCl equivalent) and high salinity (32 to >60% NaCl equivalent) inclusions with the majority of the homogenization temperatures between 250º and 450ºC. Low density inclusions accompany many of the high salinity inclusions, indicating that some boiling accompanied formation of the veinlets and that the high salinity inclusions are the result of phase separation of magmatic fluid. Some of the lower salinity, liquid-rich inclusions are explained by a portion of these fluids cooling under pressure such that phase separation did not occur.

Reynolds and Beane (1985) studied fluid inclusions and mineral assemblages in the Santa Rita stock, in an attempt to constrain the fluid characteristics of various alteration and mineralization events in the Santa Rita deposit. Samples were collected from the Santa Rita stock and the Whim Hill breccia. Fluid inclusions of three main types were observed: halite-undersaturated liquid dominant, vapor-rich inclusions with CO_2, and halite-saturated liquid-rich inclusions. Early potassic alteration, characterized by high-Mg biotite, was accompanied by quartz veins with halite-saturated liquid-rich inclusions, vapor- and CO_2- rich inclusions. Homogenization temperatures from this assemblage range from 240º to 800ºC. Inclusions from this assemblage also contain abundant metallic daughter minerals, but it was determined that these fluids were not responsible for mineralization at Santa Rita.

Hypogene mineralization at Santa Rita is determined to accompany halite-undersaturated, liquid-rich inclusions, in a quartz ± chlorite ± chalcopyrite ± pyrite ±

magnetite ± molybdenite assemblage. This relationship is seen in samples from the Whim Hill breccia, and in veinlets in the stock where biotite has undergone chloritic alteration. This assemblage has moderate- to high- Mg ratios in chlorite and lower homogenization temperatures (260º to 360ºC) than the majority of the inclusions in the potassic assemblage. Their study supports some of the conclusions of this project, given the strong chlorite-chalcopyrite overprint on potassic (magmatic) breccia matrix in the Lover's Lane breccia. The meteoric influence (determined by oxygen isotope ratios and fluid inclusions in Reynolds and Beane, 1985) of the overprint is also indicated by low-salinity, moderate temperature fluid inclusions and oxygen isotopes of anhydrite (discussed below) completed for this project. However, geologic relationships show that the mineralization in the Lover's Lane breccia is a later, though similar, event. The work done by Reynolds and Beane focused on a small area within the deposit, not near the portion of the deposit studied in this project (the region to the northwest of the main deposit).

Taylor and Fryer (1983) use strontium isotopes in rocks in and surrounding the Santa Rita deposit to document fluid flow in various alteration assemblages. The potassic and propylitic assemblages (with little mineralization) have $^{87}Sr/^{86}Sr$ ratios very similar to those of the Santa Rita stock, indicating that the potassic and propylitic alteration assemblages are largely a product of magmatic fluids. More strongly mineralized assemblages, the phyllic and argillic alteration assemblages, have higher $^{87}Sr/^{86}Sr$ ratios, closer to those of rocks surrounding the deposit, which strongly indicates that the mineralization at Santa Rita was accompanied by fluids derived from the surrounding formations.

Audétat, Pettke, and Dolejš (2004) performed petrography and LA-ICP-MS analyses on a sample of quartz-monzodiorite dike from an outcrop west of the Santa Rita deposit. Though none was remaining in the sample, they determined that there was magmatic anhydrite in the dike, which is "comagmatic with the mineralized intrusions at Santa Rita." Using the Al-in hornblende geobarometer, they determined that the dike also contained phenocrysts that originated at two different depths, 6 and 14 km. A quick rise of some of the magma is also indicated by the presence of unaltered calcite inclusions in quartz. The presence of anhydrite, and the geochemical conditions of the quartz-magnetite-sphene-Mg-rich amphibole assemblage indicate that the magma was oxidized with an oxygen fugacity greater than NNO + 1.

Audétat and Pettke (2006) conducted LA-ICP-MS analyses on melt inclusions found in igneous rocks in the vicinity of the Santa Rita deposit. They sampled basaltic andesite, hornblende-diorite, quartz-monzodiorite, and rhyodacite. None of the samples were taken from within the Santa Rita deposit, but rather are of exposed dikes located more than a mile away to the north and west of the deposit. From their observations they conclude that the igneous activity in the area consisted of magma chambers of rhyodacitic to rhyolitic composition which were repeatedly intruded by mafic magma. The magmatic evolution and its effects on the sulfur and copper content of respective magmas are also investigated. The fact that magmatic Cu-bearing sulfides are present as melt inclusions in the hornblende-diorite porphyry (a phase likely representing the mixing of basaltic andesite and rhyolite/rhyodacite) indicates that the mixing phenomenon causes a precipitation of Cu-bearing sulfides, which is suggested to be a temporary reservoir for metals. This prevents the Cu from being incorporated into

silicates during crystallization. Further development of the system (to the final mineralization stage) is not concluded by the authors, nor is the question of whether formation of magmatic sulfides is a necessary step for a productive porphyry system.

Previous work relating to the Lover's Lane breccia

The Lover's Lane breccia is mentioned in Jones et al. (1967) and Rose and Baltosser (1966), and a possible mechanism of formation is discussed in Norton and Cathles (1973). The geologic map of the Santa Rita Quadrangle published by Jones et al. (1967) (Fig. 2) does not display the brecciated outcrops of the Lover's Lane breccia, but the general location and extent of the breccia on the surface is shown in the map of the local faults near the Santa Rita deposit (their Fig. 43, p. 120). Outcrop mapping by Kennecott geologists in the 1950's does show the surface expression of the breccia (Unpublished Kennecott mine maps) (Fig. 3). The most recent publication with descriptions of the Lover's Lane breccia is in the Guidebook for the Arizona Geological Society 2006 Fall Field Trip (Thoman et al., 2006).

A joint effort by Ralph Stegen and other geologists of Phelps Dodge Exploration and Holly Stein at Colorado State University to define the age of Santa Rita involved Re-Os dating of various molybdenite-mineralized zones in the Santa Rita deposit and Lover's Lane breccia. These data are summarized in Table 1 and displayed graphically Figure 5. That work, including sampling and analyses, was done prior to the start of this project. These data are discussed below as it relates to the work done on this project regarding the timing of the molybdenite mineralization.

Re-Os Data for molybdenite samples from the Santa Rita deposit					
Location and mineralization type	**Sample site**	**Sample number**	**Re, ppm**	**187Os, ppb**	**Age, Ma**
Santa Rita stock, hypogene	D2147, 1767-1778'	MDID-712	65.8	41.66	60.43 ± 0.23
	D2147, 1767-1778'	MDID-730	66.03	41.67	60.24 ± 0.20
	D1887, 1111-1114'	MDID-713	79.5	49.37	59.30 ± 0.21
Whim Hill Breccia, hypogene event	Whim Hill Breccia	MDID-716	173.0	106.15	58.55 ± 0.20
	Whim Hill Breccia	MDID-731	203.6	124.84	58.53 ± 0.21
Lover's Lane Breccia, disseminated in matrix	D1964, 1970-1975'	MDID-732	8.10	4.883	57.53 ± 0.23
	D1974, 2447-2448'	MDID-717	69.08	41.73	57.65 ± 0.20
Intrusive breccia, disseminated in matrix	D2314, 2034'	MDID-715	52.54	30.93	57.29 ± 0.20
Crackle breccia cement	D2314, 1247'	MDID-714	406.2	243.57	57.24 ± 0.22

Table 1. Re-Os data for molybdenite from Santa Rita. Data are from Stegen and Stein (2007).

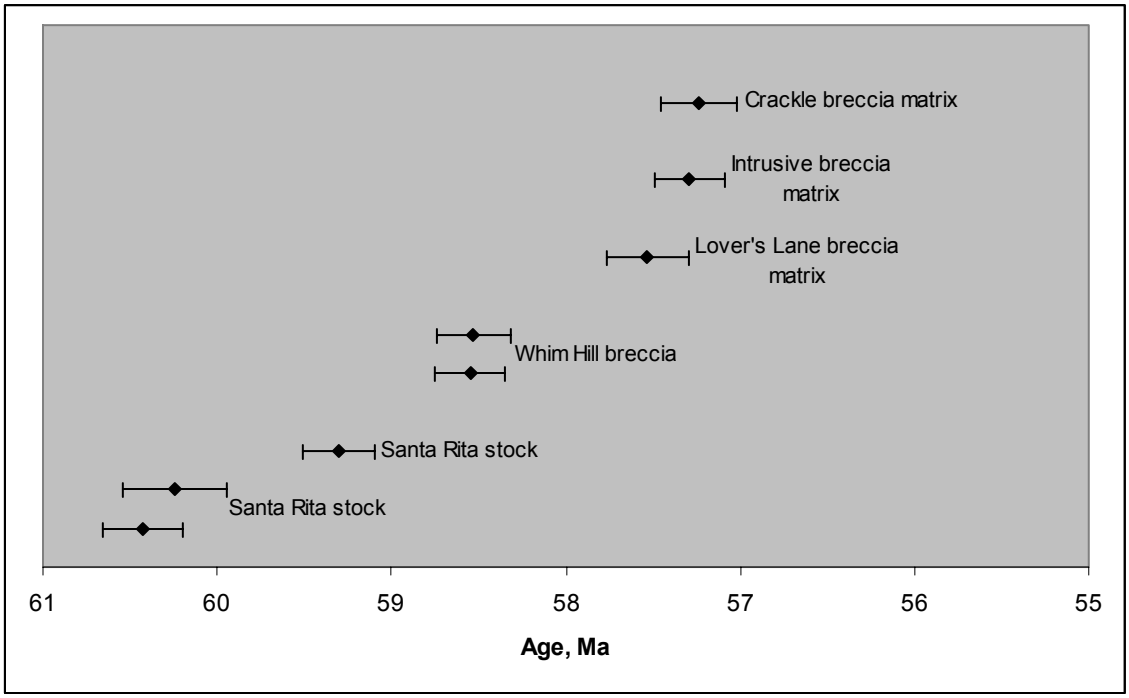

Figure 5. Graph of Re-Os dates of molybdenite at Santa Rita. Data are from Stegen and Stein (2007).

Core logging methods

The drill holes studied for this project were chosen based on location along two cross sections through the Lover's Lane breccia. The A-A' (Fig. 6) section extends from the most recent, deep drill hole (D2333, referred to as the Deep Hole) in the present Lee Hill pit, to the Hanover Hole diatreme, well northwest of the present mining area. The locations of these cross sections are shown in Figure 2. The B-B' (Fig. 7) section connects the A-A' section to the high-grade Mo zone near the perimeter of the breccia body (Fig. 2). The perimeter of the current open pit extends to the approximate location of the B-B' cross section. Plates 1 and 2 are expanded versions of these cross sections, with lithology, molybdenite mineralization type and ore grade envelopes, and alteration type and intensity indicated on the drill hole traces. These plates are intended for data presentation of the more detailed features noted during the core logging and for future reference.

The core logging was conducted during the Summer 2007 field season, at the Chino mine and other core storage facilities in the area. The core dates from the late 1960's to 2007. Drill holes were logged in selected intervals, based on relevance to this study. This was determined by checking the previous logs for brecciated intervals, copper or molybdenum mineralization, or other feature such as a specific intrusive phase that might have relevance to this project. Two of the holes, D2023 and D2333, were fully relogged, as were the core tails of D2332 and D2329. The upper portions of the remaining drill holes were not relogged, and the lithological contacts are taken from the previous logs. For the most part the drill holes went through a few hundred feet of

unbrecciated sedimentary section with a few intrusive sills before intersecting breccia or massive intrusive rock to the total depth of the hole.

Logging was done both on paper and digitally. The procedure for relogging involved choosing a lithology for distinct rock units, whether it was in agreement with the previous log or not. One of the purposes of this project was to integrate some consistency into core logging of the breccia to aid in the interpretation and construction of cross sections. In some cases, my lithology picks were different from the mine logs. These were noted in my logs. Due to the scope of this project, and also due to the fact that most of the core had been split or sawn for assay, detailed structural information was not recorded.

Alteration type and intensity were also noted during logging, though this was subject to modification as the thin section petrography and mineralogical description were completed subsequent to the field work. Describing the macroscopic paragenesis as it pertained to alteration and mineralization was an important part of the core logging process, and samples were taken of the more important relationships to verify the logs. Notes were made of the sample locations, features present in the sample, and intended use in laboratory studies. Digital photographs were taken of the majority of the core to assist in and document the interpretations.

Logging the brecciated intervals involved description of matrix mineralogy, clast types and shapes, apparent mineralization and alteration paragenesis, and other features such as veining and intrusive phases that could constrain large scale paragenesis of the breccia.

Lithologic Cross Sections based on core logging

Figures 6 and 7 show the interpreted geology based on the logging. Cross-cutting relationships used to constrain the interpretation are presented below. The following section presents general descriptions of the rock types that are shown on the sections; more detail is given about the breccia in the petrography and mineralization sections of this paper.

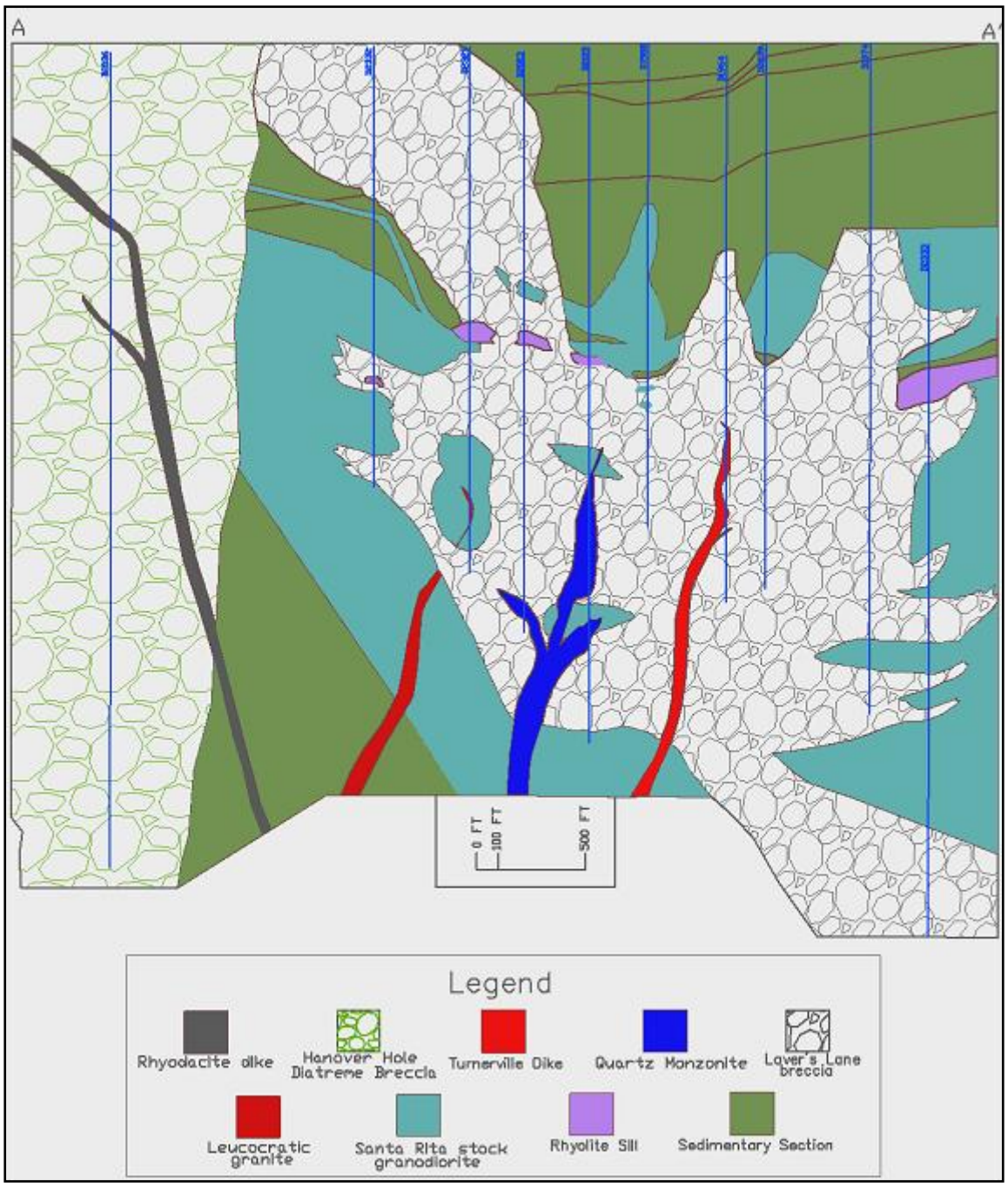

Figure 6. Cross section A-A'.

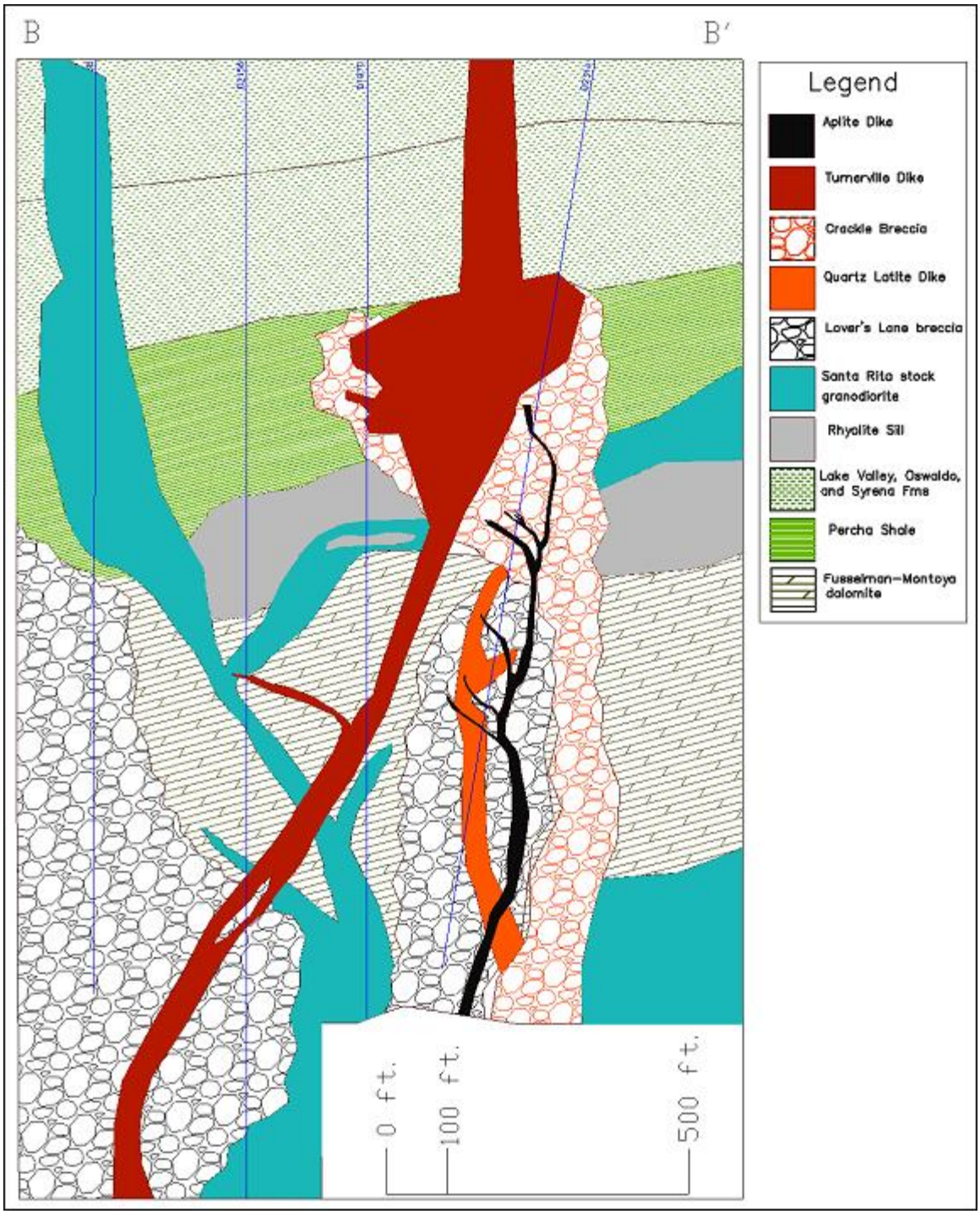

Figure 7. Cross section B-B'. This cross section presents a closer look at the high grade, molybdenite-mineralized breccia, and the upper limit of this cross section is about 550' below the current surface.

Lithology Descriptions

Breccia

The Lover's Lane breccia has considerable variations throughout its extent in clasts, matrix, alteration, and mineralization. The variations observed in core logging and surface exposure of the Lover's Lane breccia and Hanover Hole diatreme are shown in Figures 8 through 11 and summarized in Table 2. The breccia types in the chart are somewhat arbitrary divisions of the breccia body that is continuous (except the Hanover Hole diatreme), but represent the main expression types of the Lover's Lane breccia. The vertical variation in fragment type is controlled to some extent by lithology of the immediate country rock, but there is some apparent upward and downward transport of clasts. For the most part the breccia is matrix-supported with variable matrix:fragment ratios, ranging from about 80:20 to 30:70. In some places near its fringes the breccia resembles a shingle breccia with tabular fragments, but the interior of the breccia has more rounded fragments. The alteration and mineralization are described in greater detail below.

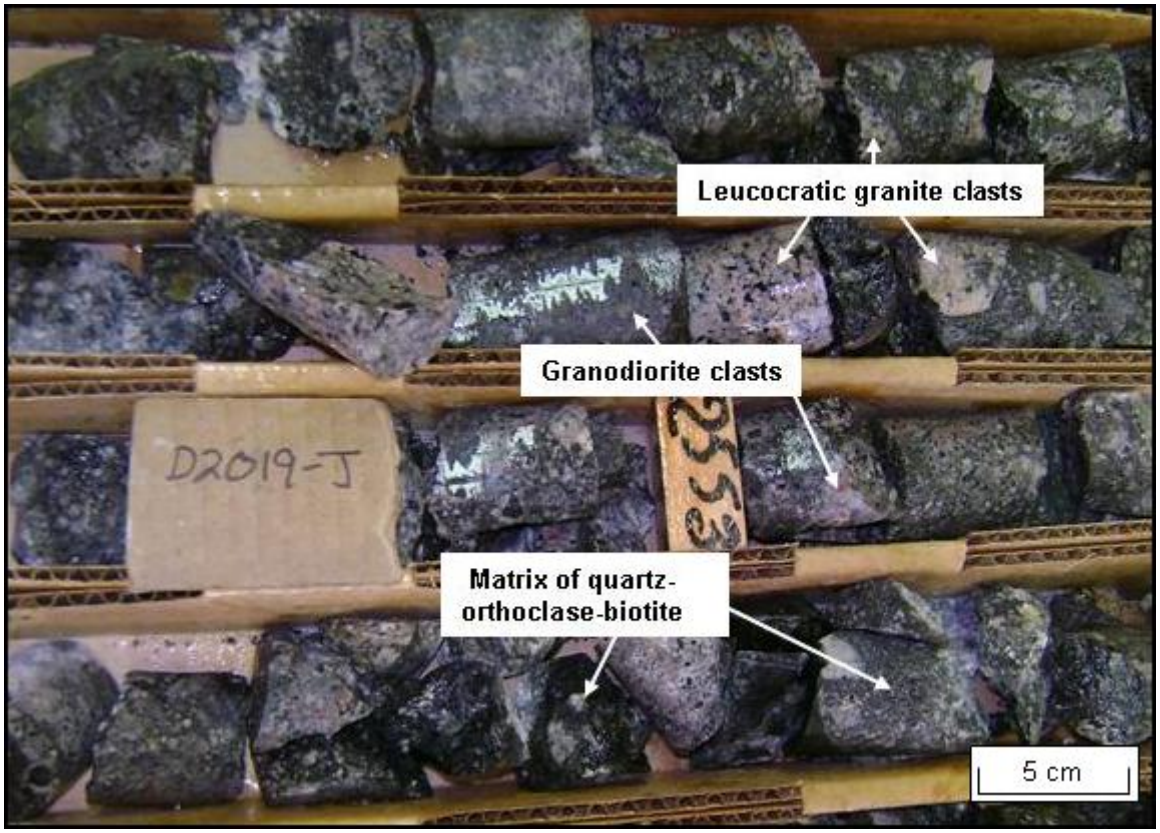

Figure 8. Deep "intrusive breccia," with clasts of leucocratic granite and variably altered granodiorite. This interval assays 0.06% Mo, with molybdenite present on fractures and a minor amount disseminated in the matrix (D2019-2553', NQ core).

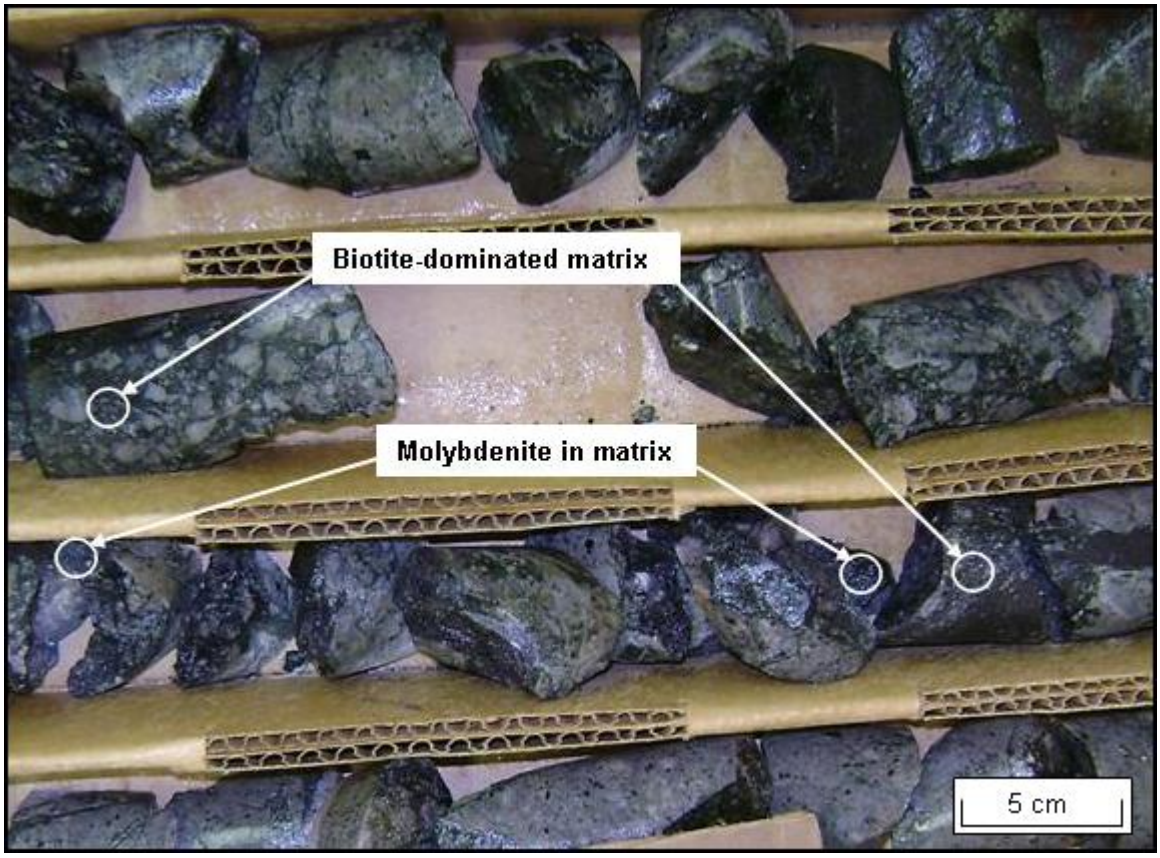

Figure 9. Breccia with disseminated molybdenite in matrix dominated by dark green biotite and minor chlorite. This interval assays 0.36% Mo (D1974-2450', NQ core).

Figure 10. Hanover Hole diatreme breccia, showing the extreme clast type variation, and changes in matrix:clast ratio (D2036-718', NQ core).

Figure 11. Molybdenite-cemented crackle breccia, assaying about 1% Mo. Clasts are mostly silicified rhyolite sill (D2314-1400').

Breccia variations observed in this study

Type, Location	Alteration	Mineralization	Support	Matrix:clast ratio	Matrix mineralogy	Clast type	Defining features of this breccia type
Biotite-healed breccia, Lover's Lane breccia interior portions	biotite, chlorite, serp/talc	disseminated molybdenite and chalcopyrite	matrix or clast	80:20 to 30:70	biotite, quartz, orthoclase, minor chlorite, anhydrite, actinolite, sericite, tourmaline	porphyry, dolomite, shale, quartzite, rhyolite sill, skarn	strong presence of green biotite or chlorite in matrix as final breccia healing
Pseudo-porphyry breccia, Lover's Lane breccia north end and local interior portions	minor potassic, some chlorite	little, some pyrite incorporated from clasts	matrix	70:30 to 10:90	quartz-orthoclase, little biotite	various intrusive phases (granodiorite, leucocratic granite) at depth, clasts approximate lithology at shallower levels	matrix appears porphyritic at a macroscopic scale
Crackle breccia, locally on perimeter of Lover's Lane	very little	molybdenite cemented	clast	10:90 to 5:95	molybdenite with minor quartz and rock flour in high grade zones	rhyolite sill, granodiorite, shale	volumetrically minor, very little or no primary silicates in breccia matrix
Skarn breccia, brecciated sedimentary section in Lover's Lane breccia	hydrous, retrograde	some molybdenite, locally strong chalcopyrite, pyrite, or magnetite	matrix or clast	varies with alteration intensity	varies: chlorite-actinolite, talc-serpentine	skarn	hydrous retrograde overprint on breccia, or breccia due to retrograde alteration of skarn
Anhydrite pseudo-breccia, locally at depth in Lover's Lane breccia and surrounding intrusive units	none	chalcopyrite, pyrite, minor molybdenite	thick fracture fill	NA	massive anhydrite	breccia, granodiorite	massive anhydrite filling fractures
Hanover Hole diatreme	minor epidote or chlorite, calcite veinlets	very little, visible chalcopyrite and pyrite at depth likely from clasts	matrix	95:5 to 30:70	rock flour, small fragments of broken wall rocks, no tuffaceous material	shale, granodiorite, skarn, quartz-latite, quartz-monzonite, re-brecciated diatreme fragments	rock flour-matrix-supported, bedding at shallower levels

Table 2. Summary of breccia types observed in this study.

Santa Rita stock and related intrusive phases

The granodiorite shown in the cross sections (Figs. 6 and 7, Plates 1 and 2) includes the Santa Rita stock and other very similar, pre-breccia intrusive phases related

to the main hypogene mineralization of the deposit. Composition (determined by phenocryst content in core) is dominantly granodiorite, but varies to quartz monzonite. Core photographs of the Santa Rita stock and other intrusive phases are shown in Figure 12. In core logged for this project the granodiorite has a crowded porphyry texture with plagioclase and orthoclase phenocrysts up to several millimeters in size and biotite that ranges from thin books to barrel-shaped crystals up to several millimeters in height. Groundmass (as determined from thin section petrography) is dominantly sugary quartz+orthoclase. Quartz phenocrysts are rare, but are more prevalent in intervals that are closer in composition to quartz monzonite.

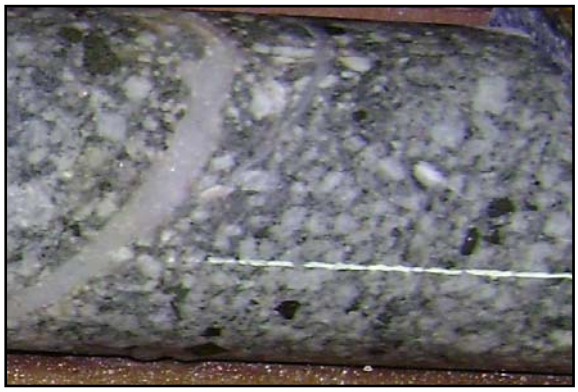

Santa Rita Stock, granodiorite porphyry

Quartz monzonite porphyry dike

Quartz latite porphyry

Leucocratic granite

Figure 12. Intrusive phases at Santa Rita

Represented by the dike in Figure 6 is an intrusive phase that is defined here as a leucocratic granite consisting of quartz and orthoclase with very minor shreddy biotite in places. This rock type is seen as breccia fragments in the Lover's Lane breccia (Fig. 13) and in the Hanover Hole diatreme, and has been previously called Precambrian granite. Though volumetrically minor, it is present in many of the deeper drill holes in the area, and evidence in the Deep Hole (D2333) and other holes suggests that it is a Tertiary intrusive that cuts the porphyritic phase of the Santa Rita stock at depth, possibly representing the escape of a small amount of magma from a deeply seated cupola.

Figure 13. Clast in deep breccia, with quartz-K-feldspar micrographic texture. This indicates brecciation following solidification of a high level, granitic cupola. The matrix here consists of quartz and K-feldspar, with interstitial brown biotite. (D2333-2770').

Rhyolite Sill

The rhyolite sill in the cross sections is very similar mineralogically and texturally to rhyolite sills described by Jones et al. (1967), with silicified groundmass and ghost phenocrysts of quartz and orthoclase. According to them the sills intrude the section at the approximate level of the Percha Shale before intrusion of the Santa Rita stock. It is possible that very large blocks of this sill were surrounded by the breccias, as shown in the cross section A-A' (Fig. 6). Where brecciated this rock forms an unaltered crackle breccia that is host to some of the high grade molybdenite mineralization (Fig. 11).

Quartz monzonite porphyry

The quartz monzonite porphyry that is shown intruding the Lover's Lane breccia in Figure 6 is a mineralogically similar dike to earlier quartz monzonite variants of the Santa Rita stock, but is unbrecciated and unmineralized, and is possibly related to exposures of quartz monzonite mapped by Jones et al. (1968) and Chino mine geologists in the Turnerville area. It is porphyritic, with small quartz, plagioclase, and biotite phenocrysts and some poikolitic orthoclase phenocrysts up to a centimeter, and was in places previously logged as granodiorite.

Quartz latite

The quartz latite porphyry dikes seen in core are tentatively correlated with the Turnerville dike which crops out south of Turnerville. Descriptions of the Turnerville dike by Jones et al. (1968) are of surface exposures with intense alteration and supergene effects, and as such vary slightly from what is seen in core. Rose and Baltosser (1966) call the Turnerville dike a quartz monzonite, but descriptions in Jones et al (1968) and what was seen during core logging for this project led to calling this phase quartz latite.

This phase is porphyritic, with what appears to be two generations of phenocrysts, with the smaller generation consisting of orthoclase and lesser plagioclase about 1 millimeter in size and more euhedral. The larger generation consists of broken orthoclase, abundant clay/sericite altered plagioclase, and embayed quartz phenocrysts. The groundmass has a greenish-beige color and makes up over 50% of the rock. There appears to be at least two separate dikes of this rock type, as determined by crosscutting relationships discussed in a later section. In places the quartz latite has inclusions of intensely chlorite-altered and pyrite-mineralized breccia fragments and fragments of unbrecciated wall rocks. Near its contacts this phase can have strong flow banding and autobrecciation with quartz latite fragments in the quartz latite matrix.

Hanover Hole diatreme

The Hanover Hole diatreme is a deeply-rooted breccia located northwest of Turnerville and underlies a topographic depression in which the town of Hanover is located. Outcrops of the infill breccia rim the known extent of the diatreme and line the bed of Hanover Creek in the center of the body. A vertical core hole into this diatreme was drilled to a depth of 3749 ft. and did not intersect the bottom of the diatreme. Mapping done for this project indicates that the Hanover Hole diatreme truncates the Lover's Lane breccia in the Turnerville area, where the intrusive-matrix Lover's Lane breccia is truncated abruptly by the bedded infill of the Hanover Hole diatreme. The infill breccia is bedded in many outcrop exposures and in shallower core, with abundant cross bedding in places. The beds dip in general toward the center of the body. Individual beds within the infill breccia can vary from well sorted sandstone to poorly-sorted conglomerate. Some exposures resemble a hydrothermal breccia with angular

fragments of shale in a clast-dominated breccia, but these exposures are minor and possibly represent the less brecciated fringes of an eruptive feature. The deeper expressions of the diatreme lack bedding, and the angular to sub-rounded fragments make up a larger proportion of the rock, up to about 70%. In core the matrix is beige to light lime-green color, which becomes a darker green near contacts with dikes that cut the breccia, which are described below. The matrix is predominantly composed of angular pieces of rock flour (Fig. 14). Sericite and local pyrophyllite fills interstitial space in the matrix. Calcite and some chlorite are present in the matrix and in veinlets cross-cutting the matrix. At depth there is a very minor amount of disseminated pyrite, chalcopyrite and magnetite, but the core was not assayed below about 700 feet (highest copper grade is less than 0.1%), and these minerals appear to be derived from brecciation of a previous mineralization event. Clasts include granodiorite (Santa Rita stock), sedimentary rocks, skarn-mineralization, quartz latite, pseudo-porphyry breccia, and equigranular granite (either Precambrian granite or Tertiary leucocratic granite).

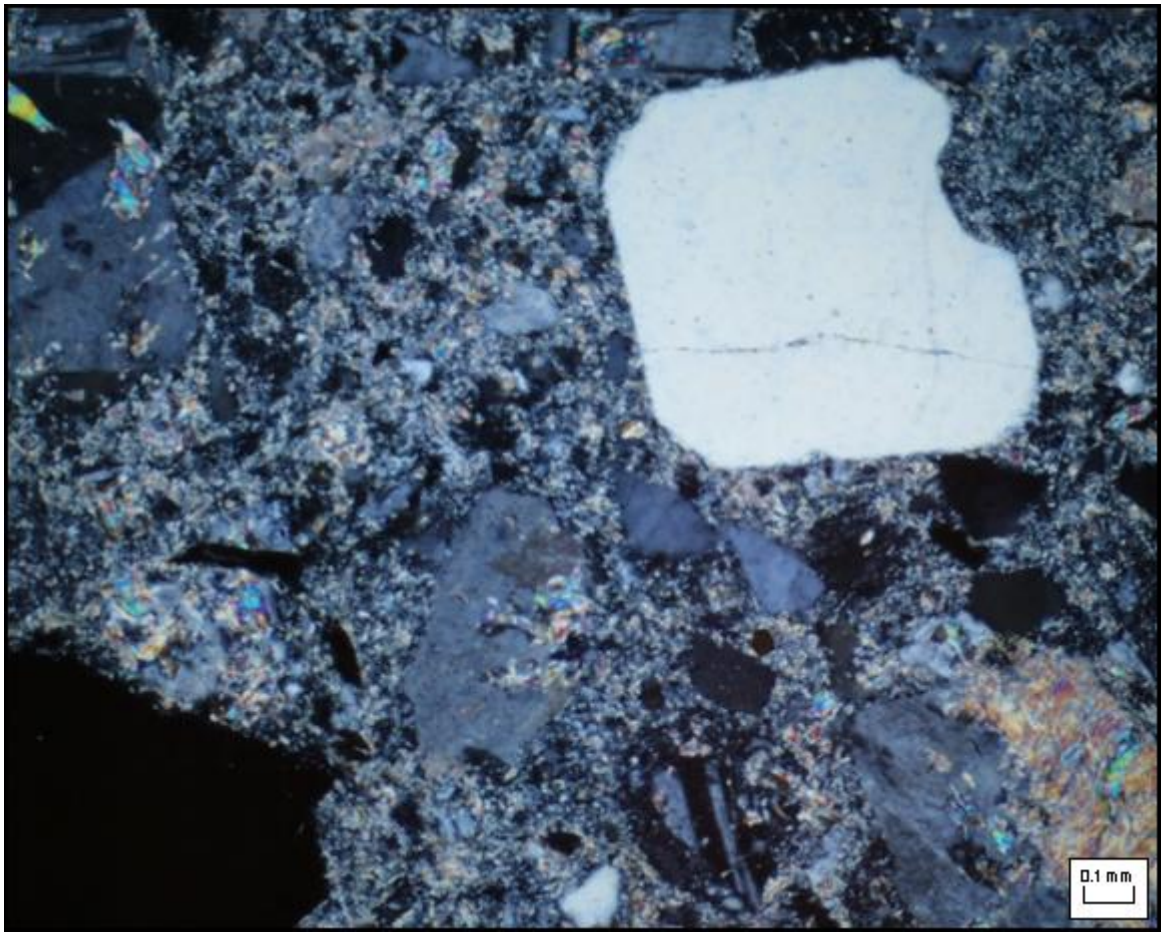

Figure 14. Photomicrograph of the matrix Hanover Hole Diatreme breccia matrix, showing the fragmental nature of the rock flour pieces and sericitic matrix. This sample is from core at 3744 ft. from the surface (D2036-3744) (Crossed polarized plane light, FOV = 1.7 mm).

Rhyodacite in Hanover Hole

Rhyodacite dikes intrude the Hanover Hole diatreme. They contain about 30% large euhedral plagioclase phenocrysts and a 2% small biotite, orthoclase, hornblende, and quartz. The groundmass is very fine grained and has a grayish color in core. The plagioclase phenocrysts have been altered to clay or sericite.

Classification and Nomenclature of the Lover's Lane breccia

The Lover's Lane breccia can be classified as a magmatic-hydrothermal breccia, using the criteria of Sillitoe (1985). The matrix is composed of hydrothermal minerals which precipitated in the void space created by breaking of the rock.

Several terms used here in the description of the breccia matrix must be defined, summarized in Table 3. "Matrix-forming minerals" are defined here as minerals which appear to have precipitated from solution in the breccia body during the emplacement of the breccia. This does not include minerals which appear to be fragments of primary lithology. This also does not include minerals which are the alteration products of matrix-forming minerals. Matrix-forming minerals and comminuted wallrock fragments are thus the two distinct components of the matrix. "Late breccia" refers to features that apparently used the matrix as a fluid pathway, presumably before the breccia was solidified to the point that veinlets and fractures could develop, but after the matrix-forming minerals had crystallized. "Post breccia" features clearly post date lithification of the breccia, and include veinlets that cut both matrix and fragments, and alteration assemblages that affect the matrix and clasts alike.

Descriptive Term	Definition	Dominant minerals and features
Matrix-forming	Minerals precipitated from hydrothermal fluids in the breccia during brecciation and settling	Shreddy green and brown biotite, fine-grained quartz and orthoclase, minor molybdenite, pyrite, anhydrite
Late-breccia	Features that used the matrix as a fluid pathway	Chlorite-chalcopyrite alteration of the matrix, ill-defined veinlets along clasts and through matrix
Post-breccia	Features that post-date lithification of the breccia	Quartz-molybdenite veinlets, alteration of both matrix and clasts

Table 3. Definition of terms used to describe breccia matrix features.

Matrix mineralogy of the Lover's Lane breccia

Petrographic studies completed during this study focused on the matrix of the Lover's Lane breccia. Textures, mineralogy and mineral relationships, were studied in detail to lead to a description of the breccia and development of a model for breccia formation and mineralization. Over 50 polished thin sections were studied. Sections were made by Spectrum Petrographics from billets that were cut from core samples taken during logging. Most of the petrology was done using an Olympus microscope with reflected light and digital camera capability and 5x, 10x, 20x, and 50x objective lenses.

The matrix-forming suite of the breccia at depth is dominated by fine-grained, shreddy biotite, quartz, and orthoclase. The quartz and orthoclase in most places display a slightly rounded, anhedral shape, with fingers of fine-grained biotite separating them (Figs. 15 through 17). Finer-grained quartz, orthoclase and biotite are locally intergrown,

resembling the groundmass in a porphyritic intrusive phase (Figs. 18 through 20). Very little crystal growth on clasts is present, such as the euhedral quartz crystals on clasts that were observed in the Whim Hill breccia (Reynolds and Beane, 1985). The Lover's Lane breccia displays a more dynamic precipitation of the matrix forming suite, and it is interpreted that the rounded quartz-orthoclase + shreddy biotite matrix was forming as magmatic fluids rushed into the mass of freshly broken rock. The open space between clasts was filled with the matrix-forming minerals before the breccia settled, and the dynamic nature of the breccia emplacement and matrix precipitation precluded nucleation and slow growth of crystals on clasts.

Figure 15. Core showing the "intrusive breccia," from which the thin section in Figure 16 was made (D1974, 2804-2796', NQ core).

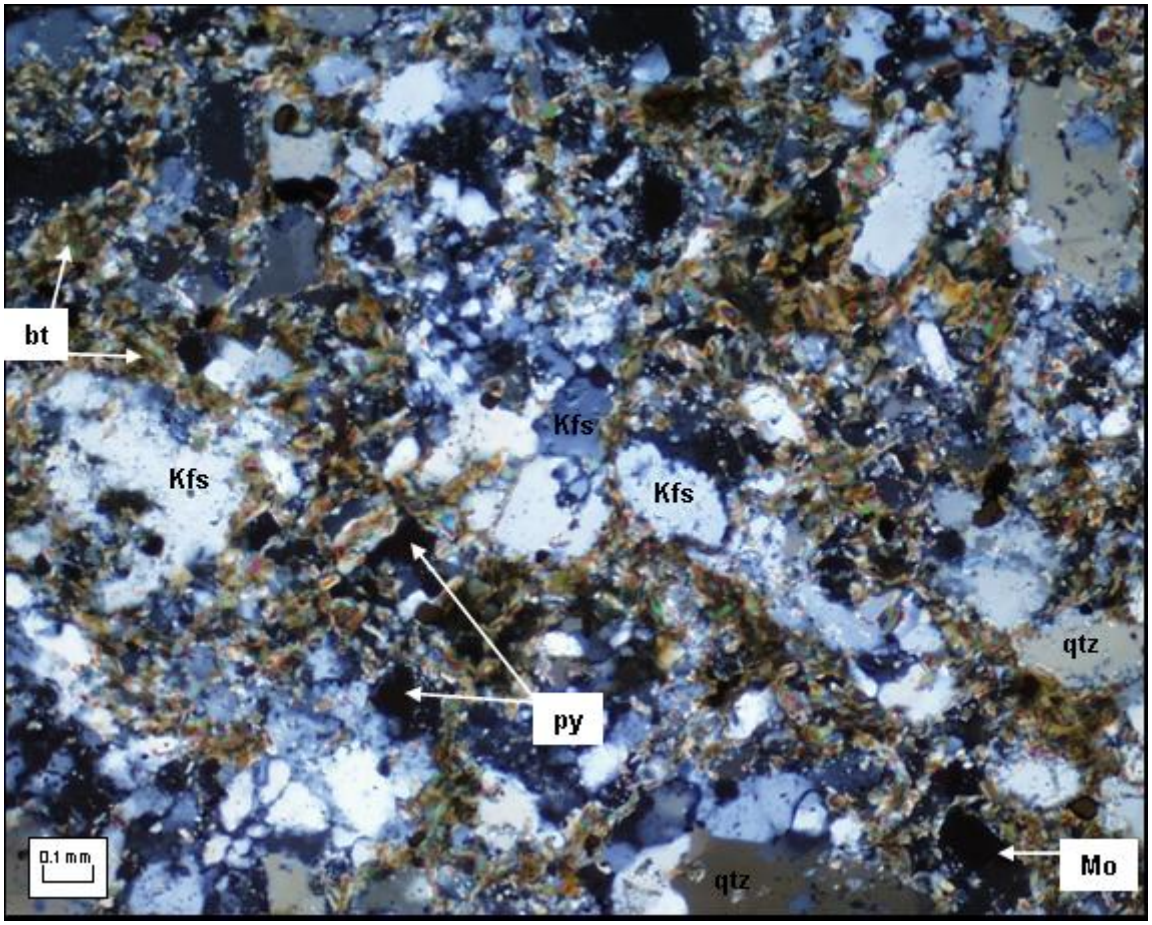

Figure 16. Thin section showing the biotite filling in between anhedral, rounded comminuted grains of quartz and K-feldspar. There is also some molybdenite, rounded pyrite grains, and chalcopyrite disseminated in the matrix (qtz = quartz, Kfs = orthoclase, bt = biotite, Mo = molybdenite, py = pyrite) (D1974-2797') (XPTL PPRL, FOV = 1.7 mm.).

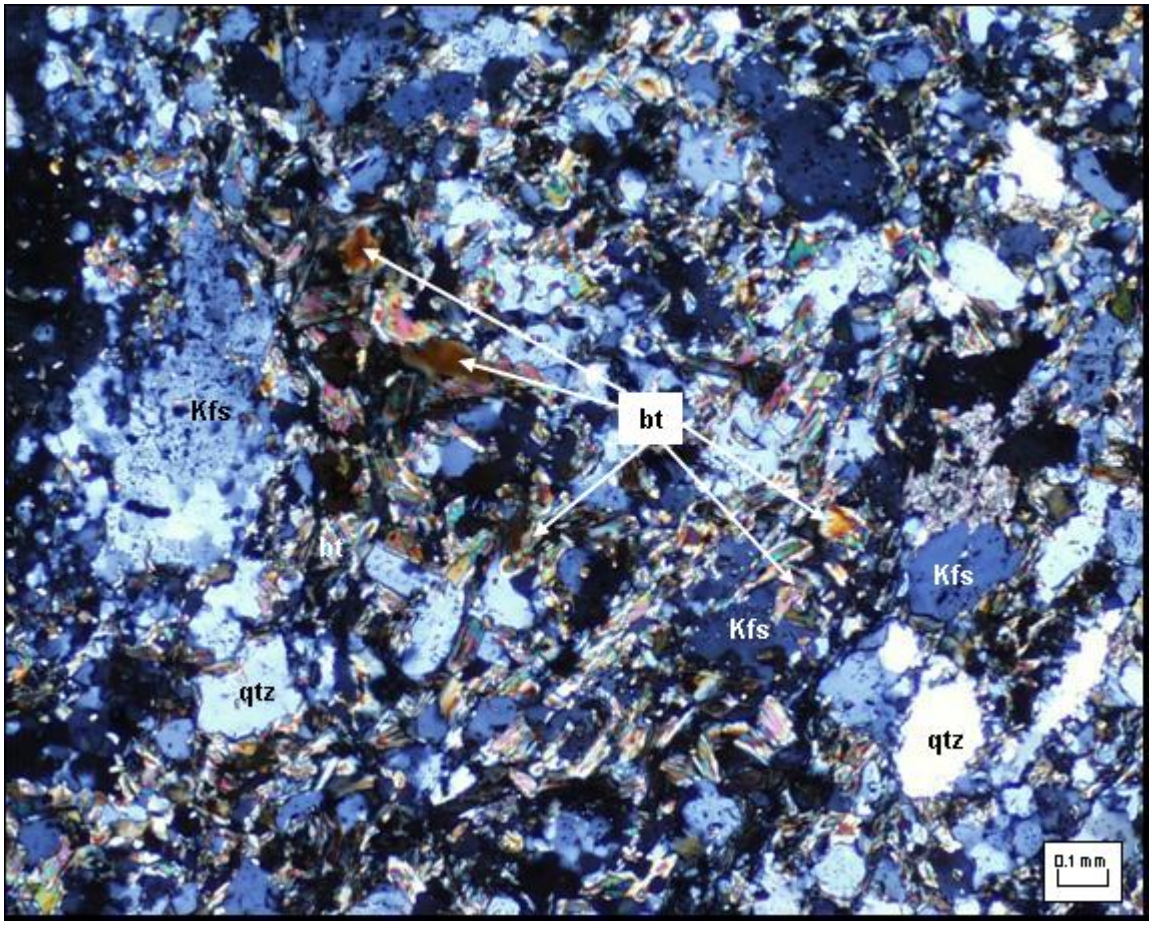

Figure 17. Deep breccia matrix: biotite, K-feldspar, and quartz as matrix-forming minerals. In this section the biotite is present as small inclusions in other minerals and also in between the anhedral grains of the other matrix-forming minerals (qtz = quartz, Kfs = orthoclase, bt = biotite) (D2333-3126) (XPTL, PPRL, FOV = 1.7 mm).

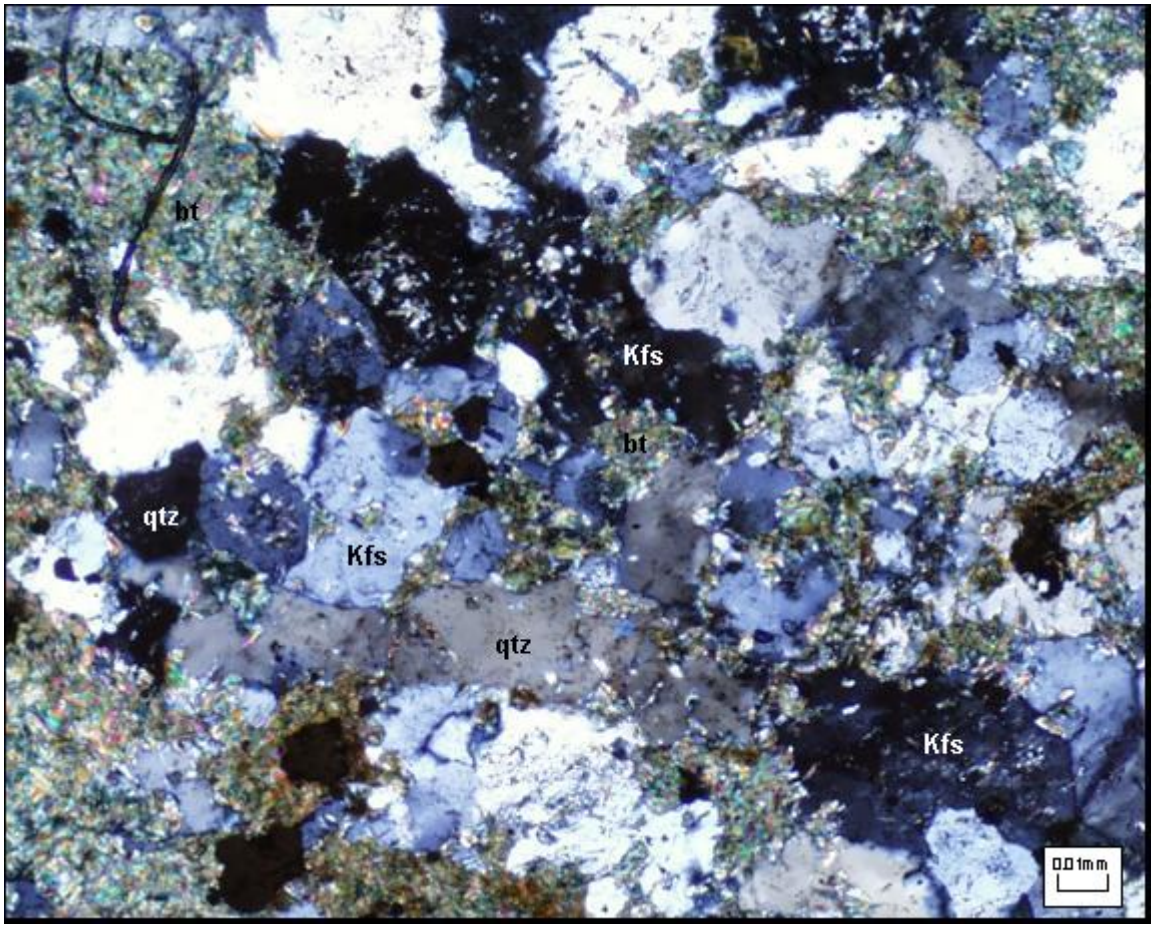

Figure 18. Photomicrograph of breccia matrix showing intergrown quartz, orthoclase and biotite in the matrix (qtz = quartz, Kfs = orthoclase, bt = biotite) (D1964-1113') (FOV = 0.17 mm).

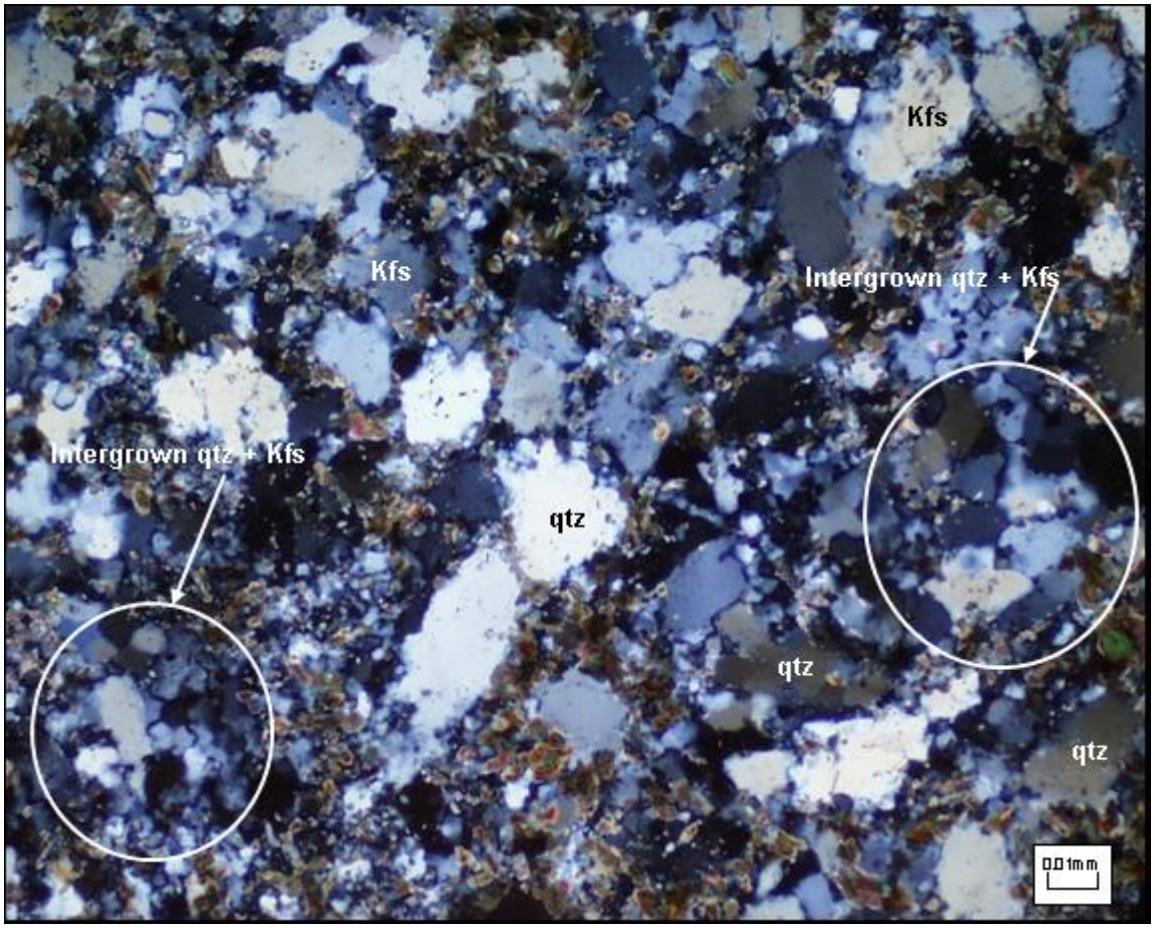

Figure 19. Photomicrograph of the breccia matrix with the matrix displaying both the rounded, comminuted texture of quartz and orthoclase surrounded by biotite, and some intergrown quartz and orthoclase. Note that the larger grains appear separated and the finer-grained quartz and orthoclase are intergrown (qtz = quartz, Kfs = orthoclase, bt = biotite) (D1964-2475) (FOV = 0.17 mm).

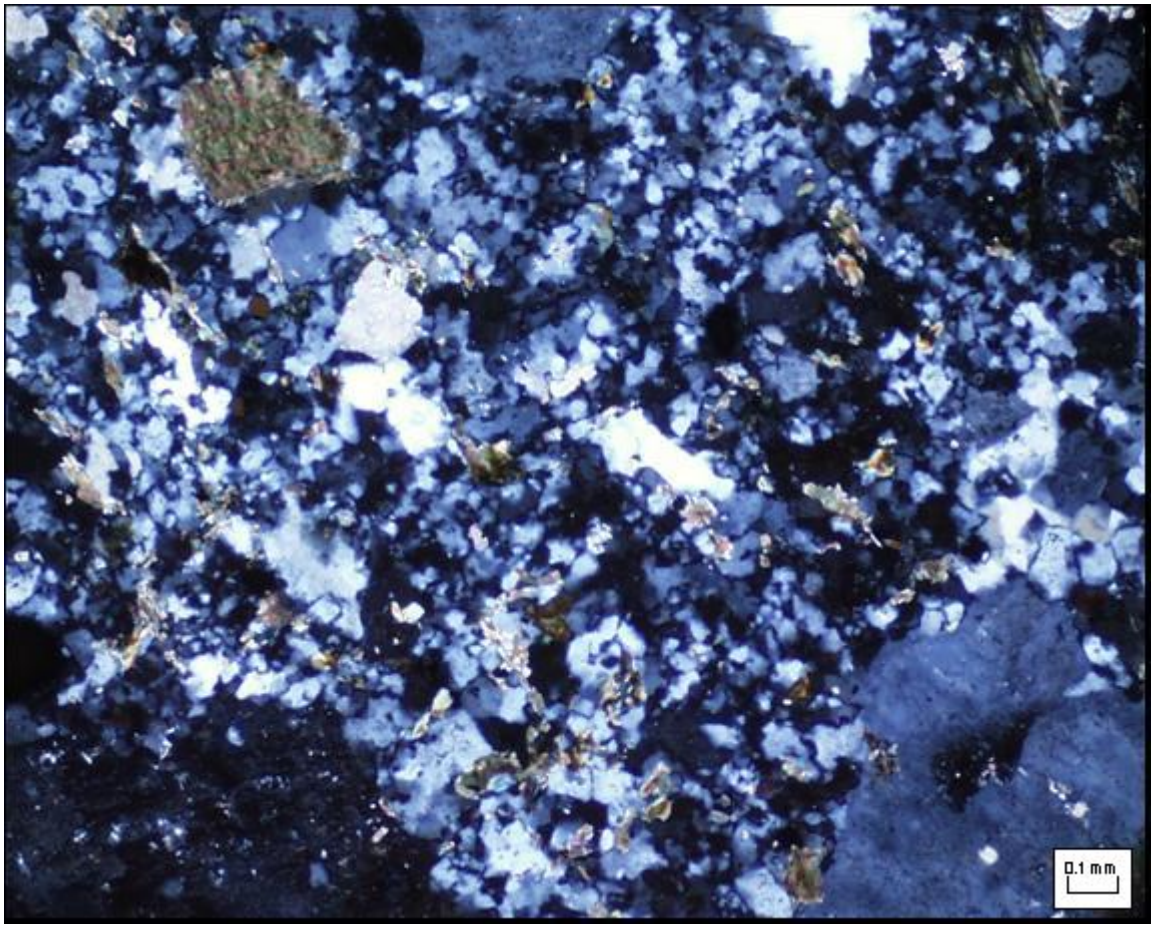

Figure 20. Photomicrograph of the breccia matrix, with fine-grained, interlocking quartz and orthoclase composing the majority of the matrix (D2023-1579) (FOV = 1.7mm).

Also present throughout the matrix are larger grains of quartz and orthoclase, which are not euhedral phenocrysts, but rather broken chunks of wall rock, such as deeper portions of the Santa Rita stock, highly potassic intrusive phases, or quartz monzonite dikes. Little plagioclase is present in the matrix, so the plagioclase-rich Santa Rita stock is not likely a strong contributor to the comminuted grains in the matrix. The core logs in the breccia refer to the deeper portions of the Lover's Lane breccia as "granodiorite-cemented" or "intrusive breccia," and shallower portions as "Lover's Lane breccia." This naming scheme leads to confusion, as it implies that there are two

different breccias in a single breccia body. The transition is (in most places) continuous and gradual. The arbitrary distinction is based on the breccia's appearance that is a function of the primary matrix mineralogy (discussed below) and also alteration of the matrix. Deeper intervals of breccia appear in hand sample to have a porphyritic, intrusive matrix, which changes at shallower depths to a matrix dominated by dark green silicates, including biotite, chlorite, and some actinolite. The dominant matrix-forming mineralogy and textures presented here of the "Lover's Lane breccia" extend to the depths reached by drilling, but change in appearance due to distance from source of brecciating fluids, wall rock lithology, and local alteration overprints.

The proportion of biotite in the matrix increases in the shallower levels of the breccia and in local biotite-rich intervals at depth, causing the macroscopic distinction in breccia appearance noted above. Biotite takes on a deeper green color, and is mistaken for chlorite in many cases in the logs. The various colors of biotite are shown in Figures 21 through 26. In thin section, biotite in the matrix is distinguished from chlorite by its much higher birefringence, and chlorite is length fast. Chlorite locally appears to be a matrix-forming mineral, but in most occurrences petrography has determined that it is an alteration product of primary biotite. The general texture of the shallower breccia is similar to the deeper breccia, with subrounded to angular fragments of wall rock cemented by matrix-forming silicates, in between the larger clasts of the breccia.

Figure 21. Scanned thin section of the breccia. The brownish regions are the matrix, dominated by brown biotite (as opposed to green), a common feature in the deeper portions of the breccia (D2333-3126').

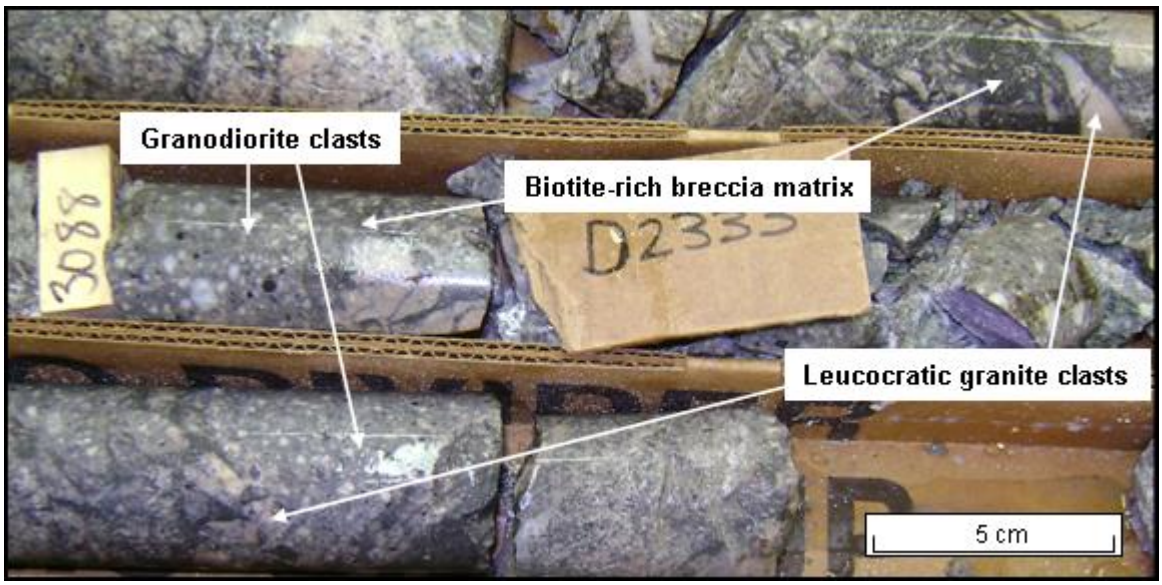

Figure 22. Core photograph of the deeper portion of the breccia, where the matrix-forming biotite has a dark brown color. The pieces in the lower left and upper right display the most evident matrix vs. clast distinction. The clasts here include porphyritic granodiorite (Santa Rita stock), and leucocratic granite (D2333-3088') (NQ core).

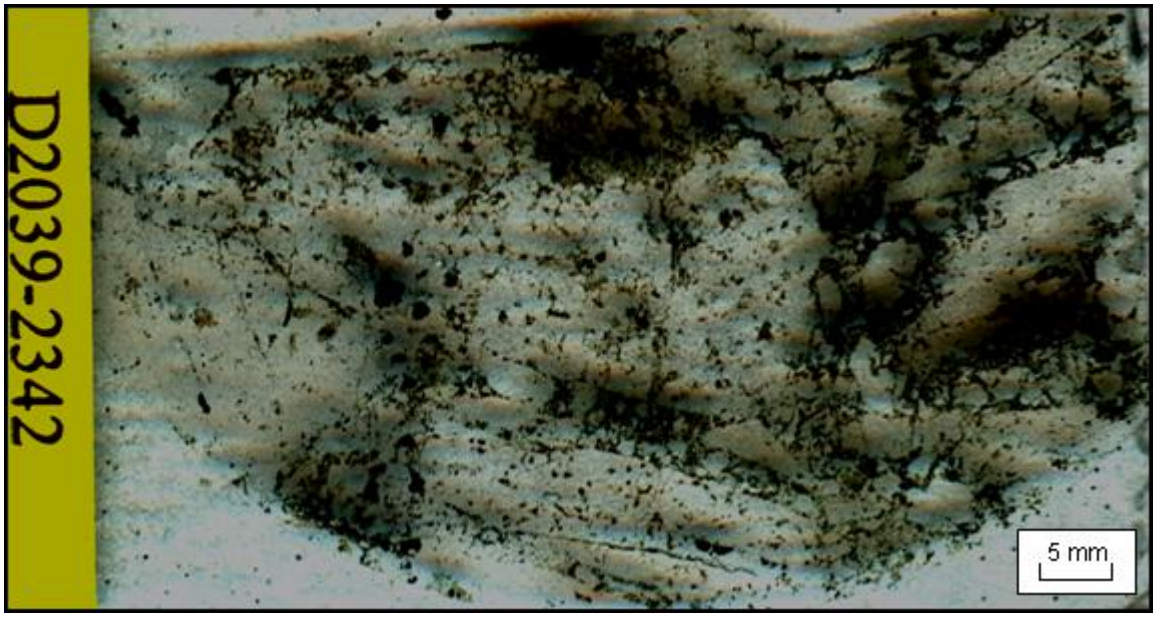

Figure 23. Scanned thin section of the breccia. Here the biotite in the matrix has a deep green color, more prevalent in the shallower portions of the breccia. The clear regions are granodiorite clasts (D2039-2342').

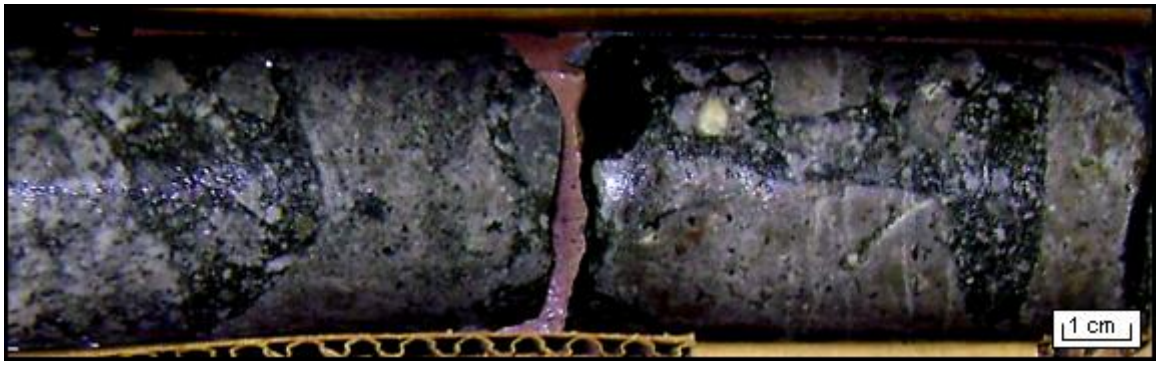

Figure 24. Core photograph of the breccia near the location of the previous thin section, showing the appearance of the matrix as the matrix-forming biotite takes on a deeper green color (D2039-2310') (NQ-size core).

Figure 25. Scanned thin section of the breccia, showing the strong green color of the matrix (and biotite-altered clasts) that is due to the higher proportion of green biotite. Minor chlorite is present in the matrix as an alteration product of biotite. (D2023-2263').

Figure 26. Core photograph of the breccia near the location of the previous thin section, showing the deep green color of the matrix (D2023-2220') (NQ-sized core).

Minor constituents of the silicate matrix-forming suite at depth include tourmaline, sericite, and actinolite. In some occurrences it is difficult to determine if these are minerals precipitated from fluid in the breccia, remnant crystals from the intrusive wall rocks, or minor expressions of alteration overprints. Locally pyrite, magnetite, chalcopyrite, and molybdenite are present in the matrix as comminuted grains and as euhedral, matrix-forming minerals. The paragenesis of sulfide and oxide mineralization is discussed below.

Anhydrite is present throughout much of the deeper Lover's Lane breccia. It varies paragenetically from being incorporated in the matrix as part of the matrix-forming

suite, to a later, vug-filling phase. Local intervals of breccia are described as "anhydrite pseudo-breccia" in the logs, where thick fractures are filled with light purple anhydrite. This feature is present in un-brecciated granodiorite (i.e. not the Lover's Lane magmatic-hydrothermal breccia), and also in open space and thick fractures that cross-cut the Lover's Lane breccia. Chalcopyrite and minor molybdenite are locally present with anhydrite; this relationship was the focus of the sulfide-sulfate isotope geothermometry discussed below. Anhydrite is also with quartz and molybdenite in post-breccia veinlets. Figures 19 and 20 show the massive and vug-filling anhydrite.

Figure 27. Purple anhydrite cutting various phases of the Santa Rita stock and breccia, the "anhydrite pseudo-breccia." (D2333-2140', NQ core).

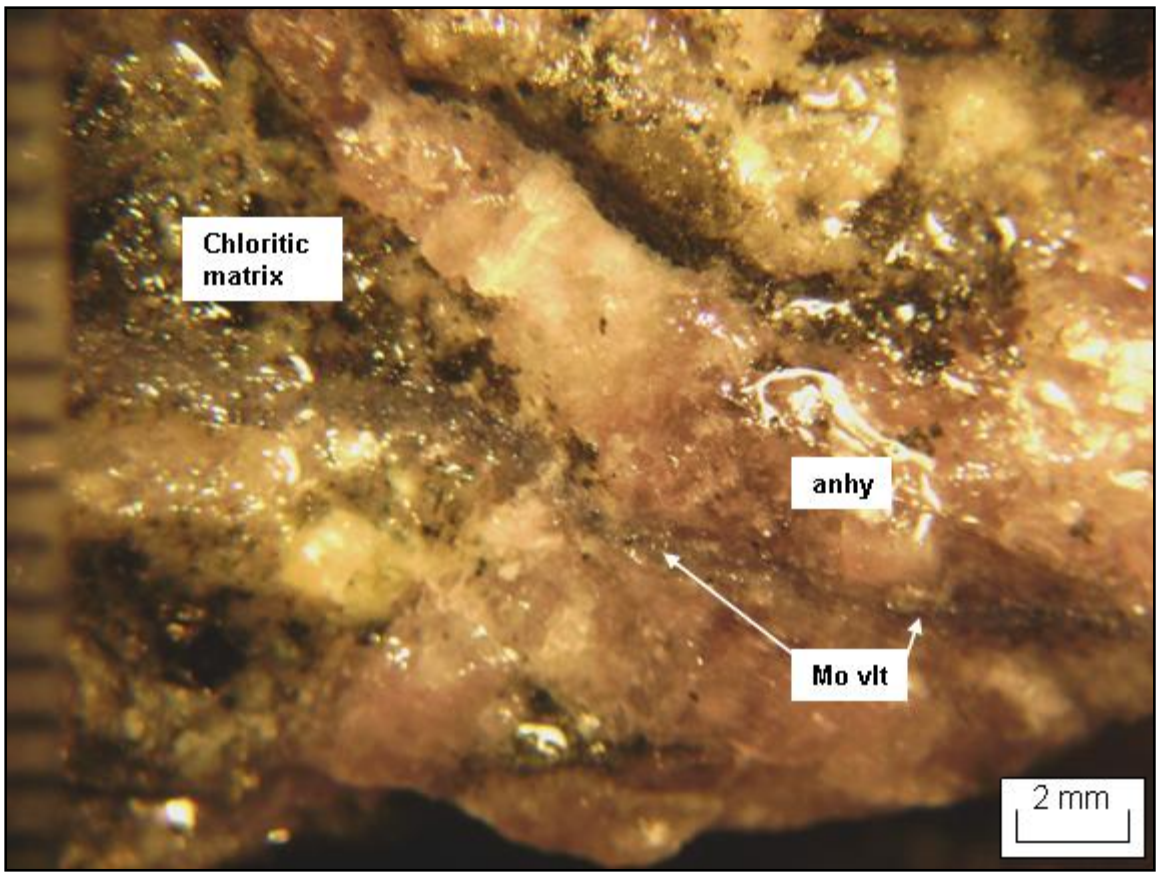

Figure 28. Photograph of light purple anhydrite truncating the breccia matrix. This feature is prevalent in the deeper portions of the Lover's Lane breccia. Also captured in this photograph is a post-breccia quartz-molybdenite veinlet cutting both the breccia matrix and the anhydrite (taken through a binocular microscope) (D1964-2466).

Brecciated skarn in the Lover's Lane

Brecciated skarn has different expressions in the Lover's Lane breccia. Where there is only weak retrograde alteration, clasts of prograde skarn are very magnetite-rich with some pyrite, garnet, with minor actinolite and epidote, and are separated by the fine-grained quartz-orthoclase-biotite matrix seen at depth. The hydrous retrograde assemblage of serpentine-talc-chlorite-actinolite-pyrite formed at the expense of the primary matrix, sedimentary clasts, and also intrusive clasts, indicating a post-breccia position in the paragenesis of the system. The fine-grained magmatic-hydrothermal

matrix texture is locally remnant in these intervals. The matrix in these intervals has a strong component of Mg-bearing silicates and oxides, including serpentine, talc, spinel (or periclase), and chlorite (Fig. 29), with locally strong molybdenite and/or chalcopyrite with this assemblage (Fig. 30). While the hydrous-after-prograde skarn assemblage is dominant in much of the shallower portions of the breccia, Mg-silicate alteration is locally present at depth, affecting igneous clast-dominated breccia.

Figure 29. Core photograph of brecciated prograde skarn. Magnetite-rich clasts in matrix dominated by serpentine, talc, and chlorite. The lighter-colored serpentine-talc matrix on the right side of the photo overprints the darker, chlorite-dominated matrix in the left side of this piece (D2314-1620') (NQ core).

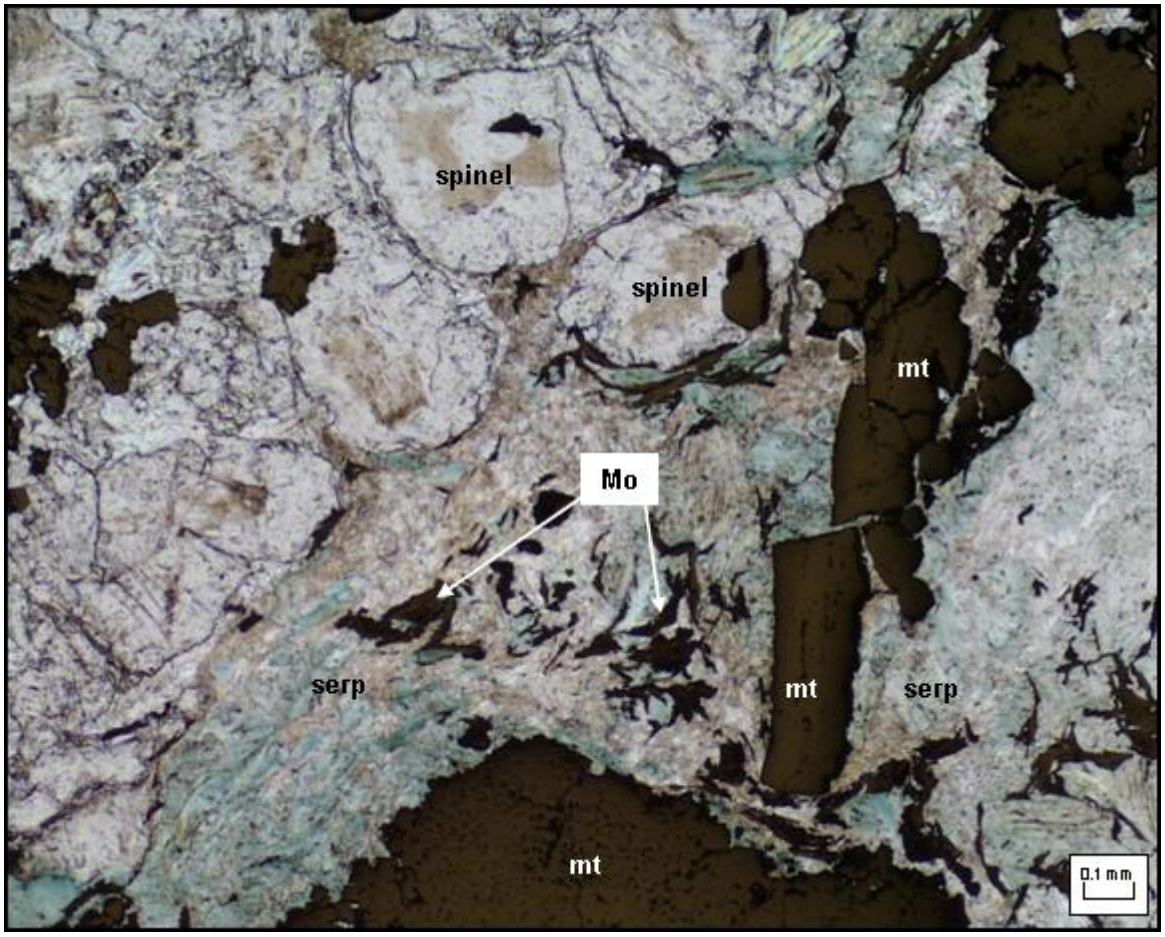

Figure 30. Photomicrograph of the breccia matrix with strong hydrous overprint, here with associated molybdenite and serpentine, with fragmental magnetite as small clasts in the matrix. The larger, rounded mineral is spinel or periclase (isotropic), alteration minerals in breccia clasts (dolomite) (serp = serpentine, Mo = molybdenite, mt = magnetite) (D2329-1642) (Plane polarized transmitted and reflected light, FOV = 1.7mm).

Late pseudo-porphyry breccia phase

In a few locations in the interior of the breccia and in the Turnerville area a late stage breccia phase is present, referred to here as the "pseudo-porphyry breccia." This phase is distinct from the majority of the Lover's Lane breccia, as it has little of the biotite in the matrix, and has fragments of biotite- and chlorite-rich breccia as clasts (Fig. 31). The matrix in the "pseudo-porphyry breccia" consists of fine-grained, interlocking

quartz and orthoclase, with “phenocrysts” or fragments of larger, anhedral, broken quartz and orthoclase, giving the breccia matrix a porphyritic appearance at a macroscopic scale (Fig. 32). Minor chlorite and calcite are also present in the matrix, possibly as alteration products of actinolite. In the limited locations where contacts of this breccia are intersected in core, it appears that the pseudo-porphyry breccia cuts earlier magnetite- and pyrite- mineralized rock, whether it is breccia or unbrecciated skarn. Small pieces of pyrite in the pseudo-porphyry breccia are likely incorporated from strong skarn mineralization.

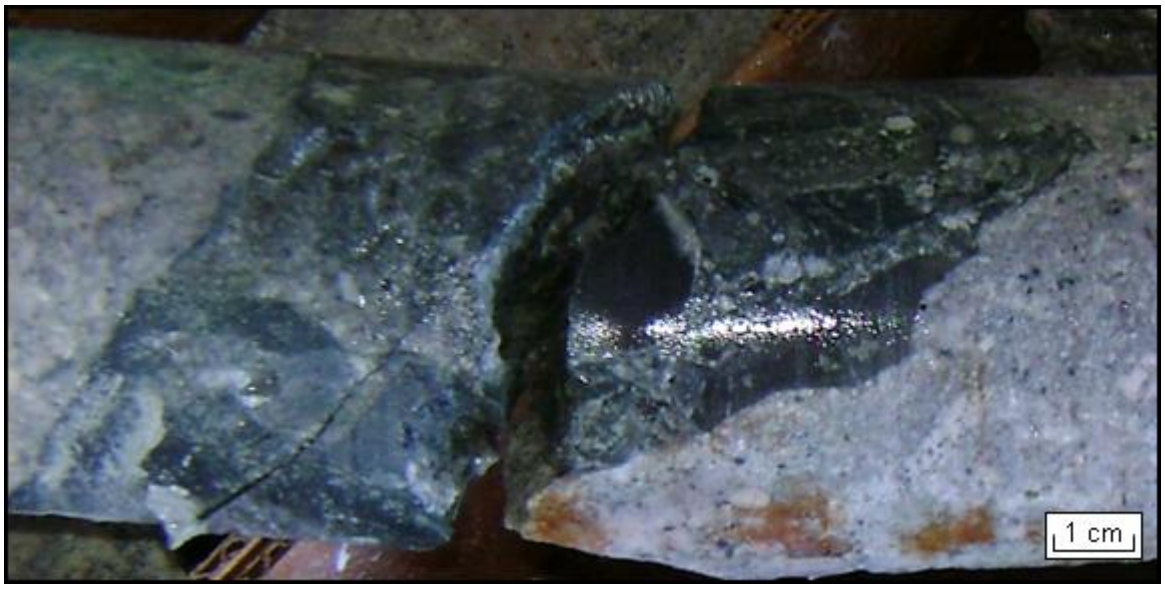

Figure 31. Core photograph of biotite- and chlorite- rich breccia as a clast in pseudo-porphyry breccia, which is the matrix on either side of the breccia clast. (D2332-2004’) (HQ-size core).

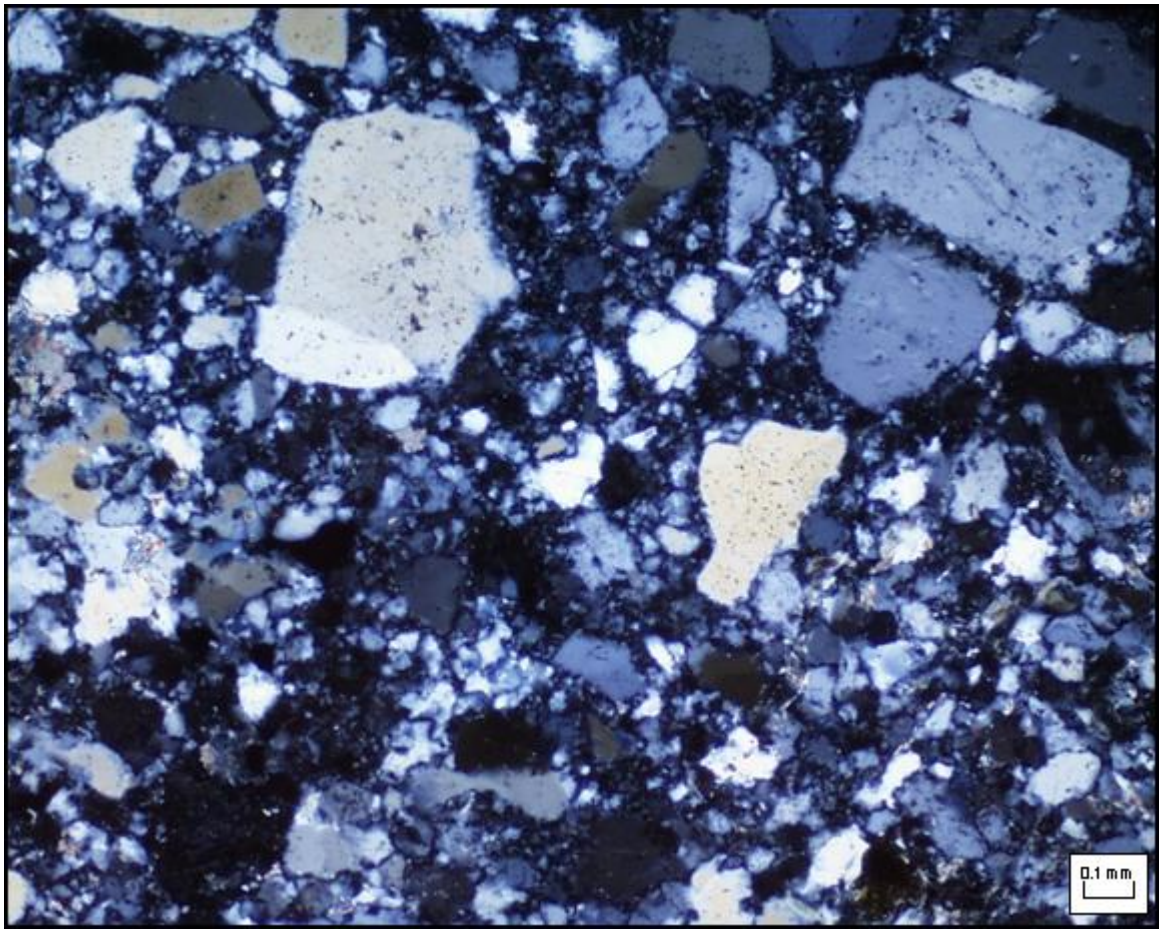

Figure 32. Photomicrograph of the matrix of the pseudo-porphyry breccia, with fine-grained, interlocking quartz and orthoclase cementing larger, fragmental quartz and minor orthoclase grains (D2332-2004) (Crossed polars, FOV = 1.7 mm).

Exposures of breccia in the Turnerville area are interpreted to be this breccia phase. This interpretation is not final, as the drilling in the Turnerville area had several hundred feet of reverse-circulation precollar (D2329 and D2332), so detailed cross-cutting relationships could not be determined (the RC chips were not studied for this project for that reason). Previous mappers described the breccia outcrops as "latite clasts in a latite matrix," which is similar to what is seen in core through the pseudo-porphyry breccia at the shallowest levels of coring. The volume of this breccia is not totally apparent, due to drill spacing (and possible unrecognition during core logging), but it is

likely that this breccia is a minor late phase concentrated in the northern portions of the Lover's Lane breccia. Cross cutting relationships indicate that the biotite-rich breccia-healing stage ended prior to this stage of brecciation (the clast of breccia mentioned above, Fig. 31). Local intervals of this breccia phase have some stronger chloritic alteration in the matrix, and quartz±molybdenite±pyrite veins cut the matrix, indicating that hydrothermal activity continued after this episode of brecciation.

The mapping done for this project in the Hanover Hole indicates that the diatreme cross-cuts this breccia phase, so the timing is constrained in a relative sense. Timing in relation to the Turnerville dike is ambiguous, but it appears that this breccia phase is earlier than the intrusion of the Turnerville dike, due to the fact that quartz-molybdenite veinlets cut the pseudo-porphyry breccia, but are not seen in the Turnerville dike.

Paragenesis of mineralization and alteration in the breccia

This section describes observations relating to alteration and mineralization of the Lover's Lane breccia, seen during core logging and thin section petrography. Care was taken to distinguish matrix-forming mineralogy (described above) from alteration mineralogy, though in places the relationships are vague. Figure 33 displays the mineralogical paragenesis observed in the Lover's Lane breccia. Some variation in individual relationships is present throughout the breccia, but this diagram shows the relationships that are most common throughout the breccia.

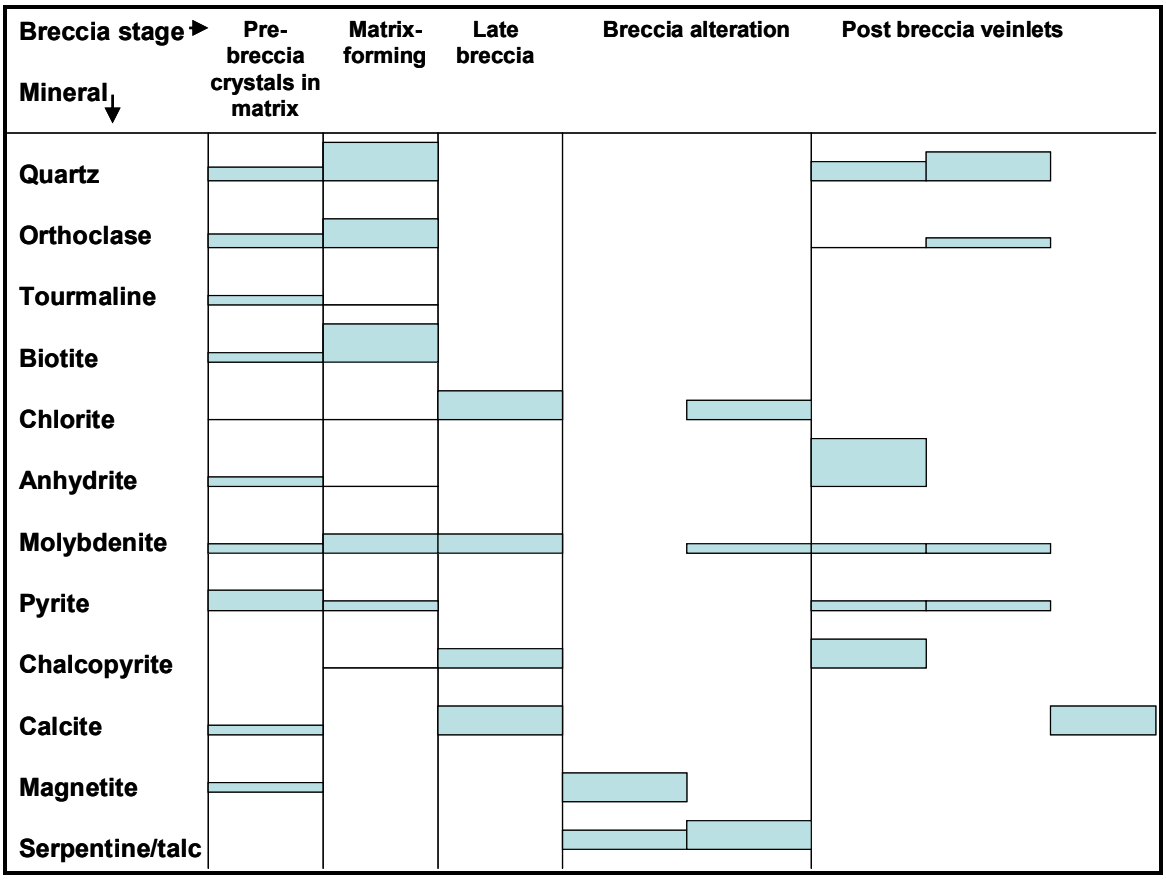

Figure 33. Paragenetic diagram of minerals in the Lover's Lane breccia, showing the most prevalent relationships throughout the development of the breccia and respective time brackets determined in this study. Thicker bars correspond to a stronger relative abundance.

The strongest mineralization in the Lover's Lane breccia is the molybdenite in the breccia matrix. Throughout much of the extent of the breccia there is at least anomalous molybdenite, and locally about 1% Mo in the matrix (Figs. 34 and 35; Plates 1 and 2). Petrographic investigation of this mineralization shows that the majority of the molybdenite is associated with the shreddy, fine grained biotite in the breccia matrix (Figs. 36 and 37). In the interior of the breccia the moderately higher molybdenite grades are above the zone of strong potassic alteration (Plate 1), in the portions of the breccia with stronger biotite in the matrix, and with (in places very localized) hydrous retrograde alteration. It is likely that these zones had higher late-breccia fluid flow than the deeper,

more potassic matrix, where molybdenite appears to be intergrown with quartz and orthoclase in the matrix (Figs. 38 and 39). Portions of the moderate to high grade breccia have molybdenite and minor chalcopyrite that appear to be a late-breccia feature, as the sulfides are present in vague, ill-defined veinlets through the breccia that in places follow clast boundaries (Fig. 40). The deep high grade zone intersected in D2333 (Fig. 34) located within granodiorite is possibly unrelated to breccia-stage molybdenite and formed prior to breccia emplacement, or is an expression of local high-grade in the wallrocks temporally associated with molybdenite in the breccia.

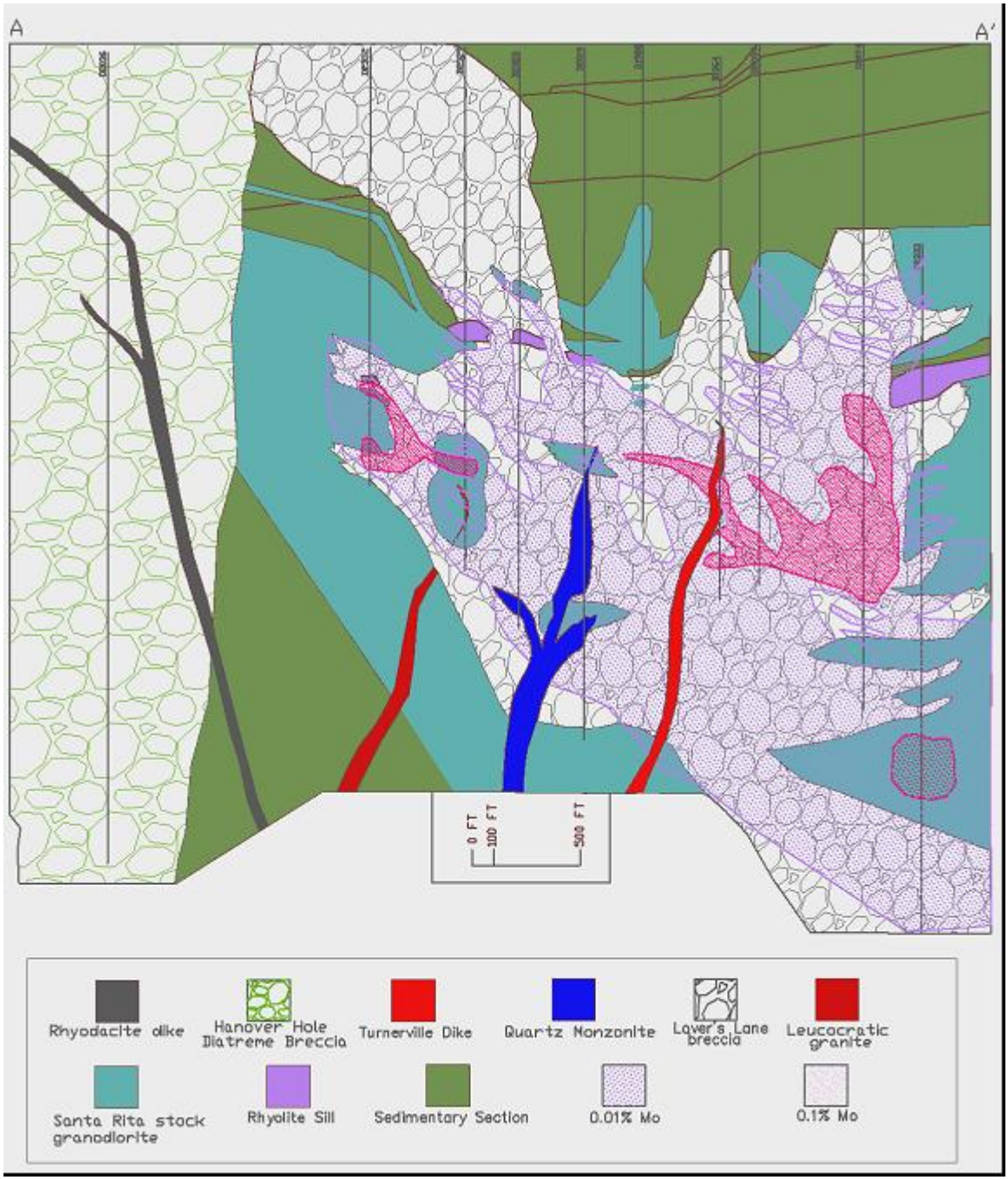

Figure 34. Generalized molybdenum grades in the A-A' cross section.

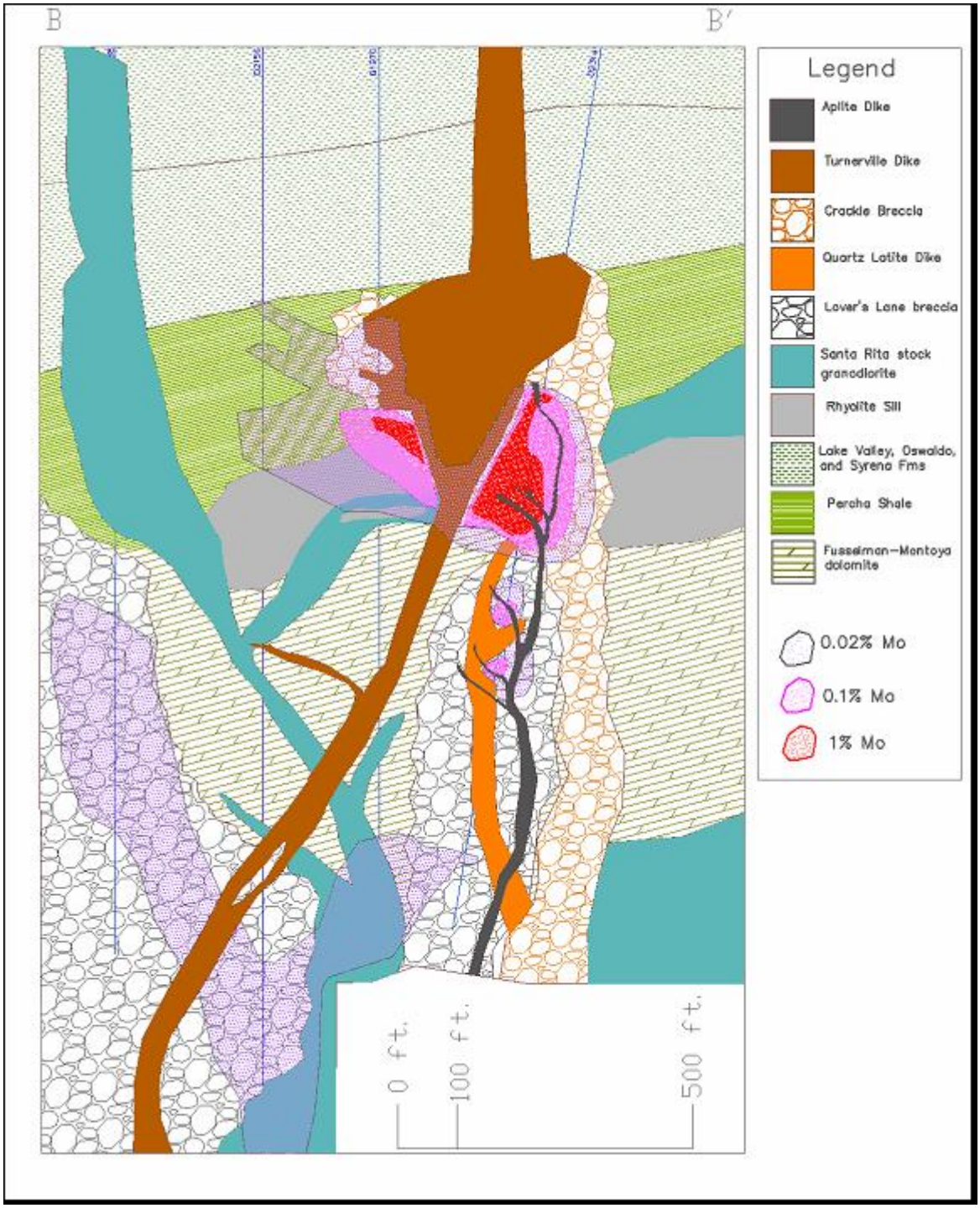

Figure 35. Generalized molybdenum grades in the B-B' cross section.

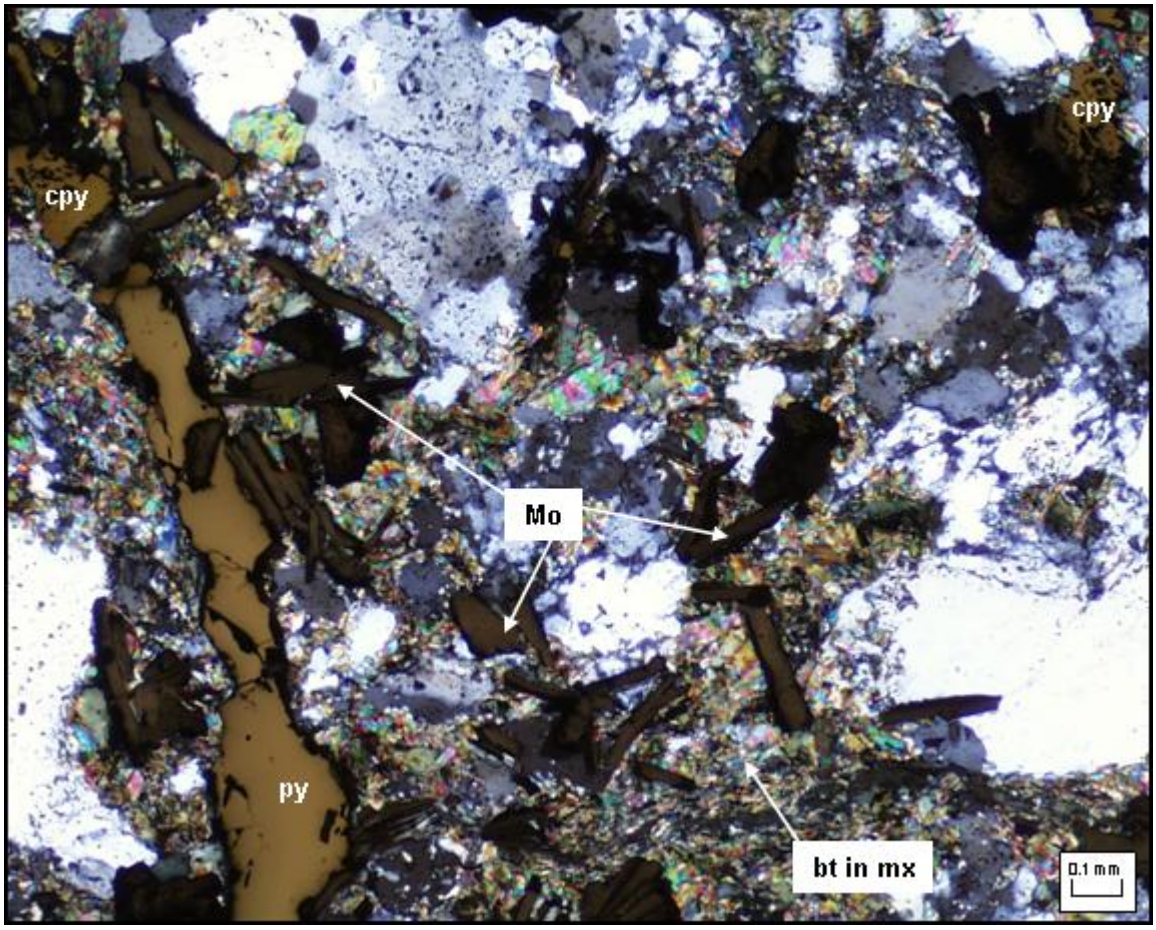

Figure 36. Photomicrograph of the breccia matrix, with scattered molybdenite flakes associated with the biotite in the matrix. In this view there is also a post-breccia pyrite-chalcopyrite veinlet (molybdenite = Mo, chalcopyrite = cpy, pyrite = py, biotite = bt, matrix = matrix) (D2039-2355) (FOV = 1.7 mm).

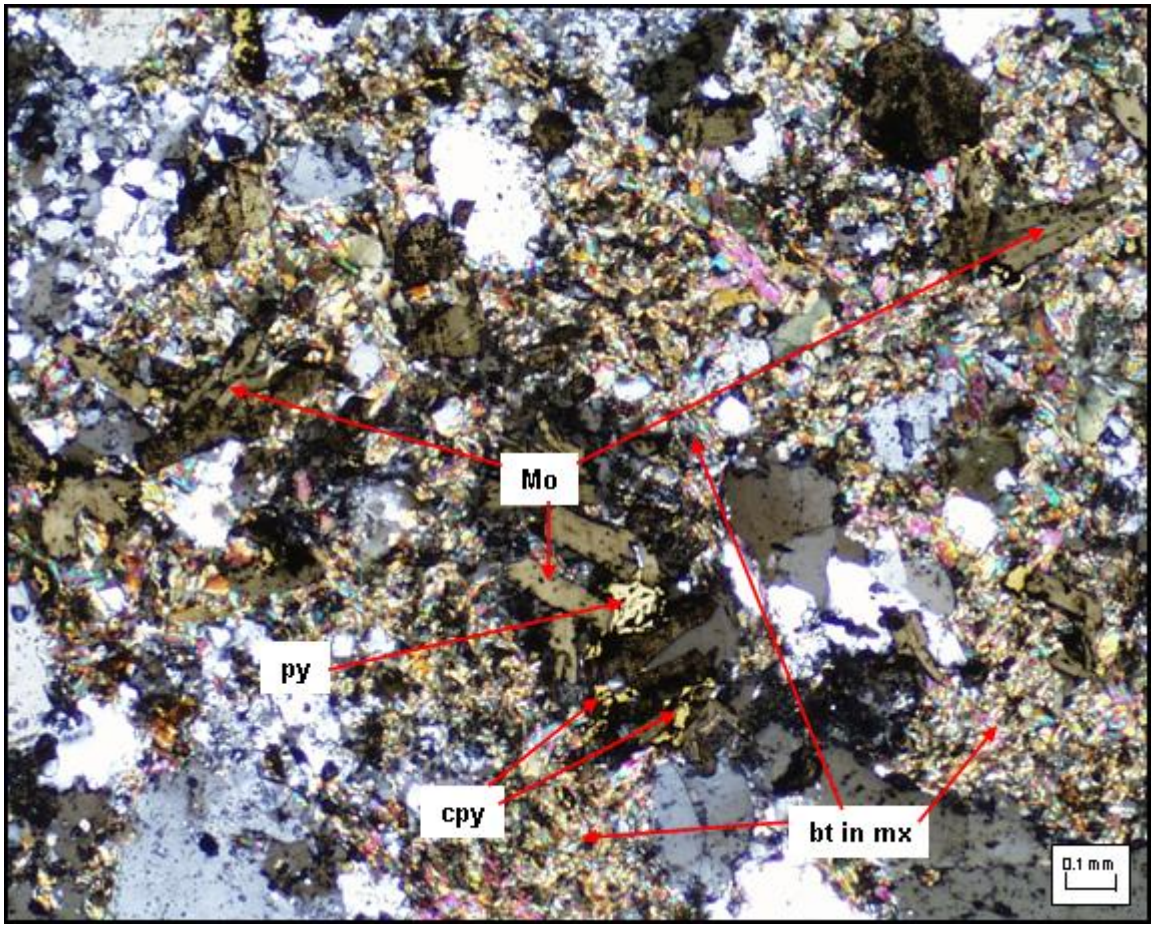

Figure 37. Photomicrograph of breccia matrix, showing molybdenite (and minor chalcopyrite and pyrite) with shreddy biotite as the final matrix healing (molybdenite = Mo, chalcopyrite = cpy, pyrite = py, biotite = bt, matrix = matrix) (D2039-2342) (FOV = 1.7mm).

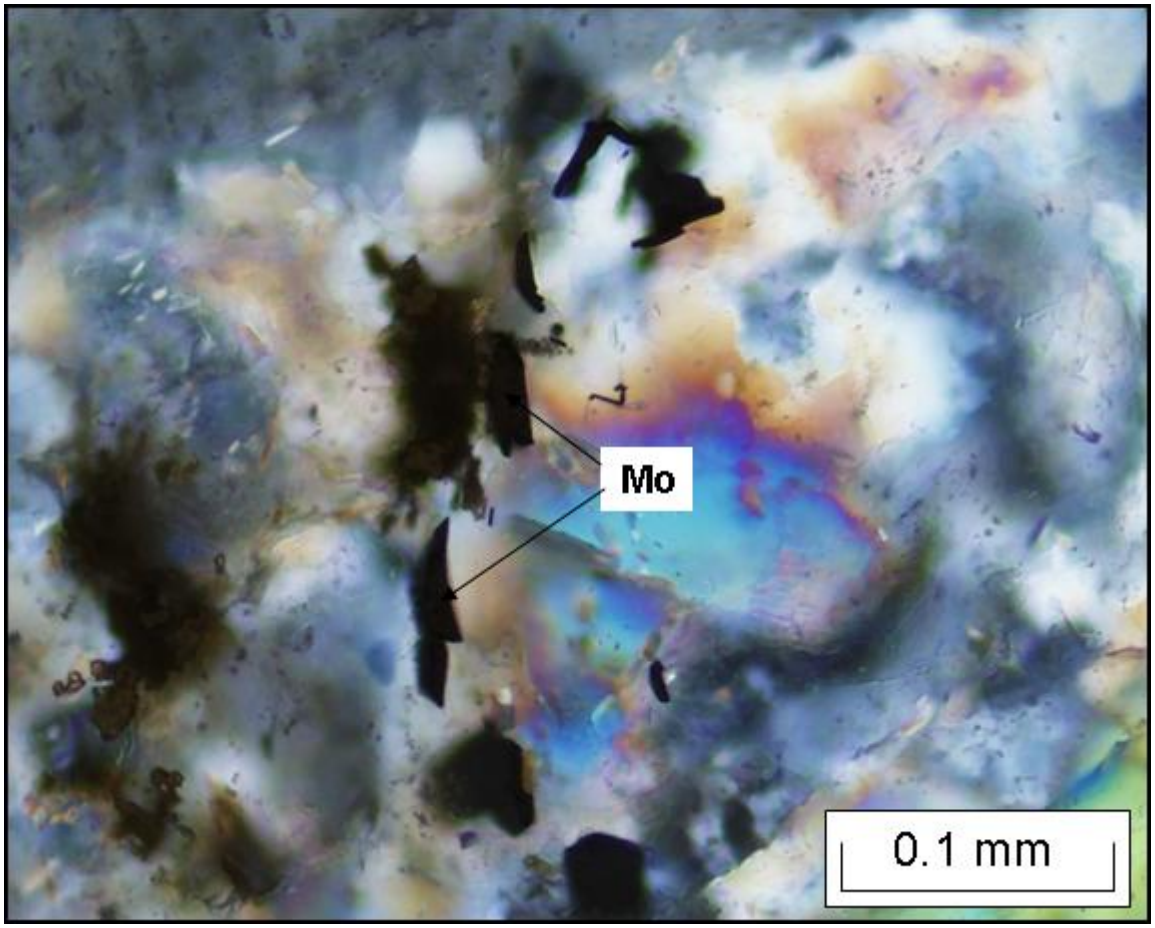

Figure 38. Photomicrograph of breccia matrix, with molybdenite (Mo) associated with quartz and orthoclase as matrix-forming minerals (D2019-1657) (FOV = 0.43mm).

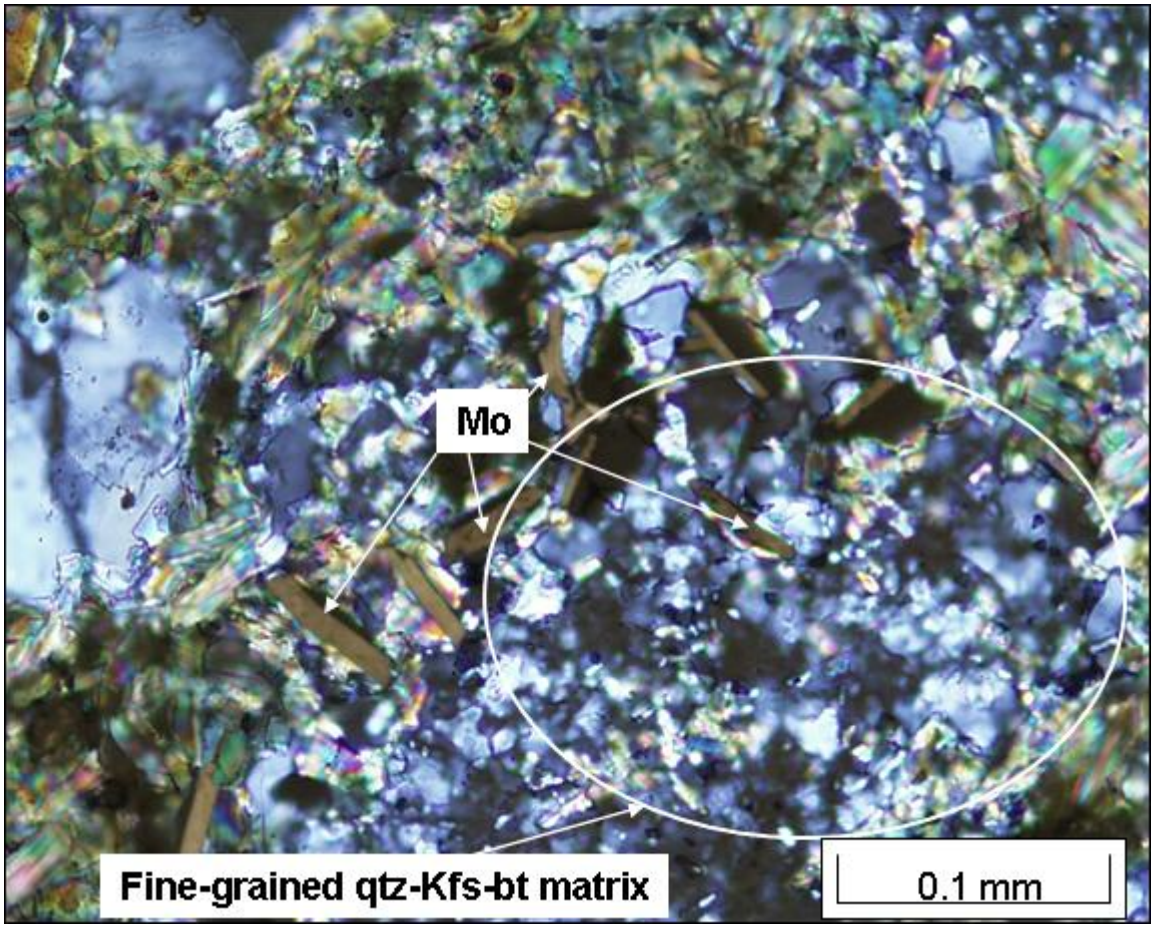

Figure 39. Photomicrograph of the breccia matrix showing molybdenite with the quartz-orthoclase-biotite matrix. Here the molybdenite appears associated with both the fine-grained quartz-orthoclase and the shreddy biotite (molybdenite = Mo, quartz = qtz, orthoclase = Kfs, biotite = bt) (D2023-2263) (FOV = 0.43 mm)

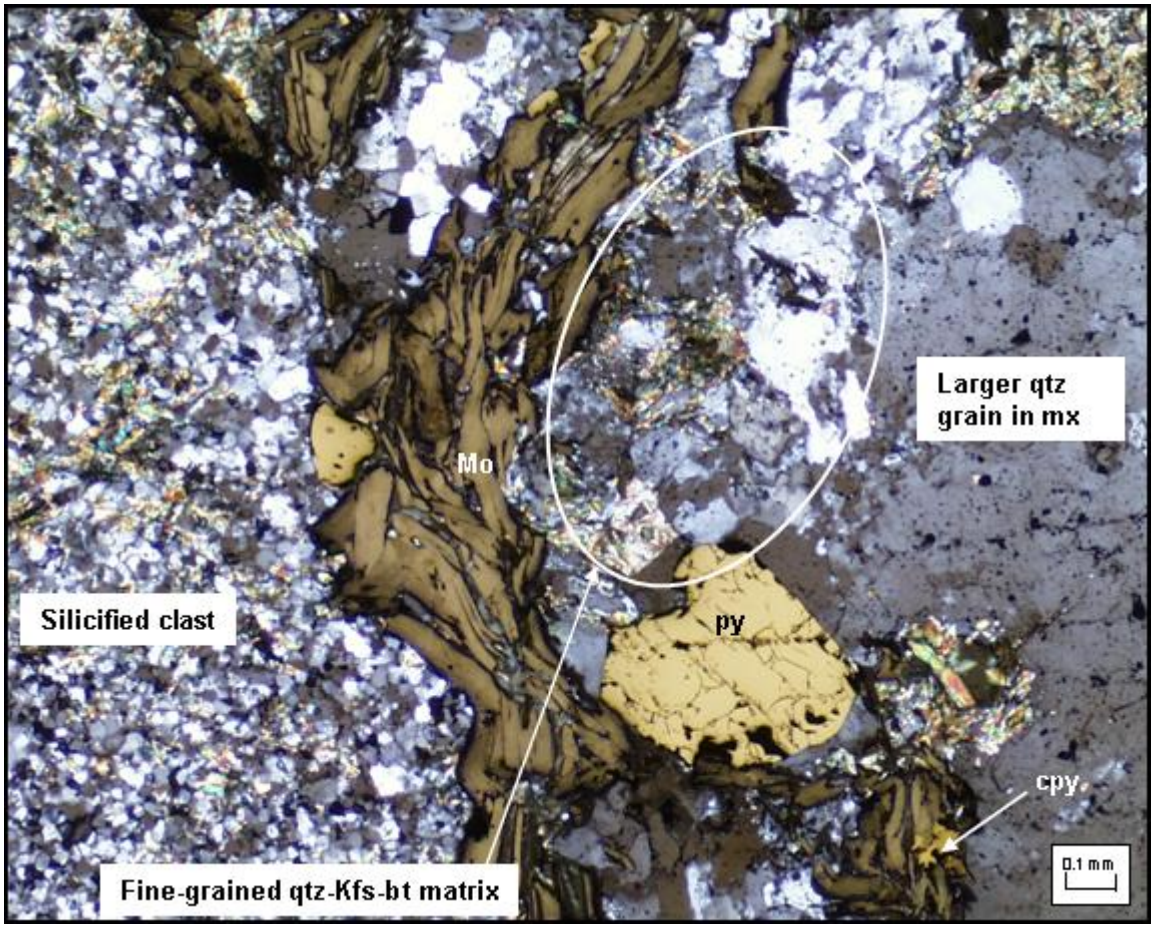

Figure 40. Photomicrograph depicting the "late-breccia" molybdenite (and minor chalcopyrite), with the molybdenite occurring as a discontinuous, irregular veinlet through the matrix and following the clast boundary (molybdenite = Mo, pyrite = py, chalcopyrite = cpy, quartz = qtz, orthoclase = Kfs, biotite = bt) (D2039-2355) (FOV = 1.7 mm).

Shallower levels of the breccia with stronger molybdenite mineralization include molybdenite with massive calcite in the matrix, along with magnetite and/or pyrite and chalcopyrite. Petrographic study of this association has determined that the calcite and molybdenite are the final breccia cement in these local intervals (Fig. 41). Though the massive calcite with molybdenite is rare, calcite is present in many of the quartz-molybdenite-bearing veinlets throughout the breccia. It is unclear whether the calcite is

always a late-stage event that follows the fracture or if it is indeed associated with the molybdenite mineralization.

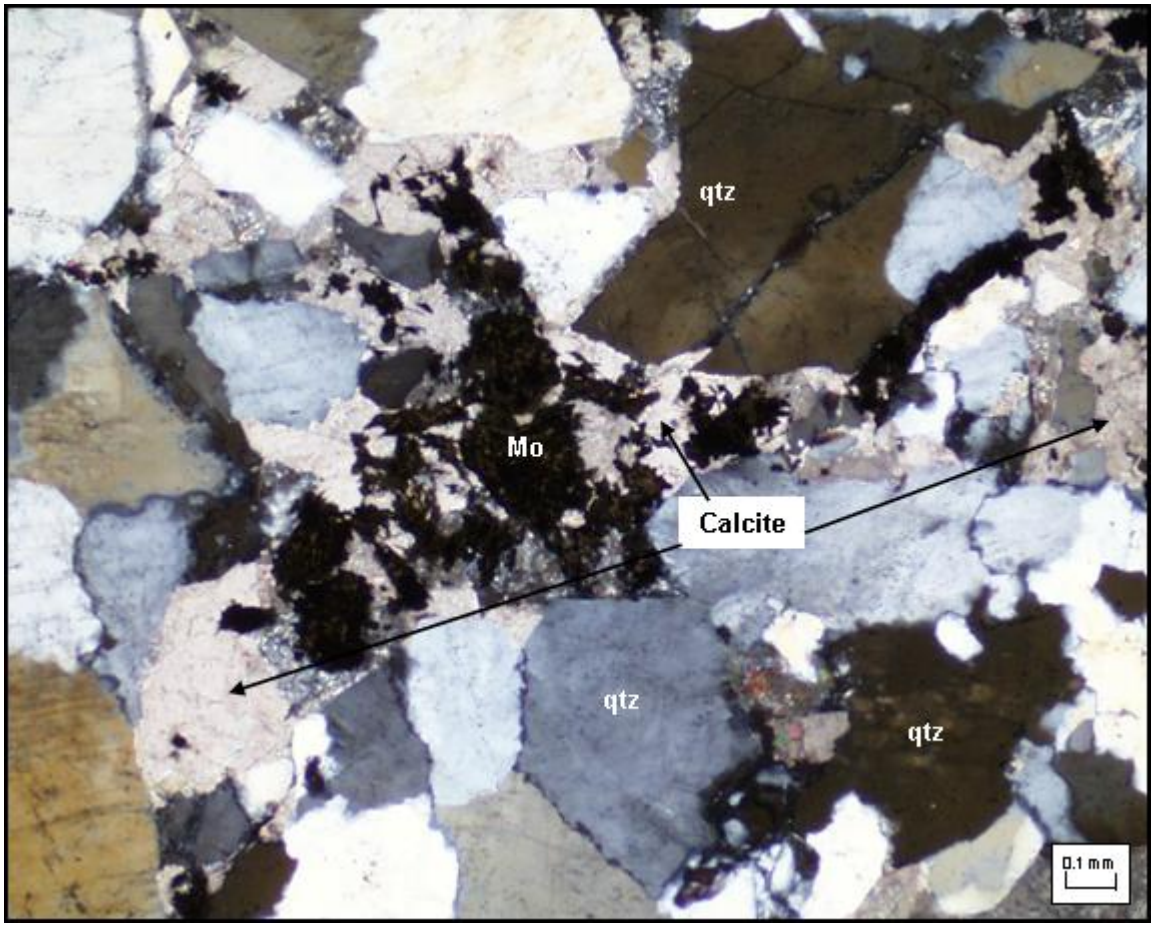

Figure 41. Photomicrograph of calcite and molybdenite (Mo) as the final breccia cement, with intergrown and fragmental quartz (qtz) clasts (D2023-747) (FOV = 1.7 mm).

Local, very high grade molybdenite intervals in breccia are described as "molybdenite-cemented," in which a crackle breccia or mosaic breccia has molybdenite and minor rock flour as the matrix (Fig. 11, location shown on Plate 2). This feature is somewhat anomalous, as the majority of the molybdenite-mineralized breccia has hydrothermal silicates as the dominant matrix-forming minerals. Timing of the different molybdenite mineralization types is discussed below.

Post-breccia molybdenite is present in quartz-molybdenite±pyrite±anhydrite veinlets, which cross-cut the breccia as through-going veinlets. These veinlets are present throughout much of the Lover's Lane breccia, and appear to impose a "background" grade of about 0.02% Mo on the breccia (the average Mo grade where mineralization was only observed in veinlets). Rare pre-breccia quartz-molybdenite veinlets are also present, in clasts with the veinlet truncated by the matrix at the clast edge (Fig. 42).

Figure 42. Evidence for two veinlet-controlled molybdenite mineralization events. There is a quartz-molybdenite veinlet that is truncated by the breccia matrix in the large leucocratic granite fragment in the left side of the picture (black arrow), and a quartz-molybdenite veinlet that cuts the matrix on the right side (white arrow). This interval assays 0.046% Mo, in veinlets (D2156-2241', NQ core).

Other metallic minerals present in the Lover's Lane breccia include magnetite, pyrite, chalcopyrite, and very minor sphalerite and galena. Magnetite dominates the matrix in some intervals, and is more prevalent in the shallower intervals with nearby skarn. Euhedral magnetite is disseminated throughout the matrix in some of the thin sections studied, which is interpreted to be part of the matrix-forming suite (Fig. 43). Magnetite locally partially replaces (pre-breccia) pyrite in the matrix where it is associated with the matrix-forming silicates (Fig. 44).

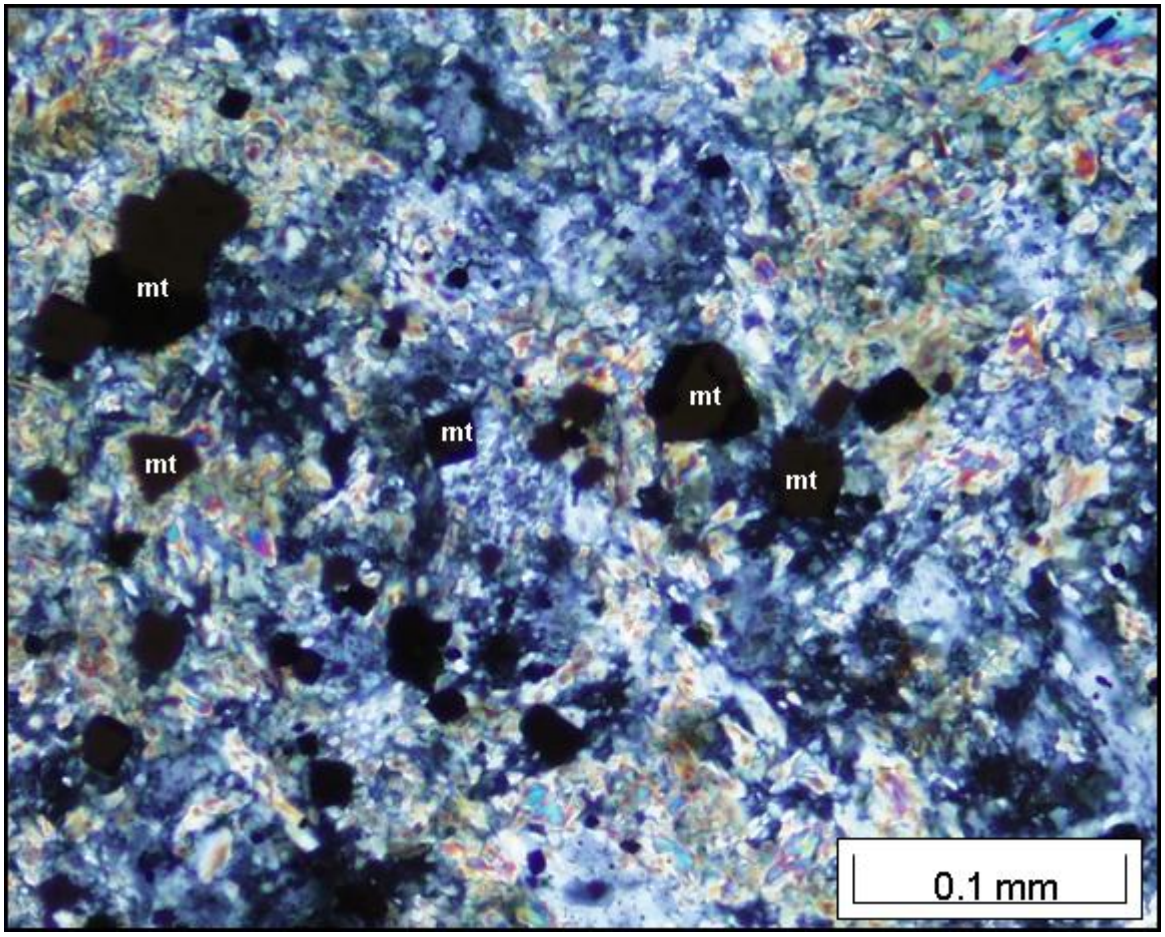

Figure 43. Photomicrograph of the breccia matrix with euhedral magnetite (mt) as part of the matrix-forming assemblage along with biotite and quartz (D2023-1052) (FOV = 0.43 mm).

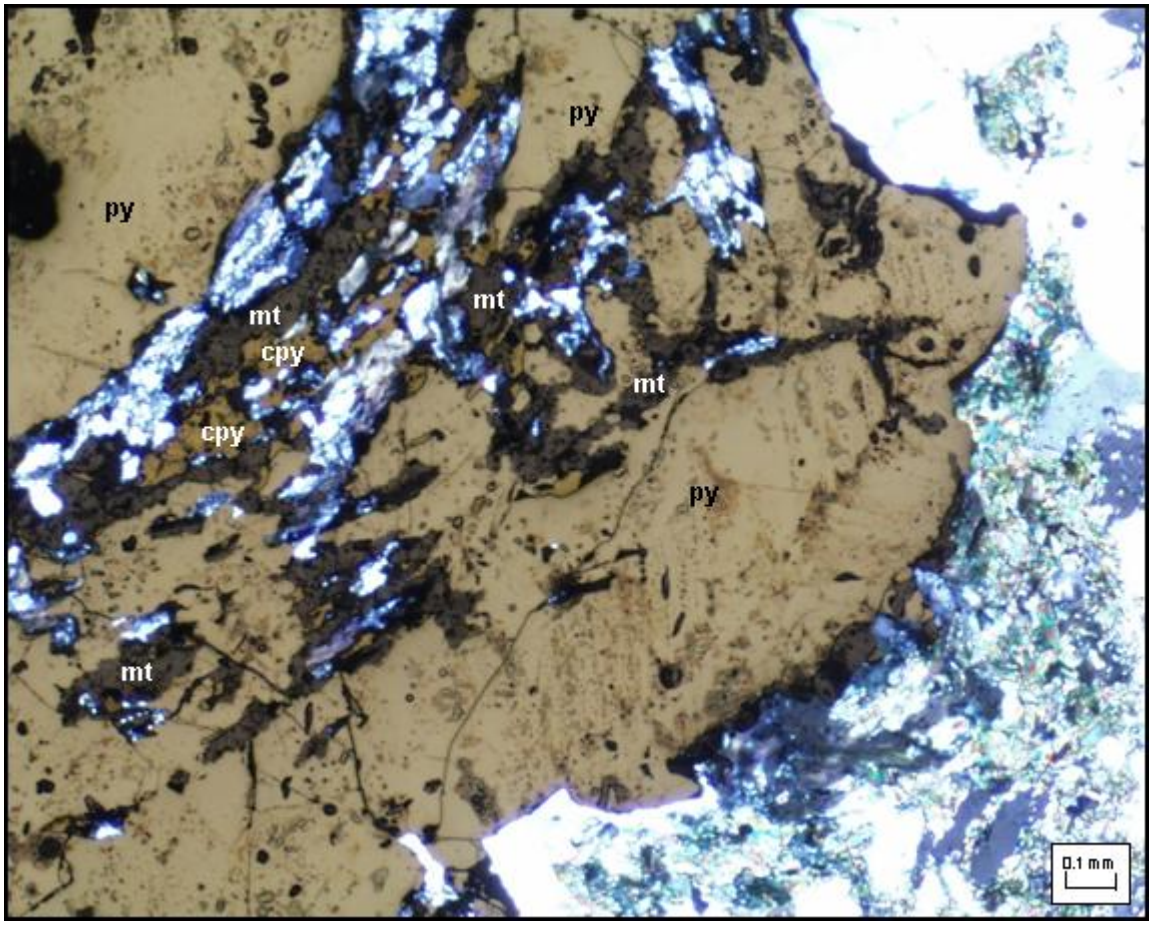

Figure 44. Magnetite and minor chalcopyrite replacing pyrite in the breccia matrix (magnetite = mt, chalcopyrite = cpy, pyrite = py) (D2023-2263) (FOV = 1.7 mm).

In other places the magnetite is fragmental, with anhedral, fractured magnetite disseminated in the matrix, which is interpreted to be pre-breccia and scattered throughout the matrix during mechanical brecciation (this is shown in Figure 30, above). This interpretation is supported by concentration of small magnetite fragments surrounding larger grains or clumps of magnetite floating in the matrix. Some magnetite coincides with late- or post- breccia alteration, such as the chlorite-chalcopyrite event discussed below. Locally matrix-forming magnetite is associated with molybdenite, but this is rare.

Pyrite displays varied paragenetic relationships throughout the extent of the breccia. The majority of the pyrite in the matrix appears to be pre-breccia, indicated by the broken, anhedral shape of pyrite grains in the matrix, which locally comprise several percent of the matrix. Minor pyrite is present with the matrix-forming suite, with the late- or post- breccia chlorite-chalcopyrite assemblage, and in post-breccia veinlets. Shallower intervals of breccia have intense pyrite-sericite-quartz mineralization in the matrix, resembling and likely related to the phyllic alteration of the Santa Rita deposit.

The most prevalent alteration in the Lover's Lane breccia is the chlorite-chalcopyrite-pyrite assemblage (Figs. 45 and 46). This assemblage occurs in the matrix as vague veinlets and disseminated patches of chlorite after primary (matrix-forming) biotite, and this event is best described as a "late breccia" feature. Macroscopic and quick microscopic observation of this mineralization/alteration of the breccia could lead to the interpretation that the primary matrix suite includes chlorite and chalcopyrite, as the chlorite has a similar green color as much of the matrix-forming biotite, and the chlorite-chalcopyrite assemblage is present mainly in the matrix, and not affecting the clasts. Anomalous gold values (where gold assays are available) closely follow the higher copper values associated with this late-breccia chalcopyrite (gold values are unrelated to molybdenite mineralization). Less chalcopyrite appears associated with shreddy biotite in the primary breccia matrix. The generalized alteration pattern of the chlorite overprint is presented in Figs. 47 and 48, along with the pattern of unaltered potassic matrix and/or potassic alteration in the wall rock.

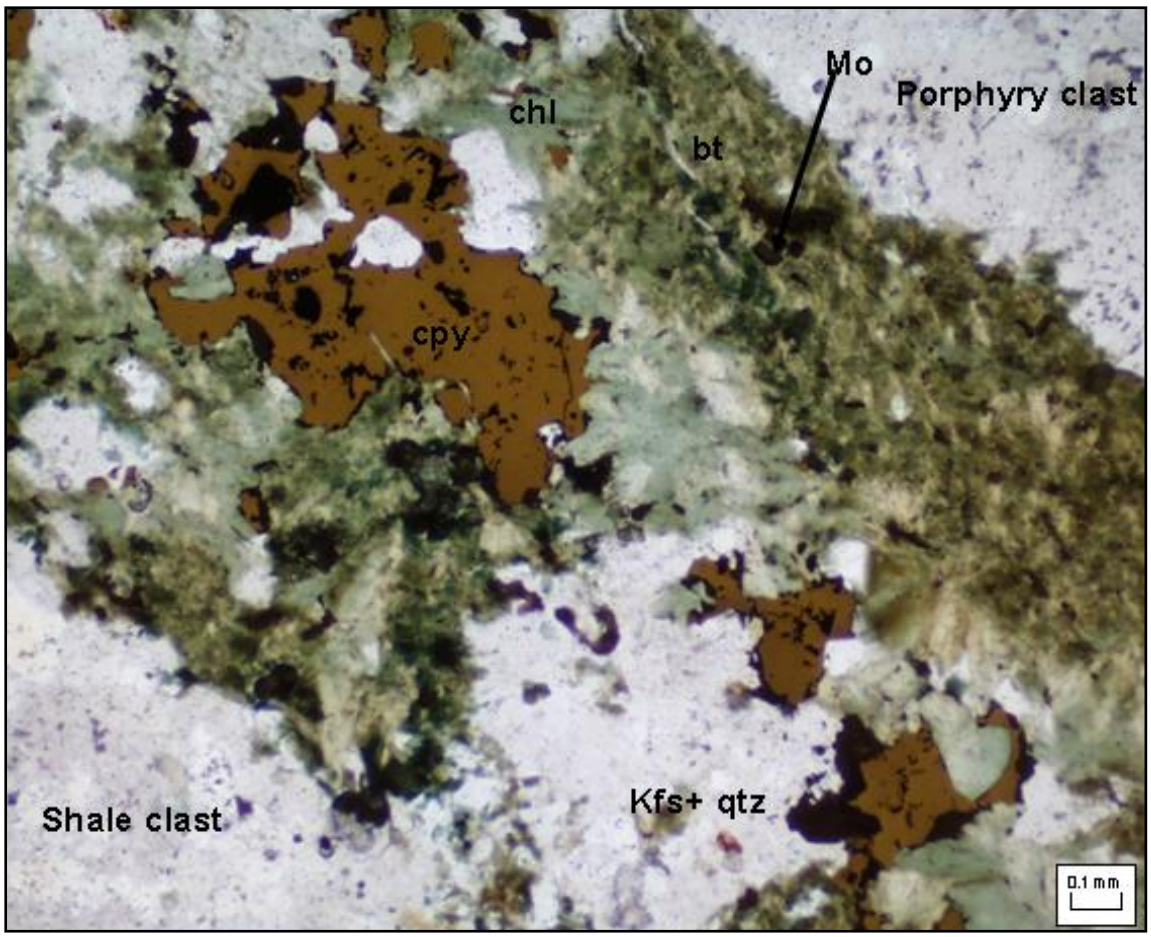

Figure 45. Photomicrograph of breccia matrix separating clasts of porphyry and shale. Here the late breccia chlorite-chalcopyrite assemblage can be seen replacing the biotite of the primary matrix mineralogy. This figure displays the common coloring of the breccia, with chlorite having a lighter green color and radial crystal shape (molybdenite = Mo, chlorite = chl, biotite = bt, chalcopyrite = cpy, orthoclase = Kfs, quartz = qtz) (D2039-1532) (Plane polarized transmitted and reflected light, FOV = 1.7 mm).

Figure 46. Core photograph showing the strong chalcopyrite (cpy) and pyrite (py) with chlorite in the breccia matrix (D2039-1550', NQ core).

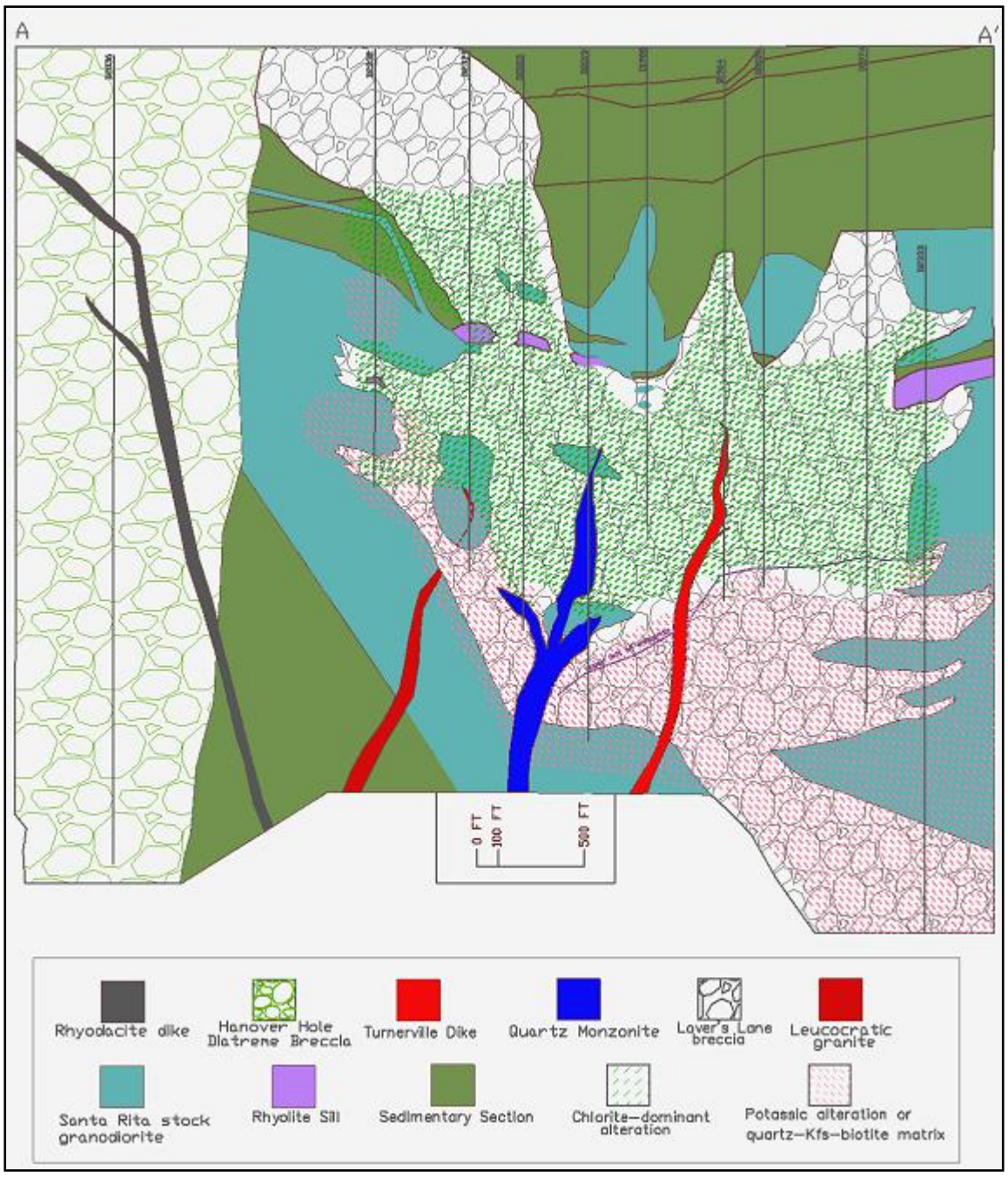

Figure 47. Generalized alteration patterns in the Lover's Lane breccia and surrounding wall rocks in the A-A' cross section. The purple line indicates the upper limit of anhydrite.

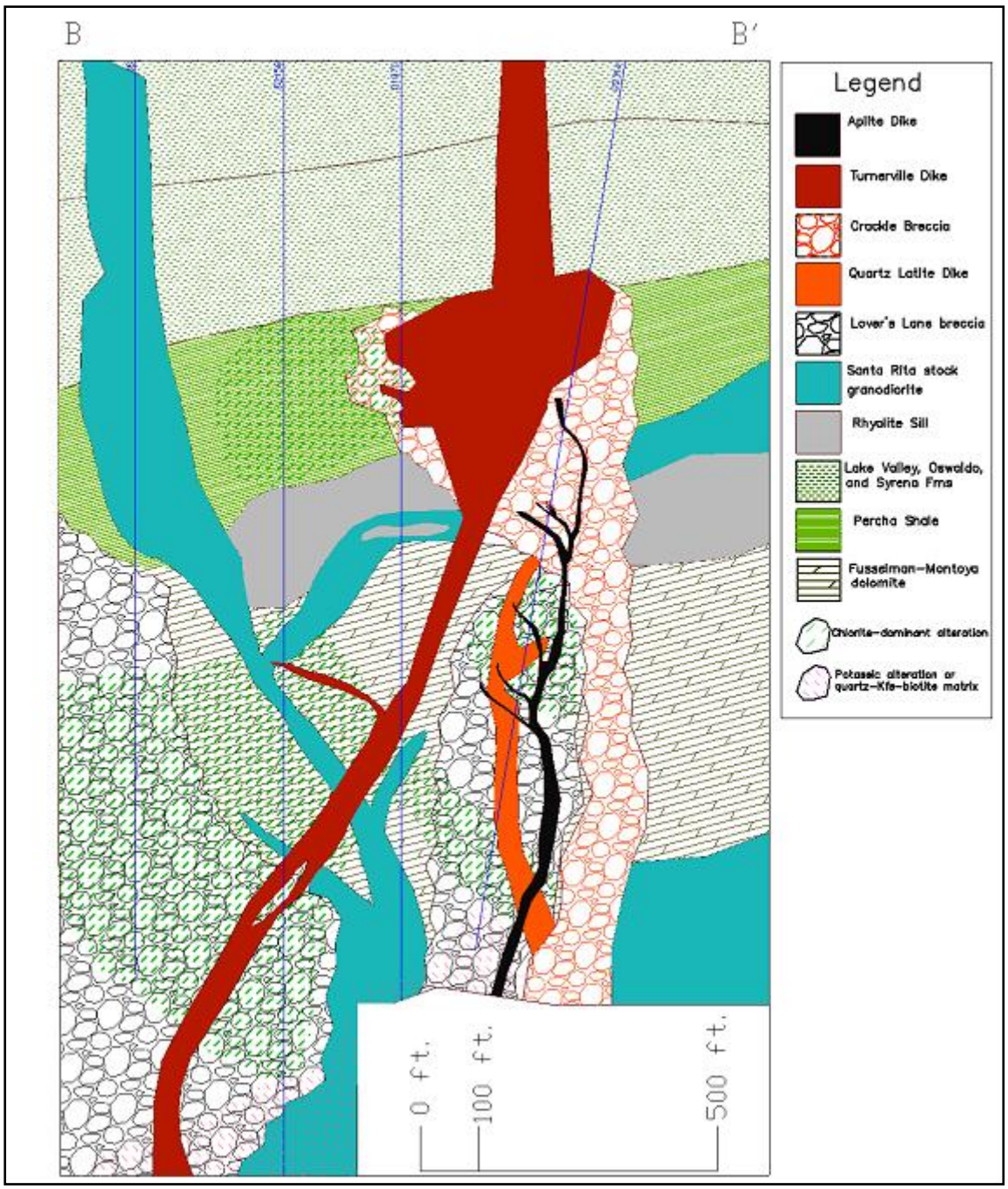

Figure 48. Generalized alteration patterns in the Lover's Lane breccia and surrounding wall rocks in the B-B' cross section.

Chalcopyrite is also associated with the anhydrite pseudo-breccia, which cross cuts the Lover's Lane silicate-cemented breccia (Fig. 49). Anhydrite and chalcopyrite are

also in the matrix of the Lover's Lane breccia, with the anhydrite ± chalcopyrite filling vugs. Some occurrences of this anhydrite-chalcopyrite in the matrix have biotite along and rimming clasts, and anhydrite-chalcopyrite filling the gap between clasts. Minor pyrite and molybdenite also occur within massive anhydrite, and are interpreted to have co-precipitated with anhydrite in most places, as there is little or no apparent incorporation of wallrock fragments in the massive anhydrite, as would likely be present if the molybdenite and pyrite were incorporated from the silicate matrix. The upper limit of the presence of anhydrite is shown on Plate 1, though there is a small possibility that anhydrite was leached out above this line by supergene fluids.

Figure 49. Core photograph of the massive anhydrite (anhy) with chalcopyrite (cpy) (D2333-1735', HQ-sized core).

Sphalerite is a very minor phase within the matrix of the breccia, and is locally associated with late-breccia chalcopyrite, and also with magnetite, likely as a pre-breccia

skarn-related mineralization. Galena was noted only in a few locations in hand sample, and appears to be associated with fragments of skarn-related mineralization in intervals of stronger magnetite (and weak sphalerite) mineralization.

Stable Isotope Analysis

Selected samples were chosen for sulfur isotope work, both of sulfide and sulfate minerals. Table 4 is a summary of the samples used, minerals, $\delta^{34}S$, and mineralization descriptions. Several of these samples were chosen for co-existing sulfide-sulfate minerals, in this case chalcopyrite-anhydrite and molybdenite-anhydrite. Stable isotope analyses were performed using an Eurovector model 3028 elemental analyzer interfaced to a Micromass IsoPrime stable isotope ratio mass spectrometer. Sulfur isotope analyses were performed by Simon Poulsen and the University of Nevada, Reno, after the method of Giesemann et al. (1994) and Grassineau et al. (2001). V2O5 was added to samples as a combustion aid.

The isotopic fractionation of these minerals (when precipitating in equilibrium) is temperature-dependent, so an estimate of the temperature of formation can be derived. Table 5 shows the temperatures that this exercise yields, and the data are graphed in Figure 50. The assumption is made that the minerals were indeed in equilibrium, which is likely the case for the chalcopyrite-anhydrite pairs. The molybdenite-anhydrite pair gives a similar temperature, but it does not match with fluid inclusion data from samples located near this pair (discussed below). The molybdenite is present as "paint" on the veinlet edge, therefore it is likely that it precipitated before the anhydrite sealed the veinlet, and the pair does not represent a true equilibrium assemblage. Figure 51 is a

photograph taken of this sample before the minerals were extracted. Figures 52 and 53 show the chalcopyrite-anhydrite pairs used for geothermometry, which appear to be in equilibrium. The temperatures of 533°C and 550°C are interpreted as the temperature of precipitation of anhydrite and chalcopyrite during healing of the "anhydrite pseudo-breccia," in which massive anhydrite fills the open space of the breccia. Lesser amounts of anhydrite are present in the silicate-dominated Lover's Lane breccia, and are in almost every case a post-breccia, vug- or vein- filling phase, paragenetically similar to the massive anhydrite on which the isotope analyses were conducted. The chalcopyrite in the anhydrite pseudo-breccia is a relatively minor occurrence of chalcopyrite, compared to the late-breccia chlorite-chalcopyrite assemblage, which is interpreted to be a much cooler event.

Sulfur Isotope Samples

Sample #	Mineral	Sample location (DH # - footage)	$\delta^{34}S_{VCDT}$ (‰) ($\pm^{0.2}$)	Descr of rock type, paragenesis, and ore mineralization
RH-1A	molybdenite	D2314-1426	-1.4	high grade moly-cemented crackle breccia
RH-1B	molybdenite	D2314-1426	-1.7	high grade moly-cemented crackle breccia
RH-2A	anhydrite	D2333-2008	11.4	anhy+qtz 1" thick veinlet in granodiorite,
RH-3A	molybdenite	D2332-1958	-1.2	short interval of high grade moly-cemented crackle breccia
RH-4A	chalcopyrite	D2333-1755	-1.3	cpy in anhy pseudo-breccia
RH-5A	anhydrite	D2333-1755	11.2	anhy in anhy pseudo-breccia
RH-6A	molybdenite	D2039-2354	-2.4	moly in matrix of breccia, chl/green bt/actin(?) matrix
RH-7A	molybdenite	D2329-1922	-1.6	moly and mt, moly later
RH-8A	molybdenite	D1988-1904	-1.8	moly in matrix, matrix is chl/green bt, also cpy in matrix
RH-9A	molybdenite	D2019-1880	-1.8	moly with chl/serp
RH-10A	molybdenite	D1964-2200	0.3	moly as thick paint on veinlet edge of anhy±qtz
RH-11A	anhydrite	D1964-2200	10.1	anhy in veinlet with thick moly paint
RH-12A	chalcopyrite	D2333-1619	-2.1	cpy in ahny pseudo-breccia
RH-13A	anhydrite	D2333-1619	9.9	anhy in pseudo-breccia

moly = molybdenite, anhy = anhydrite, qtz = quartz, cpy = chalcopyrite, chl = chlorite, bt = biotite, actin = actinolite, mt = magnetite, serp = serpentine

Table 4. Sulfur isotope data from sulfides and sulfates in the Lover's Lane breccia.

Sulfur Isotope Geothermometry

Sample #	Mineral	$\delta^{34}S_{VCDT}$ (‰) (±0.2)	Sample location	difference	T (Celsius)	min/max	equation source
RH-4A	chalcopyrite	-1.3	D2333-1755	12.5	**533**	502/567	O + R, 1979
RH-5A	anhydrite	11.2	D2333-1755				
RH-10A	molybdenite	0.3	D1964-2200	9.8	**540**	515/556	O + L, 1982
RH-11A	anhydrite	10.1	D1964-2200				
RH-12A	chalcopyrite	-2.1	D2333-1619	12	**550**	517/587	O + R, 1979
RH-13A	anhydrite	9.9	D2333-1619				

References:

Field, C.W., Zhang, L., Dilles, J.H., Rye, R.O., and Reed, M.H., 2005, Sulfur and oxygen record in sulfide and sulfate minerals of early, deep, pre-Main Stage porphyry Cu-Mo and late Main Stage base-metal mineral deposits, Butte district, Montana: Chemical Geology, v. 215, pp. 61-93.

Ohmoto, H., and Lasaga, A.C., 1982, Kinetics of reactions between aqueous sulfates and sulfides in hydrothermal systems: Geochimica et Cosmochimica Acta, v. 46, pp 1727-1745.

Ohmoto, H, and Rye, R.O., 1979, Isotopes of sulfur and carbon: *in* Barnes, H.L. (ed), Geochemistry of Hydrothermal Ore Deposits, Wiley, New York, pp. 509-567.

Table 5. Results of sulfide-sulfate geothermometry. Pairs used in calculations are boxed and color coded.

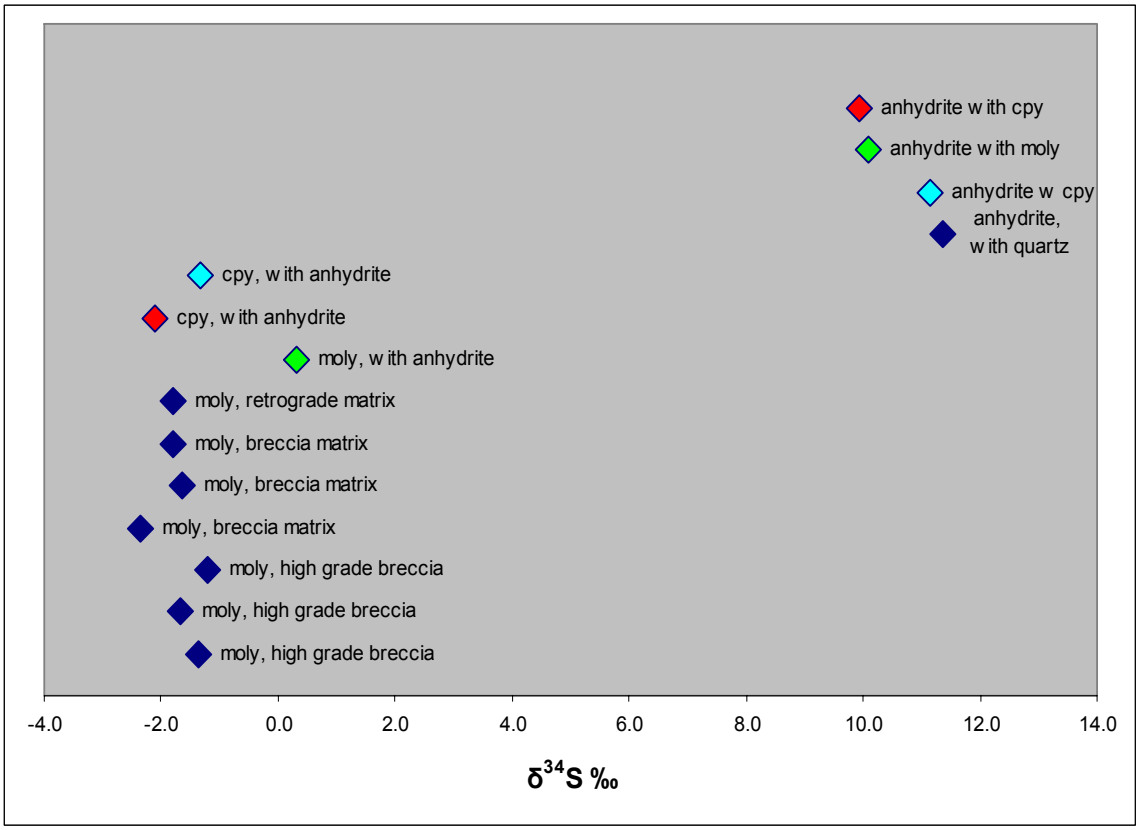

Figure 50. Graph of sulfur isotopes. Pairs used in geothermometry are color coded.

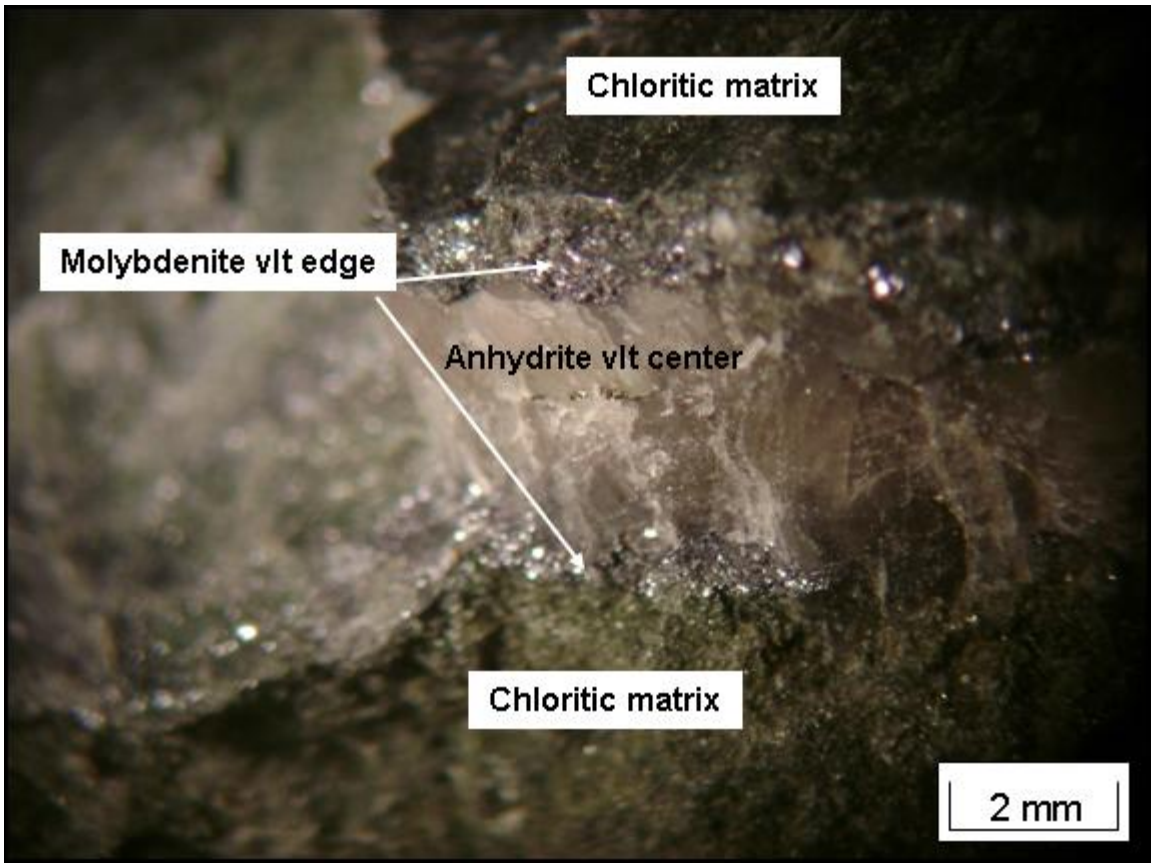

Figure 51. Sample D1964-2200, showing the molybdenite paint on the walls of the veinlet, with anhydrite and minor chalcopyrite filling the veinlet. The veinlet is approximately 4mm wide.

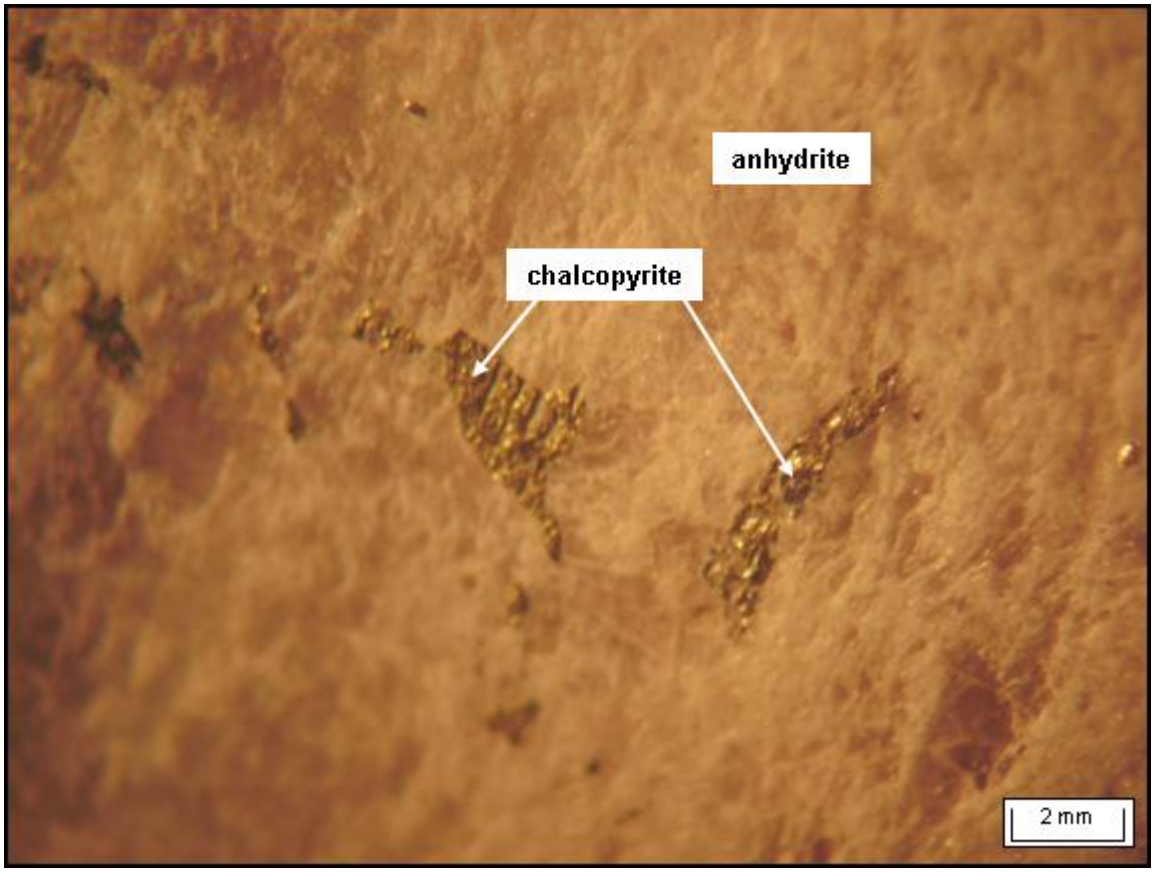

Figure 52. D2333-1619, chalcopyrite in massive anhydrite. (FOV = ~2 cm)

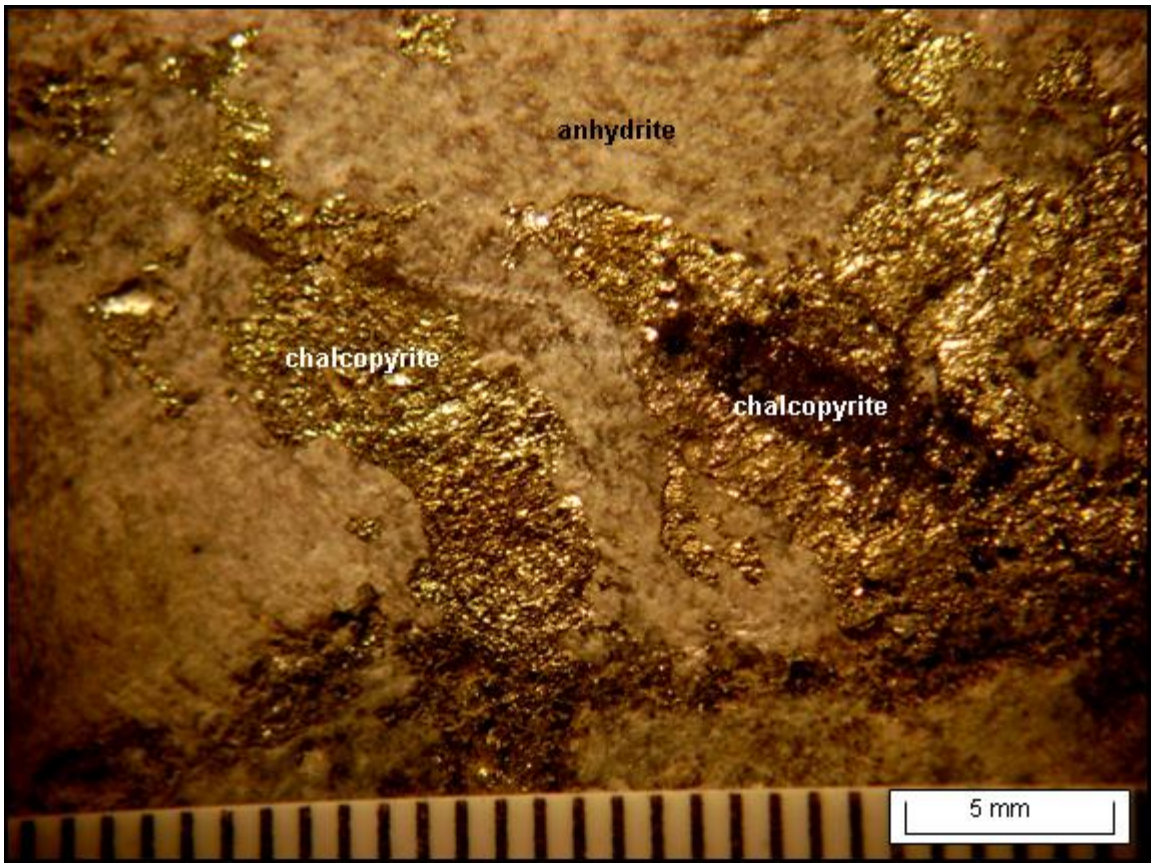

Figure 53. D2333-1755, chalcopyrite in massive anhydrite, which is the matrix of the "anhydrite pseudo-breccia." Scale bar is in millimeters.

The $\delta^{18}O$ of anhydrite was also determined, and the data are presented in Table 6, along with the calculated $\delta^{18}O$ of the fluid from which it precipitated, using the temperatures derived from sulfide-sulfate geothermometry. The calculated $\delta^{18}O$ of the water is between 3.4 and 4.7 ‰, which is lower than average magmatic water (5 – 10 ‰)). Calculations using an average of 7‰ $\delta^{18}O$ as magmatic water and the $\delta^{18}O$ of the anhydrite determined here yield temperatures 200-250°C higher than the sulfide-sulfate geothermometry, indicating that the assemblages did not precipitate from pristine magmatic fluids.

The chalcopyrite, molybdenite, and anhydrite sulfur isotope values fall within previously published data for Santa Rita/Chino sulfides and sulfates (Ohmoto and Rye,

1979), which suggest magmatic sulfur derivation. A mixing of meteoric water (providing some of the oxygen), and magmatic water (the sulfur source), could lead to the values obtained here. The mixing or contamination of magmatic fluids by meteoric fluid is likely, due to the fact that there are well-documented recurrences of magmatic mineral precipitation (in the breccia matrix and alteration overprints on breccia) that occur after precipitation of cooler and/or meteoric-influenced mineral assemblages at Santa Rita, such as the chlorite-chalcopyrite and hydrous retrograde assemblages (see paragenesis discussion). The presence of anhydrite veinlets with molybdenite paint cutting strongly chloritized breccia matrix (Fig. 51) also suggests that the chlorite-chalcopyrite alteration assemblage occurred between the multiple magmatic stages, and that mixing of different fluids occurred throughout the late-breccia stage.

Sample	Location	Mineralization type	$\delta^{18}O_{VSMOW}$ (‰)	T (ºC) used in calculation	Water (calculated) $\delta^{18}O_{VSMOW}$
RH-2A	D2333-2008	anhy+qtz in 1" thick veinlet in granodiorite	**7.4**	540 (1)	4.4
RH-5A	D2333-1755	anhy in "anhy pseudo-breccia"	**7.8**	533 (pair with cpy)	4.7
RH-11A	D1964-2200	anhy in veinlet with thick moly paint	**6.4**	540 (2) (pair with moly)	3.4
RH-13A	D2333-1619	anhy in "anhy pseudo-breccia"	**6.6**	550 (pair with cpy)	3.8
(1) T assumed based on other anhy-cpy geothermometry					
(2) Likely not in equilibrium, see text					
Equation and coefficients for calculations from Faure, 1986					

Table 6. Measured $\delta^{18}O$ of anhydrite, with calculated $\delta^{18}O$ of water at T determined by sulfide-sulfate geothermometry (using equations and coefficients from Faure, 1986).

Figure 54 shows the calculated oxygen isotope ratios of the hydrothermal fluid over a temperature range of 300-600ºC, for each of the samples listed in Table 6. The

$\delta^{18}O$ of the fluid for the respective sulfide-sulfate geothermometry determinations are also shown, which fall towards the higher end of the temperature spectrum, indicating substantial heating of meteoric water (based on the isotope ratios).

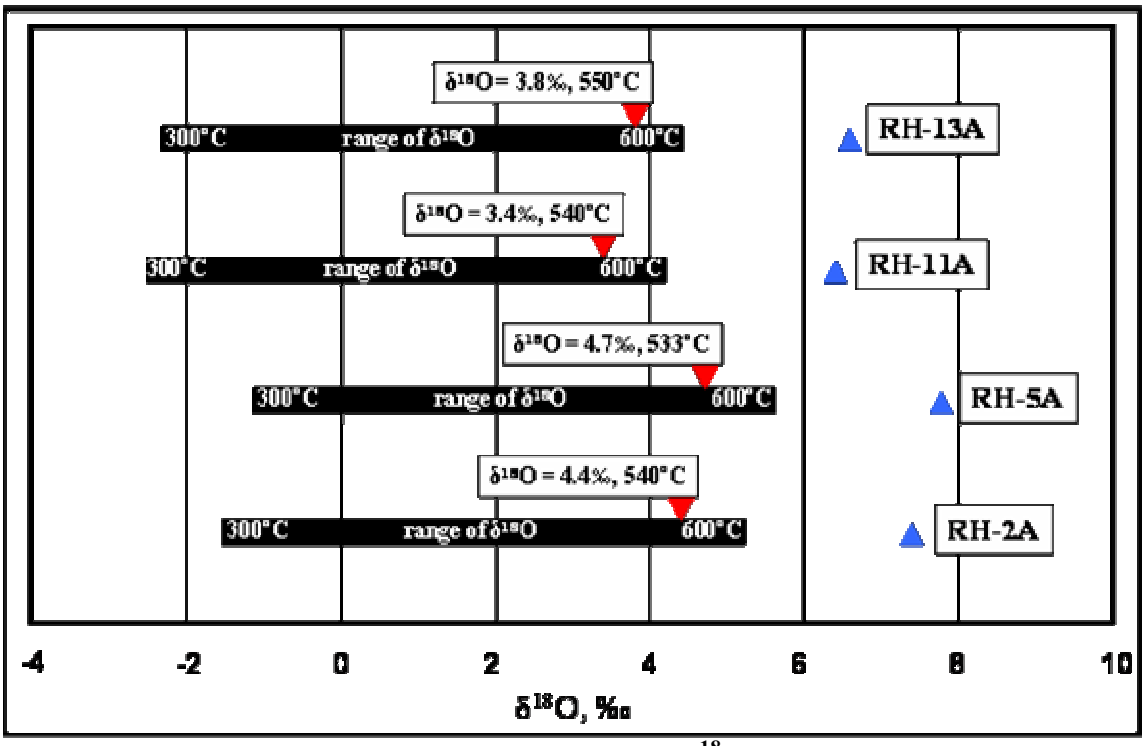

Figure 54. Graph showing range of calculated $\delta^{18}O$ of fluid for the temperature range of 300-600ºC, for each sample. Blue triangles are the $\delta^{18}O$ of the anhydrite, and red triangles show the $\delta^{18}O$ of the fluid for specific temperatures derived from sulfide-sulfate geothermometry.

Fluid inclusions analysis

Fluid inclusion analyses were completed on selected samples to develop a general idea of the fluid temperature and chemistry of the molybdenite mineralization associated with pre- and post- breccia veinlets. Thin sections were searched for fluid inclusions in matrix-forming minerals, but adequate inclusions were not found that would constrain the conditions of breccia-healing fluids. A Fluid Inc. adapted USGS gas-flow

heating/freezing stage was used, in which the thermocouple is placed directly on the chips being analyzed in a convective chamber with 3 glass plates above and below the chamber. The stage is periodically calibrated using artificial inclusions and accuracy is within 2 degrees for heating runs and 0.1 degree near zero. The Olympus BX51 transmitted light scope used has 5x, 10x, and 40x objective lenses and camera capability. Heating runs were completed on 56 inclusions, and freezing runs were completed on 17 fluid inclusions to determine salinity. These data and description are presented in Appendix I and graphed in Figures 55 and 56. The sample numbers refer to drill hole number and depth, so the locations can be correlated spatially within the studied area.

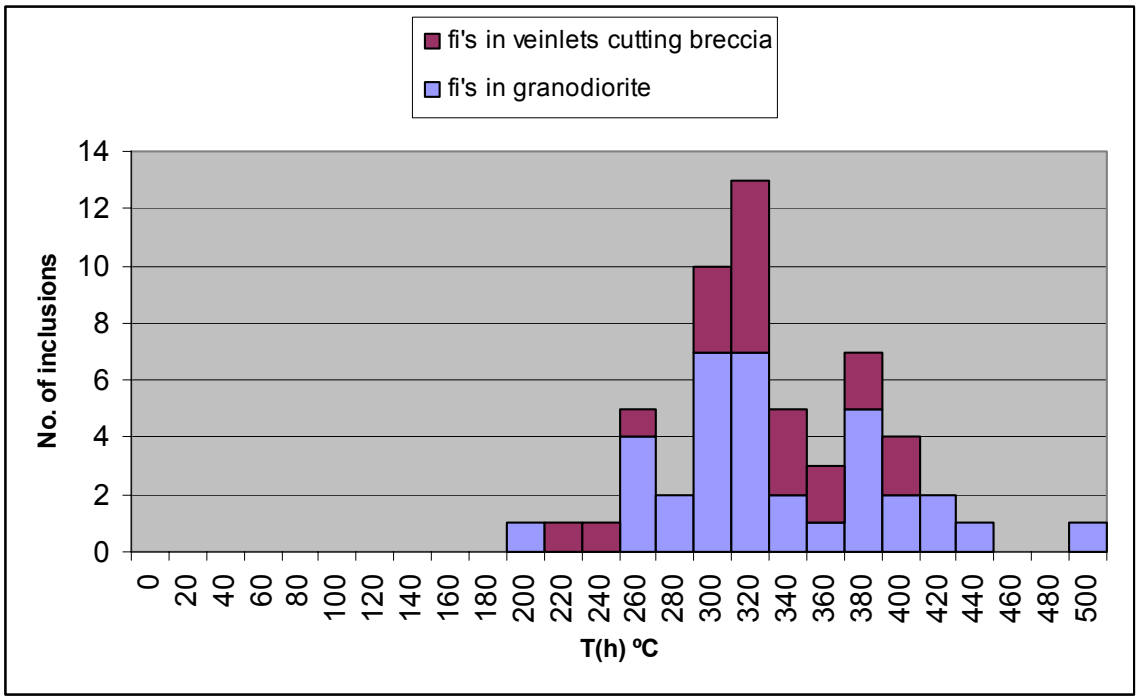

Figure 55. Homogenization temperatures of fluid inclusions in quartz-molybdenite veinlets in the Lover's Lane breccia and surrounding wall rock (n = 56).

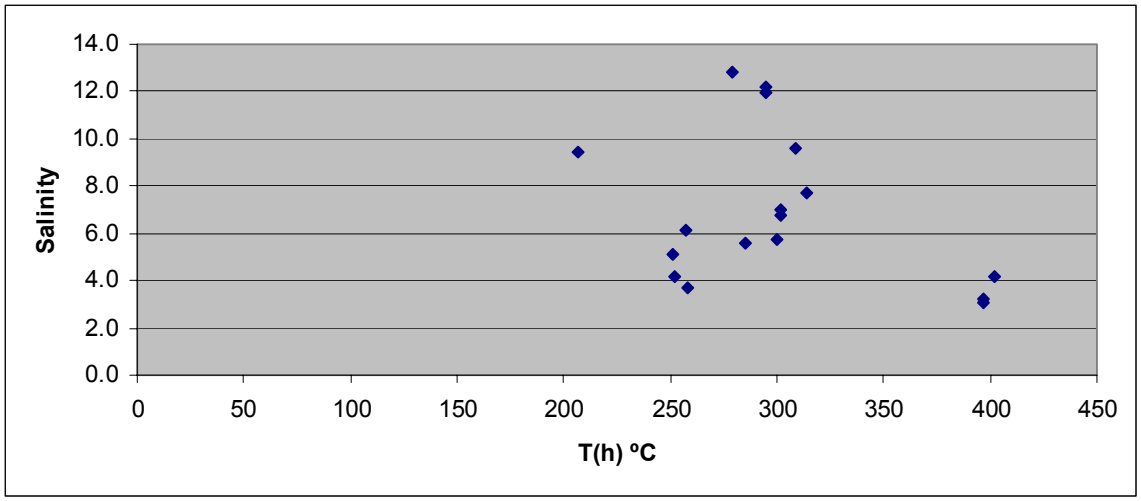

Figure 56. Salinities (in wt. % NaCl equiv.) of selected fluid inclusions plotted with temperature.

This study focused on inclusions in quartz within quartz-molybdenite veinlets that cross-cut breccia and unbrecciated granodiorite. Transmitted light petrography was conducted prior to the heating and freezing analyses to verify the quartz-molybdenite association, and Figs. 57 through 61 show some of the relationships as seen through the fluid inclusion microscope. In most cases, the inclusions analyzed were surrounded by or directly adjacent to molybdenite flakes, within defined veinlets. A few quartz grains appeared to have small molybdenite flakes as mineral inclusions. No inclusions were analyzed that were not in quartz that did not display a clear relationship with molybdenite. Where possible, several inclusions within a small area in a single crystal were analyzed, following a fluid inclusion assemblage (FIA) approach with moderate success in obtaining similar homogenization temperatures across the FIA. A minor amount of fine-grained biotite, anhydrite, and pyrite were present in a few of the veinlets associated with quartz-molybdenite.

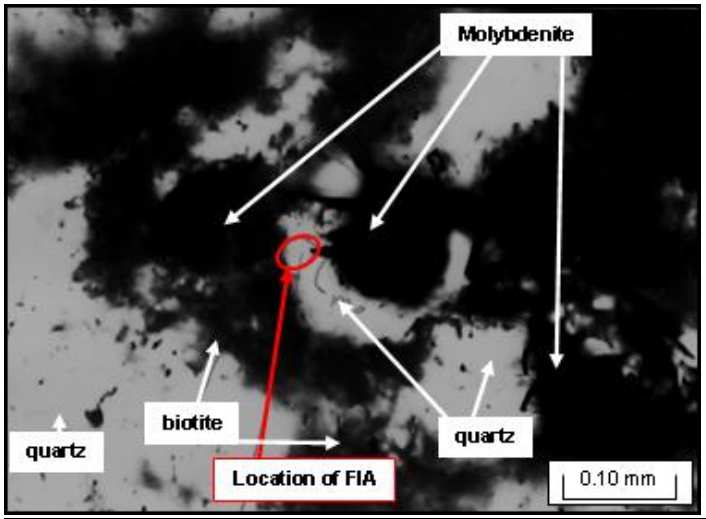

Fig. 57. Location of a fluid inclusion assemblage in quartz-molybdenite veinlet, with molybdenite and biotite surrounding quartz (D2329-1374-1, 2a in FIA, Th = 314ºC).

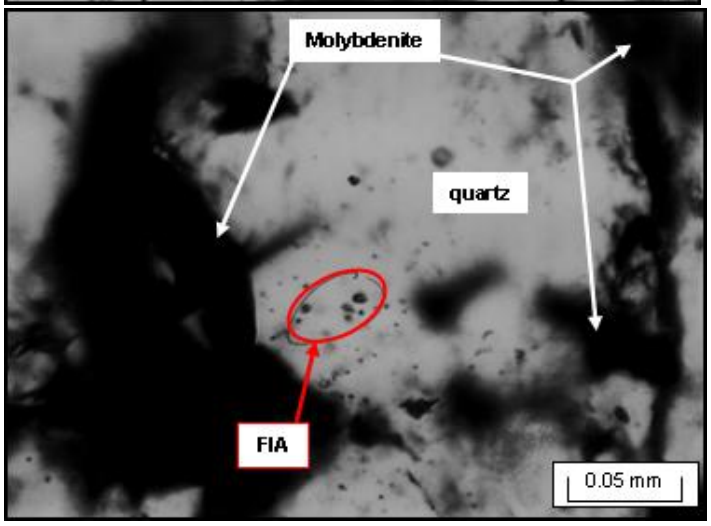

Fig. 58. Example of a fluid inclusion assemblage in quartz-molybdenite veinlet, with molybdenite surrounding quartz grain and as mineral inclusions (D2329-2303-1, 1a-1c, 1e, in FIA, Th = 279-402ºC).

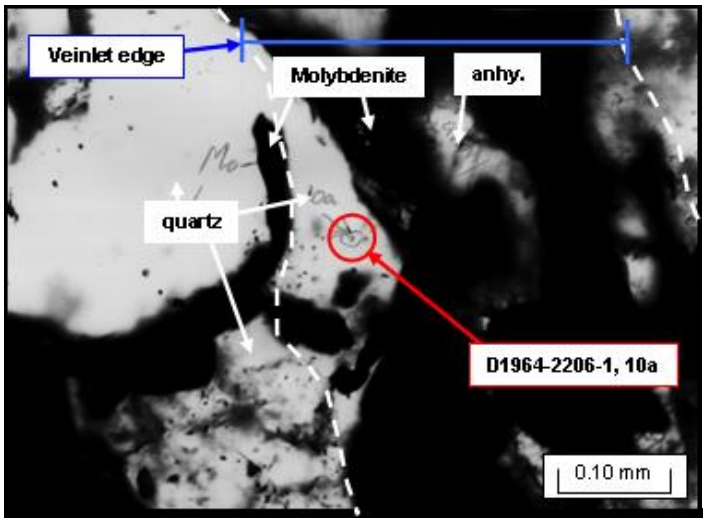

Fig. 59. Fluid inclusion location in quartz-molybdenite veinlet, with molybdenite, fine-grained quartz, and minor anhydrite in the molybdenite "paint" on veinlet edge (D1964-2206-1, 10a, Th = 295ºC).

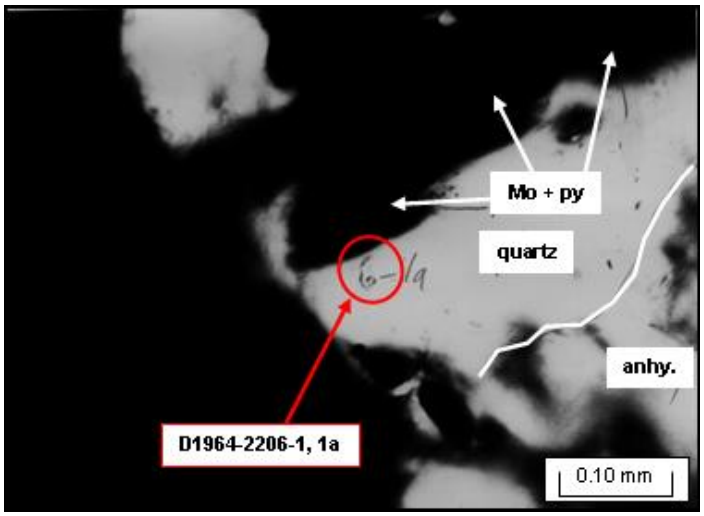

Fig. 60. Fluid inclusion in quartz-molybdenite veinlet, with molybdenite, pyrite, and anhydrite surrounding quartz (D1964-2206-1, 1a, Th = 241°C).

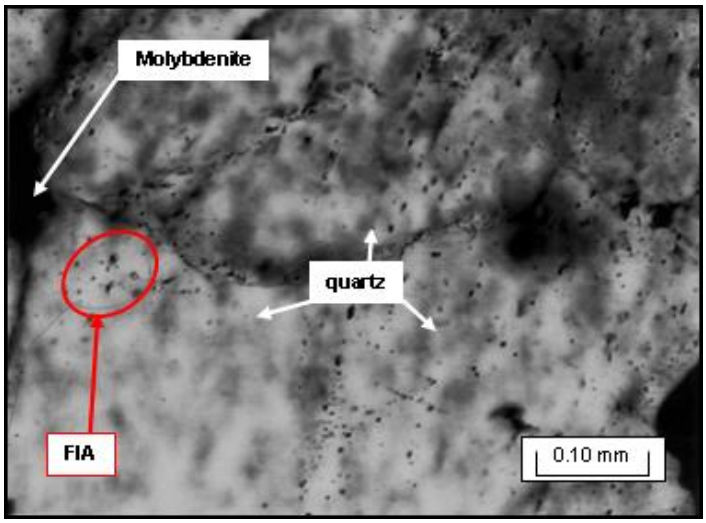

Fig. 61. Location of a fluid inclusion assemblage in quartz-molybdenite veinlet, with molybdenite and biotite surrounding quartz (D2329-1374-1, 6a-6f in FIA, Th = 375-382°C)

The vast majority of the inclusions with clear association with molybdenite were halite-undersaturated, liquid-dominant, with no metallic daughters (Figs. 62 through 64). A few inclusions had halite daughters (Fig. 63), but most attempts to homogenize the halite were unsuccessful due to heat limits of the stage (500° C) or very small size of the daughter mineral. Vapor-dominant inclusions were present in some of the relevant crystals, but could not be homogenized due decrepitation or the heat limits of the stage. Little evidence for boiling was present, as co-existing liquid- and vapor- dominant inclusions were very rare in the relevant quartz. Liquid-dominant inclusions, which

homogenize to liquid, had vapor bubbles ranging from 15-50% of the size of the inclusion in plan view, with the majority in the 30-35% range, based on visual estimate. Inclusions ranged in size from 0.002 mm to 0.015 mm measured in the longest dimension in plan view (Fig. 64).

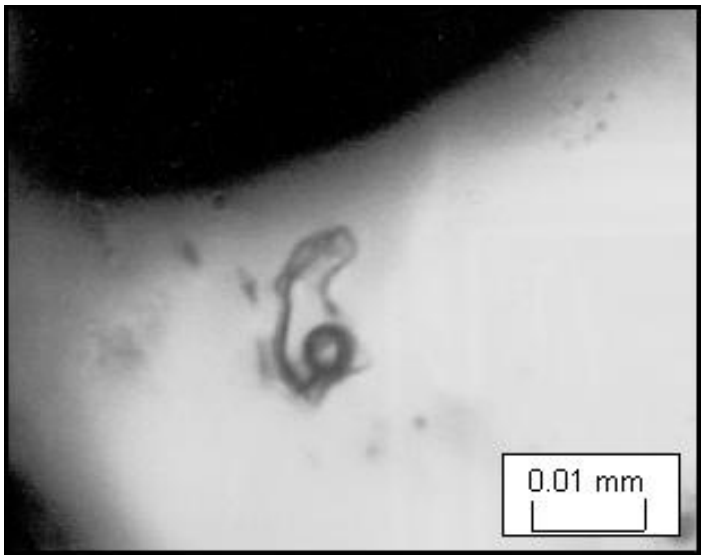

Fig. 62. Typical fluid inclusion in quartz, liquid-dominant with vapor bubble ~20% of inclusion in plan view (D1964-2206-1, 1a, Th = 241ºC).

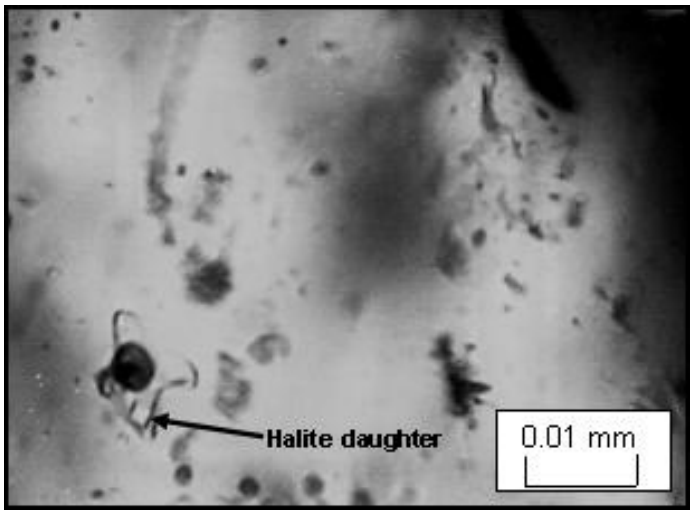

Fig 63. Rare halite-saturated fluid inclusion that homogenized below 500ºC (D2329-1374-2, 1a, Th = 482ºC, Th(halite) = 215ºC).

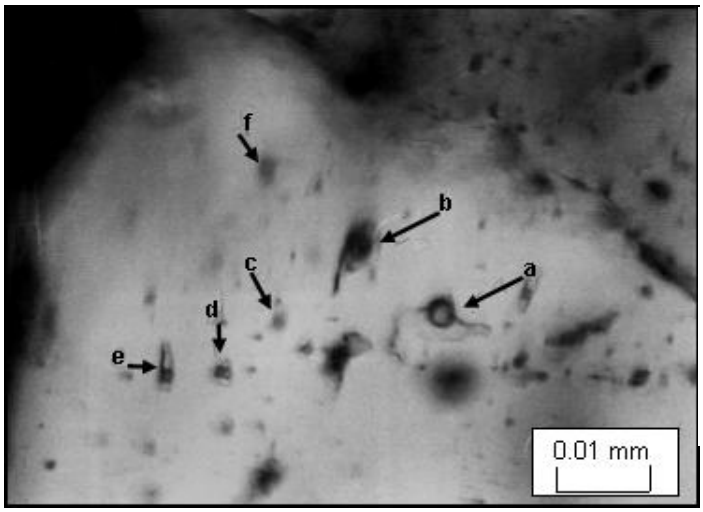

Fig. 64. High magnification view of fluid inclusion assemblage in Fig 61. (D2329-1374-1, 6a-6f, Th = 375-382ºC)

Salinities of selected inclusions were determined by freezing point depression, by cooling the chip to below -100ºC using cooled nitrogen gas and noting the temperature of the final melting point of the ice in the inclusion as it was heated slowly to above freezing.

Corrections for trapping pressure to the data with salinity determination, based on depth in drill hole and previously published estimates of 1500 ft. of premineral cover (Nielson, 1968), yield numbers about 30ºC higher than homogenization temperatures. Sulfide-sulfate isotope geothermometry (discussed above in detail) on a sample in D1964 near 2200 ft. depth resulted in a temperature of 540ºC, which is 150ºC higher than the highest inclusion analyzed in a nearby quartz-anhydrite-molybdenite veinlet. The amount of premineral cover necessary to provide the required pressure to correct the sulfide-sulfate and fluid inclusion temperatures would be 13,800 ft (using the graph for 10% salinity in Potter, 1977). However, Reynolds and Beane (1985) suggest that little correction for pressure was needed for their fluid inclusion data due to similar temperatures derived from oxygen isotopes and fluid inclusions in specific mineral assemblages. Also, work done by Jones et al. (1967) and others within indicates that the

maximum overburden during mineralization at Santa Rita was about 4,000 ft. (discussed in the district geology section above), which would be added to the current surface, as the deposit (or top of the Santa Rita stock) was near the pre-mining surface. With the addition of 2,200 ft. of drilling depth, the total is 6,200 ft. Thus, it is very unlikely that enough premineral cover existed to require such a large pressure correction, and it is interpreted that the sulfide-sulfate pair and fluid inclusions do not represent the same vein-filling event (Note that the analyses were conducted on different samples). No pressure correction was applied to data gathered during this study.

No trend is apparent in salinity versus temperature (Fig. 56), which is possibly due to the low number of inclusions for which both heating and freezing runs were accomplished. Based on these data, there is no apparent difference in homogenization temperature or salinity between veinlets that truncate the breccia and veinlets that are in granodiorite. If multiple pulses are present, there is not a significant temperature difference that can be determined from this fluid inclusion work.

Uranium/lead dating of selected intrusive phases

Uranium/lead dating on zircons was attempted on several igneous phases in the vicinity of the Lover's Lane breccia and the Hanover Hole. Samples were collected from outcrop exposures and drill core of the Santa Rita stock, quartz-monzonite porphyry, quartz latite dikes, and rhyodacite dike. The phases chosen include both relatively younger and older rocks than the Lover's Lane breccia and Hanover Hole diatreme; therefore the intent was to constrain the age of these two breccias. The separates and analyses were performed by Paul O'Sullivan and Ray Donelick at Apatite to Zircon, Inc.,

using the LA-ICP-MS at the GeoAnalytical Lab at Washington State University. These results are presented in Table 7 and Figure 65, with the methodology and raw data listed in Appendix II. The data fit the geologic relationships in a relative sense, except for the quartz latite dike in the Lee Hill pit, which crosscuts the Santa Rita stock in the vicinity.

The U-Pb ages are younger by several million years than Re-Os age dates for molybdenite mineralization in the Santa Rita stock. It is possible that lead loss due to hydrothermal activity occurred and resulted in the younger absolute U-Pb ages. While this is a possible scenario for the Santa Rita stock, it is much less likely a factor in the late quartz-latite dikes and the rhyodacite dike, as they cross cut the hypogene mineralization at Santa Rita. At this point, no conclusion is drawn from these data, or from the large discrepancy between the K-Ar/Ar-Ar/Re-Os dates and the U-Pb dates.

Intrusive Phase	**Location**	**Age, Ma**
Santa Rita stock	Lee Hill pit	55.49 ± 0.24
Tgr/Tgb stock	Chino pit	56.91 ± 0.25
Townsite	Townsite Island, Chino pit	55.07 ± 0.22
Quartz monzonite dike	D1550	54.78 ± 0.36
Quartz latite dike	D1964	54.1 ± 0.36
Quartz latite dike	Lee Hill pit	55.81 ± 0.35
Rhyodacite dike	Hanover Hole	53.87 ± 0.26

Table 7. U-Pb age date data for intrusive phases at Santa Rita.

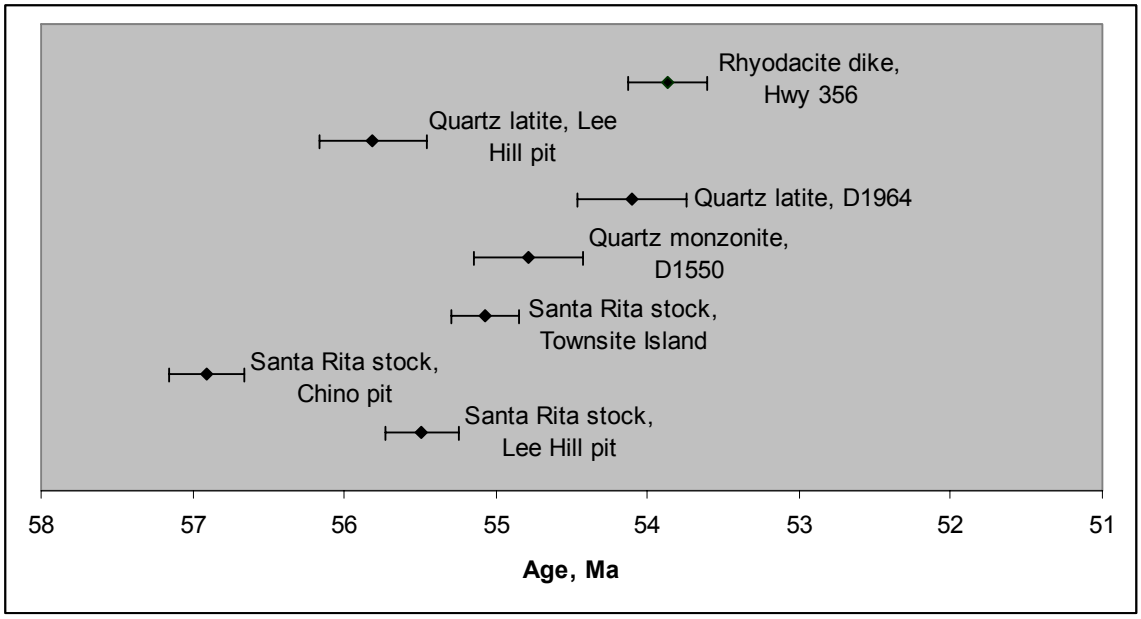

Figure 65. U-Pb age date graph for intrusive phases at Santa Rita.

Summary of Cross-cutting Relationships

In addition to mineralogical paragenesis discussed above, several large-scale relationships were noted that are key to interpreting the Lover's Lane breccia and accompanying intrusive activity as a whole. Figure 70 summarizes the sequences of events at Santa Rita. The key relationships seen in core are as follows:

- Alteration of the Santa Rita granodiorite stock varies, from relatively fresh, to orthoclase- and/or biotite- rich potassic alteration. Altered and unaltered clasts are present in breccia (Fig. 66).

- Leucocratic granite is recognized intruding potassically altered Santa Rita stock , and as clasts in the Lover's Lane breccia (Figs. 12, 66, and 67). Nowhere does the leucocratic granite cross cut the breccia.

- Molybdenite-bearing veinlets are locally truncated at the clast margins, indicating at least some molybdenite mineralization occurred before breccia emplacement (Fig. 42).

- Chlorite-chalcopyrite mineralization and hydrous/retrograde alteration dominantly affects the breccia matrix, but chlorite-chalcopyrite is also present in clasts within the pseudo-porphyry breccia phase (Fig. 31).

- Post-breccia quartz-molybdenite veinlets crosscut the Lover's Lane breccia matrix and pseudo-porphyry breccia matrix (Figs 42 and 66).

- In the interior portions of the Lover's Lane breccia, quartz latite and quartz monzonite dikes are unaltered and unmineralized.

- In the vicinity of the high grade crackle breccia, a quartz latite dike is brecciated with molybdenite rimming clasts (Fig. 68). However, the mineralogically similar Turnerville dike intrudes weakly mineralized breccia above the high grade zone (Fig. 69).

- A thin, barren, aplite dike intrudes into the high grade crackle breccia, cross-cutting mineralization.

- The Hanover Hole diatreme breccia has mineralized clasts, but no mineralization-related alteration within the matrix, and cross-cuts pseudo-porphyry breccia in surface exposures. The unaltered and unmineralized rhyodacite dike intrudes into the Hanover Hole diatreme breccia body.

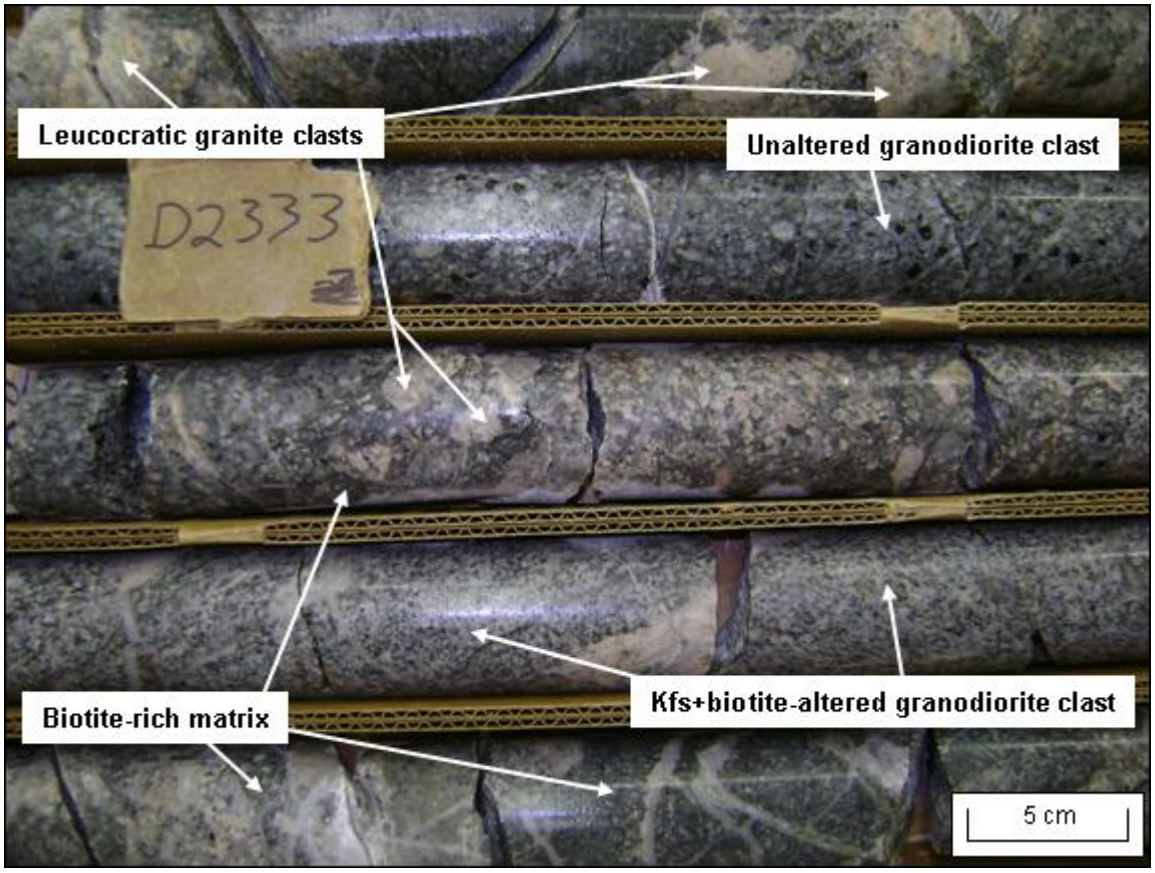

Figure 66. Several cross-cutting relationships preserved in core. Breccia clasts are dominantly leucocratic granite (middle row and top row) with some larger clasts of Santa Rita stock (row second from top). Quartz veinlets (with some molybdenite and anhydrite) are present cross-cutting the breccia (middle row) and granodiorite (second from top). The bottom row consists of breccia with sparser clasts and very strong biotite in the matrix. The second from bottom row consists of potassic-altered stock, with fine grained secondary biotite and patches of strong orthoclase replacement, and is a large clast in the breccia (D2333, 2810-2819 ft).

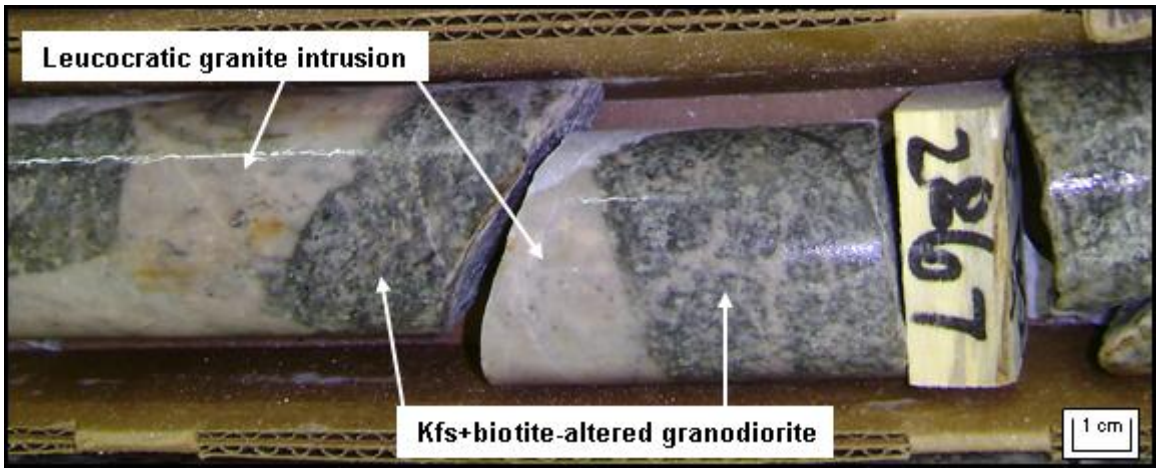

Figure 67. Intrusion of leucocratic granite cross-cutting potassically altered granodiorite (nominal Santa Rita stock). Thin fingers of this quartz + orthoclase ± biotite intrusive are prevalent at depth, cutting granodiorite, and as clasts in the Lover's Lane breccia (D2333-2867', NQ core).

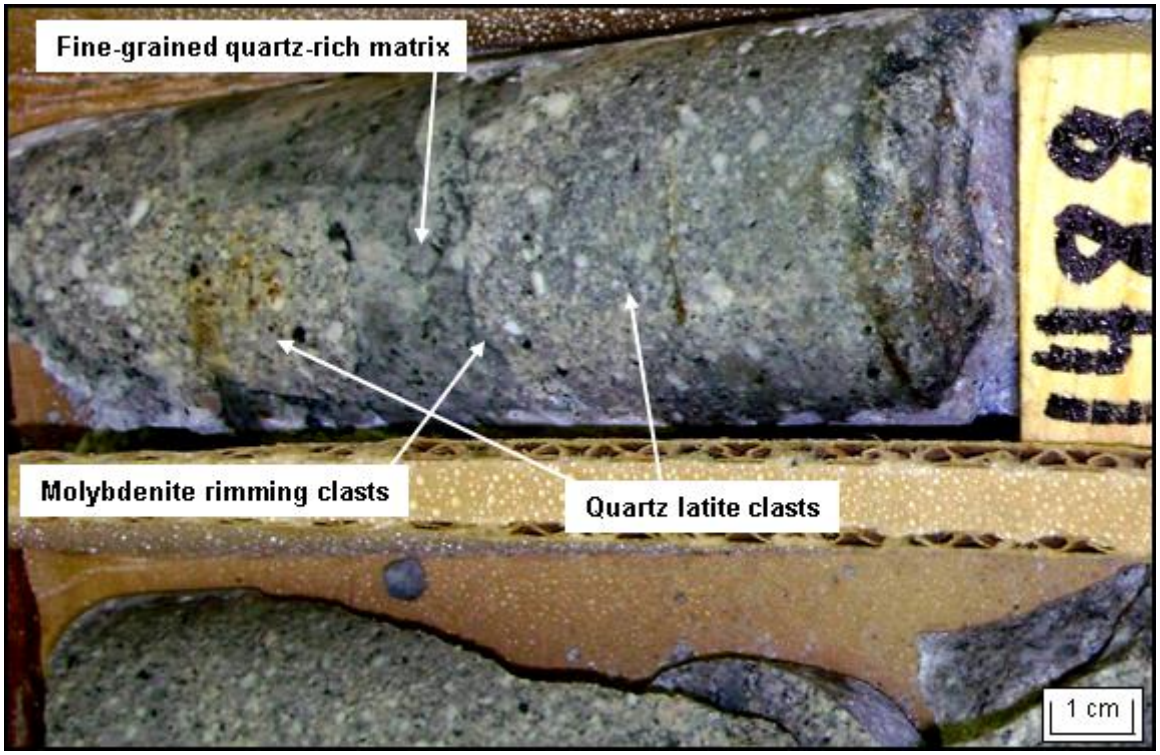

Figure 68. Brecciated quartz latite just below the level of the high grade crackle breccia. Some of the clast margins have molybdenite paint, indicating that this phase of quartz latite intrusion is earlier than the unmineralized, unbrecciated Turnerville quartz latite dike (Fig. 69) (D2314-1488 ft, NQ core).

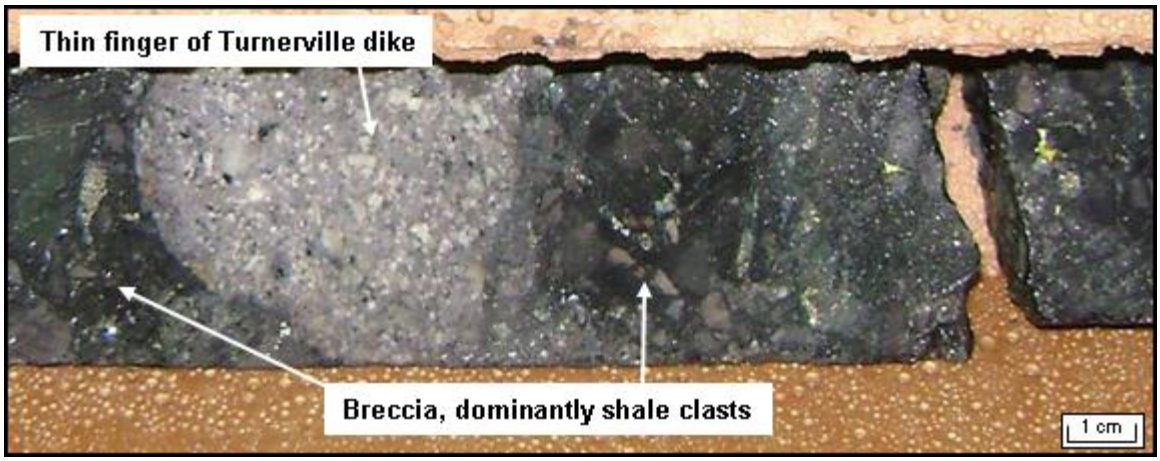

Figure 69. Thin finger of the Turnerville dike (quartz latite, light colored porphyry) intruding breccia above the high grade zone (D2314-1150 ft).

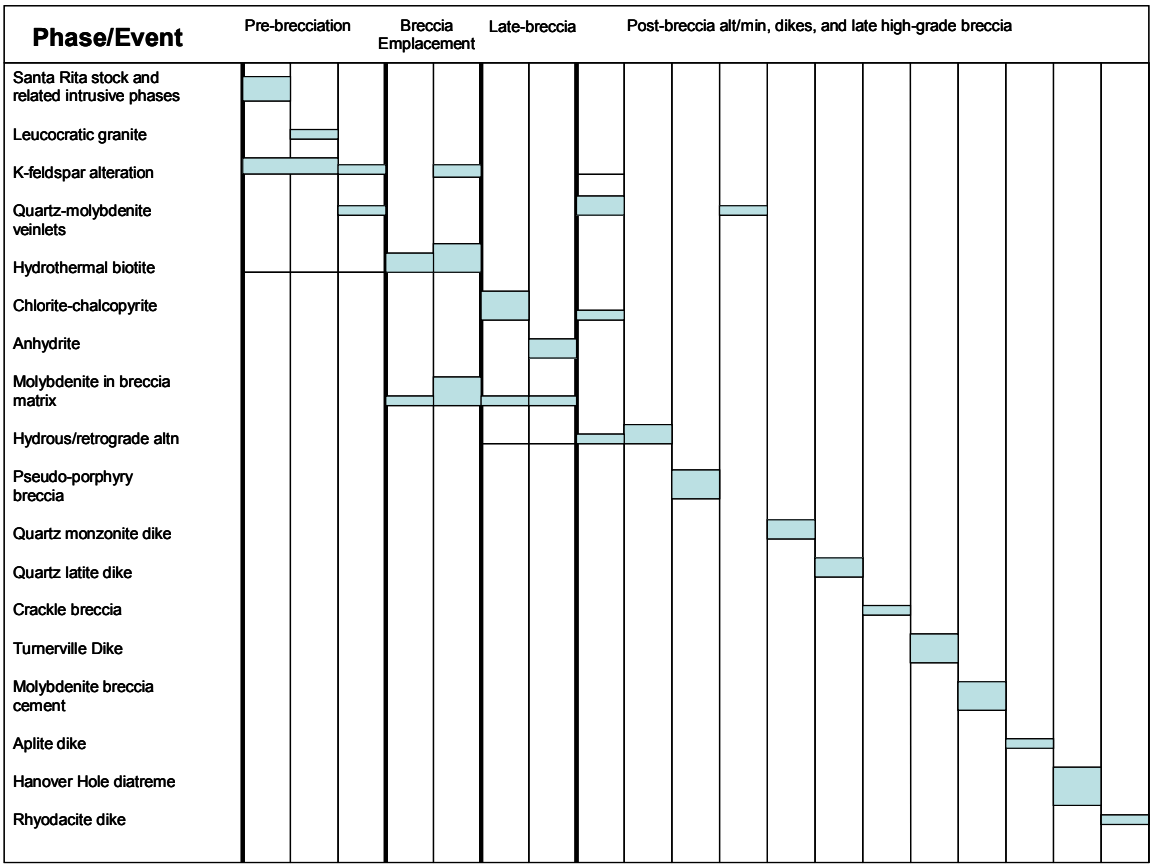

Figure 70. Paragenetic diagram showing the majority of the crosscutting relationships in the portion of the Santa Rita deposit including the Lover's Lane breccia. Thicker bars indicate a stronger relative presence of a phase or stage. Some alteration assemblages assigned to the same time bracket are not associated physically but are interpreted to be coeval and located in different portions of the breccia.

Discussion: Sequence of events in the Lover's Lane breccia

The Lover's Lane breccia is associated with intrusive activity responsible for the mineralization at Santa Rita. As indicated by crosscutting relationships listed above, there are several distinct stages in the development of the breccia and associated hydrothermal system. Figures 71 through 78 depict the interpreted progression of the system including the Lover's Lane breccia and associated mineralization, located in the northwest portion of the Santa Rita deposit, approximately correlative with the A-A' cross section (Fig. 6). Theoretical cross sections are shown, and include features that are not on the A-A' cross section.

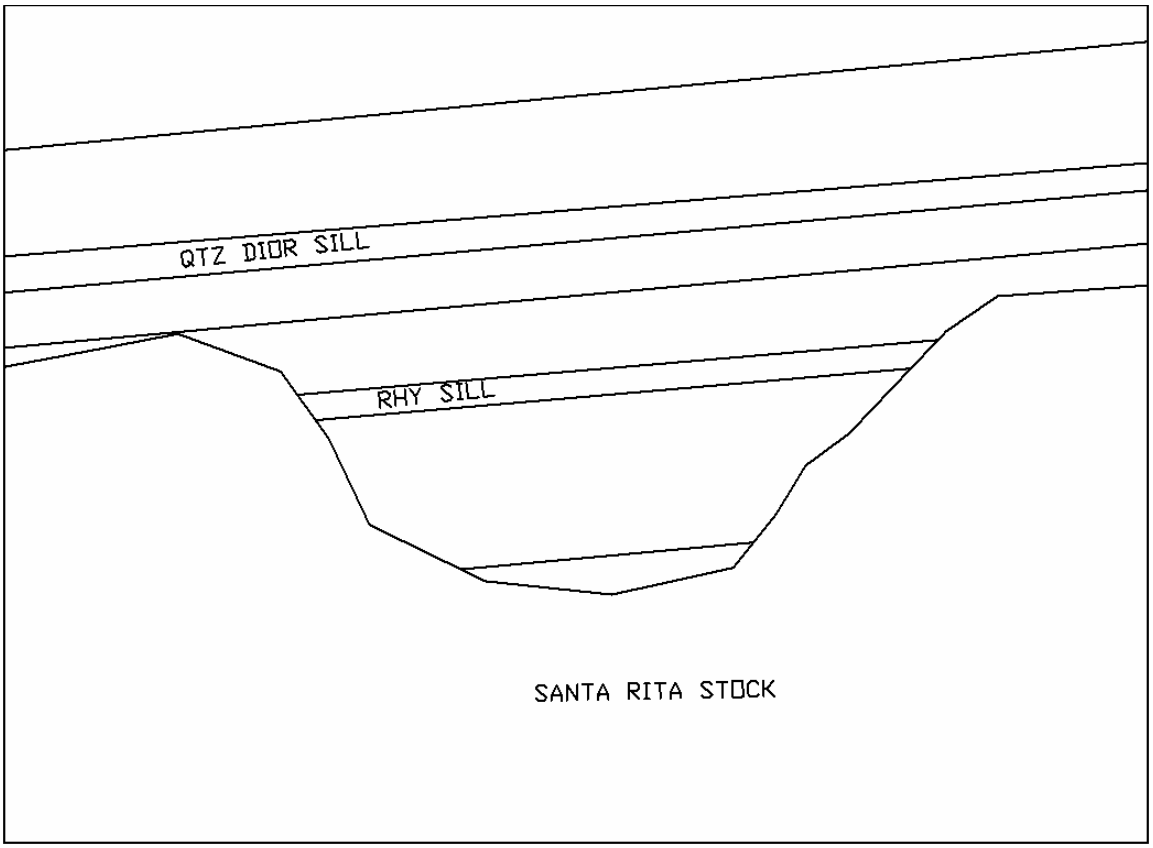

Figure 71. Theoretical cross section showing the outline of the Santa Rita stock and generalized sedimentary section prior to mineralization. This and the following cross sections are approximately correlative with the A-A' cross section (Fig. 6).

Figure 71 shows the host rocks, quartz diorite and rhyolite sills, and intrusion of the Santa Rita stock. The intrusive phases of Santa Rita stock include crowded porphyry granodiorite, equigranular granodiorite, and mineralized quartz monzonite porphyry.

Following the intrusion of the Santa Rita stock a cupola that developed during progressive crystallization (Fig. 72) is likely responsible for the early molybdenite mineralization seen in breccia clasts. Strong potassic alteration of intrusive phases would also be included in this stage, as some breccia clasts of granodiorite have strong potassic alteration (Fig. 66). This stage includes the skarn and stockwork mineralization that is the bulk of the Santa Rita deposit, and the Whim Hill breccia. The minor intrusions of

leucocratic granite accompany this phase of cupola development, likely the result of leakage of highly fractionated magma from the cupola (Figs. 66 and 67). Some meteoric input is present in this stage, recorded in the fluid inclusions analyzed by Reynolds and Beane (1985) associated with chalcopyrite-chlorite mineralization.

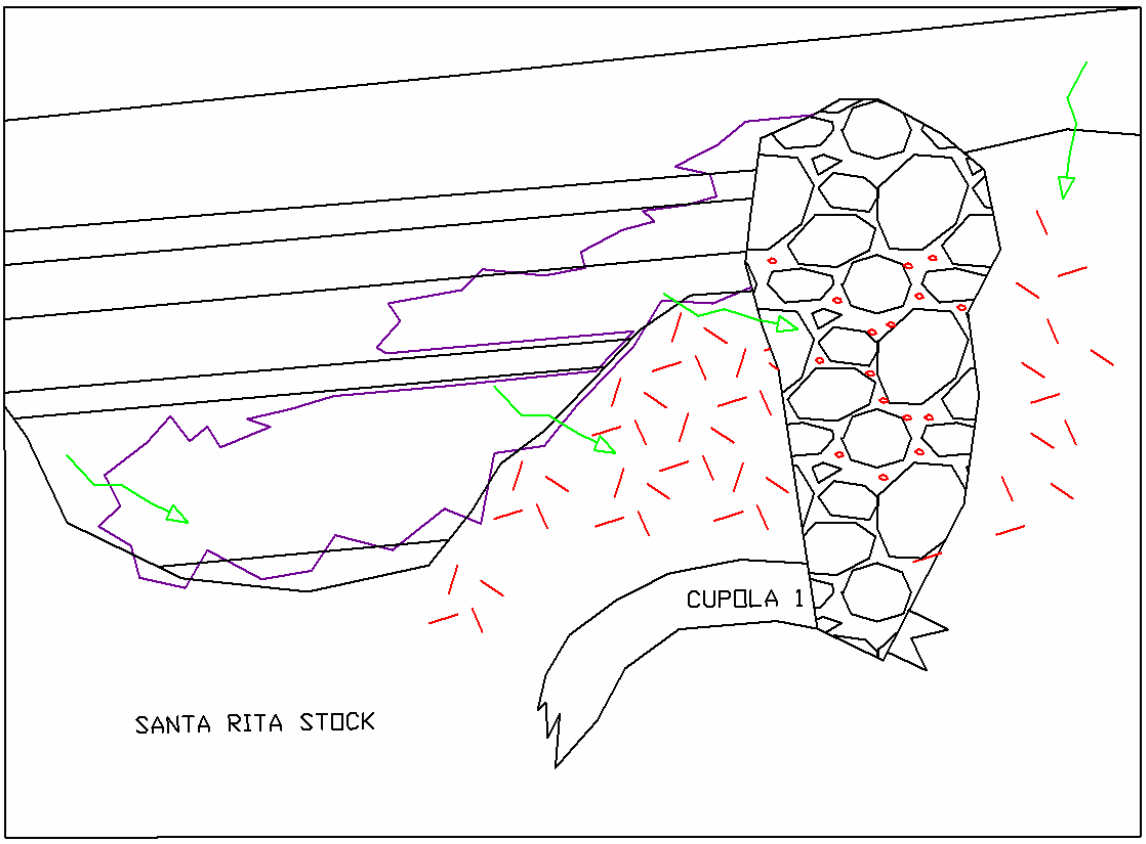

Figure 72. Cross section showing hypogene mineralization at Santa Rita. Red lines and circles indicate veinlet and breccia hosted (Whim Hill breccia) mineralization, the purple outline indicates skarn alteration and mineralization. Green arrows indicate meteoric water influx.

Following stockwork and skarn mineralization, another cupola (Cupola 2) developed and the void space and mineralized fluids created by it resulted in the formation of the Lover's Lane breccia as shown in Figure 73. It is interpreted that this stage of breccia did not breach the surface, as the upper portion of the breccia is less

intense or ends somewhat abruptly into fractured sedimentary or igneous rocks. Based on this study, the mechanisms that caused the Whim Hill breccia and Lover's Lane breccia are temporally distinct, but similar. The cave stoping model proposed by Norton and Cathles (1973) seems to be applicable for the Lover's Lane breccia, as the upper reaches of breccia are in fractured country rock above the intrusion.

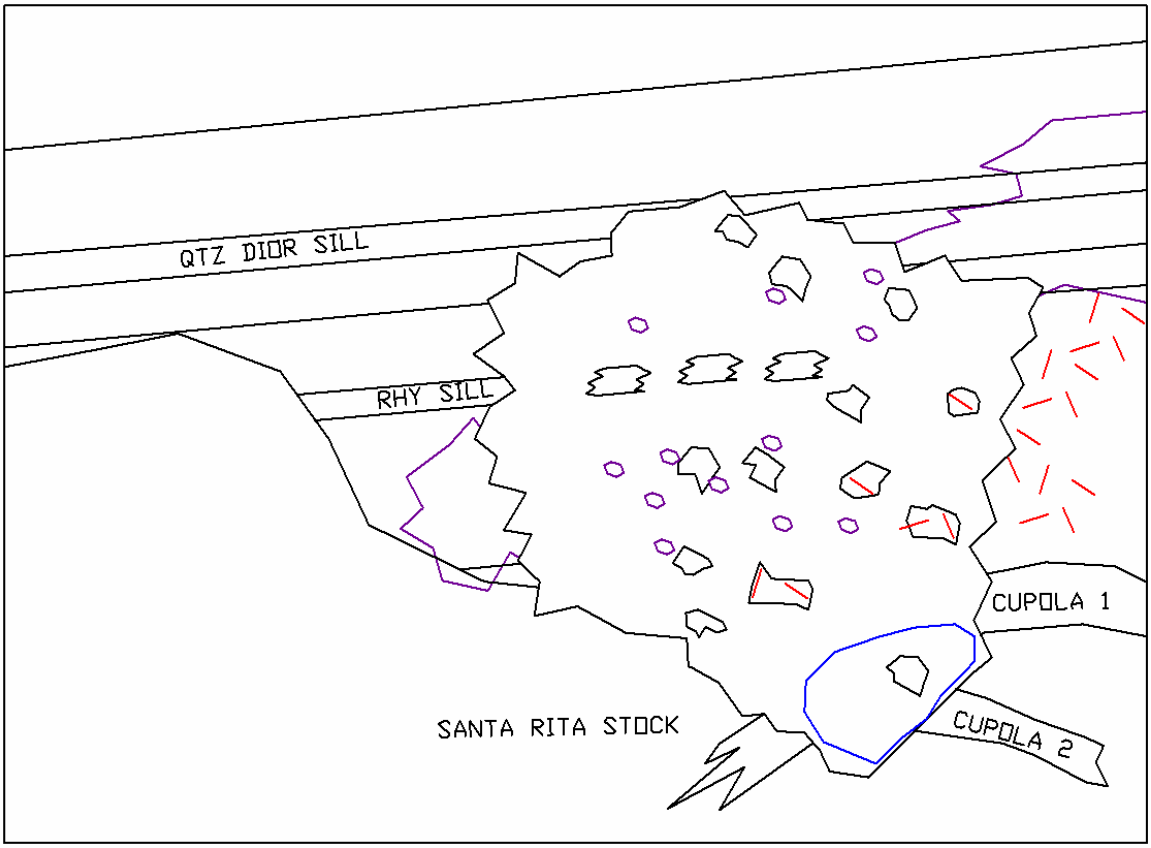

Figure 73. Cross section showing brecciation event of the Lover's Lane breccia. The clasts in the breccia include skarn-mineralized clasts and clasts with veinlet chalcopyrite from the previous stage. The blue region is the location of an interpreted vapor bubble that provided the void space necessary for brecciation, following the model of Norton and Cathles (1973) for formation of the Lover's Lane breccia. Stope caving likely occurred in the region outlined here for the breccia. This theoretical section does not show the Whim Hill breccia for simplicity.

Breccia healing-related mineralization and late breccia mineralization and alteration are depicted in Figure 74. The matrix-forming suite defined above fills the

space between clasts as magmatic fluids depressurize and cool on their path through the rock. Matrix-forming minerals precipitated during brecciation of the rock and upward transport of the fragments as magmatic fluids depressurized and cooled, resulting in textures that appear both clastic and hydrothermal. The Whim Hill breccia, on the other hand, appears to have settled before matrix crystallization, indicated by euhedral crystal growth on clasts.

The late breccia stage affects the freshly-formed matrix, and includes the massive and vug-filling anhydrite, the chalcopyrite-chlorite assemblage, and the retrograde-type alteration and mineralization within the breccia. This stage overprints the breccia, and resulted from an influx of meteoric water into the permeable breccia and mixing with magmatic fluids, which is supported by isotope data presented above and by the data of Reynolds and Beane (1985).

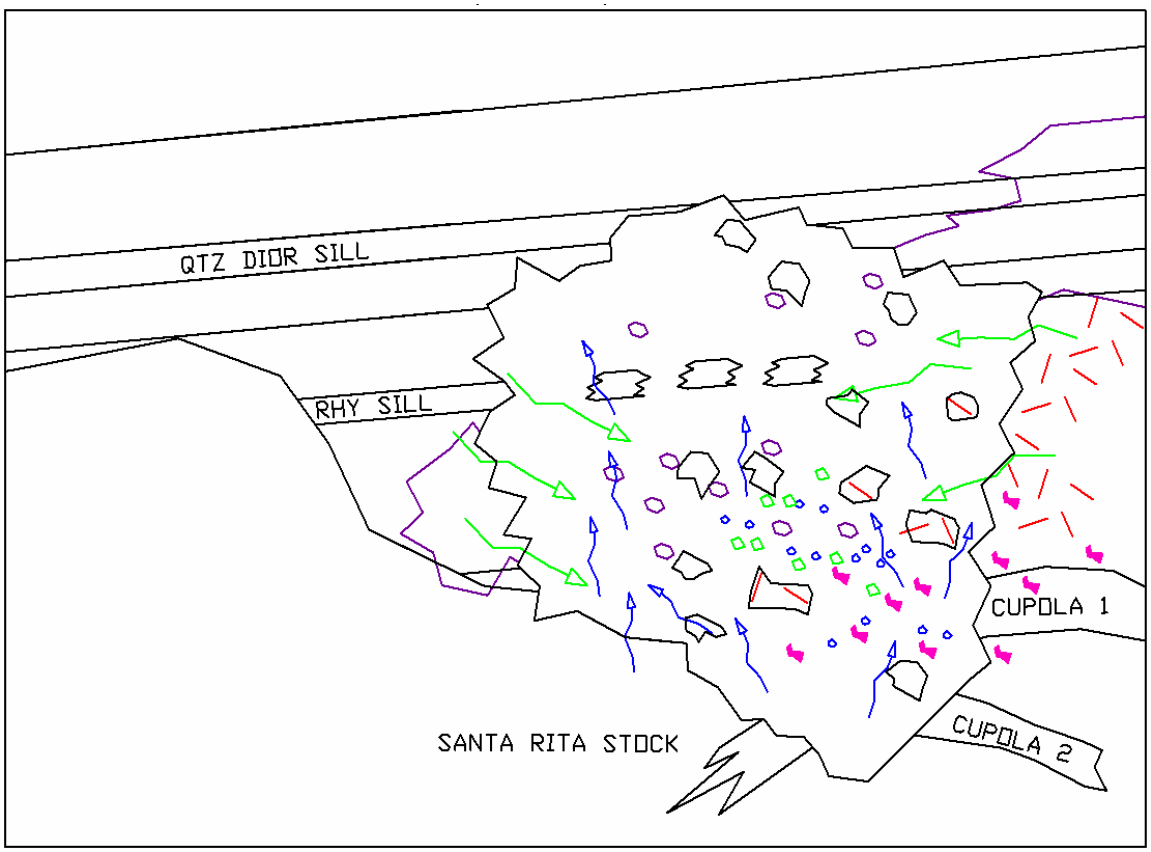

Figure 74. Mineralization and alteration of the breccia, including primary matrix healing by quartz-orthoclase-biotite-molybdenite (molybdenite in matrix: blue circles) from magmatic fluids (blue arrows) and overprint with some meteoric influence (chlorite-chalcopyrite and retrograde/hydrous assemblages, green arrows and circles). Pink shapes indicate the late- or post- breccia massive anhydrite. This stage likely had various assemblages forming coevally.

Following the late breccia alteration within the Lover's Lane breccia, a later stage of breccia within the Lover's Lane breccia has been recognized, noted above as the "pseudo-porphyry" breccia (Fig. 75). Due to the location of this distinct breccia type (to the northwest of the deeper Lover's Lane breccia) and the magmatic minerals and textures which compose the matrix of this breccia, another cupola is interpreted to be responsible for this breccia stage (Cupola 3). Cupola 3 was not intersected in core, but the presence of orthoclase alteration at shallower depths in D2332 (see Plate 1) is indicative of its presence at depth.

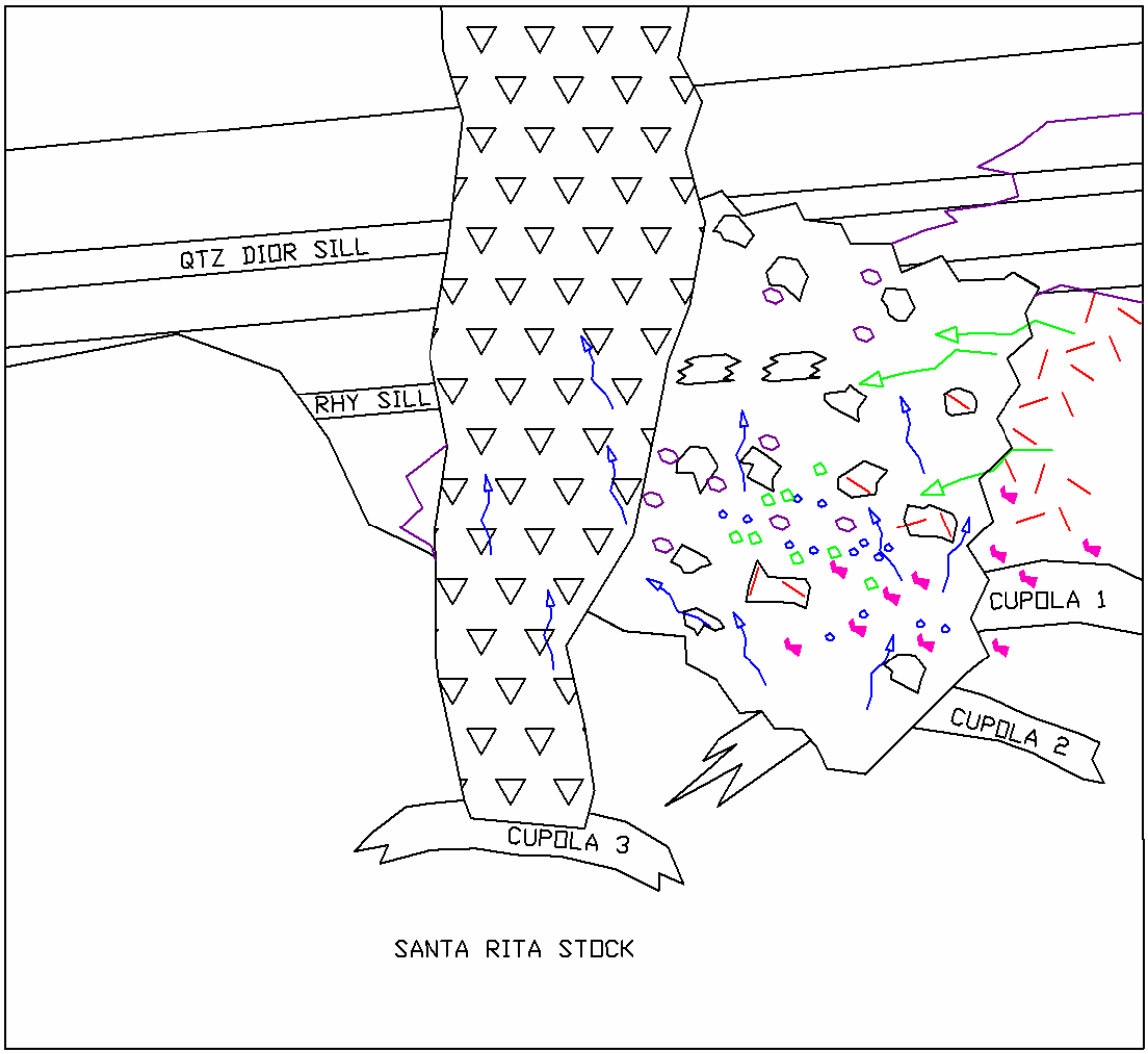

Figure 75. Intrusion of the "pseudo-porphyry" breccia. Fragments of chloritized breccia are present as clasts within this "breccia," indicating that this phase is later than at least some alteration of the breccia as a whole. The quartz-orthoclase matrix of this breccia indicates magmatic origin for the fluids which were present during breccia healing (blue arrows).

Post-breccia veinlets developed at a point when the breccia body (Lover's Lane and pseudo-porphyry) was sufficiently lithified to withstand fracturing along defined planes. The fractures were filled with quartz, molybdenite, anhydrite, pyrite, minor magnetite and chalcopyrite, without producing visible alteration in the matrix or breccia clasts. In Figure 76, another cupola is shown as the source for this molybdenite

mineralization (Cupola 4). Though not intersected by drilling, presence of Cupola 4 is indicated by late molybdenite, and would thus not be represented by the quartz-K-feldspar exsolution clasts in the deeper portions of the Lover's Lane breccia (Fig. 13). The fluid inclusion data in this study indicate that there might have been some meteoric influence on the fluid responsible for veinlet molybdenite mineralization (dominated by low- to moderate- salinity, possibly due to fluid mixing), and this is possible since the "late-breccia" chlorite-chalcopyrite is interpreted to be influenced by meteoric incursion between breccia emplacement and later, post-breccia magmatic mineralization stages. Thus, meteoric water was present in the breccia body by the time the veinlets came in. The late, minor, K-feldspar alteration of breccia at substantial depth also indicates presence of Cupola 4. The Deep Hole, D2333, which went down to about 3200 ft. from the pit bottom, ended in breccia with the potassic overprint, and could be close to this feature (see Plate 1).

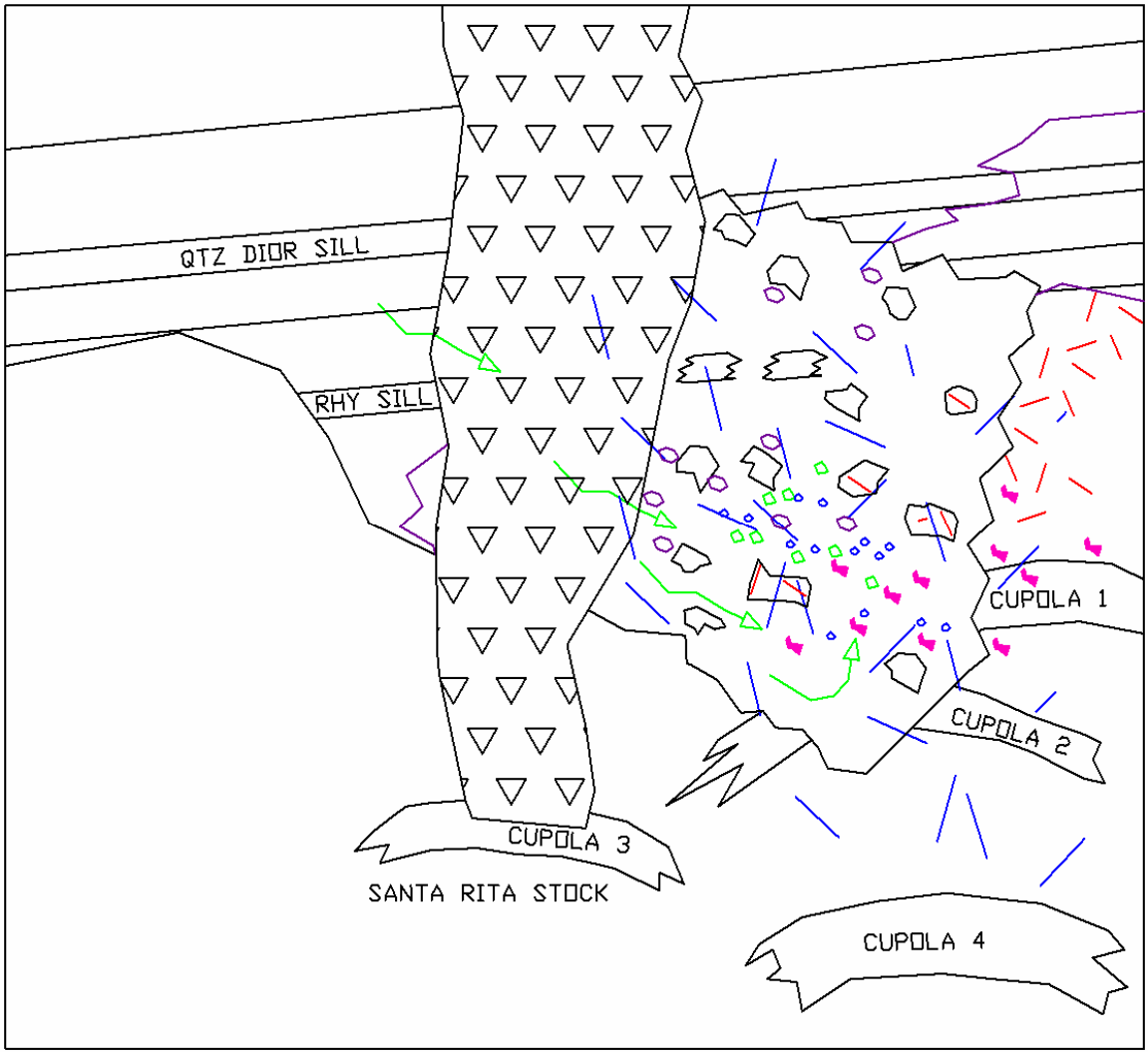

Figure 76. Post-breccia veinlet-controlled molybdenite mineralization (blue lines), and interpreted location of Cupola 2. Meteoric water is indicated by green arrows.

Quartz latite dikes (including the Turnerville dike) in the main breccia body are unaltered and unmineralized. The Turnerville Dike is shown schematically in Figure 77 cutting through the breccia. It is interpreted that the Turnerville Dike intrudes and incorporates clasts of the crackle breccia above the high grade molybdenite zone (Fig. 69 and Plate 2). The crackle breccia is a small zone of broken rhyolite sill, granodiorite, and shale, with minimal rock flour or matrix between fragments, possibly caused by

overpressurized vapors from Cupola 4. The mineralization is apparently capped by the Turnerville Dike, but a separate quartz latite dike at the base of the crackle breccia is broken and fragments are coated with molybdenite (Fig. 68 and Plate 2), indicating that this stage of brecciation and mineralization occurred between earlier quartz latite dikes and the later Turnerville dike.

The high grade molybdenite crackle breccia mineralization is also shown in Figure 77. Re/Os dating (Stegen and Stein, 2007) and cross-cutting relationships indicate that this molybdenite is the latest mineralization. The conduit from the high grade zone to Cupola 4 is drawn schematically to indicate that it is a possible source for the latest mineralization, but it was not intersected by drilling.

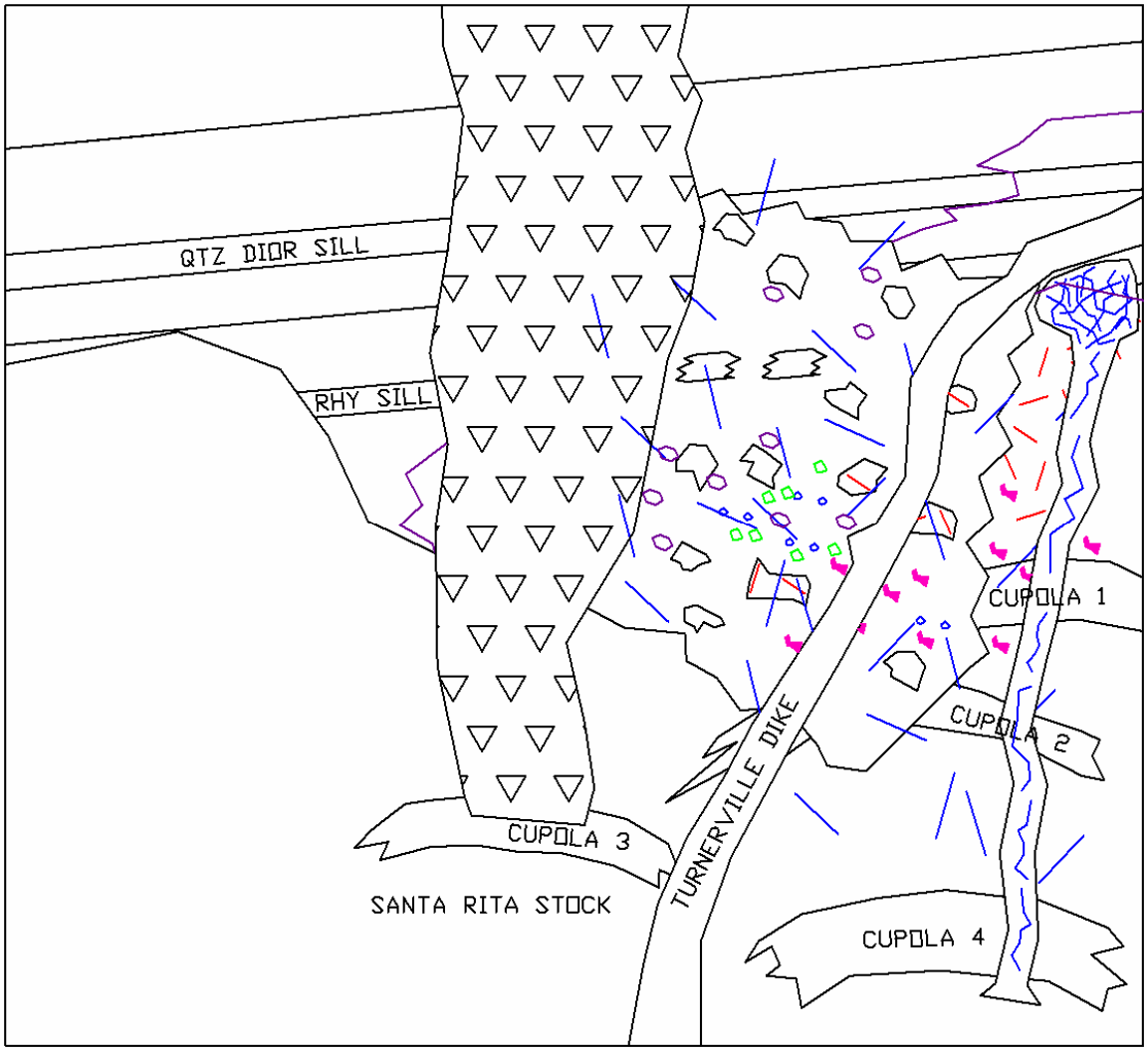

Figure 77. Intrusion of the Turnerville dike and mineralization of the high grade crackle breccia (jagged blue lines). It is interpreted that the Turnerville dike (distinct from other, unnamed quartz-latite dikes) was intruded slightly after the high grade breccia was emplaced. The conduit from Cupola 4 to the high grade zone is somewhat schematic, as it is not intersected by drilling.

The Hanover Hole diatreme is shown in Figure 78, along with the rhyodacite dike which intrudes the diatreme. This feature closely resembles the crater infill breccia described by Landtwing et al. (2002) at Aqua Rica, Argentina, which also post-dates mineralization and is intruded by a late dike. The highly comminuted matrix, paucity of matrix composed of magmatic-hydrothermal minerals, and lack of breccia-related

molybdenite indicate that this breccia was not the result of release of fluids from yet another cupola development. Portions of the diatreme at depth resemble auto-brecciated quartz-latite similar to that seen cutting the interior portion of the Lover's Lane breccia, indicating that the Hanover Hole diatreme breccia is related to post-Lover's Lane breccia igneous phases intruding into the sedimentary section in the area of the diatreme. The intrusion of the rhyodacite dike through the Hanover Hole diatreme concludes the igneous and hydrothermal activity in the portion of the deposit studied.

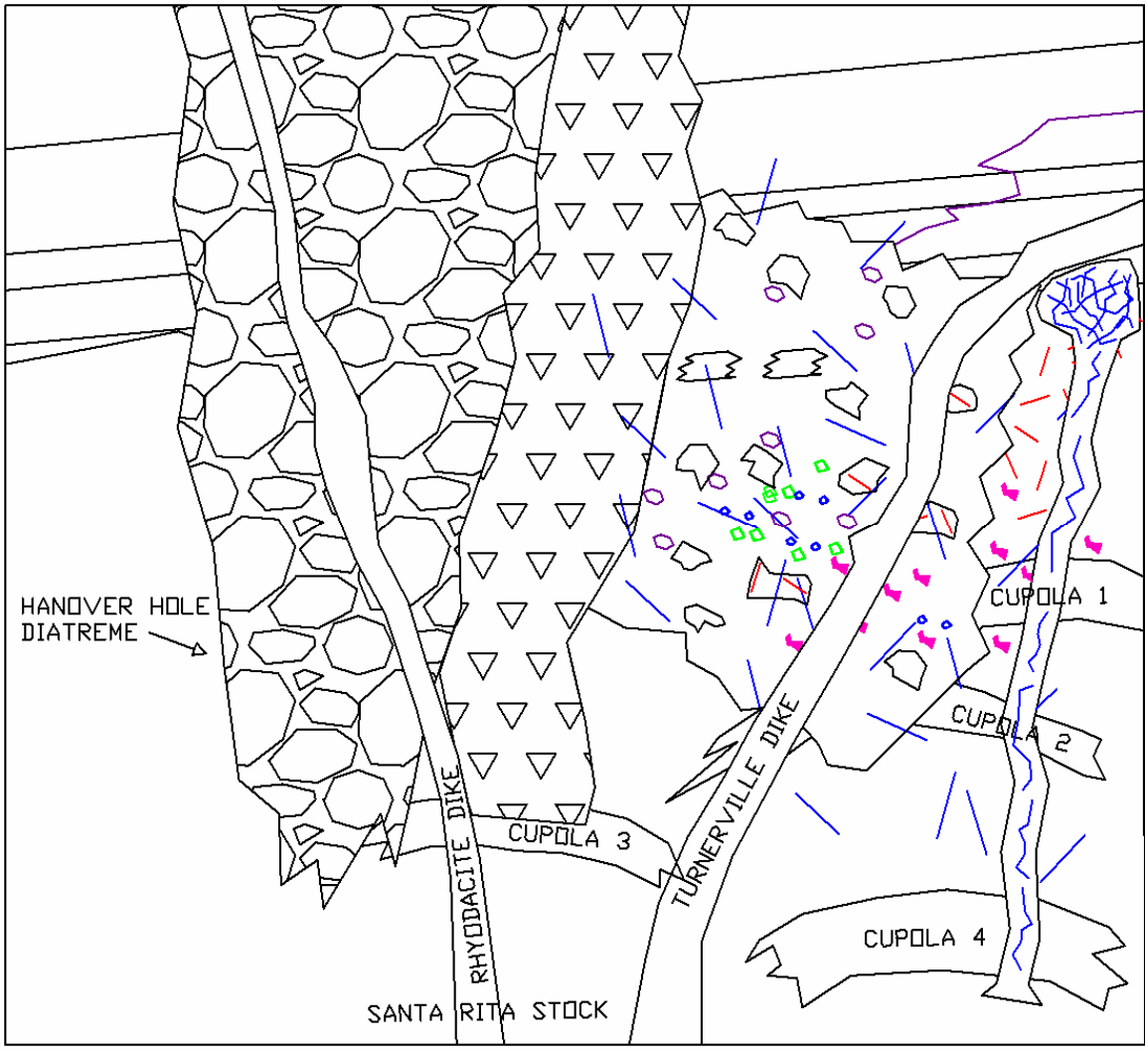

Figure 78. Hanover Hole Diatreme and intrusion of the rhyodacite dike. This is the final igneous event observed in this study.

Conclusion

This study has documented the cyclic nature of the fluid flow in porphyry systems. Early, magmatic fluids produced copper and molybdenite mineralization in the Santa Rita stock, skarn mineralization in the surrounding sedimentary wall rock, and breccia-hosted copper and molybdenite in the Whim Hill breccia, with some meteoric influence, as evidenced by Reynolds and Beane (1985) in the chlorite-chalcopyrite assemblage. Following this, the Lover's Lane breccia was accompanied by another event dominated by magmatic fluids, precipitating the quartz-orthoclase-biotite matrix during dynamic emplacement of the breccia. Significant molybdenite was also introduced with these magmatic fluids, and precipitated within the matrix during emplacement. Incursion of meteoric water followed breccia healing, altering a much of the magmatic matrix and forming the chlorite-chalcopyrite, hydrous retrograde skarn breccia, and anhydrite±chalcopyrite assemblages within the Lover's Lane breccia.

The next fluid cycle is represented by the pseudo-porphyry breccia, with the quartz-orthoclase matrix forming from magmatic fluids in the north end of the Lover's Lane breccia. Continued introduction of magmatic fluids produced quartz-molybdenite veinlets which cross-cut the matrix and clasts of the Lover's Lane and pseudo-porphyry breccias. These fluids were dominantly low- to moderate- salinity, moderate temperature (250-420°C), indicating cooling and/or mixing with meteoric water, with little boiling present during quartz-molybdenite precipitation.

Igneous activity continued with the intrusion of quartz monzonite and quartz latite dikes into the Lover's Lane breccia, which are unmineralized except for a local zone

where quartz latite is brecciated and molybdenite cemented. This high grade zone is likely the result of the last pulse of magmatic fluid into the system.

These repeated pulses of magmatic and meteoric fluids using the large volume of brecciated rock as a pathway produced the strong mineralization in the Lover's Lane breccia. Hydrothermal minerals precipitated from magmatic fluids in the matrix were easily altered when encountered by meteoric fluids, leading to the deposition of the copper in the matrix.

References

Ahmad, S.N., and Rose, A.W., 1980, Fluid Inclusions in porphyry and skarn ore at Santa Rita, New Mexico: Economic Geology, v. 73, pp. 229-250.

Audétat, A., and Pettke, T., 2006, Evolution of a Porphyry-Cu Mineralized Magma System at Santa Rita, New Mexico (USA): Journal of Petrology, v. 47, pp. 2021-2046.

Audétat, A., Pettke, T., and Dolejš, D., 2004, Magmatic anhydrite and calcite in the ore-forming quartz-monzodiorite magma at Santa Rita, New Mexico (USA): genetic constraints on porphyry-Cu mineralization: Lithos, v. 72, pp. 147-161.

Bushnell, S.E., 1988, Mineralization at Cananea, Sonora, Mexico, and the Paragenesis and Zoning of Breccia Pipes in Quartzofeldspathic Rock: Economic Geology, v. 83, pp. 1760-1781.

Faure, G., 1986, Principles of Isotope Geology, Second Edition: John Wiley and Sons, Inc., New York, 589 p.

Field, C.W., Zhang, L., Dilles, J.H., Rye, R.O., and Reed, M.H., 2005, Sulfur and oxygen record in sulfide and sulfate minerals of early, deep, pre-Main Stage porphyry Cu-Mo and late Main Stage base-metal mineral deposits, Butte district, Montana: Chemical Geology, v. 215, pp. 61-93.

Giesemann A., Jager H.J., Norman A.L., Krouse H.P. and Brand W.A., 1994, On-line sulfur-isotope determination using an elemental analyzer coupled to a mass spectrometer: Analytical Chemistry, v. 66, pp. 2816-2819.

Grassineau N.V., Mattey D.P. and Lowry D., 2001, Sulfur Isotope Analysis of Sulfide and Sulfate minerals by Continuous Flow-Isotope Ratio Mass Spectrometry: Analytical Chemistry, v. 73, pp. 220-225.

Jacobs, D.C., and Parry, W.T., 1979, Geochemistry of Biotite in the Santa Rita Porphyry Copper Deposit, New Mexico: Economic Geology, v. 74, pp. 860-887.

Jones, W.R., Hernon, R.M., and Moore, S.L., 1967, General geology of the Santa Rita Quadrangle, Grant County New Mexico: U.S. Geological Survey Professional Paper 555, 144 pp.

Landtwing, M.R., Dillenbeck, E.D., Leake, M.H., and Heinrich, C.A., 2002, Evolution of the Breccia-Hosted Porphyry Cu-Mo-Au Deposit at Aqua Rica, Argentina: Progressive Unroofing of a Magmatic Hydrothermal System: Economic Geology, v. 97, pp. 1273-1292.

Neilson, R.L., 1968, Hypogene Texture and Mineral Zoning in a Copper-Bearing Granodiorite Porphyry Stock, Santa Rita, New Mexico: Economic Geology, v. 63, pp. 37-50.

Norton, D.L., and Cathles, L.M., 1973, Breccia Pipes-Products of Exsolved Vapor from Magmas: Economic Geology, v. 68, pp. 540-546.

Ohmoto, H., and Lasaga, A.C., 1982, Kinetics of reactions between aqueous sulfates and sulfides in hydrothermal systems: Geochimica et Cosmochimica Acta, v. 46, pp 1727-1745.

Ohmoto, H, and Rye, R.O., 1979, Isotopes of sulfur and carbon: in Barnes, H.L. (ed), Geochemistry of Hydrothermal Ore Deposits, Wiley, New York, pp. 509-567.

Parry, W.T., Ballantyne, J.M., and Jacobs, D.C., 1984, Geochemistry of Hydrothermal Sericite from Roosevelt Hot Springs and the Tintic and Santa Rita Porphyry Copper Systems: Economic Geology, v. 79, pp. 72-86.

Potter, R.W., 1977, Pressure Corrections for Fluid-Inclusion Homogenization Temperatures based on the Volumetric Properties of the System NaCl-H_2O: Journal of Research of the U.S. Geological Survey, v. 5, pp. 603-607.

Reynolds, T.J., and Beane, R.E., 1985, Evolution of Hydrothermal Fluid Characteristics at the Santa Rita, New Mexico, Porphyry Copper Deposit: Economic Geology, v. 80, pp. 1328-1347.

Rose, A.W., and Baltosser, W.W., 1966, The porphyry copper deposit at Santa Rita, New Mexico, *in* Titley, S.R., and Hicks, C.L., eds., Geology of the porphyry copper deposits, Southwestern North America: Tucson, Univ. Arizona Press, pp. 205-220.

Sillitoe, R.H., 1985, Ore-Related Breccias in Volcanoplutonic Arcs: Economic Geology, v. 80, pp. 1467-1514.

Stegen, R., and Stein, H., 2007, Re-Os data for Molybdenite Samples from the Santa Rita Porphyry Cu Deposit, New Mexico: Unpublished data

Taylor, R.P., and Fryer, B.J., 1983, Strontium Isotope Geochemistry of the Santa Rita Porphyry Copper Deposit, New Mexico: Economic Geology, v. 78, pp. 170-174.

Thoman, M.W., North, R.M., and Worthington, W.T., 2006, Santa Rita Porphyry Copper Deposit, Grant County, New Mexico: A Summary: Guidebook for the Arizona Geological Society Fall Field Trip, 55 pp.

Titley, S.R., ed., 1982, Advances in Geology of the Porphyry Copper Deposits: Southwestern North America: Tucson, Univ. Arizona Press, 560 p.

Appendix I: Fluid inclusion data

Fluid inclusion data						
Sample (DH # - footage - chip #)	FI #	T(h) (degrees C)	T(fpd) (degrees C)	Mineral relationships	FI description	Mineralization/veinlet type
D1974-3061-2	1a	302	-4.2	in qtz adjacent to moly	L, n.a.d.	qtz-anhy-moly vlt in Tgr/granodiorite
	1b	330				qtz-anhy-moly vlt in Tgr/granodiorite
	2a	327		in qtz vlt	L, possibly very small daughter	qtz-anhy-moly vlt in Tgr/granodiorite
	3a	283		in qtz adjacent to moly	L, n.a.d.	qtz-anhy-moly vlt in Tgr/granodiorite
D1974-3061-1	1a	302		vlt with moly paint and minor moly in vlt	L, possibly halite daughter (very small FI)	qtz-anhy-moly vlt in Tgr/granodiorite
	2a	290		in qtz adjacent to moly	L, possibly very small daughter	qtz-anhy-moly vlt in Tgr/granodiorite
	3b	345		in qtz surrounded by moly with minor anhy	L, possibly very small daughter	qtz-anhy-moly vlt in Tgr/granodiorite
	3c	290			L, halite, no halite dissoln to 400 C	qtz-anhy-moly vlt in Tgr/granodiorite
D1964-2206-1	1a	241		in qtz with adjacent moly and anhy	L, n.a.d.	qtz-moly vlt cutting breccia
	2a	239		in qtz adj to moly paint, small amt of FI's in this grain, some very small V-dom?	L, poss daughter (very small and vague if present)	qtz-moly vlt cutting breccia
	4a	207	-6.2	in qtz surrounded by moly and py	L, n.a.d.	qtz-moly vlt cutting breccia
	5a	302	-4.4	in qtz adjacent to moly, a few other very small FI's in same xl, very few V-dom in this and surrounding qtz xls	L, n.a.d.	qtz-moly vlt cutting breccia
	7a	309	-6.3	in qtz within moly paint in small xl fully surrounded by moly	L, n.a.d.	qtz-moly vlt cutting breccia
	8a	291		in larger qtz adjacent to moly flake and anhy, a few similar sized L and V dom FI's in same xl	L, poss very small opaque daughter	qtz-moly vlt cutting breccia
	9a	384		in qtz adj to moly flake and anhy	L, poss very small opaque daughter	qtz-moly vlt cutting breccia
	10a	295	-8.4	in qtz in moly paint, near anhy, low FI content this xl, some L and V dom, inclusion of moly in this qtz xl	L, n.a.d.	qtz-moly vlt cutting breccia
	10b	293	-8.2	very small FI next to 10a	L, n.a.d.	qtz-moly vlt cutting breccia
D2039-1560-1	7b	332		qtz	L, n.a.d.	qtz-py-moly vlt cutting breccia
	7c	314		qtz	L, n.a.d.	qtz-py-moly vlt cutting breccia
	9d	306		qtz	L, n.a.d.	qtz-py-moly vlt cutting breccia
	9e	325		qtz	L, n.a.d.	qtz-py-moly vlt cutting breccia
	9f	325		qtz	L, n.a.d.	qtz-py-moly vlt cutting breccia
	10a	385		in qtz adj to pyrite	L, some halite in other FI's in vicinity (not run, small)	qtz-py-moly vlt cutting breccia
	10b	353		in qtz adj to pyrite	L, some halite in other FI's in vicinity (not run, small)	qtz-py-moly vlt cutting breccia
	11a	378		in qtz adj to pyrite	L, n.a.d.	qtz-py-moly vlt cutting breccia
	12a	374		in qtz adj to pyrite	L, poss small halite?, Th not observed	qtz-py-moly vlt cutting breccia
	14a	316		in qtz surr by pyrite	L, n.a.d.	qtz-py-moly vlt cutting breccia
	14d	304		in qtz surr by pyrite	L, n.a.d.	qtz-py-moly vlt cutting breccia

	14f	348		in qtz surr by pyrite	L, poss halite daughter, Th not observed	qtz-py-moly vlt cutting breccia
D2039-1204-1	1a	287		in qtz vlt	L, n.a.d.	qtz-py-moly vlt in granodiorite
	7a	378		in qtz vlt	V?, poss daughter remains unchanged	qtz-py-moly vlt in granodiorite
D2329-1374-1	1a	191		in qtz vlt	L, poss vague halite daughter	qtz-moly vlt in granodiorite
	2a	314	-4.9	in qtz vlt	L, n.a.d.	qtz-moly vlt in granodiorite
	5a	305		in qtz vlt	L, daughter very vague	qtz-moly vlt in granodiorite
	5b	307		in qtz vlt	L, n.a.d.	qtz-moly vlt in granodiorite
	6a	382		in qtz adj to moly	L, n.a.d.	qtz-moly vlt in granodiorite
	6b	375		in qtz adj to moly	L, n.a.d.	qtz-moly vlt in granodiorite
	6f	375		in qtz adj to moly	L, n.a.d.	qtz-moly vlt in granodiorite
	7a	369		in qtz adj to moly	L, n.a.d.	qtz-moly vlt in granodiorite
D2329-1374-2	1a	482		in qtz adj to moly, many L, V, with d and n.a.d. FI's in area	L, daughter with Th 215 C	qtz-moly vlt in granodiorite
	2a	422		in qtz adj to moly	L, daughter but Th not observed	qtz-moly vlt in granodiorite
	3a	411		near edge of qtz xl by moly grain	L, n.a.d.	qtz-moly vlt in granodiorite
	4a	295		in qtz with a few flakes of moly in the qtz xl	L, poss daughter (very small and vague if present)	qtz-moly vlt in granodiorite
	4c	307		in qtz with a few flakes of moly in the qtz xl	L, n.a.d.	qtz-moly vlt in granodiorite
D2329-2303-1	1a	402	-2.5	in qtz with moly adj and within xl	L, n.a.d.	qtz-moly vlt in granodiorite (or qtz-monzonite?)
	1b	397	-1.9	in qtz with moly adj and within xl	L, n.a.d.	qtz-moly vlt in granodiorite (or qtz-monzonite?)
	1c		-1.8	in qtz with moly adj and within xl	L, n.a.d.	qtz-moly vlt in granodiorite (or qtz-monzonite?)
	1e	279	-9	in qtz with moly adj and within xl	L, n.a.d.	qtz-moly vlt in granodiorite (or qtz-monzonite?)
	2a	300	-3.5	in qtz adj to chlorite(?) and py and moly	L, n.a.d.	qtz-moly vlt in granodiorite (or qtz-monzonite?)
	2c	285	-3.4	in qtz adj to chlorite(?) and py and moly	L, poss halite? Th not seen	qtz-moly vlt in granodiorite (or qtz-monzonite?)
	2d	318		in qtz adj to chlorite(?) and py and moly	L, n.a.d.	qtz-moly vlt in granodiorite (or qtz-monzonite?)
	3a	258	-2.2	in qtz, in a qtz-moly "vlt" b/w larger qtz along moly paint in vlt	L, n.a.d.	qtz-moly vlt in granodiorite (or qtz-monzonite?)
	4a	380		in qtz adj to moly paint	L, n.a.d.	qtz-moly vlt in granodiorite (or qtz-monzonite?)
	5a	269		in qtz xl b/w chl and moly in moly paint	L, n.a.d.	qtz-moly vlt in granodiorite (or qtz-monzonite?)
	6a	251	-3.1	in qtz b/w moly grains	L, n.a.d.	qtz-moly vlt in granodiorite (or qtz-monzonite?)
	7a	257	-3.8	in granular qtz intergrown with moly flakes, low amnt of FI's in this qtz, V-dom are rare or absent	L, n.a.d.	qtz-moly vlt in granodiorite (or qtz-monzonite?)
	7b	252	-2.5	in granular qtz intergrown with moly flakes, low amnt of FI's in this qtz, V-dom are rare or absent	L, n.a.d.	qtz-moly vlt in granodiorite (or qtz-monzonite?)

n.a.d.: no apparent daughter, qtz: quartz, moly: molybdenite, anhy: anhydrite, vlt: veinlet, L: liquid dominant fluid inclusion, V: vapor dominant, adj: adjacent to

Appendix II: U-Pb isotope data

Sample Preparation and Instrumentation

Zircons were extracted using standard mineral-separation techniques at the laboratories of Apatite To Zircon, Inc. Zircons (both standards and unknowns) were then mounted in 1 cm^2 epoxy wafers, and ground down to expose internal grain surfaces prior to final polishing. Grains, and the locations for laser spots on these grains, were selected for analysis from all sizes and morphologies present using transmitted light with an optical microscope at a magnification of 2000x. This approach is preferred over the use of cathodoluminescence 2-D imaging as it allows the recognition and characterization of features below the surface of individual grains, including the presence of inclusions and the orientation of cracks, which may result in spurious isotopic counts.

Isotopic analyses were performed with a New Wave UP-213 laser ablation system in conjunction with a ThermoFinnigan Element2 single collector double-focusing magnetic sector inductively coupled plasma-mass spectrometer (LA-ICP-MS) in the GeoAnalytical Lab at Washington State University. In comparison to a quadropole ICP-MS, the Element2 has flat-top peaks and higher sensitivity, resulting in larger Pb signals, better counting statistics, and more precise and accurate measurement of isotopic ratios. For all analyses (both standard and unknown), the diameter of the laser-beam was set at 20 μm and the laser frequency was set at 5 Hz; yielding ablation pits ~10-15 μm deep. He and Ar gas were used to deliver the ablated material into the plasma source of the mass spectrometer. Each analysis of 250 cycles took approximately 30 seconds to complete, and consisted of a 6 second integration on peaks with the laser turned off (for background measurements), followed by a 25 second integration with the laser firing. A delay of up to 30 seconds occurred between analyses in order to purge the previous analysis and prepare for the next. The isotopes measured included ^{202}Hg, $^{204}(Hg + Pb)$, ^{206}Pb, ^{207}Pb, ^{208}Pb, ^{232}Th, ^{235}U, and ^{238}U. The Element2 detector was set at analog mode for ^{232}Th and ^{238}U, and at pulse counting mode for all other isotopes. Common Pb correction was made by using the measured ^{204}Pb content and assuming an initial Pb composition from Stacey and Kramers (1975).

Interelement fractionation of Pb/U is generally <20%, whereas fractionation of Pb isotopes is generally <5%. At the beginning of each LA-ICP-MS session, zircon standards (Peixe and FC1) were analyzed until fractionation was stable and the variance in the measured $^{206}Pb/^{238}U$ and $^{207}Pb/^{206}Pb$ ratios was at or near 1 percent. In order to correct for interelement fractionation during the session, these standards were generally reanalyzed each 15-25 unknowns. Fractionation also increases with depth into the laser pit. The accepted isotopic ratios were accordingly determined by least-squares projection through the measured values back to the initial determination.

Sample D1964: Quartz latite in drill hole D1964

	Measured Isotopic Ratios							U and Th		
Analysis_#	207Pb/235Uc *	207Pb/235Uc * (±2σ)	206Pb/238U	206Pb/238U (±2σ)	207Pb/206Pb	207Pb/206Pb (±2σ)		U (ppm)	Th (ppm)	U/Th (ppm)
87001_1	0.0731	0.0058	0.0097	0.0003	0.0539	0.0044	-	1800.12	789.00	2.282
87001_2	0.0558	0.0011	0.0081	0.0002	0.0496	0.0011	-	1794.63	2154.73	0.833
87001_3	2.8763	0.0390	0.2309	0.0046	0.0902	0.0015	-	941.91	213.65	4.409
87001_4	0.0592	0.0018	0.0085	0.0002	0.0501	0.0016	-	954.96	626.08	1.525
87001_5	2.9440	0.0406	0.2347	0.0047	0.0909	0.0015	-	1748.83	145.58	12.013
87001_6	0.0604	0.0013	0.0088	0.0002	0.0495	0.0012	-	1176.26	1005.41	1.170
87001_7	2.8610	0.0388	0.2301	0.0046	0.0900	0.0015	-	935.79	212.95	4.394
87001_8	2.8846	0.0387	0.2314	0.0046	0.0904	0.0015	-	2302.19	161.96	14.215
87001_9	2.7397	0.0440	0.2238	0.0046	0.0889	0.0017	-	829.20	387.96	2.137
87001_10	3.0139	0.0410	0.2405	0.0048	0.0907	0.0015	-	1912.85	386.09	4.954
87001_11	3.0708	0.0438	0.2452	0.0050	0.0906	0.0015	-	3493.47	284.87	12.263
87001_12	0.0619	0.0037	0.0084	0.0002	0.0536	0.0033	-	1285.70	841.42	1.528
87001_13	2.9178	0.0412	0.2297	0.0047	0.0921	0.0016	-	3344.38	186.09	17.972
87001_14	0.0555	0.0013	0.0083	0.0002	0.0483	0.0012	-	1818.70	1691.77	1.075
87001_15	0.0551	0.0011	0.0082	0.0002	0.0485	0.0011	-	2984.10	1925.61	1.550
87001_16	2.9468	0.0405	0.2415	0.0048	0.0884	0.0015	-	761.53	676.28	1.126
87001_17	2.9471	0.0406	0.2413	0.0048	0.0884	0.0015	-	760.01	676.18	1.124
87001_18	3.0721	0.0439	0.2454	0.0050	0.0906	0.0015	-	3491.06	284.08	12.289
87001_19	0.0586	0.0011	0.0085	0.0002	0.0497	0.0011	-	2099.78	2040.78	1.029
87001_20	3.0957	0.0408	0.2432	0.0048	0.0922	0.0015	-	2455.33	31.30	78.453
87001_21	0.0590	0.0015	0.0086	0.0002	0.0498	0.0014	-	1227.36	1306.77	0.939
87001_22	0.0575	0.0013	0.0084	0.0002	0.0494	0.0012	-	1668.17	2082.90	0.801
87001_23	0.0587	0.0011	0.0085	0.0002	0.0497	0.0011	-	2098.35	2039.75	1.029
87001_24	0.0550	0.0011	0.0082	0.0002	0.0485	0.0011	-	2986.02	1920.27	1.555
87001_25	0.0592	0.0018	0.0085	0.0002	0.0501	0.0016	-	955.24	621.18	1.538
87001_26	0.0575	0.0013	0.0084	0.0002	0.0494	0.0012	-	1668.16	2080.67	0.802
87001_27	3.0207	0.0411	0.2410	0.0048	0.0907	0.0015	-	1908.99	383.62	4.976
87001_28	0.0591	0.0015	0.0086	0.0002	0.0498	0.0014	-	1226.72	1303.86	0.941
87001_29	0.0558	0.0011	0.0081	0.0002	0.0496	0.0011	-	1794.94	2137.17	0.840
87001_30	3.0219	0.0411	0.2411	0.0048	0.0907	0.0015	-	1908.32	383.26	4.979

	Apparent Ages							Preferred Ages						
Analysis_#	207Pb/235Uc *	207Pb/235Uc * (±2σ)	206Pb/238U	206Pb/238U (±2σ)	207Pb/206Pb	207Pb/206Pb (±2σ)	Analysis_#	Preferred Age (Ma)	Absolute Error (±2σ)	Age Type	Fit Quality 1=best	Clean Quality 1=best	Pb204 Quality	2σ Conc. Scans
87001_1	71.61	5.87	61.96	1.95	366.49	178.60	87001_1	61.96	1.95	Pb/U wmean conc.	0.7577	0.1111	0.3047	45
87001_2	55.16	1.12	52.32	1.04	176.54	51.49	87001_2	52.32	1.04	Pb/U wmean conc.	0.0127	1.0000	0.4884	102
87001_3	1375.73	39.22	1338.96	29.42	1430.04	31.58	87001_3	1338.96	29.42	Pb/U wmean conc.	0.1192	1.0000	0.3167	132
87001_4	58.44	1.87	54.88	1.11	201.67	75.34	87001_4	54.88	1.11	Pb/U wmean conc.	0.0149	0.5000	0.3555	66
87001_5	1393.31	40.80	1359.05	30.24	1444.33	31.93	87001_5	1444.33	31.93	Pb/Pb wmean conc.	0.0141	1.0000	0.4482	30
87001_6	59.59	1.35	56.72	1.14	172.33	56.13	87001_6	56.72	1.14	Pb/U wmean conc.	0.0120	1.0000	0.3120	110
87001_7	1371.71	39.02	1335.22	29.33	1425.33	31.60	87001_7	1335.22	29.33	Pb/U wmean conc.	0.1192	1.0000	0.3167	134
87001_8	1377.89	38.89	1342.06	29.50	1433.72	31.40	87001_8	1433.72	31.40	Pb/Pb wmean conc.	0.0129	0.5000	0.3907	113
87001_9	1339.30	44.15	1301.68	29.86	1401.35	35.65	87001_9	1301.68	29.86	Pb/U wmean conc.	0.0841	0.5000	0.4087	23
87001_10	1411.13	41.24	1389.51	30.89	1441.05	31.65	87001_10	1441.05	31.65	Pb/Pb wmean conc.	0.0196	1.0000	0.3733	155
87001_11	1425.44	44.01	1413.52	32.11	1438.07	32.32	87001_11	1438.07	32.32	Pb/Pb wmean conc.	0.0119	1.0000	0.4403	149
87001_12	60.99	3.78	53.77	1.24	353.46	136.34	87001_12	53.77	1.24	Pb/U wmean conc.	0.7798	0.2000	0.2676	30
87001_13	1386.54	41.39	1333.03	30.18	1469.54	32.67	87001_13	1469.54	32.67	Pb/Pb wmean conc.	0.0297	1.0000	0.5407	152
87001_14	54.82	1.29	53.30	1.11	115.87	59.04	87001_14	53.30	1.11	Pb/U wmean conc.	0.0206	1.0000	0.4138	74
87001_15	54.43	1.10	52.87	1.06	123.57	51.77	87001_15	52.87	1.06	Pb/U wmean conc.	0.0228	0.5000	0.2946	62
87001_16	1394.03	40.76	1394.24	31.03	1390.49	31.97	87001_16	1394.24	31.03	Pb/U wmean conc.	0.9346	0.5000	0.3907	112
87001_17	1394.10	40.80	1393.68	31.02	1391.61	31.98	87001_17	1393.68	31.02	Pb/U wmean conc.	0.9346	0.5000	0.3907	111
87001_18	1425.75	44.06	1414.49	32.14	1437.52	32.34	87001_18	1437.52	32.34	Pb/Pb wmean conc.	0.0119	1.0000	0.4403	148
87001_19	57.85	1.11	54.83	1.10	178.95	49.36	87001_19	54.83	1.10	Pb/U wmean conc.	0.0232	0.5000	0.4266	77
87001_20	1431.63	41.02	1403.20	30.73	1470.90	30.85	87001_20	1470.90	30.85	Pb/Pb wmean conc.	0.1385	1.0000	0.4961	85
87001_21	58.22	1.50	55.05	1.12	185.60	62.98	87001_21	55.05	1.12	Pb/U wmean conc.	0.0116	1.0000	0.4580	65
87001_22	56.79	1.31	54.09	1.09	169.15	57.05	87001_22	54.09	1.09	Pb/U wmean conc.	0.0209	0.1667	0.4760	79
87001_23	57.92	1.11	54.86	1.10	180.74	49.19	87001_23	54.86	1.10	Pb/U wmean conc.	0.0232	0.5000	0.4266	78
87001_24	54.38	1.10	52.83	1.06	123.57	51.77	87001_24	52.83	1.06	Pb/U wmean conc.	0.0228	0.5000	0.2946	62
87001_25	58.43	1.87	54.85	1.11	201.67	75.34	87001_25	54.85	1.11	Pb/U wmean conc.	0.0149	0.5000	0.3555	66
87001_26	56.79	1.31	54.09	1.09	169.15	57.05	87001_26	54.09	1.09	Pb/U wmean conc.	0.0209	0.1667	0.4760	79
87001_27	1412.87	41.33	1392.02	30.95	1441.05	31.65	87001_27	1441.05	31.65	Pb/Pb wmean conc.	0.0196	1.0000	0.3733	155
87001_28	58.26	1.50	55.08	1.12	185.60	62.98	87001_28	55.08	1.12	Pb/U wmean conc.	0.0116	1.0000	0.4580	65
87001_29	55.14	1.12	52.28	1.04	176.54	51.49	87001_29	52.28	1.04	Pb/U wmean conc.	0.0127	1.0000	0.4884	102
87001_30	1413.16	41.35	1392.46	30.96	1441.05	31.65	87001_30	1441.05	31.65	Pb/Pb wmean conc.	0.0196	1.0000	0.3733	155

	Preferred Ages - Sorted							Fitted Discordia						
Analysis_#	Preferred Age (Ma)	Absolute Error (±2σ)	Age Type	Fit Quality 1=best	Clean Quality 1=best	Pb204 Quality	2σ Conc. Scans	Age - Lower Intercept (Ma)	Age - Lower Intercept (±2σ)	Age - Upper Intercept (Ma)	Age - Upper Intercept (±2σ)	Regression Intercept	Regression Intercept (±1σ)	Regression Slope	Regression Slope (±1σ)
87001_29	52.28	1.04	Pb/U wmean conc.	0.0127	1.0000	0.4884	102	59.02	2.45	undefined	undefined	0.008661	0.000132	0.008978	0.000472
87001_2	52.32	1.04	Pb/U wmean conc.	0.0127	1.0000	0.4884	102	52.91	1.57	4560.00	769.39	0.007760	0.000237	0.009003	0.004415
87001_14	53.30	1.11	Pb/U wmean conc.	0.0206	1.0000	0.4138	74	588.15	132.76	1486.50	53.91	0.044890	0.004662	0.064534	0.001661
87001_19	54.83	1.10	Pb/U wmean conc.	0.0232	0.5000	0.4266	77	55.80	1.79	undefined	undefined	0.009928	0.000176	-0.021866	0.002833
87001_25	54.85	1.11	Pb/U wmean conc.	0.0149	0.5000	0.3555	66	1005.10	207.36	1778.85	200.28	0.086763	0.010228	0.048475	0.003403
87001_23	54.86	1.10	Pb/U wmean conc.	0.0232	0.5000	0.4266	78	56.30	1.72	undefined	undefined	0.010117	0.000313	-0.023586	0.004960
87001_4	54.88	1.11	Pb/U wmean conc.	0.0149	0.5000	0.3555	66	597.95	138.61	1488.55	58.43	0.045665	0.004723	0.064253	0.001683
87001_21	55.05	1.12	Pb/U wmean conc.	0.0116	1.0000	0.4580	65	undefined	undefined	undefined	undefined	-0.019491	0.010957	0.086518	0.003822
87001_28	55.08	1.12	Pb/U wmean conc.	0.0116	1.0000	0.4580	65	undefined	undefined	undefined	undefined	-0.006617	0.004858	0.082280	0.001867
87001_9	1301.68	29.86	Pb/U wmean conc.	0.0841	0.5000	0.4087	23	184.11	260.65	1454.35	43.88	0.014070	0.009820	0.074963	0.003283
87001_17	1393.68	31.02	Pb/U wmean conc.	0.9346	0.5000	0.3907	111	undefined	undefined	undefined	undefined	-0.005131	0.009280	0.081282	0.003030
87001_16	1394.24	31.03	Pb/U wmean conc.	0.9346	0.5000	0.3907	112	55.70	1.94	undefined	undefined	0.008065	0.000090	0.010891	0.000088
87001_8	1433.72	31.40	Pb/Pb wmean conc.	0.0129	0.5000	0.3907	113	489.70	202.49	1528.55	60.55	0.038411	0.007174	0.065368	0.002466
87001_18	1437.52	32.34	Pb/Pb wmean conc.	0.0119	1.0000	0.4403	148	54.10	1.71	4560.00	494.17	0.007937	0.000174	0.008978	0.003354
87001_11	1438.07	32.32	Pb/Pb wmean conc.	0.0119	1.0000	0.4403	149	54.83	1.95	3463.04	785.30	0.007208	0.000295	0.024042	0.005444
87001_10	1441.05	31.65	Pb/Pb wmean conc.	0.0196	1.0000	0.3733	155	1389.90	85.44	2636.95	1022.51	0.158866	0.018919	0.027894	0.006377
87001_27	1441.05	31.65	Pb/Pb wmean conc.	0.0196	1.0000	0.3733	155	1389.80	79.84	2604.35	996.74	0.157487	0.018921	0.028362	0.006377
87001_30	1441.05	31.65	Pb/Pb wmean conc.	0.0196	1.0000	0.3733	155	undefined	undefined	undefined	undefined	-0.004585	0.009312	0.081097	0.003039
87001_5	1444.33	31.93	Pb/Pb wmean conc.	0.0141	1.0000	0.4482	30	54.63	2.09	3647.00	787.61	0.007332	0.000267	0.021345	0.004708
87001_13	1469.54	32.67	Pb/Pb wmean conc.	0.0297	1.0000	0.5407	152	294.15	188.71	1503.05	39.27	0.022963	0.006590	0.070598	0.002149
87001_20	1470.90	30.85	Pb/Pb wmean conc.	0.1385	1.0000	0.4961	85	54.57	1.48	undefined	undefined	0.008534	0.000107	-0.000584	0.001790
87001_15	rej 52	_ _ Pb _	Pb/U wmean conc.	0.0228	0.5000	0.2946	62	54.45	1.75	4560.00	191.37	0.008231	0.000221	0.004553	0.003977
87001_24	rej 52	_ _ Pb _	Pb/U wmean conc.	0.0228	0.5000	0.2946	62	54.65	2.13	3596.57	761.15	0.007294	0.000270	0.022056	0.004767
87001_12	rej 53	_ C Pb _	Pb/U wmean conc.	0.7798	0.2000	0.2676	30	54.90	2.01	3249.80	764.68	0.007023	0.000301	0.027542	0.005538
87001_22	rej 54	_ C _ _	Pb/U wmean conc.	0.0209	0.1667	0.4760	79	55.85	1.81	undefined	undefined	0.009928	0.000199	-0.021685	0.003193
87001_26	rej 54	_ C _ _	Pb/U wmean conc.	0.0209	0.1667	0.4760	79	54.45	1.73	4560.00	172.60	0.008237	0.000223	0.004479	0.004005
87001_6	rej 56	_ _ Pb _	Pb/U wmean conc.	0.0120	1.0000	0.3120	110	123.06	229.25	1451.90	42.83	0.009415	0.009162	0.076516	0.003059
87001_1	rej 61	_ C Pb _	Pb/U wmean conc.	0.7577	0.1111	0.3047	45	54.60	1.49	undefined	undefined	0.008521	0.000111	-0.000285	0.001869
87001_7	rej 1335	_ _ Pb _	Pb/U wmean conc.	0.1192	1.0000	0.3167	134	53.00	1.73	3852.36	749.66	0.007254	0.000270	0.018660	0.005031
87001_3	rej 1338	_ _ Pb _	Pb/U wmean conc.	0.1192	1.0000	0.3167	132	113.60	202.19	1451.54	42.50	0.008691	0.009100	0.076758	0.003038

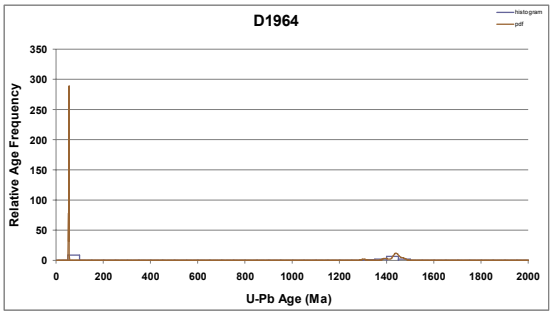
D1964
histogram
pdf
Relative Age Frequency
U-Pb Age (Ma)

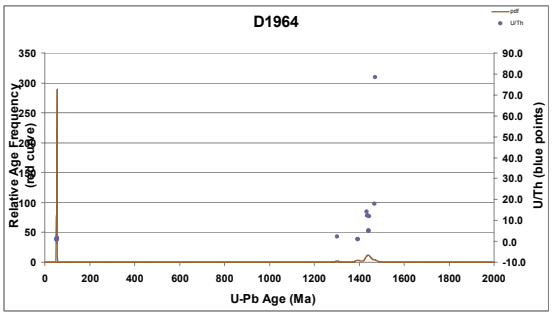
D1964
pdf
U/Th
Relative Age Frequency (red curve)
U/Th (blue points)
U-Pb Age (Ma)

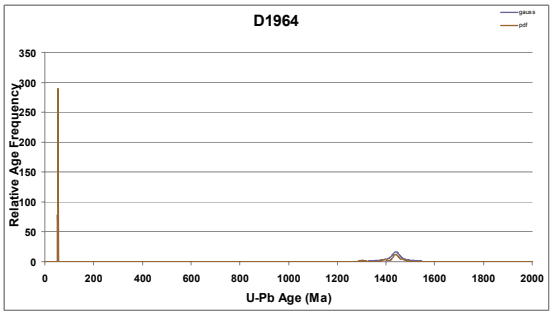
D1964
gauss
pdf
Relative Age Frequency
U-Pb Age (Ma)

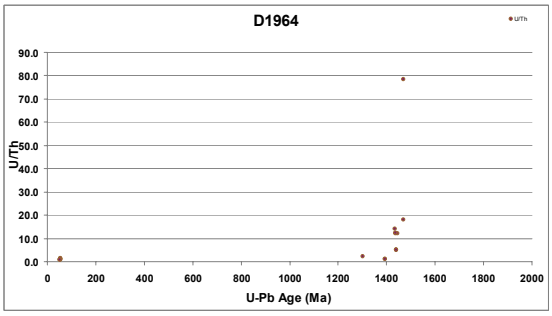
D1964
U/Th
U/Th
U-Pb Age (Ma)

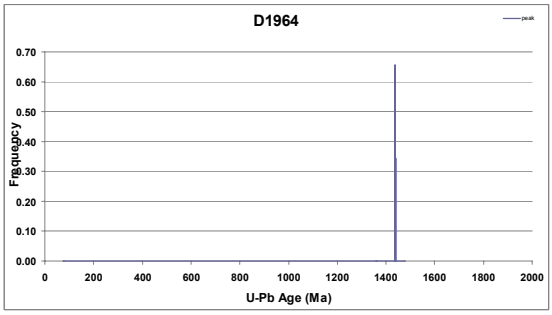
D1964
peak
Frequency
U-Pb Age (Ma)

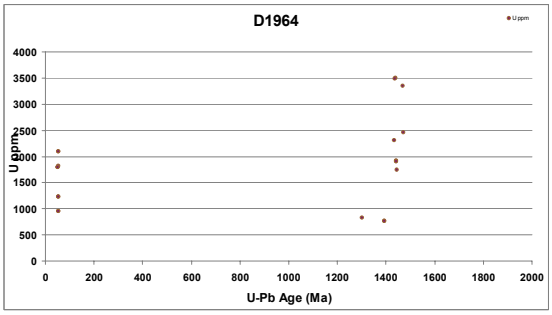
D1964
U ppm
U ppm
U-Pb Age (Ma)

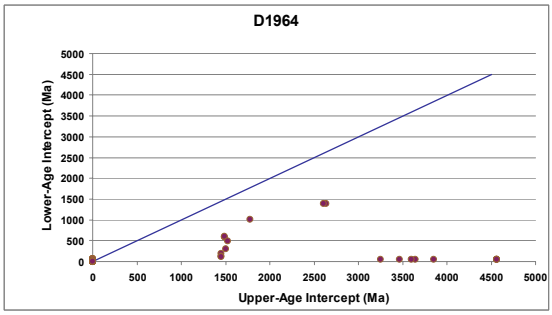
D1964
Lower-Age Intercept (Ma)
Upper-Age Intercept (Ma)

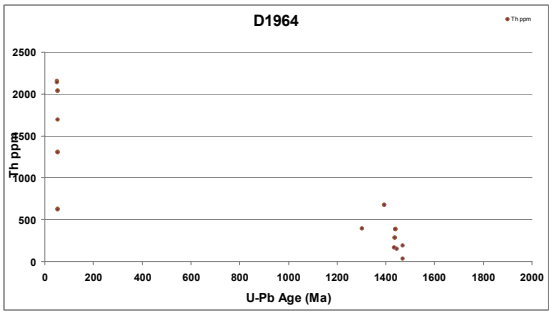
D1964
Th ppm
Th ppm
U-Pb Age (Ma)

Sample D1550: Quartz monzonite from D1550

	Measured Isotopic Ratios							U and Th		
Analysis_#	207Pb/235Uc *	207Pb/235Uc * (±2σ)	206Pb/238U	206Pb/238U (±2σ)	207Pb/206Pb	207Pb/206Pb (±2σ)		U (ppm)	Th (ppm)	U/Th (ppm)
87002_1	0.0588	0.0013	0.0087	0.0002	0.0488	0.0012	-	1809.11	2264.68	0.799
87002_2	0.0615	0.0014	0.0087	0.0002	0.0511	0.0013	-	1404.65	1497.45	0.938
87002_3	0.0582	0.0012	0.0084	0.0002	0.0500	0.0012	-	1265.60	1310.10	0.966
87002_4	0.0604	0.0013	0.0088	0.0002	0.0496	0.0012	-	1528.50	1586.47	0.963
87002_5	0.0553	0.0012	0.0083	0.0002	0.0481	0.0012	-	1962.45	2188.84	0.897
87002_6	0.0616	0.0014	0.0087	0.0002	0.0511	0.0013	-	1404.12	1496.13	0.938
87002_7	0.0608	0.0017	0.0088	0.0002	0.0499	0.0015	-	1618.69	1783.56	0.908
87002_8	0.0608	0.0017	0.0088	0.0002	0.0499	0.0015	-	1618.54	1783.16	0.908
87002_9	0.0697	0.0021	0.0090	0.0002	0.0561	0.0018	-	574.81	332.57	1.728
87002_10	0.0599	0.0013	0.0085	0.0002	0.0509	0.0012	-	1601.66	1999.69	0.801
87002_11	0.0582	0.0012	0.0084	0.0002	0.0500	0.0012	-	1265.14	1307.63	0.968
87002_12	0.0592	0.0015	0.0085	0.0002	0.0509	0.0014	-	1193.37	959.37	1.244
87002_13	0.0585	0.0023	0.0082	0.0002	0.0515	0.0021	-	636.84	407.20	1.564
87002_14	0.0608	0.0012	0.0088	0.0002	0.0501	0.0011	-	1026.89	843.13	1.218
87002_15	0.0581	0.0021	0.0084	0.0002	0.0501	0.0019	-	1393.43	1106.14	1.260
87002_16	0.0584	0.0014	0.0085	0.0002	0.0497	0.0013	-	1325.03	1356.50	0.977
87002_17	0.0589	0.0014	0.0086	0.0002	0.0495	0.0013	-	1230.78	1037.89	1.186
87002_18	0.0589	0.0014	0.0086	0.0002	0.0495	0.0013	-	1230.65	1037.73	1.186
87002_19	0.0565	0.0010	0.0083	0.0002	0.0494	0.0010	-	2330.06	2562.40	0.909
87002_20	0.0604	0.0014	0.0087	0.0002	0.0504	0.0013	-	1425.16	1161.35	1.227
87002_21	0.0604	0.0014	0.0087	0.0002	0.0504	0.0013	-	1425.03	1161.18	1.227
87002_22	0.0565	0.0010	0.0083	0.0002	0.0494	0.0010	-	2329.76	2561.54	0.910
87002_23	0.0585	0.0023	0.0082	0.0002	0.0515	0.0021	-	635.89	406.49	1.564
87002_24	0.0604	0.0014	0.0087	0.0002	0.0504	0.0013	-	1424.69	1160.73	1.227
87002_25	3.2571	0.0427	0.2558	0.0050	0.0923	0.0015	-	7815.60	356.29	21.936
87002_26	0.0582	0.0012	0.0084	0.0002	0.0501	0.0012	-	1267.26	1311.10	0.967
87002_27	0.0617	0.0014	0.0087	0.0002	0.0511	0.0013	-	1401.00	1490.80	0.940
87002_28	0.0590	0.0014	0.0086	0.0002	0.0495	0.0013	-	1229.44	1036.38	1.186
87002_29	0.0604	0.0014	0.0087	0.0002	0.0504	0.0013	-	1424.20	1160.13	1.228
87002_30	3.2608	0.0428	0.2562	0.0050	0.0923	0.0015	-	7801.79	355.86	21.924

	Apparent Ages							Preferred Ages						
Analysis_#	207Pb/235Uc *	207Pb/235Uc * (±2σ)	206Pb/238U	206Pb/238U (±2σ)	207Pb/206Pb	207Pb/206Pb (±2σ)	Analysis_#	Preferred Age (Ma)	Absolute Error (±2σ)	Age Type	Fit Quality 1=best	Clean Quality 1=best	Pb204 Quality	2σ Conc. Scans
87002_1	58.05	1.31	55.88	1.18	137.41	56.01	87002_1	55.88	1.18	Pb/U wmean conc.	0.0160	1.0000	0.3086	73
87002_2	60.64	1.42	56.68	1.15	245.80	56.98	87002_2	56.68	1.15	Pb/U wmean conc.	0.0229	1.0000	0.3192	78
87002_3	57.44	1.21	54.16	1.10	196.80	53.23	87002_3	54.16	1.10	Pb/U wmean conc.	0.0444	0.5000	0.3200	93
87002_4	59.55	1.35	56.41	1.15	176.69	56.01	87002_4	56.41	1.15	Pb/U wmean conc.	0.0164	1.0000	0.3086	87
87002_5	54.69	1.21	53.56	1.14	103.82	56.39	87002_5	53.56	1.14	Pb/U wmean conc.	0.0097	1.0000	0.3227	68
87002_6	60.66	1.42	56.70	1.15	245.80	56.98	87002_6	56.70	1.15	Pb/U wmean conc.	0.0229	1.0000	0.3192	78
87002_7	59.90	1.71	56.60	1.20	188.13	68.37	87002_7	56.60	1.20	Pb/U wmean conc.	0.0346	1.0000	0.2780	38
87002_8	59.91	1.71	56.60	1.20	188.13	68.37	87002_8	56.60	1.20	Pb/U wmean conc.	0.0346	1.0000	0.2780	38
87002_9	68.46	2.13	57.75	1.19	455.72	70.15	87002_9	57.75	1.19	Pb/U wmean conc.	0.0066	0.5000	0.3375	105
87002_10	59.11	1.29	54.71	1.09	234.87	53.86	87002_10	54.71	1.09	Pb/U wmean conc.	0.0116	1.0000	0.2974	79
87002_11	57.44	1.21	54.16	1.10	196.80	53.23	87002_11	54.16	1.10	Pb/U wmean conc.	0.0444	0.5000	0.3200	93
87002_12	58.39	1.54	54.29	1.10	236.15	63.57	87002_12	54.29	1.10	Pb/U wmean conc.	0.0249	0.5000	0.3408	52
87002_13	57.70	2.33	52.88	1.17	263.48	93.47	87002_13	52.88	1.17	Pb/U wmean conc.	0.0132	1.0000	0.3589	37
87002_14	59.92	1.27	56.26	1.13	199.89	52.85	87002_14	56.26	1.13	Pb/U wmean conc.	0.0067	1.0000	0.3514	135
87002_15	57.30	2.13	53.95	1.14	200.66	86.91	87002_15	53.95	1.14	Pb/U wmean conc.	0.0164	1.0000	0.3631	30
87002_16	57.60	1.38	54.40	1.11	182.50	58.29	87002_16	54.40	1.11	Pb/U wmean conc.	0.0203	0.5000	0.3894	111
87002_17	58.10	1.42	55.07	1.11	172.96	59.83	87002_17	55.07	1.11	Pb/U wmean conc.	0.0133	0.5000	0.3850	81
87002_18	58.11	1.42	55.08	1.11	172.96	59.83	87002_18	55.08	1.11	Pb/U wmean conc.	0.0133	0.5000	0.3850	81
87002_19	55.85	1.04	53.17	1.06	165.85	47.99	87002_19	53.17	1.06	Pb/U wmean conc.	0.0135	0.5000	0.2796	97
87002_20	59.50	1.46	55.65	1.13	212.13	59.92	87002_20	55.65	1.13	Pb/U wmean conc.	0.0319	1.0000	0.2818	61
87002_21	59.51	1.46	55.66	1.13	212.13	59.92	87002_21	55.66	1.13	Pb/U wmean conc.	0.0319	1.0000	0.2818	61
87002_22	55.85	1.04	53.18	1.06	165.85	47.99	87002_22	53.18	1.06	Pb/U wmean conc.	0.0135	0.5000	0.2796	97
87002_23	57.77	2.33	52.96	1.18	263.48	93.47	87002_23	52.96	1.18	Pb/U wmean conc.	0.0132	1.0000	0.3589	37
87002_24	59.52	1.46	55.68	1.13	212.13	59.92	87002_24	55.68	1.13	Pb/U wmean conc.	0.0319	1.0000	0.2818	61
87002_25	1470.87	42.90	1468.48	32.35	1473.57	30.50	87002_25	1473.57	30.50	Pb/Pb wmean conc.	0.7967	1.0000	0.3385	124
87002_26	57.44	1.21	54.12	1.09	198.80	53.02	87002_26	54.12	1.09	Pb/U wmean conc.	0.0444	0.5000	0.3200	94
87002_27	60.79	1.43	55.84	1.15	245.80	56.98	87002_27	55.84	1.15	Pb/U wmean conc.	0.0229	1.0000	0.3192	78
87002_28	58.16	1.42	55.13	1.11	172.96	59.83	87002_28	55.13	1.11	Pb/U wmean conc.	0.0133	0.5000	0.3850	81
87002_29	59.54	1.46	55.70	1.13	212.13	59.92	87002_29	55.70	1.13	Pb/U wmean conc.	0.0319	1.0000	0.2818	61
87002_30	1471.75	42.96	1470.31	32.40	1473.23	30.50	87002_30	1473.23	30.50	Pb/Pb wmean conc.	0.7967	1.0000	0.3385	122

	Preferred Ages - Sorted							Fitted Discordia						
Analysis_#	Preferred Age (Ma)	Absolute Error (±2σ)	Age Type	Fit Quality 1=best	Clean Quality 1=best	Pb204 Quality	2σ Conc. Scans	Age - Lower Intercept (Ma)	Age - Lower Intercept (±2σ)	Age - Upper Intercept (Ma)	Age - Upper Intercept (±2σ)	Regression Intercept	Regression Intercept (±1σ)	Regression Slope	Regression Slope (±1σ)
87002_13	52.88	1.17	Pb/U wmean conc.	0.0132	1.0000	0.3589	37	54.70	2.39	3587.07	892.36	0.007292	0.000335	0.022192	0.005847
87002_23	52.96	1.18	Pb/U wmean conc.	0.0132	1.0000	0.3589	37	53.67	2.28	3312.09	527.85	0.006924	0.000278	0.026482	0.004173
87002_15	53.95	1.14	Pb/U wmean conc.	0.0164	1.0000	0.3631	30	53.70	1.80	4426.00	628.96	0.007676	0.000193	0.012689	0.003211
87002_12	54.29	1.10	Pb/U wmean conc.	0.0249	0.5000	0.3408	52	55.10	1.94	4560.00	516.82	0.008114	0.000215	0.008450	0.003582
87002_16	54.40	1.11	Pb/U wmean conc.	0.0203	0.5000	0.3894	111	54.37	1.54	undefined	undefined	0.008892	0.000195	-0.007663	0.003477
87002_17	55.07	1.11	Pb/U wmean conc.	0.0133	0.5000	0.3850	81	53.68	2.24	3301.74	543.76	0.006916	0.000279	0.026657	0.004197
87002_18	55.08	1.11	Pb/U wmean conc.	0.0133	0.5000	0.3850	81	54.97	2.18	3930.08	597.17	0.007579	0.000202	0.017719	0.003246
87002_28	55.13	1.11	Pb/U wmean conc.	0.0133	0.5000	0.3850	81	54.98	2.12	3924.87	585.58	0.007576	0.000202	0.017780	0.003248
87002_14	56.26	1.13	Pb/U wmean conc.	0.0067	1.0000	0.3514	135	52.07	3.07	2475.94	512.73	0.005784	0.000414	0.044235	0.005675
87002_9	57.75	1.19	Pb/U wmean conc.	0.0066	0.5000	0.3375	105	54.65	1.72	3887.60	613.68	0.007506	0.000185	0.018226	0.003364
87002_30	1473.23	30.50	Pb/Pb wmean conc.	0.7967	1.0000	0.3385	122	53.72	1.87	4386.16	589.39	0.007661	0.000194	0.013038	0.003226
87002_25	1473.57	30.50	Pb/Pb wmean conc.	0.7967	1.0000	0.3385	124	57.00	2.33	3478.12	545.86	0.007506	0.000221	0.023800	0.003848
87002_5	rej 53	__Pb_	Pb/U wmean conc.	0.0097	1.0000	0.3227	68	53.47	1.85	undefined	undefined	0.008846	0.000167	-0.009535	0.003160
87002_19	rej 53	__Pb_	Pb/U wmean conc.	0.0135	0.5000	0.2796	97	56.32	1.96	4560.00	364.51	0.008693	0.000393	0.001439	0.006405
87002_22	rej 53	__Pb_	Pb/U wmean conc.	0.0135	0.5000	0.2796	97	55.37	1.97	4040.24	565.83	0.007705	0.000152	0.016464	0.003123
87002_3	rej 54	__Pb_	Pb/U wmean conc.	0.0444	0.5000	0.3200	93	53.42	1.95	2879.43	226.38	0.006448	0.000142	0.034695	0.002226
87002_10	rej 54	__Pb_	Pb/U wmean conc.	0.0116	1.0000	0.2974	79	53.63	2.10	4560.00	886.36	0.007830	0.000310	0.009672	0.005068
87002_11	rej 54	__Pb_	Pb/U wmean conc.	0.0444	0.5000	0.3200	93	53.63	2.14	4560.00	895.88	0.007827	0.000310	0.009730	0.005070
87002_26	rej 54	__Pb_	Pb/U wmean conc.	0.0444	0.5000	0.3200	94	53.22	2.52	2484.08	667.49	0.005923	0.000403	0.044011	0.007194
87002_1	rej 55	__Pb_	Pb/U wmean conc.	0.0160	1.0000	0.3086	73	54.12	1.85	undefined	undefined	0.008429	0.000147	0.000041	0.002374
87002_2	rej 55	__Pb_	Pb/U wmean conc.	0.0229	1.0000	0.3192	78	54.12	1.85	undefined	undefined	0.008430	0.000147	0.000033	0.002374
87002_6	rej 55	__Pb_	Pb/U wmean conc.	0.0229	1.0000	0.3192	78	53.25	2.50	2477.00	603.36	0.005914	0.000403	0.044195	0.007195
87002_20	rej 55	__Pb_	Pb/U wmean conc.	0.0319	1.0000	0.2818	61	53.55	1.88	undefined	undefined	0.008926	0.000168	-0.008971	0.003185
87002_21	rej 55	__Pb_	Pb/U wmean conc.	0.0319	1.0000	0.2818	61	54.15	1.80	undefined	undefined	0.008433	0.000147	0.000021	0.002373
87002_24	rej 55	__Pb_	Pb/U wmean conc.	0.0319	1.0000	0.2818	61	undefined	undefined	undefined	undefined	-0.015773	0.007404	0.083297	0.002297
87002_27	rej 55	__Pb_	Pb/U wmean conc.	0.0229	1.0000	0.3192	78	53.80	1.85	4366.51	584.21	0.007663	0.000194	0.013214	0.003220
87002_29	rej 55	__Pb_	Pb/U wmean conc.	0.0319	1.0000	0.2818	61	53.80	2.26	3303.58	579.82	0.006933	0.000284	0.026625	0.004255
87002_4	rej 56	__Pb_	Pb/U wmean conc.	0.0164	1.0000	0.3086	87	53.68	2.11	4560.00	928.35	0.007825	0.000311	0.009906	0.005073
87002_7	rej 56	__Pb_	Pb/U wmean conc.	0.0346	1.0000	0.2780	38	54.17	1.83	undefined	undefined	0.008440	0.000147	-0.000007	0.002367
87002_8	rej 56	__Pb_	Pb/U wmean conc.	0.0346	1.0000	0.2780	38	undefined	undefined	undefined	undefined	-0.015606	0.007418	0.083247	0.002300

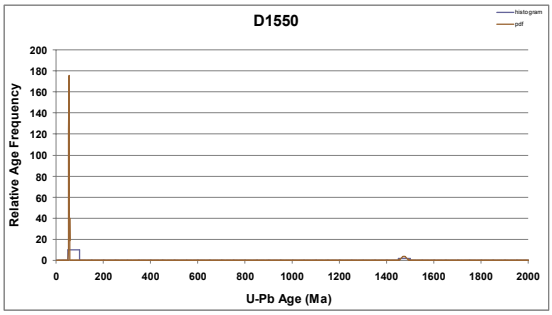
D1550
histogram
pdf
Relative Age Frequency
U-Pb Age (Ma)

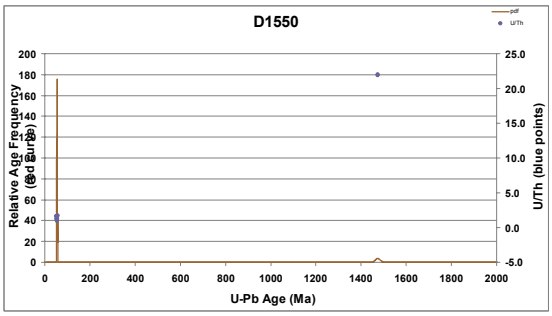
D1550
pdf
U/Th
Relative Age Frequency (Red curve)
U/Th (blue points)
U-Pb Age (Ma)

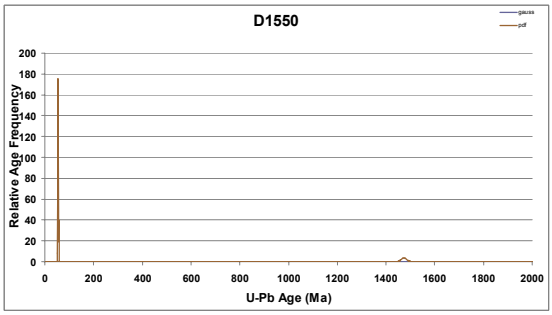
D1550
gauss
pdf
Relative Age Frequency
U-Pb Age (Ma)

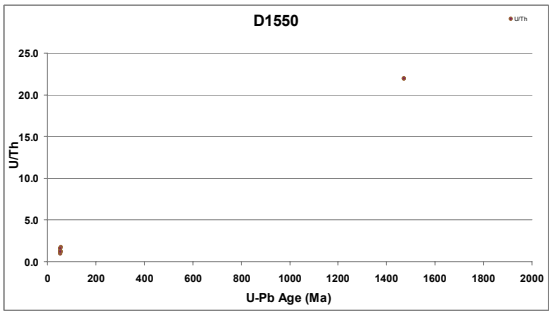
D1550
U/Th
U/Th
U-Pb Age (Ma)

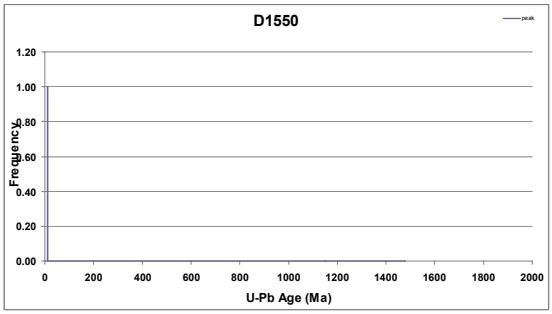
D1550
peak
Frequency
U-Pb Age (Ma)

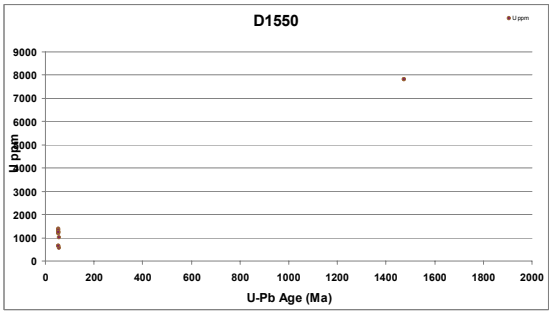
D1550
U ppm
U ppm
U-Pb Age (Ma)

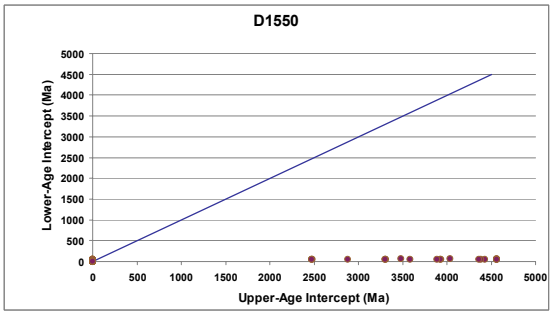
D1550
Lower-Age Intercept (Ma)
Upper-Age Intercept (Ma)

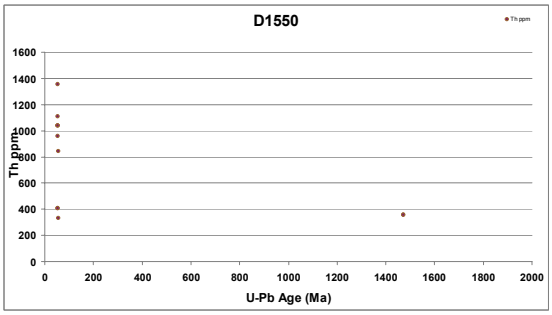
D1550
Th ppm
Th ppm
U-Pb Age (Ma)

Sample Tgr Lee Hill: Santa Rita stock (granodiorite), Lee Hill pit

	Measured Isotopic Ratios							U and Th		
Analysis_#	207Pb/235Uc *	207Pb/235Uc * (±2σ)	206Pb/238U	206Pb/238U (±2σ)	207Pb/206Pb	207Pb/206Pb (±2σ)		U (ppm)	Th (ppm)	U/Th (ppm)
87003_1	3.2823	0.0436	0.2530	0.0050	0.0941	0.0015	-	1480.31	334.28	4.428
87003_2	0.0601	0.0014	0.0087	0.0002	0.0500	0.0012	-	1761.12	1969.76	0.894
87003_3	0.0611	0.0016	0.0087	0.0002	0.0512	0.0014	-	922.13	696.87	1.323
87003_4	0.0536	0.0127	0.0083	0.0004	0.0469	0.0113	-	383.91	426.58	0.900
87003_5	0.0592	0.0016	0.0085	0.0002	0.0502	0.0015	-	1172.24	1100.48	1.065
87003_6	0.0609	0.0014	0.0085	0.0002	0.0519	0.0013	-	1534.03	1721.72	0.891
87003_7	0.0631	0.0019	0.0091	0.0002	0.0503	0.0016	-	783.10	492.45	1.590
87003_8	0.0598	0.0015	0.0086	0.0002	0.0504	0.0014	-	1687.36	1846.31	0.914
87003_9	3.1210	0.0410	0.2450	0.0048	0.0923	0.0015	-	2415.46	30.36	79.551
87003_10	3.2834	0.0436	0.2531	0.0050	0.0941	0.0015	-	1479.93	334.22	4.428
87003_11	0.0610	0.0012	0.0090	0.0002	0.0493	0.0011	-	1359.22	887.49	1.532
87003_12	0.0635	0.0015	0.0088	0.0002	0.0521	0.0013	-	1023.06	621.79	1.645
87003_13	0.0612	0.0013	0.0086	0.0002	0.0516	0.0012	-	1239.22	1342.81	0.923
87003_14	0.0583	0.0017	0.0084	0.0002	0.0503	0.0016	-	1246.77	1185.70	1.051
87003_15	0.0594	0.0013	0.0087	0.0002	0.0495	0.0012	-	1460.21	1493.81	0.978
87003_16	0.0566	0.0014	0.0083	0.0002	0.0496	0.0013	-	1660.02	1832.45	0.906
87003_17	0.0614	0.0015	0.0088	0.0002	0.0506	0.0014	-	1006.79	743.69	1.354
87003_18	0.0586	0.0016	0.0087	0.0002	0.0488	0.0014	-	1140.15	925.37	1.232
87003_19	0.0566	0.0014	0.0083	0.0002	0.0496	0.0013	-	1659.71	1832.59	0.906
87003_20	0.0594	0.0013	0.0087	0.0002	0.0495	0.0012	-	1459.76	1494.01	0.977
87003_21	0.0602	0.0014	0.0087	0.0002	0.0500	0.0012	-	1757.77	1970.81	0.892
87003_22	0.0586	0.0016	0.0087	0.0002	0.0488	0.0014	-	1139.92	925.56	1.232
87003_23	0.0595	0.0014	0.0086	0.0002	0.0500	0.0013	-	1187.18	1046.30	1.135
87003_24	0.0593	0.0021	0.0086	0.0002	0.0499	0.0019	-	678.95	371.27	1.829
87003_25	0.0612	0.0016	0.0087	0.0002	0.0512	0.0014	-	921.43	697.93	1.320
87003_26	0.0586	0.0016	0.0087	0.0002	0.0488	0.0014	-	1139.69	925.82	1.231
87003_27	2.8502	0.0386	0.2296	0.0045	0.0899	0.0015	-	911.52	208.80	4.365
87003_28	0.0612	0.0016	0.0087	0.0002	0.0512	0.0014	-	921.43	698.26	1.320
87003_29	0.0594	0.0016	0.0086	0.0002	0.0502	0.0015	-	1167.73	1100.64	1.061
87003_30	2.9685	0.0409	0.2421	0.0048	0.0888	0.0015	-	758.04	672.31	1.128

	Apparent Ages					
Analysis_#	207Pb/235Uc *	207Pb/235Uc * (±2σ)	206Pb/238U	206Pb/238U (±2σ)	207Pb/206Pb	207Pb/206Pb (±2σ)
87003_1	1476.88	43.75	1453.79	31.99	1510.86	30.79
87003_2	59.27	1.37	55.98	1.14	194.85	57.59
87003_3	60.24	1.62	55.58	1.12	249.02	64.28
87003_4	53.01	12.85	53.23	2.49	43.11	529.30
87003_5	58.39	1.64	54.76	1.14	204.84	67.81
87003_6	60.07	1.39	54.66	1.10	281.34	55.97
87003_7	62.12	1.96	58.35	1.21	209.49	74.73
87003_8	58.94	1.54	55.03	1.11	215.29	63.03
87003_9	1437.89	41.22	1412.44	30.91	1474.43	30.76
87003_10	1477.13	43.76	1454.32	32.00	1510.86	30.79
87003_11	60.16	1.23	57.58	1.14	161.10	51.89
87003_12	62.48	1.51	56.52	1.14	289.10	58.17
87003_13	60.29	1.35	55.22	1.11	269.68	54.70
87003_14	57.52	1.71	54.00	1.12	206.74	71.36
87003_15	58.60	1.33	55.71	1.13	169.68	56.67
87003_16	55.87	1.40	53.13	1.09	174.53	61.48
87003_17	60.54	1.56	56.36	1.14	220.62	62.10
87003_18	57.78	1.62	55.60	1.18	140.07	68.30
87003_19	55.88	1.40	53.13	1.09	174.53	61.48
87003_20	58.61	1.33	55.74	1.13	169.68	56.67
87003_21	59.40	1.38	56.11	1.15	194.85	57.59
87003_22	57.78	1.62	55.62	1.18	140.07	68.30
87003_23	58.65	1.45	55.31	1.14	193.95	60.42
87003_24	58.51	2.11	55.27	1.19	192.00	85.21
87003_25	60.29	1.63	55.66	1.12	249.02	64.28
87003_26	57.79	1.62	55.64	1.18	140.07	68.30
87003_27	1368.87	38.84	1332.46	29.24	1422.61	31.60
87003_28	60.29	1.63	55.67	1.12	249.02	64.28
87003_29	58.62	1.64	55.00	1.14	204.84	67.81
87003_30	1399.59	41.07	1397.46	31.11	1399.32	31.94

	Preferred Ages						
Analysis_#	Preferred Age (Ma)	Absolute Error (±2σ)	Age Type	Fit Quality 1=best	Clean Quality 1=best	Pb204 Quality	2σ Conc. Scans
87003_1	1510.86	30.79	Pb/Pb wmean conc.	0.1206	0.5000	0.5746	84
87003_2	55.98	1.14	Pb/U wmean conc.	0.0290	0.5000	0.4869	51
87003_3	55.58	1.12	Pb/U wmean conc.	0.0160	0.5000	0.5748	113
87003_4	53.23	2.49	Pb/U wmean conc.	0.0128	0.5000	0.4957	4
87003_5	54.76	1.14	Pb/U wmean conc.	0.0131	1.0000	0.6062	50
87003_6	54.66	1.10	Pb/U wmean conc.	0.0118	0.5000	0.4917	75
87003_7	58.35	1.21	Pb/U wmean conc.	0.0208	1.0000	0.5164	52
87003_8	55.03	1.11	Pb/U wmean conc.	0.0121	1.0000	0.4828	58
87003_9	1474.43	30.76	Pb/Pb wmean conc.	0.1385	1.0000	0.4961	98
87003_10	1510.86	30.79	Pb/Pb wmean conc.	0.1206	0.5000	0.5746	84
87003_11	57.58	1.14	Pb/U wmean conc.	0.0061	0.5000	0.4324	128
87003_12	56.52	1.14	Pb/U wmean conc.	0.0177	0.3333	0.4898	95
87003_13	55.22	1.11	Pb/U wmean conc.	0.0073	1.0000	0.5057	88
87003_14	54.00	1.12	Pb/U wmean conc.	0.0141	0.2000	0.4764	53
87003_15	55.71	1.13	Pb/U wmean conc.	0.0137	1.0000	0.5728	69
87003_16	53.13	1.09	Pb/U wmean conc.	0.0261	0.5000	0.3957	45
87003_17	56.36	1.14	Pb/U wmean conc.	0.0096	0.5000	0.4488	82
87003_18	55.60	1.18	Pb/U wmean conc.	0.0124	0.3333	0.4538	65
87003_19	53.13	1.09	Pb/U wmean conc.	0.0261	0.5000	0.3957	45
87003_20	55.74	1.13	Pb/U wmean conc.	0.0137	1.0000	0.5728	69
87003_21	56.11	1.15	Pb/U wmean conc.	0.0290	0.5000	0.4869	51
87003_22	55.62	1.18	Pb/U wmean conc.	0.0124	0.3333	0.4538	65
87003_23	55.31	1.14	Pb/U wmean conc.	0.0126	1.0000	0.4797	92
87003_24	55.27	1.19	Pb/U wmean conc.	0.0222	0.5000	0.4178	48
87003_25	55.66	1.12	Pb/U wmean conc.	0.0160	0.5000	0.5748	113
87003_26	55.64	1.18	Pb/U wmean conc.	0.0124	0.3333	0.4538	65
87003_27	1332.46	29.24	Pb/U wmean conc.	0.1192	1.0000	0.3167	144
87003_28	55.67	1.12	Pb/U wmean conc.	0.0160	0.5000	0.5748	113
87003_29	55.00	1.14	Pb/U wmean conc.	0.0131	1.0000	0.6062	50
87003_30	1397.46	31.11	Pb/U wmean conc.	0.9346	0.5000	0.3907	111

Preferred Ages - Sorted

Analysis_#	Preferred Age (Ma)	Absolute Error (±2σ)	Age Type	Fit Quality 1=best	Clean Quality 1=best	Pb204 Quality	2σ Conc. Scans
87003_16	53.13	1.09	Pb/U wmean conc.	0.0261	0.5000	0.3957	45
87003_19	53.13	1.09	Pb/U wmean conc.	0.0261	0.5000	0.3957	45
87003_4	53.23	2.49	Pb/U wmean conc.	0.0128	0.5000	0.4957	4
87003_6	54.66	1.10	Pb/U wmean conc.	0.0118	0.5000	0.4917	75
87003_5	54.76	1.14	Pb/U wmean conc.	0.0131	1.0000	0.6062	50
87003_29	55.00	1.14	Pb/U wmean conc.	0.0131	1.0000	0.6062	50
87003_8	55.03	1.11	Pb/U wmean conc.	0.0121	1.0000	0.4828	58
87003_13	55.22	1.11	Pb/U wmean conc.	0.0073	1.0000	0.5057	88
87003_24	55.27	1.19	Pb/U wmean conc.	0.0222	0.5000	0.4178	48
87003_23	55.31	1.14	Pb/U wmean conc.	0.0126	1.0000	0.4797	92
87003_3	55.58	1.12	Pb/U wmean conc.	0.0160	0.5000	0.5748	113
87003_18	55.60	1.18	Pb/U wmean conc.	0.0124	0.3333	0.4538	65
87003_22	55.62	1.18	Pb/U wmean conc.	0.0124	0.3333	0.4538	65
87003_26	55.64	1.18	Pb/U wmean conc.	0.0124	0.3333	0.4538	65
87003_25	55.66	1.12	Pb/U wmean conc.	0.0160	0.5000	0.5748	113
87003_28	55.67	1.12	Pb/U wmean conc.	0.0160	0.5000	0.5748	113
87003_15	55.71	1.13	Pb/U wmean conc.	0.0137	1.0000	0.5728	69
87003_20	55.74	1.13	Pb/U wmean conc.	0.0137	1.0000	0.5728	69
87003_2	55.98	1.14	Pb/U wmean conc.	0.0290	0.5000	0.4869	51
87003_21	56.11	1.15	Pb/U wmean conc.	0.0290	0.5000	0.4869	51
87003_17	56.36	1.14	Pb/U wmean conc.	0.0096	0.5000	0.4488	82
87003_12	56.52	1.14	Pb/U wmean conc.	0.0177	0.3333	0.4898	95
87003_11	57.58	1.14	Pb/U wmean conc.	0.0061	0.5000	0.4324	128
87003_7	58.35	1.21	Pb/U wmean conc.	0.0208	1.0000	0.5164	52
87003_30	1397.46	31.11	Pb/U wmean conc.	0.9346	0.5000	0.3907	111
87003_9	1474.43	30.76	Pb/Pb wmean conc.	0.1385	1.0000	0.4961	98
87003_1	1510.86	30.79	Pb/Pb wmean conc.	0.1206	0.5000	0.5746	84
87003_10	1510.86	30.79	Pb/Pb wmean conc.	0.1206	0.5000	0.5746	84
87003_14	rej 53	_ C __ _	Pb/U wmean conc.	0.0141	0.2000	0.4764	53
87003_27	rej 1332	_ _ Pb _	Pb/U wmean conc.	0.1192	1.0000	0.3167	144

Fitted Discordia

Age - Lower Intercept (Ma)	Age - Lower Intercept (±2σ)	Age - Upper Intercept (Ma)	Age - Upper Intercept (±2σ)	Regression Intercept	Regression Intercept (±1σ)	Regression Slope	Regression Slope (±1σ)
737.50	414.22	1629.55	129.05	0.060159	0.017108	0.057188	0.005201
55.97	1.71	undefined	undefined	0.009035	0.000252	-0.005530	0.004365
53.72	2.26	2840.27	358.20	0.006438	0.000210	0.035534	0.003535
64.25	4.83	2997.99	828.59	0.007914	0.000326	0.032178	0.007311
55.51	1.80	undefined	undefined	0.009007	0.000182	-0.006378	0.003258
51.00	1.92	2427.95	263.73	0.005699	0.000202	0.045513	0.003113
57.65	1.84	3472.18	346.23	0.007587	0.000130	0.023888	0.002312
55.73	1.89	undefined	undefined	0.008554	0.000247	0.002298	0.003949
301.21	193.73	1501.60	40.29	0.023493	0.006633	0.070489	0.002152
883.15	468.95	1668.15	221.21	0.072865	0.017743	0.053351	0.005390
53.96	4.84	1393.75	661.58	0.004009	0.000710	0.080574	0.011532
52.47	2.84	2439.68	366.49	0.005777	0.000313	0.045185	0.004521
56.08	1.89	undefined	undefined	0.009743	0.000387	-0.017700	0.006261
55.37	2.20	undefined	undefined	0.008792	0.000284	-0.002947	0.004901
56.10	2.07	3753.65	647.79	0.007609	0.000210	0.019902	0.003931
55.35	2.04	undefined	undefined	0.008891	0.000242	-0.004814	0.004717
56.78	2.40	4560.00	647.79	0.008746	0.000435	0.001764	0.007445
55.95	1.88	4560.00	136.16	0.008767	0.000355	-0.000869	0.006559
55.35	2.00	undefined	undefined	0.008910	0.000241	-0.005130	0.004705
56.11	2.05	3773.53	652.90	0.007627	0.000209	0.019644	0.003909
56.08	1.68	undefined	undefined	0.009067	0.000239	-0.005782	0.004129
55.96	1.86	undefined	undefined	0.008800	0.000357	-0.001406	0.006592
56.65	1.80	4560.00	598.19	0.008259	0.000200	0.009912	0.003281
56.46	1.96	undefined	undefined	0.009559	0.000184	-0.013307	0.003036
53.92	2.31	2931.32	365.57	0.006567	0.000215	0.033603	0.003620
55.98	1.90	undefined	undefined	0.008837	0.000359	-0.002033	0.006629
670.25	150.34	1495.50	64.15	0.051185	0.005293	0.062447	0.001874
53.95	2.17	2948.57	373.59	0.006590	0.000216	0.033248	0.003632
55.65	1.73	undefined	undefined	0.008997	0.000173	-0.005821	0.003097
1405.55	97.12	2381.20	830.77	0.149266	0.018055	0.031541	0.006041

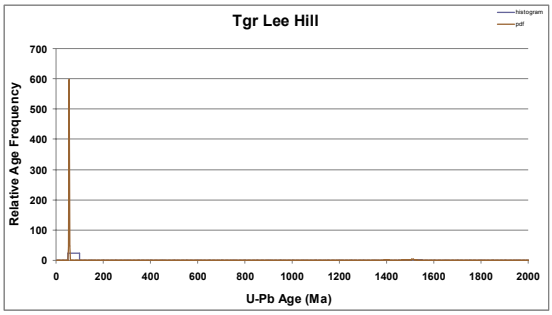
Tgr Lee Hill
histogram
pdf
Relative Age Frequency
U-Pb Age (Ma)

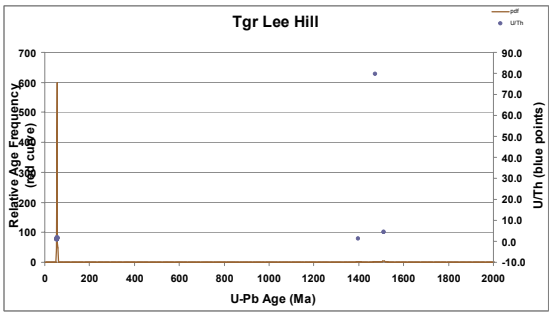
Tgr Lee Hill
pdf
U/Th
Relative Age Frequency (red cube)
U/Th (blue points)
U-Pb Age (Ma)

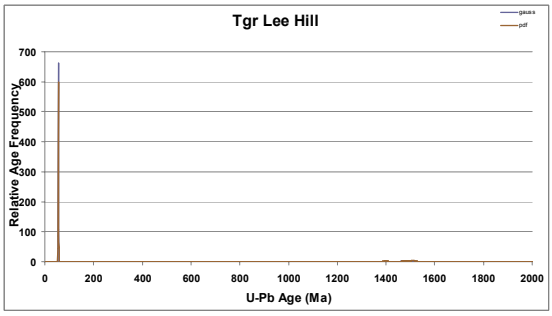
Tgr Lee Hill
gauss
pdf
Relative Age Frequency
U-Pb Age (Ma)

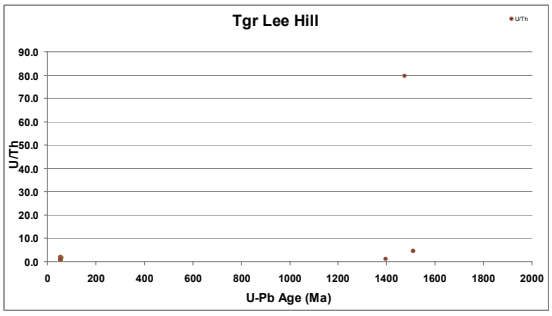
Tgr Lee Hill
U/Th
U/Th
U-Pb Age (Ma)

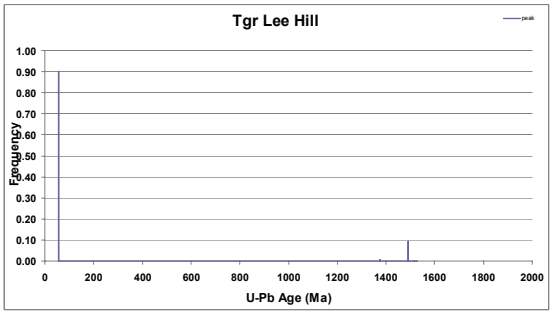
Tgr Lee Hill
peak
Frequency
U-Pb Age (Ma)

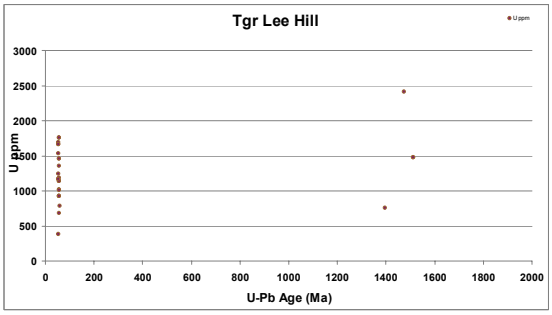
Tgr Lee Hill
U ppm
U ppm
U-Pb Age (Ma)

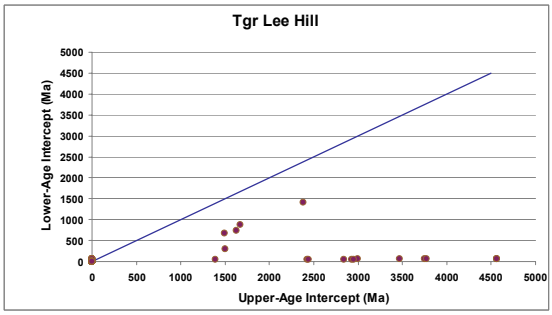
Tgr Lee Hill
Lower-Age Intercept (Ma)
Upper-Age Intercept (Ma)

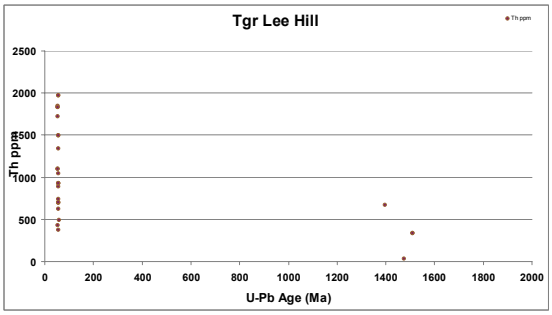
Tgr Lee Hill
Th ppm
Th ppm
U-Pb Age (Ma)

Sample Hwy 356: Rhyodacite in Hanover Hole Diatreme

	Measured Isotopic Ratios							U and Th		
Analysis_#	207Pb/235Uc *	207Pb/235Uc * (±2σ)	206Pb/238U	206Pb/238U (±2σ)	207Pb/206Pb	207Pb/206Pb (±2σ)		U (ppm)	Th (ppm)	U/Th (ppm)
87004_1	undefined	undefined	undefined	undefined	undefined	undefined	-	1295.70	325.24	3.984
87004_2	0.0557	0.0009	0.0083	0.0002	0.0488	0.0009	-	3115.09	5167.05	0.603
87004_3	0.0615	0.0014	0.0087	0.0002	0.0513	0.0013	-	949.00	718.44	1.321
87004_4	3.4459	0.0476	0.2577	0.0051	0.0971	0.0016	-	575.28	264.31	2.177
87004_5	0.0557	0.0009	0.0083	0.0002	0.0488	0.0009	-	3114.84	5169.74	0.603
87004_6	3.4327	0.0458	0.2597	0.0051	0.0962	0.0016	-	1161.62	543.76	2.136
87004_7	0.0557	0.0009	0.0083	0.0002	0.0488	0.0009	-	3114.71	5171.70	0.602
87004_8	0.0640	0.0015	0.0095	0.0002	0.0493	0.0013	-	4679.31	2032.46	2.302
87004_9	3.4438	0.0477	0.2576	0.0051	0.0970	0.0016	-	574.01	264.14	2.173
87004_10	0.0608	0.0020	0.0085	0.0002	0.0519	0.0018	-	345.66	229.44	1.507
87004_11	0.0557	0.0009	0.0083	0.0002	0.0488	0.0009	-	3114.52	5175.98	0.602
87004_12	0.0608	0.0020	0.0085	0.0002	0.0519	0.0018	-	345.63	229.53	1.506
87004_13	2.9291	0.0393	0.2349	0.0046	0.0899	0.0015	-	1348.62	515.11	2.618
87004_14	0.0622	0.0031	0.0078	0.0002	0.0577	0.0030	-	239.44	154.57	1.549
87004_15	0.0608	0.0020	0.0085	0.0002	0.0519	0.0018	-	345.59	229.68	1.505
87004_16	3.0469	0.0402	0.2436	0.0048	0.0907	0.0015	-	1824.92	241.15	7.567
87004_17	0.0708	0.0029	0.0102	0.0002	0.0497	0.0021	-	2223.98	632.27	3.517
87004_18	3.4404	0.0476	0.2574	0.0051	0.0970	0.0016	-	574.59	264.84	2.170
87004_19	2.8490	0.0405	0.2303	0.0045	0.0896	0.0015	-	317.37	291.90	1.087
87004_20	0.0567	0.0012	0.0083	0.0002	0.0497	0.0011	-	1398.35	1013.99	1.379
87004_21	0.0557	0.0009	0.0083	0.0002	0.0488	0.0009	-	3114.51	5188.83	0.600
87004_22	0.0567	0.0012	0.0083	0.0002	0.0497	0.0011	-	1398.22	1014.54	1.378
87004_23	3.4292	0.0474	0.2568	0.0051	0.0970	0.0016	-	574.16	264.98	2.167
87004_24	0.0578	0.0011	0.0084	0.0002	0.0501	0.0011	-	1842.08	1784.40	1.032
87004_25	3.1425	0.0423	0.2450	0.0049	0.0925	0.0015	-	3569.28	364.77	9.785
87004_26	3.0434	0.0402	0.2434	0.0048	0.0907	0.0015	-	1827.01	242.10	7.547
87004_27	0.0567	0.0012	0.0083	0.0002	0.0497	0.0011	-	1397.94	1016.01	1.376
87004_28	3.4291	0.0458	0.2596	0.0051	0.0961	0.0016	-	1163.57	545.26	2.134
87004_29	0.0616	0.0014	0.0087	0.0002	0.0513	0.0013	-	947.58	723.22	1.310
87004_30	0.0578	0.0011	0.0084	0.0002	0.0501	0.0011	-	1842.61	1787.83	1.031

	Apparent Ages							Preferred Ages						
Analysis_#	207Pb/235Uc *	207Pb/235Uc * (±2σ)	206Pb/238U	206Pb/238U (±2σ)	207Pb/206Pb	207Pb/206Pb (±2σ)	Analysis_#	Preferred Age (Ma)	Absolute Error (±2σ)	Age Type	Fit Quality 1=best	Clean Quality 1=best	Pb204 Quality	2σ Conc. Scans
87004_1	undefined	undefined	undefined	undefined	undefined	undefined	87004_1	1638.50	64.98	upper int.	0.3665	0.5000	0.6986	0
87004_2	55.08	0.92	53.06	1.05	139.49	44.46	87004_2	53.06	1.05	Pb/U wmean conc.	0.0171	1.0000	0.5566	110
87004_3	60.59	1.41	55.60	1.12	254.31	56.79	87004_3	55.60	1.12	Pb/U wmean conc.	0.0074	0.5000	0.7015	103
87004_4	1514.94	47.78	1477.88	33.05	1568.30	31.55	87004_4	1568.30	31.55	Pb/Pb wmean conc.	0.6048	1.0000	0.5505	50
87004_5	55.09	0.92	53.07	1.05	139.49	44.46	87004_5	53.07	1.05	Pb/U wmean conc.	0.0171	1.0000	0.5566	110
87004_6	1511.92	46.03	1488.27	32.94	1551.72	30.75	87004_6	1551.72	30.75	Pb/Pb wmean conc.	0.7475	1.0000	0.6919	66
87004_7	55.09	0.92	53.07	1.05	139.49	44.46	87004_7	53.07	1.05	Pb/U wmean conc.	0.0171	1.0000	0.5566	110
87004_8	63.03	1.52	60.71	1.25	163.60	58.89	87004_8	60.71	1.25	Pb/U wmean conc.	0.7362	0.2500	0.6096	32
87004_9	1514.45	47.84	1477.61	33.06	1567.88	31.59	87004_9	1567.88	31.59	Pb/Pb wmean conc.	0.6048	1.0000	0.5505	49
87004_10	59.95	2.04	54.28	1.12	282.57	79.05	87004_10	54.28	1.12	Pb/U wmean conc.	0.0104	1.0000	0.5195	117
87004_11	55.08	0.92	53.08	1.05	139.49	44.46	87004_11	53.08	1.05	Pb/U wmean conc.	0.0171	1.0000	0.5566	110
87004_12	59.95	2.04	54.28	1.12	282.57	79.05	87004_12	54.28	1.12	Pb/U wmean conc.	0.0104	1.0000	0.5195	117
87004_13	1389.46	39.54	1360.06	29.85	1423.29	31.47	87004_13	1360.06	29.85	Pb/U wmean conc.	0.9511	1.0000	0.6155	52
87004_14	61.27	3.12	50.19	1.11	517.63	110.68	87004_14	50.19	1.11	Pb/U wmean conc.	0.0092	1.0000	0.5848	101
87004_15	59.96	2.04	54.29	1.12	282.57	79.05	87004_15	54.29	1.12	Pb/U wmean conc.	0.0104	1.0000	0.5195	117
87004_16	1419.47	40.42	1405.52	30.78	1440.14	31.02	87004_16	1440.14	31.02	Pb/Pb wmean conc.	0.3726	1.0000	0.5300	78
87004_17	69.46	2.90	65.68	1.46	179.46	97.40	87004_17	65.68	1.46	Pb/U wmean conc.	0.0349	0.5000	0.5122	13
87004_18	1513.67	47.79	1476.67	33.04	1567.88	31.59	87004_18	1567.88	31.59	Pb/Pb wmean conc.	0.6048	1.0000	0.5505	49
87004_19	1368.55	40.75	1335.93	29.25	1416.55	32.84	87004_19	1335.93	29.25	Pb/U wmean conc.	0.0268	0.5000	0.4591	83
87004_20	55.97	1.19	52.99	1.05	181.92	53.32	87004_20	52.99	1.05	Pb/U wmean conc.	0.0125	1.0000	0.5486	118
87004_21	55.07	0.92	53.09	1.05	139.49	44.46	87004_21	53.09	1.05	Pb/U wmean conc.	0.0171	1.0000	0.5566	110
87004_22	55.97	1.19	52.99	1.05	181.92	53.32	87004_22	52.99	1.05	Pb/U wmean conc.	0.0125	1.0000	0.5486	118
87004_23	1511.12	47.59	1473.37	32.94	1566.61	31.57	87004_23	1566.61	31.57	Pb/Pb wmean conc.	0.6048	1.0000	0.5505	50
87004_24	57.08	1.11	53.63	1.07	201.77	49.36	87004_24	53.63	1.07	Pb/U wmean conc.	0.0118	1.0000	0.5911	116
87004_25	1443.16	42.55	1412.40	31.42	1478.19	31.34	87004_25	1478.19	31.34	Pb/Pb wmean conc.	0.9792	0.5000	0.6242	34
87004_26	1418.59	40.38	1404.27	30.74	1440.14	31.02	87004_26	1440.14	31.02	Pb/Pb wmean conc.	0.3726	1.0000	0.5300	78
87004_27	56.97	1.19	53.00	1.05	181.92	53.32	87004_27	53.00	1.05	Pb/U wmean conc.	0.0125	1.0000	0.5486	118
87004_28	1511.09	46.01	1487.70	32.93	1550.39	30.77	87004_28	1550.39	30.77	Pb/Pb wmean conc.	0.7475	1.0000	0.6919	65
87004_29	60.67	1.41	55.70	1.12	254.31	56.79	87004_29	55.70	1.12	Pb/U wmean conc.	0.0074	0.5000	0.7015	103
87004_30	57.06	1.11	53.62	1.06	201.77	49.36	87004_30	53.62	1.06	Pb/U wmean conc.	0.0118	1.0000	0.5911	116

	Preferred Ages - Sorted							Fitted Discordia						
Analysis_#	Preferred Age (Ma)	Absolute Error (±2σ)	Age Type	Fit Quality 1=best	Clean Quality 1=best	Pb204 Quality	2σ Conc. Scans	Age - Lower Intercept (Ma)	Age - Lower Intercept (±2σ)	Age - Upper Intercept (Ma)	Age - Upper Intercept (±2σ)	Regression Intercept	Regression Intercept (±1σ)	Regression Slope	Regression Slope (±1σ)
87004_14	50.19	1.11	Pb/U wmean conc.	0.0092	1.0000	0.5848	101	330.25	77.92	1638.50	64.98	0.027536	0.003274	0.065119	0.001420
87004_20	52.99	1.05	Pb/U wmean conc.	0.0125	1.0000	0.5486	118	52.75	1.52	4037.40	822.75	0.007336	0.000289	0.016503	0.005235
87004_22	52.99	1.05	Pb/U wmean conc.	0.0125	1.0000	0.5486	118	55.87	1.84	undefined	undefined	0.008773	0.000299	-0.001194	0.004756
87004_27	53.00	1.05	Pb/U wmean conc.	0.0125	1.0000	0.5486	118	847.20	104.21	1709.95	61.45	0.071427	0.004400	0.052957	0.001310
87004_2	53.06	1.05	Pb/U wmean conc.	0.0171	1.0000	0.5566	110	52.76	1.55	4048.38	816.05	0.007345	0.000286	0.016382	0.005182
87004_5	53.07	1.05	Pb/U wmean conc.	0.0171	1.0000	0.5566	110	672.10	256.51	1656.15	65.83	0.055711	0.009837	0.057728	0.002861
87004_7	53.07	1.05	Pb/U wmean conc.	0.0171	1.0000	0.5566	110	52.77	1.51	4053.51	807.28	0.007349	0.000284	0.016326	0.005146
87004_11	53.08	1.05	Pb/U wmean conc.	0.0171	1.0000	0.5566	110	57.76	4.90	1584.15	62.65	0.004738	0.000156	0.072836	0.000824
87004_21	53.09	1.05	Pb/U wmean conc.	0.0171	1.0000	0.5566	110	852.85	103.05	1711.25	60.65	0.071929	0.004453	0.052819	0.001325
87004_30	53.62	1.06	Pb/U wmean conc.	0.0118	1.0000	0.5911	116	54.18	2.07	undefined	undefined	0.008852	0.000217	-0.007485	0.003546
87004_24	53.63	1.07	Pb/U wmean conc.	0.0118	1.0000	0.5911	116	52.78	1.52	4041.96	808.10	0.007344	0.000280	0.016452	0.005072
87004_10	54.28	1.12	Pb/U wmean conc.	0.0104	1.0000	0.5195	117	54.20	1.99	undefined	undefined	0.008857	0.000217	-0.007561	0.003537
87004_12	54.28	1.12	Pb/U wmean conc.	0.0104	1.0000	0.5195	117	442.05	88.76	1490.35	46.17	0.034056	0.003143	0.067687	0.001139
87004_15	54.29	1.12	Pb/U wmean conc.	0.0104	1.0000	0.5195	117	51.11	1.76	undefined	undefined	0.008448	0.000127	-0.009457	0.001747
87004_3	55.60	1.12	Pb/U wmean conc.	0.0074	0.5000	0.7015	103	54.20	2.00	undefined	undefined	0.008865	0.000216	-0.007663	0.003524
87004_29	55.70	1.12	Pb/U wmean conc.	0.0074	0.5000	0.7015	103	undefined	undefined	undefined	undefined	-0.006759	0.005428	0.081679	0.001832
87004_17	65.68	1.46	Pb/U wmean conc.	0.0349	0.5000	0.5122	13	43.50	7.02	1269.85	56.23	0.003001	0.000223	0.086150	0.000965
87004_19	1335.93	29.25	Pb/U wmean conc.	0.0268	0.5000	0.4591	83	866.30	113.21	1715.10	63.12	0.073145	0.004571	0.052475	0.001360
87004_13	1360.06	29.85	Pb/U wmean conc.	0.9511	1.0000	0.6155	52	1321.72	36.17	4560.00	727.77	0.203957	0.007243	0.008824	0.002492
87004_16	1440.14	31.02	Pb/Pb wmean conc.	0.3726	1.0000	0.5300	78	53.26	1.50	undefined	undefined	0.008307	0.000236	-0.000182	0.004200
87004_26	1440.14	31.02	Pb/Pb wmean conc.	0.3726	1.0000	0.5300	78	52.80	1.54	4011.73	799.71	0.007329	0.000271	0.016788	0.004901
87004_25	1478.19	31.34	Pb/Pb wmean conc.	0.9792	0.5000	0.6242	34	53.26	1.53	undefined	undefined	0.008306	0.000235	-0.000156	0.004184
87004_28	1550.39	30.77	Pb/Pb wmean conc.	0.7475	1.0000	0.6919	65	874.60	111.17	1717.80	63.76	0.073908	0.004642	0.052256	0.001381
87004_6	1551.72	30.75	Pb/Pb wmean conc.	0.7475	1.0000	0.6919	66	54.21	1.38	undefined	undefined	0.010765	0.000200	-0.042298	0.003429
87004_23	1566.61	31.57	Pb/Pb wmean conc.	0.6048	1.0000	0.5505	50	887.40	108.47	1670.30	74.28	0.073275	0.004416	0.053216	0.001464
87004_9	1567.88	31.59	Pb/Pb wmean conc.	0.6048	1.0000	0.5505	49	undefined	undefined	undefined	undefined	-0.007934	0.005655	0.082087	0.001909
87004_18	1567.88	31.59	Pb/Pb wmean conc.	0.6048	1.0000	0.5505	49	53.27	1.50	undefined	undefined	0.008297	0.000233	0.000018	0.004141
87004_4	1568.30	31.55	Pb/Pb wmean conc.	0.6048	1.0000	0.5505	50	744.35	303.08	1668.90	85.06	0.061864	0.011199	0.055974	0.003255
87004_1	1638.50	64.98	upper int.	0.3665	0.5000	0.6986	0	56.05	1.73	undefined	undefined	0.008968	0.000278	-0.004147	0.004411
87004_8	rej 60	_C__	Pb/U wmean conc.	0.7362	0.2500	0.6096	32	54.19	1.37	undefined	undefined	0.010675	0.000195	-0.040734	0.003340

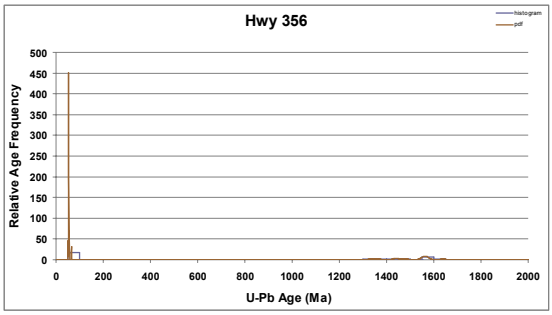
Hwy 356
histogram
pdf
Relative Age Frequency
U-Pb Age (Ma)

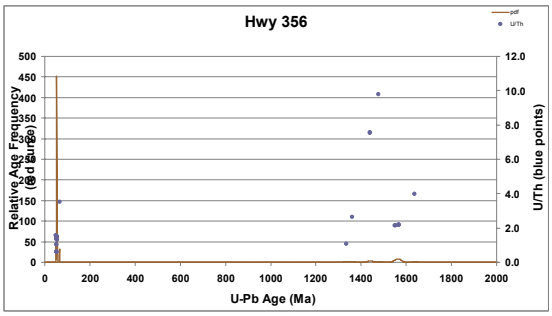
Hwy 356
pdf
U/Th
Relative Age Frequency (pdf curves)
U/Th (blue points)
U-Pb Age (Ma)

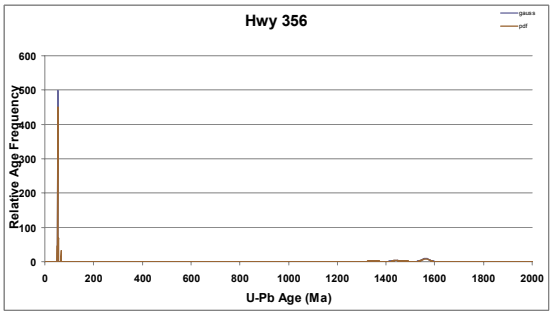
Hwy 356
gauss
pdf
Relative Age Frequency
U-Pb Age (Ma)

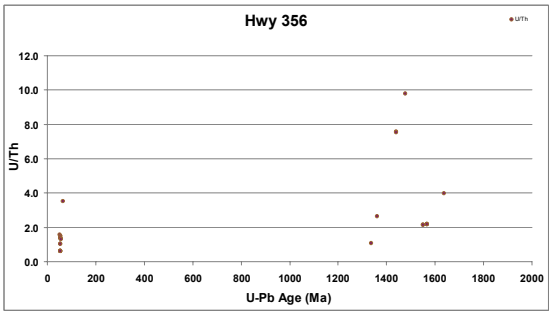
Hwy 356
U/Th
U/Th
U-Pb Age (Ma)

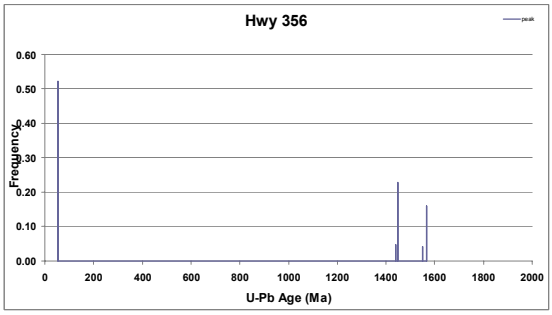
Hwy 356
peak
Frequency
U-Pb Age (Ma)

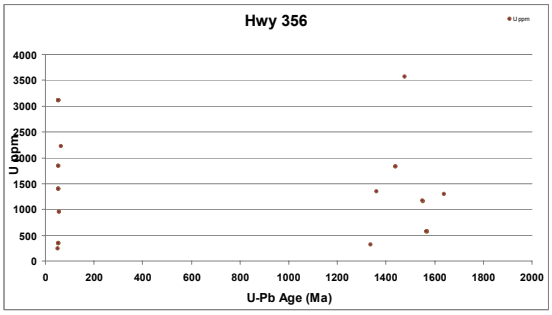
Hwy 356
U ppm
U ppm
U-Pb Age (Ma)

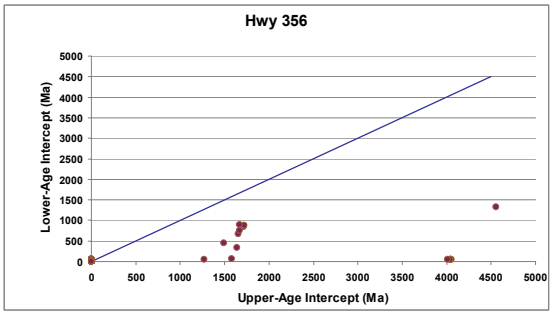
Hwy 356
Lower-Age Intercept (Ma)
Upper-Age Intercept (Ma)

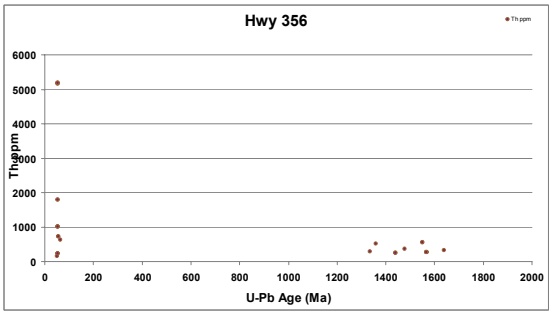
Hwy 356
Th ppm
Th ppm
U-Pb Age (Ma)

Sample Tgr/Tgb "stock": Santa Rita Stock, Chino pit

	Measured Isotopic Ratios							U and Th		
Analysis_#	207Pb/235Uc *	207Pb/235Uc * (±2σ)	206Pb/238U	206Pb/238U (±2σ)	207Pb/206Pb	207Pb/206Pb (±2σ)		U (ppm)	Th (ppm)	U/Th (ppm)
87005_1	0.0610	0.0014	0.0088	0.0002	0.0501	0.0012	-	1113.31	907.46	1.227
87005_2	0.0569	0.0080	0.0086	0.0004	0.0477	0.0069	-	748.67	553.23	1.353
87005_3	0.0624	0.0028	0.0089	0.0002	0.0508	0.0024	-	928.02	479.39	1.936
87005_4	0.0618	0.0015	0.0089	0.0002	0.0504	0.0014	-	1242.16	1177.93	1.055
87005_5	0.0597	0.0017	0.0089	0.0002	0.0486	0.0015	-	855.86	787.67	1.087
87005_6	0.0646	0.0017	0.0093	0.0002	0.0502	0.0014	-	1201.05	827.95	1.451
87005_7	0.0608	0.0020	0.0087	0.0002	0.0507	0.0018	-	1059.33	893.83	1.185
87005_8	0.0587	0.0030	0.0083	0.0002	0.0509	0.0028	-	675.08	637.11	1.060
87005_9	0.0612	0.0013	0.0089	0.0002	0.0499	0.0012	-	1208.00	1279.72	0.944
87005_10	0.0609	0.0014	0.0088	0.0002	0.0501	0.0012	-	1114.71	911.05	1.224
87005_11	0.0607	0.0017	0.0087	0.0002	0.0506	0.0015	-	776.20	491.74	1.578
87005_12	0.0641	0.0015	0.0091	0.0002	0.0513	0.0013	-	1317.97	1046.41	1.260
87005_13	0.0641	0.0015	0.0091	0.0002	0.0513	0.0013	-	1317.90	1046.84	1.259
87005_14	0.0633	0.0020	0.0090	0.0002	0.0509	0.0017	-	976.85	908.26	1.076
87005_15	0.0624	0.0028	0.0089	0.0002	0.0508	0.0024	-	929.06	482.06	1.927
87005_16	0.0630	0.0020	0.0088	0.0002	0.0518	0.0018	-	557.41	367.27	1.518
87005_17	0.0616	0.0015	0.0089	0.0002	0.0503	0.0013	-	1043.02	636.68	1.638
87005_18	0.0588	0.0014	0.0087	0.0002	0.0490	0.0013	-	1455.30	1318.53	1.104
87005_19	0.0654	0.0026	0.0092	0.0002	0.0510	0.0021	-	2216.37	2779.16	0.797
87005_20	0.0620	0.0027	0.0087	0.0002	0.0516	0.0024	-	730.44	486.89	1.500
87005_21	0.0612	0.0015	0.0085	0.0002	0.0521	0.0014	-	1329.46	1200.56	1.107
87005_22	0.0612	0.0015	0.0085	0.0002	0.0521	0.0014	-	1329.56	1201.13	1.107
87005_23	0.0624	0.0014	0.0088	0.0002	0.0513	0.0012	-	1178.44	845.89	1.393
87005_24	0.0623	0.0028	0.0089	0.0002	0.0508	0.0024	-	930.28	484.47	1.920
87005_25	0.0607	0.0017	0.0087	0.0002	0.0506	0.0015	-	775.94	494.74	1.568
87005_26	0.0621	0.0017	0.0088	0.0002	0.0507	0.0015	-	768.57	512.90	1.498
87005_27	0.0656	0.0026	0.0093	0.0002	0.0510	0.0021	-	2212.11	2786.51	0.794

	Apparent Ages					
Analysis_#	207Pb/235Uc *	207Pb/235Uc * (±2σ)	206Pb/238U	206Pb/238U (±2σ)	207Pb/206Pb	207Pb/206Pb (±2σ)
87005_1	60.10	1.41	56.50	1.13	198.73	57.30
87005_2	56.21	8.12	55.13	2.45	84.28	325.56
87005_3	61.50	2.89	57.10	1.26	233.95	107.24
87005_4	60.91	1.54	56.96	1.17	214.04	61.48
87005_5	58.89	1.74	57.09	1.16	127.18	71.07
87005_6	63.52	1.74	59.83	1.23	203.03	65.73
87005_7	59.97	2.03	55.69	1.18	229.45	79.85
87005_8	57.90	3.09	53.57	1.25	238.06	122.41
87005_9	60.32	1.33	57.12	1.15	190.25	54.72
87005_10	60.02	1.40	56.42	1.13	198.73	57.30
87005_11	59.79	1.69	55.76	1.16	223.53	68.28
87005_12	63.08	1.53	58.08	1.18	253.98	58.56
87005_13	63.08	1.53	58.08	1.18	253.98	58.56
87005_14	62.28	2.02	57.85	1.24	234.87	76.32
87005_15	61.42	2.88	57.02	1.26	233.95	107.24
87005_16	62.04	2.04	56.50	1.17	276.42	76.80
87005_17	60.72	1.51	57.05	1.18	206.92	60.41
87005_18	57.99	1.39	55.79	1.12	147.69	59.30
87005_19	64.35	2.66	59.32	1.43	241.11	95.45
87005_20	61.11	2.78	55.91	1.37	267.65	104.47
87005_21	60.34	1.55	54.68	1.17	290.49	61.45
87005_22	60.33	1.55	54.67	1.17	290.49	61.45
87005_23	61.42	1.39	56.46	1.17	254.67	55.37
87005_24	61.34	2.88	56.95	1.26	233.95	107.24
87005_25	59.82	1.69	55.79	1.16	223.53	68.28
87005_26	61.21	1.72	56.68	1.21	229.13	67.30
87005_27	64.47	2.67	59.43	1.43	241.11	95.45

	Preferred Ages						
Analysis_#	Preferred Age (Ma)	Absolute Error (±2σ)	Age Type	Fit Quality 1=best	Clean Quality 1=best	Pb204 Quality	2σ Conc. Scans
87005_1	56.50	1.13	Pb/U wmean conc.	0.0120	0.5000	0.8868	92
87005_2	55.13	2.45	Pb/U wmean conc.	0.0112	1.0000	0.5723	3
87005_3	57.10	1.26	Pb/U wmean conc.	0.0092	1.0000	0.7765	23
87005_4	56.96	1.17	Pb/U wmean conc.	0.0151	0.5000	0.7052	71
87005_5	57.09	1.16	Pb/U wmean conc.	0.0131	0.5000	0.7346	71
87005_6	59.83	1.23	Pb/U wmean conc.	0.0088	1.0000	0.7917	47
87005_7	55.69	1.18	Pb/U wmean conc.	0.0132	1.0000	0.8285	35
87005_8	53.57	1.25	Pb/U wmean conc.	0.0074	0.2500	0.7386	27
87005_9	57.12	1.15	Pb/U wmean conc.	0.0309	0.5000	0.5891	90
87005_10	56.42	1.13	Pb/U wmean conc.	0.0120	0.5000	0.8868	92
87005_11	55.76	1.16	Pb/U wmean conc.	0.0771	0.2000	0.7223	66
87005_12	58.08	1.18	Pb/U wmean conc.	0.0147	1.0000	0.6531	86
87005_13	58.08	1.18	Pb/U wmean conc.	0.0147	1.0000	0.6531	86
87005_14	57.85	1.24	Pb/U wmean conc.	0.0093	1.0000	0.7050	51
87005_15	57.02	1.26	Pb/U wmean conc.	0.0092	1.0000	0.7765	23
87005_16	56.50	1.17	Pb/U wmean conc.	0.0127	1.0000	0.6776	83
87005_17	57.05	1.18	Pb/U wmean conc.	0.0125	1.0000	0.7816	70
87005_18	55.79	1.12	Pb/U wmean conc.	0.0179	1.0000	0.6633	74
87005_19	59.32	1.43	Pb/U wmean conc.	0.0111	1.0000	0.7323	12
87005_20	55.91	1.37	Pb/U wmean conc.	0.0241	1.0000	0.5762	27
87005_21	54.68	1.17	Pb/U wmean conc.	0.0444	1.0000	0.8664	72
87005_22	54.67	1.17	Pb/U wmean conc.	0.0444	1.0000	0.8664	72
87005_23	56.46	1.17	Pb/U wmean conc.	0.0086	1.0000	0.7183	102
87005_24	56.95	1.26	Pb/U wmean conc.	0.0092	1.0000	0.7765	23
87005_25	55.79	1.16	Pb/U wmean conc.	0.0771	0.2000	0.7223	66
87005_26	56.68	1.21	Pb/U wmean conc.	0.0165	1.0000	0.7075	73
87005_27	59.43	1.43	Pb/U wmean conc.	0.0111	1.0000	0.7323	12

Preferred Ages - Sorted

Analysis_#	Preferred Age (Ma)	Absolute Error (±2σ)	Age Type	Fit Quality 1=best	Clean Quality 1=best	Pb204 Quality	2σ Conc. Scans
87005_22	54.67	1.17	Pb/U wmean conc.	0.0444	1.0000	0.8664	72
87005_21	54.68	1.17	Pb/U wmean conc.	0.0444	1.0000	0.8664	72
87005_2	55.13	2.45	Pb/U wmean conc.	0.0112	1.0000	0.5723	3
87005_7	55.69	1.18	Pb/U wmean conc.	0.0132	1.0000	0.8285	35
87005_18	55.79	1.12	Pb/U wmean conc.	0.0179	1.0000	0.6633	74
87005_20	55.91	1.37	Pb/U wmean conc.	0.0241	1.0000	0.5762	27
87005_10	56.42	1.13	Pb/U wmean conc.	0.0120	0.5000	0.8868	92
87005_23	56.46	1.17	Pb/U wmean conc.	0.0086	1.0000	0.7183	102
87005_1	56.50	1.13	Pb/U wmean conc.	0.0120	0.5000	0.8868	92
87005_16	56.50	1.17	Pb/U wmean conc.	0.0127	1.0000	0.6776	83
87005_26	56.68	1.21	Pb/U wmean conc.	0.0165	1.0000	0.7075	73
87005_24	56.95	1.26	Pb/U wmean conc.	0.0092	1.0000	0.7765	23
87005_4	56.96	1.17	Pb/U wmean conc.	0.0151	0.5000	0.7052	71
87005_15	57.02	1.26	Pb/U wmean conc.	0.0092	1.0000	0.7765	23
87005_17	57.05	1.18	Pb/U wmean conc.	0.0125	1.0000	0.7816	70
87005_5	57.09	1.16	Pb/U wmean conc.	0.0131	0.5000	0.7346	71
87005_3	57.10	1.26	Pb/U wmean conc.	0.0092	1.0000	0.7765	23
87005_9	57.12	1.15	Pb/U wmean conc.	0.0309	0.5000	0.5891	90
87005_14	57.85	1.24	Pb/U wmean conc.	0.0093	1.0000	0.7050	51
87005_12	58.08	1.18	Pb/U wmean conc.	0.0147	1.0000	0.6531	86
87005_13	58.08	1.18	Pb/U wmean conc.	0.0147	1.0000	0.6531	86
87005_19	59.32	1.43	Pb/U wmean conc.	0.0111	1.0000	0.7323	12
87005_27	59.43	1.43	Pb/U wmean conc.	0.0111	1.0000	0.7323	12
87005_6	59.83	1.23	Pb/U wmean conc.	0.0088	1.0000	0.7917	47
87005_8	rej 53	_C__	Pb/U wmean conc.	0.0074	0.2500	0.7386	27
87005_11	rej 55	_C__	Pb/U wmean conc.	0.0771	0.2000	0.7223	66
87005_25	rej 55	_C__	Pb/U wmean conc.	0.0771	0.2000	0.7223	66

Fitted Discordia

Age - Lower Intercept (Ma)	Age - Lower Intercept (±2σ)	Age - Upper Intercept (Ma)	Age - Upper Intercept (±2σ)	Regression Intercept	Regression Intercept (±1σ)	Regression Slope	Regression Slope (±1σ)
55.85	1.98	4560.00	366.20	0.008340	0.000238	0.006397	0.004087
55.55	2.42	undefined	undefined	0.009369	0.000214	-0.012706	0.005151
58.13	1.99	undefined	undefined	0.008832	0.000149	0.003844	0.002405
57.52	1.53	undefined	undefined	0.009924	0.000137	-0.016496	0.002179
57.81	2.13	4560.00	269.26	0.008599	0.000188	0.007001	0.003124
58.98	1.75	undefined	undefined	0.010250	0.000158	-0.017677	0.002734
55.72	1.56	4560.00	249.07	0.008128	0.000115	0.009809	0.001788
55.66	1.96	undefined	undefined	0.009218	0.000251	-0.009690	0.004709
56.33	2.03	4560.00	793.31	0.008319	0.000326	0.008026	0.005124
55.85	1.93	4560.00	259.71	0.008378	0.000233	0.005687	0.004008
56.60	1.97	undefined	undefined	0.008538	0.000160	0.004887	0.002588
58.22	1.76	4169.96	480.06	0.008183	0.000171	0.015085	0.002031
58.22	1.73	4168.85	483.56	0.008182	0.000170	0.015097	0.002626
57.75	2.09	undefined	undefined	0.008715	0.000241	0.004837	0.003400
58.10	2.03	undefined	undefined	0.008825	0.000148	0.003889	0.002382
57.03	1.79	undefined	undefined	0.009563	0.000179	-0.011698	0.002860
57.13	2.15	undefined	undefined	0.008721	0.000260	0.003135	0.003759
56.37	1.51	undefined	undefined	0.010119	0.000141	-0.023396	0.002543
54.25	2.47	3623.31	633.90	0.007263	0.000310	0.021678	0.003986
57.65	1.64	undefined	undefined	0.009438	0.000079	-0.007778	0.001252
53.05	2.06	3632.14	377.39	0.007108	0.000178	0.021558	0.002430
53.06	2.02	3635.57	377.71	0.007111	0.000178	0.021510	0.002429
58.09	1.62	undefined	undefined	0.011558	0.000328	-0.042568	0.005249
58.06	2.04	undefined	undefined	0.008819	0.000146	0.003884	0.002357
56.52	1.89	undefined	undefined	0.008517	0.000154	0.005062	0.002503
57.82	2.22	4560.00	793.04	0.008442	0.000269	0.009698	0.004397
54.37	2.46	3694.52	670.66	0.007333	0.000311	0.020694	0.004009

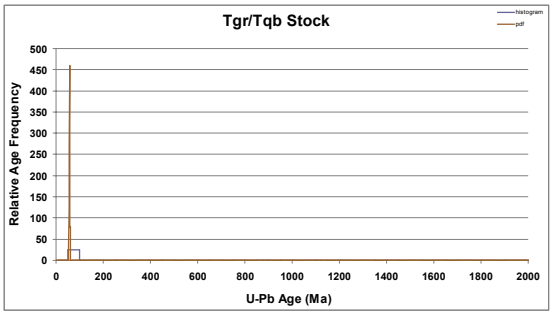
Tgr/Tqb Stock
histogram
pdf
Relative Age Frequency
U-Pb Age (Ma)

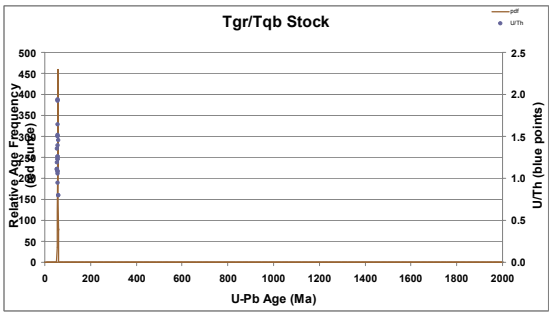
Tgr/Tqb Stock
pdf
U/Th
Relative Age Frequency (red curve)
U/Th (blue points)
U-Pb Age (Ma)

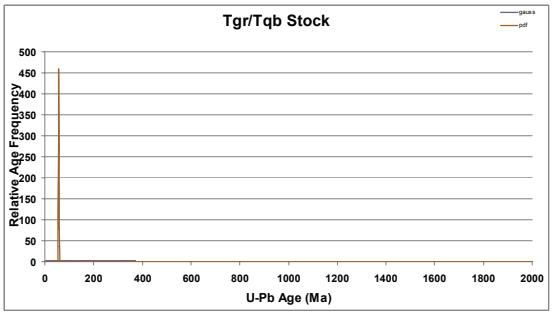
Tgr/Tqb Stock
gauss
pdf
Relative Age Frequency
U-Pb Age (Ma)

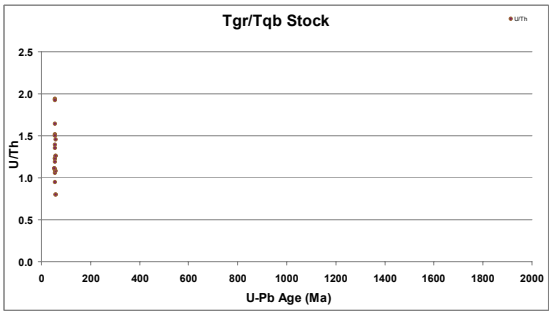
Tgr/Tqb Stock
U/Th
U/Th
U-Pb Age (Ma)

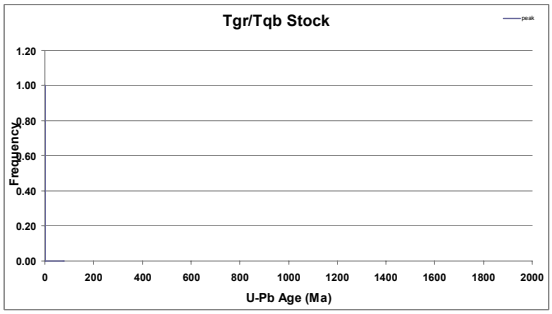
Tgr/Tqb Stock
peak
Frequency
U-Pb Age (Ma)

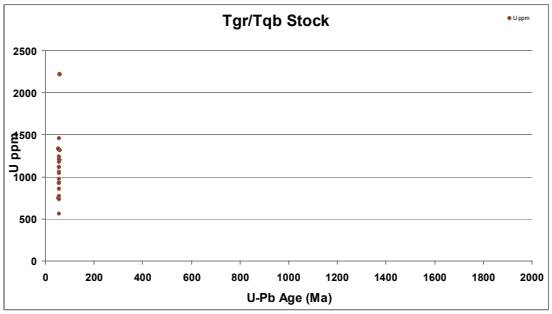
Tgr/Tqb Stock
U ppm
U ppm
U-Pb Age (Ma)

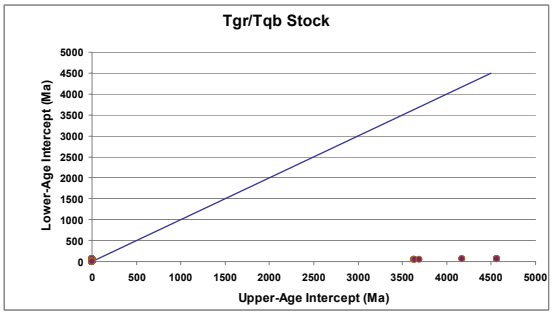
Tgr/Tqb Stock
Lower-Age Intercept (Ma)
Upper-Age Intercept (Ma)

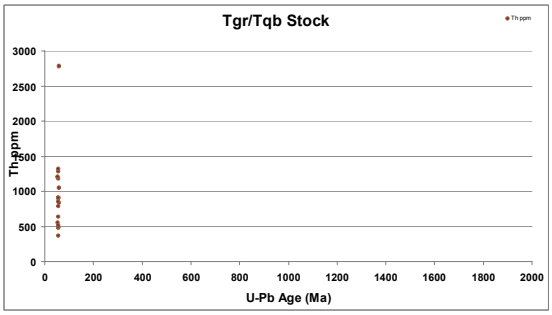
Tgr/Tqb Stock
Th ppm
Th ppm
U-Pb Age (Ma)

Sample Tli(?) Lee Hill: Quartz latite in Lee Hill pit

	Measured Isotopic Ratios							U and Th		
Analysis_#	207Pb/235Uc *	207Pb/235Uc * (±2σ)	206Pb/238U	206Pb/238U (±2σ)	207Pb/206Pb	207Pb/206Pb (±2σ)		U (ppm)	Th (ppm)	U/Th (ppm)
87006_1	0.0629	0.0019	0.0088	0.0002	0.0519	0.0016	-	1084.57	661.31	1.640
87006_2	0.0616	0.0014	0.0088	0.0002	0.0507	0.0013	-	1677.30	2255.95	0.744
87006_3	3.5167	0.0477	0.2624	0.0052	0.0974	0.0016	-	605.98	218.23	2.777
87006_4	3.7777	0.0506	0.2738	0.0054	0.1002	0.0017	-	708.84	384.13	1.845
87006_5	3.7767	0.0506	0.2738	0.0054	0.1002	0.0017	-	709.02	384.36	1.845
87006_6	0.0544	0.0065	0.0064	0.0002	0.0613	0.0075	-	156.00	176.15	0.886
87006_7	3.1462	0.0432	0.2555	0.0051	0.0895	0.0015	-	484.97	178.02	2.724
87006_8	0.0583	0.0011	0.0089	0.0002	0.0476	0.0011	-	2292.55	2070.29	1.107
87006_9	0.0583	0.0011	0.0089	0.0002	0.0476	0.0011	-	2293.03	2071.67	1.107
87006_10	3.6325	0.0480	0.2694	0.0053	0.0986	0.0016	-	940.25	214.47	4.384
87006_11	0.0616	0.0014	0.0088	0.0002	0.0507	0.0013	-	1679.15	2268.74	0.740
87006_12	undefined	undefined	undefined	undefined	undefined	undefined	-	1204.22	568.49	2.118
87006_13	2.6383	0.0414	0.2216	0.0046	0.0866	0.0016	-	1138.32	246.77	4.613
87006_14	0.0636	0.0025	0.0085	0.0002	0.0543	0.0022	-	1147.28	996.14	1.152
87006_15	3.0026	0.0399	0.2418	0.0048	0.0902	0.0015	-	1796.75	497.14	3.614
87006_16	0.0702	0.0026	0.0101	0.0002	0.0504	0.0020	-	447.53	185.92	2.407
87006_17	3.6449	0.0483	0.2698	0.0053	0.0987	0.0016	-	944.94	214.14	4.413
87006_18	0.0615	0.0014	0.0088	0.0002	0.0507	0.0013	-	1681.07	2279.59	0.737
87006_19	3.1802	0.0421	0.2504	0.0049	0.0923	0.0015	-	563.63	192.46	2.929
87006_20	0.0629	0.0019	0.0088	0.0002	0.0519	0.0016	-	1084.53	667.80	1.624
87006_21	0.0629	0.0019	0.0088	0.0002	0.0519	0.0016	-	1084.53	668.16	1.623
87006_22	3.4005	0.0490	0.2568	0.0052	0.0962	0.0017	-	1173.94	327.46	3.585
87006_23	2.9392	0.0391	0.2410	0.0047	0.0887	0.0015	-	1226.84	532.46	2.304
87006_24	3.0626	0.0405	0.2466	0.0048	0.0902	0.0015	-	2007.49	218.68	9.180
87006_25	0.0634	0.0029	0.0087	0.0002	0.0532	0.0026	-	1993.22	2403.92	0.829

	Apparent Ages					
Analysis_#	207Pb/235Uc *	207Pb/235Uc * (±2σ)	206Pb/238U	206Pb/238U (±2σ)	207Pb/206Pb	207Pb/206Pb (±2σ)
87006_1	61.91	1.88	56.31	1.15	281.60	71.26
87006_2	60.71	1.39	56.37	1.18	228.96	56.81
87006_3	1530.97	47.85	1501.87	33.27	1574.69	31.02
87006_4	1588.01	50.77	1560.29	34.59	1627.36	30.50
87006_5	1587.81	50.75	1559.93	34.59	1627.36	30.50
87006_6	53.78	6.56	41.32	1.37	648.15	252.92
87006_7	1444.07	43.39	1466.86	32.70	1413.97	32.06
87006_8	57.53	1.16	56.89	1.18	81.39	52.09
87006_9	57.52	1.16	56.88	1.18	81.39	52.09
87006_10	1556.68	48.13	1537.89	34.05	1598.09	30.38
87006_11	60.66	1.39	56.32	1.18	228.96	56.81
87006_12	undefined	undefined	undefined	undefined	undefined	undefined
87006_13	1311.37	41.62	1290.27	29.70	1351.36	35.85
87006_14	62.63	2.52	54.59	1.17	384.49	90.71
87006_15	1408.29	40.13	1396.05	30.60	1430.39	31.19
87006_16	68.92	2.63	64.99	1.37	215.61	88.49
87006_17	1559.39	48.42	1539.70	34.13	1600.47	30.43
87006_18	60.60	1.39	56.27	1.18	228.96	56.81
87006_19	1452.36	42.34	1440.34	31.55	1473.46	30.96
87006_20	61.92	1.88	56.32	1.15	281.60	71.26
87006_21	61.92	1.88	56.32	1.15	281.60	71.26
87006_22	1504.52	49.17	1473.68	33.37	1552.65	32.50
87006_23	1392.08	39.36	1391.71	30.45	1397.16	31.37
87006_24	1423.40	40.72	1420.97	31.13	1430.26	31.07
87006_25	62.43	2.97	55.71	1.28	338.65	106.83

	Preferred Ages						
Analysis_#	Preferred Age (Ma)	Absolute Error (±2σ)	Age Type	Fit Quality 1=best	Clean Quality 1=best	Pb204 Quality	2σ Conc. Scans
87006_1	56.31	1.15	Pb/U wmean conc.	0.0385	1.0000	0.7578	53
87006_2	56.37	1.18	Pb/U wmean conc.	0.0222	1.0000	0.7818	53
87006_3	1574.69	31.02	Pb/Pb wmean conc.	0.2672	0.5000	0.7059	128
87006_4	1627.36	30.50	Pb/Pb wmean conc.	0.0785	1.0000	0.8050	107
87006_5	1627.36	30.50	Pb/Pb wmean conc.	0.0785	1.0000	0.8050	107
87006_6	41.32	1.37	Pb/U wmean conc.	0.0199	0.5000	0.7351	41
87006_7	1466.86	32.70	Pb/U wmean conc.	0.6572	0.2000	0.6086	99
87006_8	56.89	1.18	Pb/U wmean conc.	0.0088	1.0000	0.7179	99
87006_9	56.88	1.18	Pb/U wmean conc.	0.0088	1.0000	0.7179	99
87006_10	1598.09	30.38	Pb/Pb wmean conc.	0.1245	1.0000	0.8094	77
87006_11	56.32	1.18	Pb/U wmean conc.	0.0222	1.0000	0.7818	53
87006_12	1763.60	176.01	upper int.	0.6808	1.0000	0.7863	0
87006_13	1290.27	29.70	Pb/U wmean conc.	0.2497	1.0000	0.7173	15
87006_14	54.59	1.17	Pb/U wmean conc.	0.0284	0.5000	0.6325	26
87006_15	1430.39	31.19	Pb/Pb wmean conc.	0.5419	1.0000	0.7593	69
87006_16	64.99	1.37	Pb/U wmean conc.	0.0073	0.5000	0.7411	90
87006_17	1600.47	30.43	Pb/Pb wmean conc.	0.1245	1.0000	0.8094	70
87006_18	56.27	1.18	Pb/U wmean conc.	0.0222	1.0000	0.7818	53
87006_19	1473.46	30.96	Pb/Pb wmean conc.	0.0641	0.5000	0.5154	108
87006_20	56.32	1.15	Pb/U wmean conc.	0.0385	1.0000	0.7578	53
87006_21	56.32	1.15	Pb/U wmean conc.	0.0385	1.0000	0.7578	53
87006_22	1552.65	32.50	Pb/Pb wmean conc.	0.1792	1.0000	0.6553	21
87006_23	1391.71	30.45	Pb/U wmean conc.	0.2008	1.0000	0.6032	72
87006_24	1430.26	31.07	Pb/Pb wmean conc.	0.2454	1.0000	0.7407	79
87006_25	55.71	1.28	Pb/U wmean conc.	0.0856	0.5000	0.7357	9

Preferred Ages - Sorted

Analysis_#	Preferred Age (Ma)	Absolute Error (±2σ)	Age Type	Fit Quality 1=best	Clean Quality 1=best	Pb204 Quality	2σ Conc. Scans
87006_6	41.32	1.37	Pb/U wmean conc.	0.0199	0.5000	0.7351	41
87006_14	54.59	1.17	Pb/U wmean conc.	0.0284	0.5000	0.6325	26
87006_25	55.71	1.28	Pb/U wmean conc.	0.0856	0.5000	0.7357	9
87006_18	56.27	1.18	Pb/U wmean conc.	0.0222	1.0000	0.7818	53
87006_1	56.31	1.15	Pb/U wmean conc.	0.0385	1.0000	0.7578	53
87006_11	56.32	1.18	Pb/U wmean conc.	0.0222	1.0000	0.7818	53
87006_20	56.32	1.15	Pb/U wmean conc.	0.0385	1.0000	0.7578	53
87006_21	56.32	1.15	Pb/U wmean conc.	0.0385	1.0000	0.7578	53
87006_2	56.37	1.18	Pb/U wmean conc.	0.0222	1.0000	0.7818	53
87006_9	56.88	1.18	Pb/U wmean conc.	0.0088	1.0000	0.7179	99
87006_8	56.89	1.18	Pb/U wmean conc.	0.0088	1.0000	0.7179	99
87006_16	64.99	1.37	Pb/U wmean conc.	0.0073	0.5000	0.7411	90
87006_13	1290.27	29.70	Pb/U wmean conc.	0.2497	1.0000	0.7173	15
87006_23	1391.71	30.45	Pb/U wmean conc.	0.2008	1.0000	0.6032	72
87006_24	1430.26	31.07	Pb/Pb wmean conc.	0.2454	1.0000	0.7407	79
87006_15	1430.39	31.19	Pb/Pb wmean conc.	0.5419	1.0000	0.7593	69
87006_19	1473.46	30.96	Pb/Pb wmean conc.	0.0641	0.5000	0.5154	108
87006_22	1552.65	32.50	Pb/Pb wmean conc.	0.1792	1.0000	0.6553	21
87006_3	1574.69	31.02	Pb/Pb wmean conc.	0.2672	0.5000	0.7059	128
87006_10	1598.09	30.38	Pb/Pb wmean conc.	0.1245	1.0000	0.8094	77
87006_17	1600.47	30.43	Pb/Pb wmean conc.	0.1245	1.0000	0.8094	70
87006_4	1627.36	30.50	Pb/Pb wmean conc.	0.0785	1.0000	0.8050	107
87006_5	1627.36	30.50	Pb/Pb wmean conc.	0.0785	1.0000	0.8050	107
87006_12	1763.60	176.01	upper int.	0.6808	1.0000	0.7863	0
87006_7	rej 1466	_c___	Pb/U wmean conc.	0.6572	0.2000	0.6086	99

Fitted Discordia

Age - Lower Intercept (Ma)	Age - Lower Intercept (±2σ)	Age - Upper Intercept (Ma)	Age - Upper Intercept (±2σ)	Regression Intercept	Regression Intercept (±1σ)	Regression Slope	Regression Slope (±1σ)
56.65	1.86	undefined	undefined	0.009459	0.000168	-0.011041	0.002385
56.03	2.17	4560.00	746.67	0.008257	0.000290	0.008355	0.004805
1393.50	82.78	2235.80	255.97	0.141222	0.006667	0.033989	0.001872
1505.46	51.23	3054.78	608.44	0.189360	0.011873	0.021646	0.003119
1505.65	51.22	3065.43	578.81	0.189800	0.011825	0.021523	0.003107
39.57	2.15	3807.07	298.62	0.005392	0.000140	0.019270	0.001697
undefined	undefined	undefined	undefined	-0.037313	0.005557	0.093461	0.001532
58.00	2.80	1831.00	595.34	0.005291	0.000550	0.063753	0.009425
58.00	2.61	1835.49	569.90	0.005299	0.000551	0.063597	0.009433
811.85	179.24	1717.80	68.89	0.068815	0.007249	0.053406	0.002003
55.95	2.14	4560.00	700.41	0.008255	0.000288	0.008166	0.004776
759.30	142.85	1763.60	176.01	0.065867	0.007123	0.053165	0.002995
1251.45	35.92	3202.57	360.05	0.162116	0.005237	0.021459	0.001823
55.03	1.82	undefined	undefined	0.008568	0.000092	0.000118	0.000926
undefined	undefined	undefined	undefined	-0.037424	0.006763	0.092402	0.002308
66.47	2.29	undefined	undefined	0.010334	0.000158	0.000470	0.001951
831.85	174.82	1724.80	70.50	0.070670	0.007100	0.052859	0.001965
55.87	2.10	4560.00	655.52	0.008248	0.000287	0.008075	0.004778
1265.90	186.02	1885.05	461.14	0.112915	0.015131	0.041981	0.004820
56.52	1.88	undefined	undefined	0.009516	0.000167	-0.012373	0.002375
56.52	1.82	undefined	undefined	0.009519	0.000167	-0.012457	0.002377
1363.80	51.62	2693.85	330.19	0.158276	0.007914	0.027314	0.002314
496.85	197.02	1450.65	56.03	0.037353	0.006917	0.067759	0.002416
886.65	517.53	1585.15	238.22	0.070166	0.018483	0.055417	0.006071
53.51	1.42	undefined	undefined	0.008101	0.000049	0.004362	0.000502

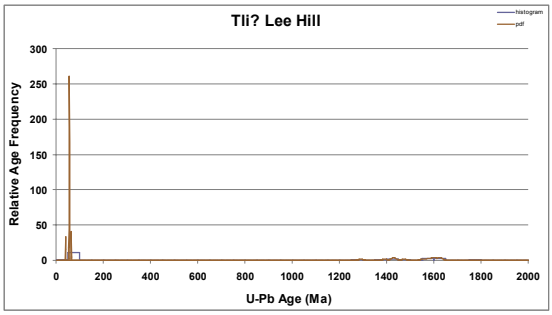
Tli? Lee Hill
histogram
pdf
Relative Age Frequency
U-Pb Age (Ma)

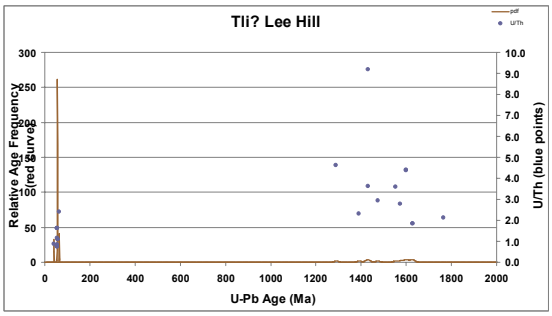
Tli? Lee Hill
pdf
U/Th
Relative Age Frequency (red curves)
U/Th (blue points)
U-Pb Age (Ma)

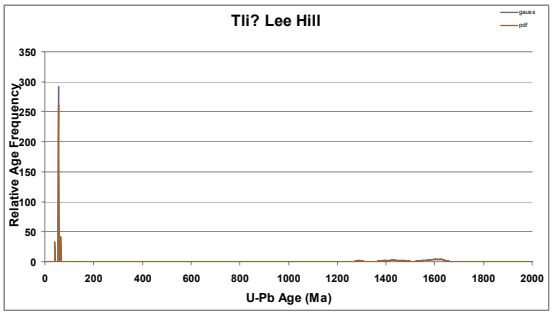
Tli? Lee Hill
gauss
pdf
Relative Age Frequency
U-Pb Age (Ma)

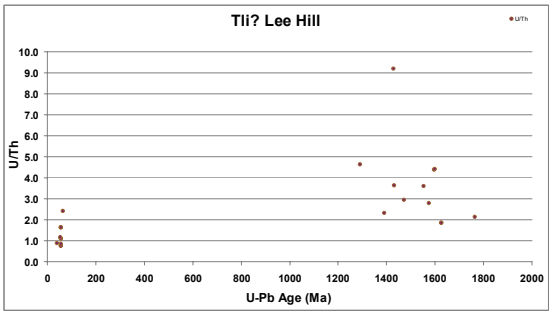
Tli? Lee Hill
U/Th
U/Th
U-Pb Age (Ma)

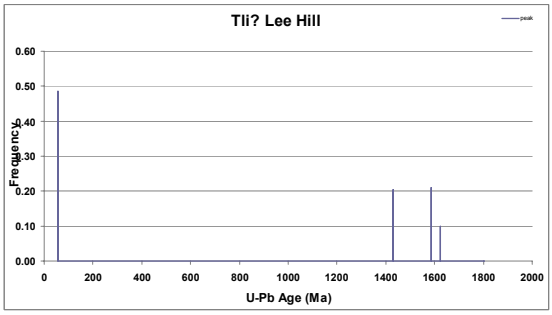
Tli? Lee Hill
peak
Frequency
U-Pb Age (Ma)

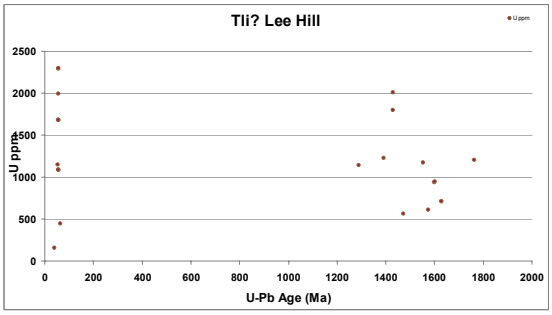
Tli? Lee Hill
U ppm
U ppm
U-Pb Age (Ma)

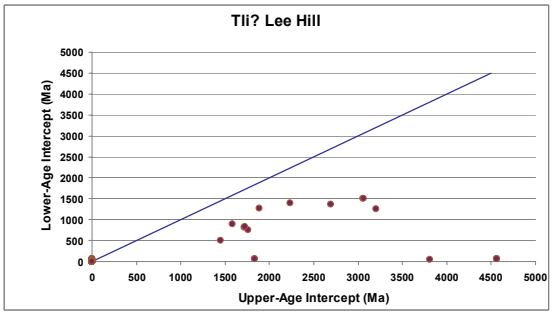
Tli? Lee Hill
Lower-Age Intercept (Ma)
Upper-Age Intercept (Ma)

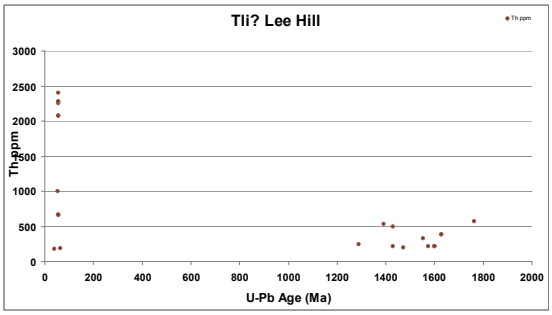
Tli? Lee Hill
Th ppm
Th ppm
U-Pb Age (Ma)

Sample Townsite: Santa Rita stock, Townsite Island

	Measured Isotopic Ratios							U and Th		
Analysis_#	207Pb/235Uc *	207Pb/235Uc * (±2σ)	206Pb/238U	206Pb/238U (±2σ)	207Pb/206Pb	207Pb/206Pb (±2σ)		U (ppm)	Th (ppm)	U/Th (ppm)
87007_1	0.0579	0.0019	0.0084	0.0002	0.0500	0.0018	-	1572.64	1485.34	1.059
87007_2	0.0604	0.0013	0.0086	0.0002	0.0512	0.0012	-	1568.74	1942.27	0.808
87007_3	0.0657	0.0018	0.0087	0.0002	0.0550	0.0016	-	925.98	443.03	2.090
87007_4	0.0593	0.0013	0.0086	0.0002	0.0501	0.0012	-	1644.87	1896.01	0.868
87007_5	0.0567	0.0025	0.0081	0.0002	0.0509	0.0024	-	593.88	843.39	0.704
87007_6	0.0633	0.0017	0.0090	0.0002	0.0509	0.0015	-	703.22	630.16	1.116
87007_7	0.0656	0.0018	0.0086	0.0002	0.0550	0.0016	-	927.03	444.23	2.087
87007_8	0.0567	0.0025	0.0081	0.0002	0.0509	0.0024	-	594.42	845.76	0.703
87007_9	0.0566	0.0025	0.0081	0.0002	0.0509	0.0024	-	594.61	846.58	0.702
87007_10	0.0577	0.0011	0.0088	0.0002	0.0476	0.0011	-	2315.32	2121.22	1.092
87007_11	0.0615	0.0016	0.0089	0.0002	0.0499	0.0015	-	920.53	1053.56	0.874
87007_12	0.0605	0.0013	0.0088	0.0002	0.0499	0.0012	-	1221.55	1330.01	0.918
87007_13	2.8357	0.0396	0.2294	0.0046	0.0896	0.0015	-	1508.03	553.31	2.725
87007_14	0.0614	0.0016	0.0089	0.0002	0.0499	0.0015	-	921.61	1056.19	0.873
87007_15	0.0609	0.0017	0.0084	0.0002	0.0523	0.0016	-	1263.33	1446.70	0.873
87007_16	2.8296	0.0396	0.2292	0.0046	0.0895	0.0015	-	1510.65	553.43	2.730
87007_17	0.0654	0.0018	0.0086	0.0002	0.0550	0.0016	-	929.78	447.29	2.079
87007_18	0.0600	0.0013	0.0085	0.0002	0.0512	0.0012	-	1578.57	1969.32	0.802
87007_19	0.0641	0.0020	0.0092	0.0002	0.0506	0.0017	-	804.97	756.82	1.064
87007_20	0.0566	0.0013	0.0085	0.0002	0.0480	0.0012	-	1646.02	1633.79	1.007
87007_21	0.0587	0.0014	0.0086	0.0002	0.0496	0.0013	-	1639.36	1375.55	1.192
87007_22	0.0608	0.0018	0.0089	0.0002	0.0492	0.0016	-	1042.18	624.80	1.668
87007_23	0.0560	0.0020	0.0083	0.0002	0.0490	0.0018	-	713.45	673.25	1.060
87007_24	0.0653	0.0018	0.0086	0.0002	0.0550	0.0016	-	931.84	449.49	2.073
87007_25	0.0628	0.0017	0.0089	0.0002	0.0509	0.0015	-	706.08	638.91	1.105
87007_26	0.0564	0.0013	0.0085	0.0002	0.0480	0.0012	-	1651.10	1645.04	1.004
87007_27	0.0562	0.0025	0.0080	0.0002	0.0509	0.0024	-	599.02	863.35	0.694
87007_28	0.0610	0.0016	0.0088	0.0002	0.0499	0.0015	-	927.53	1069.29	0.867
87007_29	0.0602	0.0013	0.0087	0.0002	0.0499	0.0012	-	1228.82	1347.98	0.912
87007_30	0.0651	0.0018	0.0086	0.0002	0.0550	0.0016	-	932.00	450.18	2.070

	Apparent Ages							Preferred Ages						
Analysis_#	207Pb/235Uc *	207Pb/235Uc * (±2σ)	206Pb/238U	206Pb/238U (±2σ)	207Pb/206Pb	207Pb/206Pb (±2σ)	Analysis_#	Preferred Age (Ma)	Absolute Error (±2σ)	Age Type	Fit Quality 1=best	Clean Quality 1=best	Pb204 Quality	2σ Conc. Scans
87007_1	57.18	1.95	53.97	1.16	194.70	80.90	87007_1	53.97	1.16	Pb/U wmean conc.	0.0287	0.5000	0.7793	25
87007_2	59.56	1.31	54.88	1.10	249.21	54.04	87007_2	54.88	1.10	Pb/U wmean conc.	0.0062	1.0000	0.5203	98
87007_3	64.60	1.81	55.58	1.14	411.79	64.79	87007_3	55.58	1.14	Pb/U wmean conc.	0.0140	0.5000	0.6018	84
87007_4	58.52	1.30	55.04	1.11	197.69	55.14	87007_4	55.04	1.11	Pb/U wmean conc.	0.0258	1.0000	0.5851	64
87007_5	56.02	2.57	51.83	1.15	238.52	105.85	87007_5	51.83	1.15	Pb/U wmean conc.	0.0278	0.3333	0.6404	37
87007_6	62.29	1.74	57.76	1.20	237.81	67.41	87007_6	57.76	1.20	Pb/U wmean conc.	0.0374	0.3333	0.6404	80
87007_7	64.52	1.80	55.51	1.14	411.79	64.79	87007_7	55.51	1.14	Pb/U wmean conc.	0.0140	0.5000	0.6018	84
87007_8	55.97	2.57	51.77	1.15	238.52	105.85	87007_8	51.77	1.15	Pb/U wmean conc.	0.0278	0.3333	0.6404	37
87007_9	55.95	2.57	51.75	1.15	238.52	105.85	87007_9	51.75	1.15	Pb/U wmean conc.	0.0278	0.3333	0.6404	37
87007_10	57.01	1.15	56.35	1.17	81.39	52.09	87007_10	56.35	1.17	Pb/U wmean conc.	0.0088	1.0000	0.7179	99
87007_11	60.56	1.65	57.25	1.29	192.66	67.11	87007_11	57.25	1.29	Pb/U wmean conc.	0.0071	0.5000	0.6020	84
87007_12	59.67	1.31	56.42	1.13	190.25	54.72	87007_12	56.42	1.13	Pb/U wmean conc.	0.0309	0.5000	0.5891	90
87007_13	1365.04	39.86	1331.57	29.81	1416.87	32.39	87007_13	1331.57	29.81	Pb/U wmean conc.	0.0124	0.5000	0.6368	144
87007_14	60.49	1.65	57.18	1.29	192.66	67.11	87007_14	57.18	1.29	Pb/U wmean conc.	0.0071	0.5000	0.6020	84
87007_15	60.01	1.75	54.16	1.23	299.76	68.72	87007_15	54.16	1.23	Pb/U wmean conc.	0.0070	1.0000	0.6166	53
87007_16	1363.40	39.84	1330.38	29.81	1414.46	32.44	87007_16	1330.38	29.81	Pb/U wmean conc.	0.0124	0.5000	0.6368	141
87007_17	64.34	1.80	55.32	1.14	411.79	64.79	87007_17	55.32	1.14	Pb/U wmean conc.	0.0140	0.5000	0.6018	84
87007_18	59.21	1.30	54.55	1.09	249.21	54.04	87007_18	54.55	1.09	Pb/U wmean conc.	0.0062	1.0000	0.5203	98
87007_19	63.11	2.03	58.91	1.26	221.17	75.91	87007_19	58.91	1.26	Pb/U wmean conc.	0.0180	1.0000	0.6092	63
87007_20	55.87	1.29	54.77	1.12	98.85	57.95	87007_20	54.77	1.12	Pb/U wmean conc.	0.0205	0.5000	0.5954	74
87007_21	57.90	1.46	54.92	1.19	176.85	62.52	87007_21	54.92	1.19	Pb/U wmean conc.	0.0545	1.0000	0.6432	58
87007_22	59.92	1.86	57.40	1.31	159.51	75.31	87007_22	57.40	1.31	Pb/U wmean conc.	0.0077	1.0000	0.5742	41
87007_23	55.34	1.98	53.20	1.17	146.66	85.25	87007_23	53.20	1.17	Pb/U wmean conc.	0.0127	1.0000	0.5441	53
87007_24	64.20	1.80	55.18	1.13	411.79	64.79	87007_24	55.18	1.13	Pb/U wmean conc.	0.0140	0.5000	0.6018	84
87007_25	61.84	1.74	57.43	1.20	234.42	67.85	87007_25	57.43	1.20	Pb/U wmean conc.	0.0374	0.3333	0.6404	79
87007_26	55.71	1.29	54.58	1.12	98.85	57.95	87007_26	54.58	1.12	Pb/U wmean conc.	0.0205	0.5000	0.5954	74
87007_27	55.49	2.54	51.24	1.14	238.52	105.85	87007_27	51.24	1.14	Pb/U wmean conc.	0.0278	0.3333	0.6404	37
87007_28	60.13	1.64	56.75	1.28	192.66	67.11	87007_28	56.75	1.28	Pb/U wmean conc.	0.0071	0.5000	0.6020	84
87007_29	59.35	1.30	56.02	1.12	190.25	54.72	87007_29	56.02	1.12	Pb/U wmean conc.	0.0309	0.5000	0.5891	90
87007_30	64.07	1.79	55.01	1.13	413.11	64.59	87007_30	55.01	1.13	Pb/U wmean conc.	0.0140	0.5000	0.6018	85

	Preferred Ages - Sorted							Fitted Discordia						
Analysis_#	Preferred Age (Ma)	Absolute Error (±2σ)	Age Type	Fit Quality 1=best	Clean Quality 1=best	Pb204 Quality	2σ Conc. Scans	Age - Lower Intercept (Ma)	Age - Lower Intercept (±2σ)	Age - Upper Intercept (Ma)	Age - Upper Intercept (±2σ)	Regression Intercept	Regression Intercept (±1σ)	Regression Slope	Regression Slope (±1σ)
87007_27	51.24	1.14	Pb/U wmean conc.	0.0278	0.3333	0.6404	37	54.85	1.60	undefined	undefined	0.008803	0.000149	-0.004649	0.002747
87007_9	51.75	1.15	Pb/U wmean conc.	0.0278	0.3333	0.6404	37	53.65	1.69	3379.82	650.59	0.006982	0.000277	0.026364	0.004448
87007_8	51.77	1.15	Pb/U wmean conc.	0.0278	0.3333	0.6404	37	54.06	2.04	undefined	undefined	0.008259	0.000150	0.002983	0.001946
87007_5	51.83	1.15	Pb/U wmean conc.	0.0278	0.3333	0.6404	37	54.75	1.61	undefined	undefined	0.008285	0.000144	0.004417	0.002229
87007_23	53.20	1.17	Pb/U wmean conc.	0.0127	1.0000	0.5441	53	52.41	1.71	undefined	undefined	0.008377	0.000085	-0.004009	0.001564
87007_1	53.97	1.16	Pb/U wmean conc.	0.0287	0.5000	0.7793	25	57.50	1.73	undefined	undefined	0.009354	0.000133	-0.006777	0.001988
87007_15	54.16	1.23	Pb/U wmean conc.	0.0070	1.0000	0.6166	53	54.00	2.03	undefined	undefined	0.008255	0.000150	0.002891	0.001948
87007_18	54.55	1.09	Pb/U wmean conc.	0.0062	1.0000	0.5203	98	52.36	1.72	undefined	undefined	0.008363	0.000086	-0.003903	0.001577
87007_26	54.58	1.12	Pb/U wmean conc.	0.0205	0.5000	0.5954	74	52.35	1.72	undefined	undefined	0.008358	0.000086	-0.003872	0.001582
87007_20	54.77	1.12	Pb/U wmean conc.	0.0205	0.5000	0.5954	74	57.55	3.12	1686.50	578.16	0.004945	0.000574	0.068965	0.009908
87007_2	54.88	1.10	Pb/U wmean conc.	0.0062	1.0000	0.5203	98	56.90	1.48	4560.00	203.70	0.008283	0.000087	0.010115	0.001445
87007_21	54.92	1.19	Pb/U wmean conc.	0.0545	1.0000	0.6432	58	55.81	2.00	4560.00	429.00	0.008448	0.000344	0.004396	0.005475
87007_30	55.01	1.13	Pb/U wmean conc.	0.0140	0.5000	0.6018	85	1327.43	34.05	4560.00	439.01	0.214773	0.010161	0.005148	0.003557
87007_4	55.04	1.11	Pb/U wmean conc.	0.0258	1.0000	0.5851	64	56.83	1.47	4560.00	221.30	0.008274	0.000088	0.010104	0.001461
87007_24	55.18	1.13	Pb/U wmean conc.	0.0140	0.5000	0.6018	84	54.00	1.58	3880.81	421.14	0.007412	0.000138	0.018310	0.002349
87007_17	55.32	1.14	Pb/U wmean conc.	0.0140	0.5000	0.6018	84	1325.60	34.33	4560.00	583.50	0.213389	0.010828	0.005545	0.003795
87007_7	55.51	1.14	Pb/U wmean conc.	0.0140	0.5000	0.6018	84	53.83	2.06	undefined	undefined	0.008243	0.000150	0.002638	0.001967
87007_3	55.58	1.14	Pb/U wmean conc.	0.0140	0.5000	0.6018	84	53.35	1.68	3388.41	574.46	0.006949	0.000268	0.025227	0.004330
87007_29	56.02	1.12	Pb/U wmean conc.	0.0309	0.5000	0.5891	90	57.46	2.17	4560.00	767.09	0.008325	0.000260	0.010825	0.003828
87007_10	56.35	1.17	Pb/U wmean conc.	0.0088	1.0000	0.7179	99	55.28	1.55	undefined	undefined	0.009014	0.000140	-0.007178	0.002446
87007_12	56.42	1.13	Pb/U wmean conc.	0.0309	0.5000	0.5891	90	55.40	1.60	undefined	undefined	0.008725	0.000178	-0.001664	0.002915
87007_28	56.75	1.28	Pb/U wmean conc.	0.0071	0.5000	0.6020	84	58.92	2.15	2504.72	419.60	0.006589	0.000281	0.043419	0.005072
87007_14	57.18	1.29	Pb/U wmean conc.	0.0071	0.5000	0.6020	84	55.10	2.23	4275.67	619.68	0.007801	0.000204	0.014052	0.003593
87007_11	57.25	1.29	Pb/U wmean conc.	0.0071	0.5000	0.6020	84	53.70	2.01	undefined	undefined	0.008232	0.000152	0.002447	0.001992
87007_22	57.40	1.31	Pb/U wmean conc.	0.0077	1.0000	0.5742	41	57.08	1.82	undefined	undefined	0.009300	0.000142	-0.007020	0.002143
87007_25	57.43	1.20	Pb/U wmean conc.	0.0374	0.3333	0.6404	79	55.13	1.54	undefined	undefined	0.009005	0.000142	-0.007428	0.002491
87007_6	57.76	1.20	Pb/U wmean conc.	0.0374	0.3333	0.6404	80	51.97	1.80	undefined	undefined	0.008268	0.000092	-0.003279	0.001710
87007_19	58.91	1.26	Pb/U wmean conc.	0.0180	1.0000	0.6092	63	56.50	1.51	4560.00	266.64	0.008220	0.000097	0.010168	0.001616
87007_16	1330.38	29.81	Pb/U wmean conc.	0.0124	0.5000	0.6368	141	55.35	2.07	4560.00	787.73	0.008281	0.000367	0.006107	0.005879
87007_13	1331.57	29.81	Pb/U wmean conc.	0.0124	0.5000	0.6368	144	53.57	2.07	undefined	undefined	0.008222	0.000153	0.002271	0.002022

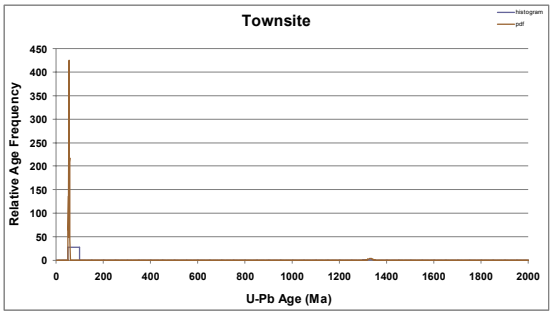
Townsite
histogram
pdf
Relative Age Frequency
U-Pb Age (Ma)

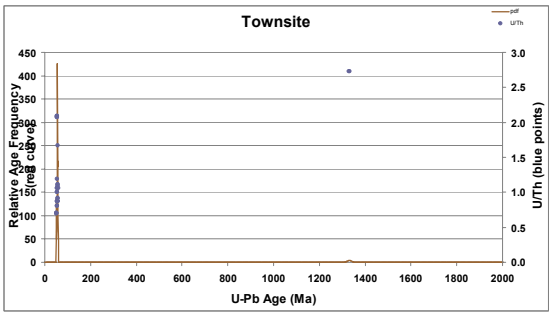
Townsite
pdf
U/Th
Relative Age Frequency (red curve)
U/Th (blue points)
U-Pb Age (Ma)

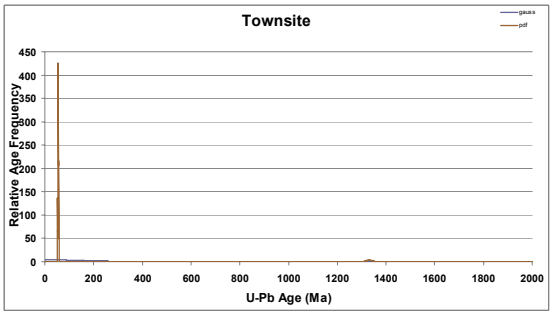
Townsite
gauss
pdf
Relative Age Frequency
U-Pb Age (Ma)

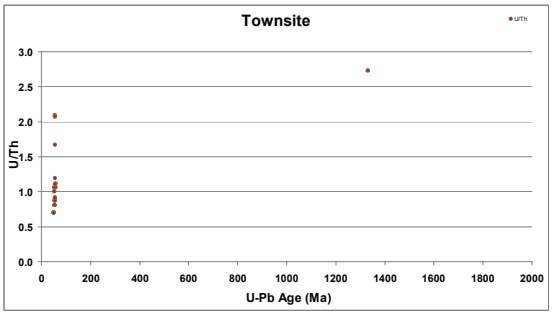
Townsite
U/Th
U/Th
U-Pb Age (Ma)

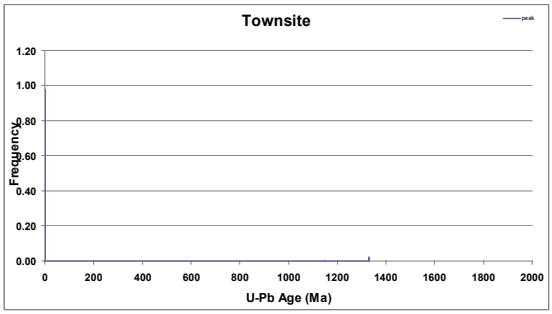
Townsite
peak
Frequency
U-Pb Age (Ma)

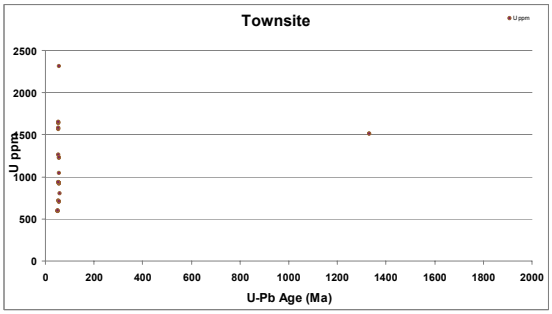
Townsite
U ppm
U ppm
U-Pb Age (Ma)


Townsite
Lower-Age Intercept (Ma)
Upper-Age Intercept (Ma)

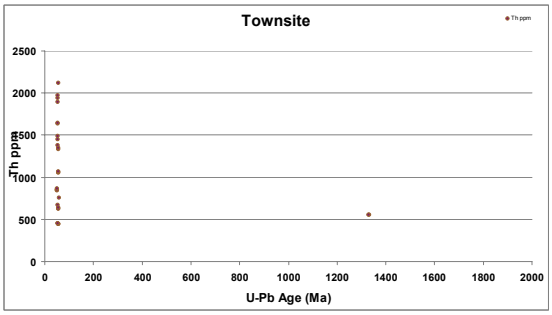
Townsite
Th ppm
Th ppm
U-Pb Age (Ma)